Limit state analysis: Adaptive finite element upper and lower bound approach to the evaluation of the limit load of a Von Mises rigid-plastic material body in plane stress.

Cordero, Raymundo

UNIVERSITY OF WALES SWANSEA

SCHOOL OF ENGINEERING

LIMIT STATE ANALYSIS: ADAPTIVE FINITE ELEMENT UPPER AND LOWER BOUND APPROACH TO THE EVALUATION OF THE LIMIT LOAD OF A VON MISES RIGID-PLASTIC MATERIAL BODY IN PLANE STRESS

RAYMUNDO CORDERO
Ingeniero Civil (ITESM Campus Monterrey, Mexico)
Maestria en Ingenieria Estructural (ITESM Campus Monterrey, Mexico)

THESIS SUBMITTED TO THE UNIVERSITY OF WALES IN CANDIDATURE FOR THE DEGREE OF DOCTOR OF PHILOSOPHY

SEPTEMBER 2005

To Angel, Dinorah, Adrian, and especially Leticia

To my parents

Acknowledgements

First of all, I would like to thank Professor Javier Bonet for the excellent advise, for his availability for discussion and support at every step, for his kind contributions to my personal knowledge in the field, his optimism and good manners to treat all sorts of problems during the course of this research work.

I also thank Professor Jaume Peraire, at Massachusetts Institute of Technology, Boston, for his contribution to the present work on the flux equilibration technique, which has been essential to the attainment of the present solution.

Thanks to my friends and colleagues at the Civil Engineering Department at my home university, Tecnologico de Monterrey at Campus Monterrey, for their support and encouragement to pursue this postgraduate degree.

A special remembrance and gratitude to Dr. Felipe Orozco, whose kind advise and always friendly words will guide me forever.

Thanks to all my friends in Swansea, you helped make things kinder.

Thanks to my parents, Don Efrain y Doña Victoria, for their everlasting care and consideration.

I would like to express my deepest love and consideration to my wife Leticia and kids Adrian, Dinorah, and to Angel, who shares with us every moment. You represent the stone on which my highest aims and wishes for the future are founded. Thanks for your unlimited love and support, and the gift of your smiles every day, but especially in the hardest of times.

This research work was funded by Consejo Nacional de Ciencia y Tecnologia, CONACYT, Mexico, under scholarship reference number: 161990/170856. Their support and great service has been essential to the completion of the present work.

I would also like to acknowledge and thank ever so much the support given by the PEX program, at Tecnologico de Monterrey, Campus Monterrey, and especially to the Department of Civil Engineering, and the Engineering and Architectural Division.

Summary

A new approach to the computation of the limit load of a Von Mises rigid-plastic material structure modelled in plane stress is assessed. Most international design codes require the engineer to establish the safety of a structure for a given set of design loads under the so-called limit state conditions. The limit state represents the failure point at which the structure begins to exhibit unbounded deformations. Under limit state conditions, the deformation of the solids tend to concentrate on thin failure bands, known as slip-lines. This makes the finite element analysis a challenging task as the mesh needs to be adapted to capture these bands accurately. In order to achieve this, an adaptive technique is required whereby the error produced in each finite element is measured and if required the element is subdivided automatically. In order to measure this error both an upper and lower bound of the exact solution need to be evaluated. In this thesis, a novel technology to obtain the lower bound is derived and implemented together with mesh adaptivity technology. A lower bound is found from a state of stresses in equilibrium with the external forces. The proposed technique obtains such equilibrated state using the stresses obtained during the upper bound evaluation. These stresses, although not strictly in equilibrium, can be balanced using procedures available in the literature. The present aim of the research project is to develop numerical technology based on the finite element method to calculate the limit state of two-dimensional solids in plane stress. The upper bound theorem of limit analysis is implemented by means of a Lagrangian optimization technique solved by the Newton-Raphson method with Line Search. A control parameter to deal with the singularity of the tangent stiffness matrix due to the yielding condition is used along the range of admissible rate of deformations for a rigid-plastic material. The lower bound theorem is then applied by performing a technique to equilibrate the inter-element tractions, kinematically solving a sequence of local problems using the equilibrated tractions as an updated load input, which lets us determine the element-wise contribution to both the upper and lower bounds. An adaptive technique is then implemented, based on the elemental contributions to the difference between the upper bound and the lower bound of the collapse multiplier. Both non-adaptive and adaptive results are evaluated. Results show a good performance of the solution technique, both in comparison with well known plane stress bound values and also in the graphical output obtained in the form of refined regions which describe the occurrence of slip-line patterns and/or localized yielding regions.

Contents

Chapter 3: Finite element upper bound evaluation

Chapter 4: Lower bound evaluation

Chapter 5: Implementation and adaptivity

Chapter 6: Test cases and applications

Chapter 7: Conclusions

Notation

σ_y	: yield stress
f	: yield function
σ_{ij}, s_{ij}	: stress tensor / deviatoric stress tensor
J_1, J_2, J_3	: deviatoric stress tensor invariants
$\dot{\varepsilon}^e_{ij}, \dot{\varepsilon}^p_{ij}$	: elastic / plastic strain-rate tensor
$\dot{\lambda}$	: scalar proportionality factor
$\sigma_1, \sigma_2, \sigma_3$	: principal stresses
C_{ijkl}	: elastic constitutive tensor
D_p	: plastic dissipation rate
$\dot{\varepsilon}'^p_{ij}$	: plastic strain-rate deviator tensor
$\dot{\bar{\varepsilon}}$	: equivalent strain-rate
$b_i, \mathbf{b}$	: body forces field / vector per unit volume
$t_i, \mathbf{t}$	: external forces field / vector per unit area
$n_i, \mathbf{n}$	: surface normal vector
$\dot{u}_i, \dot{\mathbf{u}}$	: generalized velocity field / vector
$v_i, \mathbf{v}$	: collapse velocity field / vector
$\gamma^c, \gamma^s, \gamma^k$	: exact / static / kinematic collapse load multiplier
Π_p	: total plastic work-rate or internal plastic work-rate
Π_t	: external forces work-rate
$\boldsymbol{B}$	: space of statically admissible stresses
$\boldsymbol{C}$	: reduced space of kinematically admissible velocities
$\boldsymbol{d}$	: 2-dimensional strain-rate tensor
$\mathbb{C}_{ijkl}$	: tangent plastic modulus
$Y, \hat{Y}, Y_H, Y_h$	: generalized / broken / coarse / fine velocities space
$\overline{Y}, \hat{\overline{Y}}, \overline{Y}_H, \overline{Y}_h$	: reduced generalized / broken / coarse / fine velocities space
$\mathbf{K}$	: tangent matrix
$\mathbf{D}_p$	: 2-dimensional plastic constitutive matrix
$\gamma, \gamma_H, \gamma_h$	: generalized / coarse / fine collapse multiplier
$\overline{Z}^e_h$	: local reduced velocities space
v^e_h	: elemental collapse velocity field form the global solution on $\overline{Y}_h$
$\hat{v}^e_h$	: elemental collapse velocity field from the local solution on $\overline{Z}^e_h$
g, g_e	: total / elemental gap

Chapter 1

Introduction

"Galileo's (1638) calculation of the collapse load of a cantilever beam, though inaccurate due to wrong assumptions, is an indicator of the early efforts to analyze and handle the required elements for the design of mayor structures. The first realistic approach to the static analysis of failure along with concepts like the yield condition was made by Coulomb in 1776 while studying earth-retaining walls for military fortifications. Many other pioneers in the study of plasticity theory like Lüders (1854), Tresca (1868), St. Vénant (1870), Lévy (1870), Rankine (1876), Bauschinger (1881), Considére (1891) Engesser (1895), Hartmann (1896) and Mohr (1900) have greatly contributed to the present development. The anticipation of the static theorem of limit analysis by Rankine in 1859 and Kötter in 1899, and its intuitive enunciations can be found in the work of Kazinczy (1914) and Kist (1917). During the first quarter of the 20th century the concepts of yield surface, flow rules, slip lines and plastic friction appeared due to the work of von Kármán (1909), von Mises (1913), Hencky (1924) and Reuß (1930). The static and kinematic theorems of limit analysis were in general first proven in a Russian conference proceedings article by Gvozdev (1938), long unknown in the West. At about the same time, the static shakedown theorem was first proven by Melan (1936), being anticipated a few years by himself and Bleich (1932). The fact that Melan's theorem implies the static theorem of limit analysis was recognized much later. Concepts and theory that comprise the general multiaxial stress-strain relations, normality and convexity, maximization of plastic energy dissipation, limit state theorems, shakedown, optimum design, plastic hinges, yield line theory of plates and slip line theory were established shortly after World War II by Shanley (1947), Hill (1950), Drucker (1950), Greenberg and Prager (1951), Prager and Hodge (1951), Symonds and Neal (1951), Koiter (1953) and others. The last half of the 20th century was a period of rapid refinement and extensive ramification, which continue at an unrelenting pace until today."

Extracted from *Inelastic Analysis of Structures*, Jirásek & Bazant [1], 2001

1.1 Overview

The search for the precise collapse load and mode for a particular structure has posed an engineering problem for a long time. More than two centuries of theory development and the establishment of mathematical and mechanical concepts in plasticity, put together into computational-oriented approaches to the solutions have led engineering to a sound stage.

Today, engineering analysis and design codes encourage the use of limit state theory, by the use of concepts and practical procedures leading to increased efficiency not only in the analysis and design phase but also in achieving efficient structures by reducing the amount of material needed for a good and safe life-long performance. However, analysis and design tools to solve complex structural problems are not available in general, so the search and development of new approaches and practical procedures is an ongoing process in the engineering community. The present work is aimed to contribute to this effort, by seeking sound but practical new procedures.

The present research work is founded on the *theory of limit state analysis* to assess a new approach to the application of the theorems of limit analysis in order to determine accurate values for the limit load and a description of the failure mode of structures in *plane stress*. The present approach uses a *finite element* discretized context to implement a Lagrangian optimization solution via a Newtonian iteration procedure, to determine the collapse load multiplier over a kinematically admissible velocity field. An *upper bound* to the collapse load is then obtained from this analysis, while a *lower bound* is determined by recovering a continuous stress field along inter-element faces, corresponding to a statically admissible stress field, in order to compute local contributions to the capacity of the structure to withstand load within plastically admissible stress conditions.

1.2 Recent work on Limit State Analysis

A general recount of the state of the art in the field of *limit analysis* is given in the following paragraphs, with the intention of covering the main aspects of the recent developments and the aim of constructing a standpoint for the present proposals and

developments. Some of the references are presented as material of a general interest, while others possess a clear relevant role on the present developments. In any case no intention of being exhaustive is in place.

The literature review for the present research project has taken us to many of the recent efforts towards the determination of limit loads and failure modes, some of them for general application mainly as theoretical developments, and many others for application to specific material and modeling conditions, typically implemented by the finite element method and applied to specific types of structures. Some of the recent achievements of interest in the context of limit analysis lead to the work by Andersen and Christiansen (1995) [2], in which a collapse state is computed for a rigid-plastic material with a linearized von Mises yield condition. An infeasible point invariant of the dual affine scaling algorithm for linear programming is used. This work takes us back to a study by Christiansen (1981) [3] in which a family of discretizations of the mixed form based on the continuous duality problem are proposed. A linear programming solution approach is taken in this implementation, with a linearized yield condition, and a plane strain application is presented. Important aspects on duality in limit analysis and the mixed discretization approach are set out in this work.

In 1995, Liu, Cen and Xu (1995) [4] presented an upper bound solution for limit analysis in 3-D of rigid-plastic structures formulated as a discrete nonlinear mathematical programming problem with equality constraints using the finite element method, as well as in Zhang and Lu (1995) [5] which introduces an algorithm for limit analysis of perfectly plastic bodies, based on the finite element method and mathematical programming, using an ellipsoid yield surface for both upper and lower bound of the limit load. Also in 1995, Sloan and Kleeman (1995) [6] developed a method for computing rigorous upper bounds in plane strain with discontinuity velocity fields, using a linear three-noded triangular element with six unknown nodal velocities and a fixed number of plastic multiplier rates, as the solution of a linear programming problem. The objective function corresponds to the dissipation power. The proposed formulation in this reference permits inter-element velocity discontinuities and shearing directions are found automatically. This work is related to

a previous work by Yu, Sloan and Kleeman (1992) [7], in which a quadratic element is used.

In 1996, Hamilton, Mackenzie, Shi and Boyle (1996) [8] presented a simple method for determining lower bound limit loads for thin shell structures based on elastic compensation. The same year Shi, Boyle Mackenzie and Hamilton (1996) [9] presented an approximate lower bound approach for the estimation of limit states in frame structures, based also on elastic compensation. During this same year, Borges, Zouain and Huespe (1996) [10] published an interesting paper in which they proposed a new mathematical programming algorithm as a sequence of Newtonian iterations to solve the discrete version of the limit analysis problem, where plastic behavior is described by means of a multimodal yield function. In this paper, they present a mixed and kinematic finite element formulation and implementation, with corresponding numerical results for large-scale models.

In 1997, Queiroz and Ponter (1997) [11,12] presented a theoretical and numerical applications work on the theory and fundamental relations for the development of a kinematic formulation for the finite element shakedown and limit analysis of axi-symmetrical shells made of elastic-perfectly plastic material. In the same year, Capsoni and Corradi (1997) [13] presented a procedure for the finite element computation of the limit load of rigid-perfectly plastic solids based on the kinematic theorem of limit analysis, formulated to reduce the problem to a search of the essentially free minimum of a convex but not everywhere differentiable function. Damkilde and Krenk (1997) [14] presented a system for limit state analysis and material optimization, formulated as a finite element problem with stress-based elements, using the lower bound theorem where an optimal stress distribution or an optimal material distribution is determined. This same year, Pontes, Borges, Zouain and Lopes (1997) [15] presented an algorithm for limit analysis with a mixed finite element approach with application to geotechnical problems, aimed to deal with the singularity at the apex of the cone-shaped yield surface, and based on the direct application of the sub-differential concept to the flow law, essentially different from the Lagrange multipliers technique.

In middle 1997, Ponter and Carter (1997) [16] presented a method to determine the limit state of a perfectly plastic body for the von Mises yield condition, producing a sequence of incompressible linear elastic solutions defined with a spatially varying shear modulus leading to a sequence of upper bounds to the limit load, which converge to the limit state solution. The solution is based on the Rayleigh Ritz method. A *pseudo-lower* bound solution was also proposed.

In 1998, Chen, Liu, Cen and Xu (1998) [17] presented a work based on the concepts of limit load and reference stress for the analysis of defective pipelines under multi-loading systems. In 1999, Christiansen and Andersen (1999) [18] proposed a new approach to limit analysis by using a quadratic yield condition in a unified approach to the static and kinematic principles, where stress and flow fields are determined simultaneously, as in Christiansen (1981) [3]. An exact convex yield condition is used and the general case of unbounded yield set is treated. The discretization is completely defined by the yield condition and the finite element spaces for stress and velocity. Incompressibility is implicitly contained in the yield condition, due to duality. An efficient optimization procedure lets solve for finer meshes, so that an *a posteriori* error analysis on the collapse multiplier is suggested. Also by this time, Capsoni (1999) [19] presented a formulation for finite element plane strain limit analysis of rigid perfectly plastic solids governed by the von Mises plasticity condition, based on the kinematic theorem of limit analysis formulated as a minimum problem for a convex and non-smooth dissipation functional. Chen, Liu, Cen and Xu (1999) [20] presented another part of their work on the computation of the limit load and reference stress of 3-D structures under multi-loading systems. On the same year, Chen and Shu (1999) [21] presented a related work for the limit load but using intermediate variables obtained from lower and upper bound limit analysis. Heitzer and Staat (1999) [22] presented a first implementation of limit and shakedown analysis for perfectly plastic material into a general purpose finite element program.

In 1999 also, Huh, Lee and Yang (1999) [23] presented a general algorithm for limit solutions of plastic flow developed with the use of finite element limit analysis. Chen and Shu (1999) [24] presented a previously related work applying the 3-D lower an upper bound limit analysis to pipelines with one or two part-through slots of various geometrical configurations. A related work on defective pipelines was presented by

Liu, Cen, Chen and Xu (2000) [25] in which a numerical scheme path for radial loading was adopted to deal with complex multi-loading systems, using a direct iterative algorithm for solving the optimization formulation. Meanwhile, a theoretical approach to limit analysis was presented by Lenci (2001) [26], in which it is established that while an existence theorem for the statical problem can be obtained by convex analysis, no similar result is provided for the kinematical problem and must be obtained independently. An illustration of the reasons to use a Suquet's relaxed version of the kinematical approach is given, and an existence theorem is proved showing that the dissipation functional is lower semi-continuous.

Ponter, Fuschi and Engelhardt (2000) [27] presented a paper describing a generalization of the programming method presented by Ponter and Carter (1997) [16] for the evaluation of optimal upper bounds on the limit load of a body composed of rigid perfectly plastic material. The method is based upon similar principles to the elastic compensation but re-interpreted as a non-linear programming method. In the same year, Poulsen and Damkilde (2000) [28] presented a finite element formulation of rigid-plastic plates subjected to in-plane forces using stress-based elements and linear programming. It was formulated as a lower bound solution and the dual variables are interpreted as displacements. Both load and material optimization were formulated. Capsoni, Corradi and Vena (2001) [29] presented a paper on the limit analysis of orthotropic structures based on Hill's yield condition, for which an explicit expression of the dissipation power in terms of strain rates is established; previously in the same year they presented another paper [30] on the limit analysis of anisotropic structures based on the kinematic theorem.

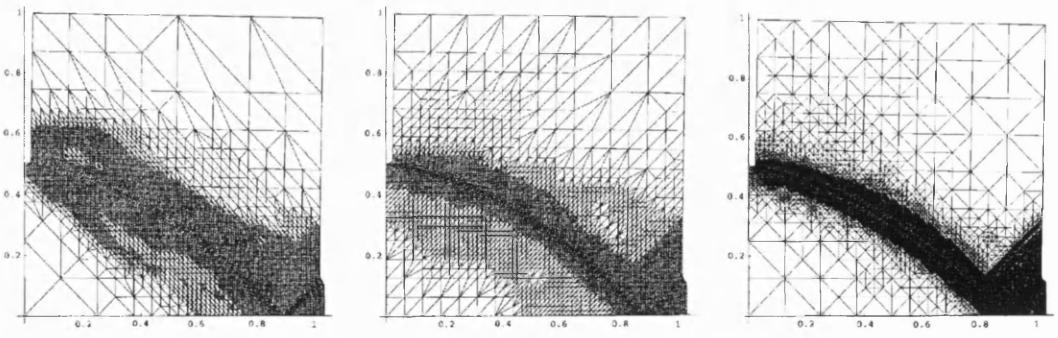

Figure 1.1 Different mesh configurations and adaptive refinement criteria for the slotted block problem in plane strain, by Christiansen and Pendersen [31]

In the same year, Christiansen and Pedersen (2001) [31], presented a strategy for the automatic refinement in limit analysis, applied to the computational methods described in Christiansen and Andersen (1999) [18] (see figure 1.1). The refinement strategy is based on deformations and on the slack in the yield condition. With piecewise linear functions for the velocities, a norm over the strain rate is proposed as a refinement criteria indicator. Test cases are presented in plane strain. Also in 2001, Chen and Ponter [32] presented a paper for a recently developed method for 3-D shakedown and limit analysis implementing the upper bound linear matching method into the commercial finite element code ABAQUS. Chen and Shu (2001) [33] presented a simplified numerical method for both the lower and upper bound limit analysis of 3-D structures applied to the analysis of pipelines with multi-defects. Staat and Heitzer (2001) [34] presented the paper: *LISA – a European project for FEM-based limit and shakedown analysis*, which shows the efforts unified in a new European research project to develop methods based on the static and kinematic theorems of limit analysis to solve large-scale analysis problems, which can be later extended towards realistic material modeling. In 2001 as well, an adaptive mesh refinement procedure for the finite element method in limit analysis was presented by Borges, Zouain, Costa and Feijoo (2001) [35], in which an *a posteriori* indicator based on the local directional interpolation error and on a recovering scheme to compute second derivatives of the finite element solution is used. Numerical examples in plane strain and plane stress are presented (see figure 1.2).

More recent work by Lyamin and Sloan (2001,2002) [36,37] has resulted in a new rigorous upper bound (2001) and lower bound (2002) formulations using linear finite elements and non-linear programming, which provides a solution tool without the need to linearize the yield surface, as it permits nonlinear constraints on the unknowns, making 3D modeling to be implemented with no special difficulties. The problem is solved using a fast quasi-Newton method whose iteration count is independent of the mesh size.

In 2003, Krabbenhoft and Damkilde (2003) [38] proposed an algorithm to solve the nonlinear programming problem generated from the discrete lower bound limit analysis problem. In this method the need to linearize the yielding criteria is avoided.

It consists of a general interior point method in the sense that no particular finite element discretization or yield criterion is required.

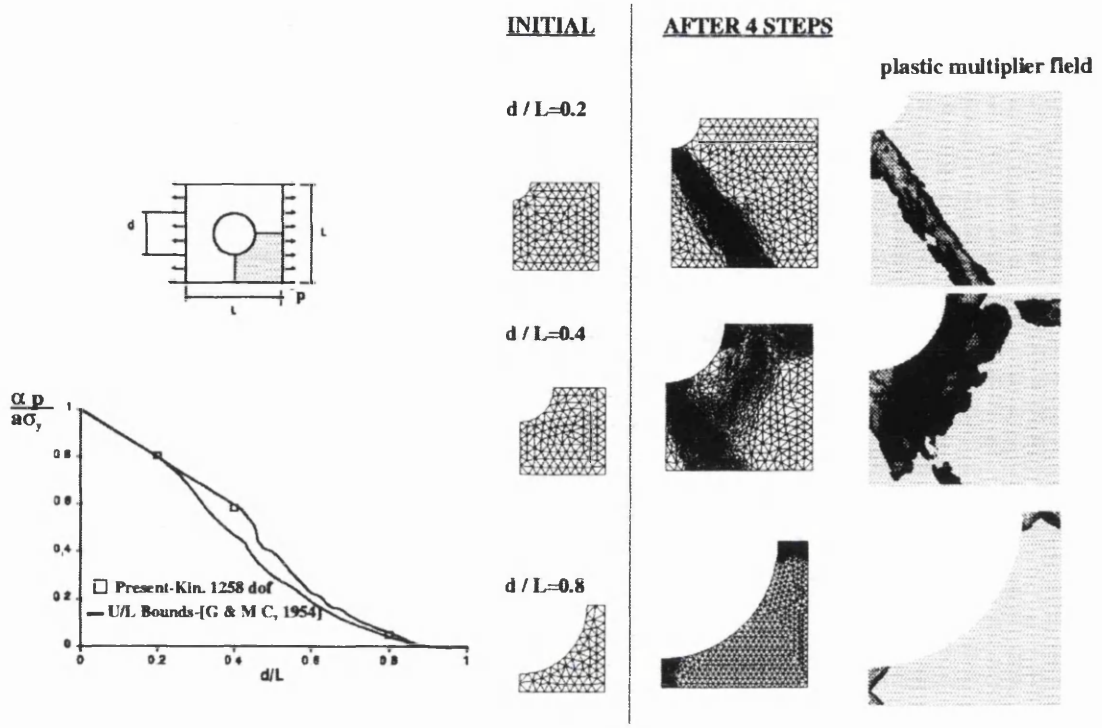

Figure 1.2 Plane-stress test case by Borges, Zouain, Costa and Feijoo [35]

The most recent reference work is the one by Ciria and Peraire (2004) [39], in which the limit analysis problem is resolved through powerful optimization techniques based on Second-Order Cone Programming, a cutting-edge extension to non-linear programming and part of recent developments on *interior point* techniques. A bounds approach based on duality principles is used in this work and is well supported by numerical results in plane stress and plane strain (see figure 1.3 below).

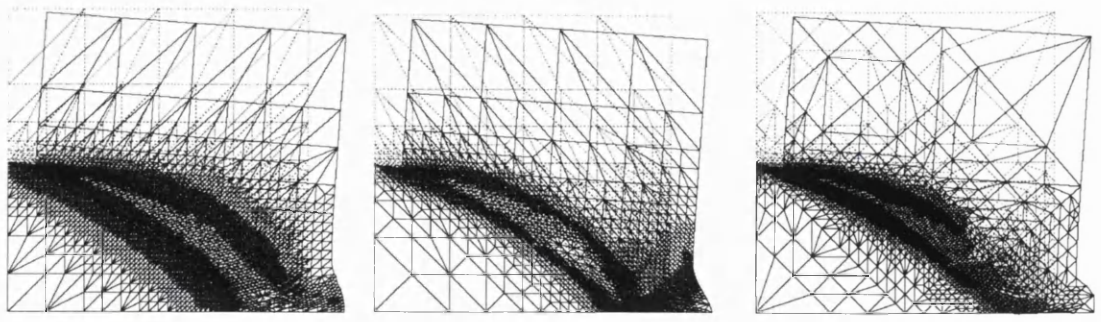

Figure 1.3 Different mesh configurations for the slotted block problem in plane strain after adaptive refinement, by Ciria and Peraire [39]

The previous summarized literature review gives a panorama of the recent efforts and interests towards the development of realistic tools for limit analysis including extensions to shakedown analysis, clearly showing the interests which motivates the present research work.

1.3 Scope of the thesis

Owing to the recent and continued interest in limit state analysis in the past, a noticeable series of innovative proposals are being developed and tested nowadays. From these proposals a distinction can be made between those which rely on a formal use of grand scale optimization techniques, ranging from linear programming to non-linear programming and second-order cone programming. In these applications, a great deal of effort is put on the correct formulation of an objective function and the constraints which reflect the material, geometry, the static, kinematic and yield conditions, and parameters that conform a well posed mechanical boundary value problem in limit analysis. Typically a finite element type of dicretization is used. Instances of these type of analysis are the ones presented recently by Lyamin and Sloan [36,37] and Ciria and Peraire [39] which yield rigorous upper and lower bounds. On the other hand, a variety of proposals resort to different optimization techniques, like steepest decent, penalty methods, Lagrange multipliers, which typically lead to linearizations that can be resolved by Newtonian approximation methods, some of them of higher order. Examples of these approaches are found in the work of Capsoni and Corradi (1997) [13], Capsoni (1999) [19] and Pontes, Borges, Zouain and Lopes (1997) [15]. Other methods have used elastic approximations to estimate plastic material behaviour, such as the ones proposed by Hamilton, Mackenzie, Shi and Boyle (1996) [8] and Ponter and Carter (1997) [16]. Other methods use a mixed approach to the finite element method as in Casciaro and Cascini (1982) [40], Borges, Zouain and Hespe [10] and Pontes, Borges, Zouain and Lopes (1997) [15]. Variations seem to be broad when it comes to formulation and solving techniques, and the variety in approaches brings up clear differences in resource demands and processing computer time. It is well known that *mathematical programming* techniques (i.e. linear-programming, interior point methods, second order cone programming, semi-definite programming) normally lead to a high

demand on storage and processor time as these techniques are grand-scale oriented and impose a great deal of overhead due to their general orientation and applicability. Other methods are likely to be more flexible in the sense that they let the solutions be tailored to specific needs and let developers experiment more easily with new proposals to reduce storage demands and computer time. Although more program design and coding is required.

The present research work is founded on an optimization technique based on the *Lagrange multipliers* method and an *upper bound* solution procedure primarily based on the *Newton-Raphson method* with *line search* relaxation. The applicability of the modeling conditions is restricted to *plane stress* at the present stage of the research, and *linear triangular elements* are used on a *finite element* discretized *velocity space.* Constant elemental *strain* and *stress functions* together with *linear velocity interpolation functions* are used. We recourse to a *flux equilibration* technique first proposed by Ladeveze and Leguillon [41] to determine a continuous stress distribution along inter-element edges. An adaptive refinement scheme is implemented and both uniform and adaptive refinement procedures are assessed. The so-called *elemental bound gap* is used as the adaptive indicator. Although a lower bound to the collapse load is determined in this proposal, only a kinematical minimization solution is used, either as a solution over the whole domain for the *upper bound* or as a series of local domain solutions for the evaluation of the *lower bound*, the latter defined in this implementation on what is called a *macro-element* domain.

In view of the previous descriptions, a set of elements of the present solution stand out as the specific contributions to the present developments in limit sate analysis. These can be summarized as follows:

1. A kinematic finite element discretization leading to a minimization problem to determine an upper bound is solved through the Newton-Raphson method, thus implying the generation of a *tangent matrix*, instead of a *secant* approach as used by Carter and Ponter [16].
2. A novel approach to the lower bound evaluation, for which a new formulation is developed and tested.

3. An adaptive refinement scheme in which an error measure is proposed, namely the *bound gap*, and used as the adaptivity control parameter (indicator).

1.4 Layout of the thesis

The structure of the present printed work is of conventional form, and comprises the following main components:

- *Chapter 1: Introduction.* Includes an initial statement of the aims of the present research work, with a description of recent related work by other researchers. The establishment of a general research framework is intended in the present chapter.
- *Chapter 2: Theory of Limit Analysis.* Describes the required theory elements that are the basis of the proposed solution.
- *Chapter 3: Finite element upper bound evaluation.* Presents the theoretical elements and the finite element discretization that lead to the present kinematic proposal, the upper bound solution.
- *Chapter 4: Lower bound evaluation.* Formulation aspects pertaining to the lower bound evaluation are described in this chapter. The flux equilibration technique used herein is described in this chapter.
- *Chapter5: Implementation and adaptivity.* Development and implementation issues are treated and detailed in this chapter, departing from the algorithmic description of the main procedures which give shape to the final solution package. Adaptivity aspects are also discussed in this chapter leading to the adaptive refinement algorithm programmed in the present implementation.
- *Chapter 6: Test cases and applications.* A series of validation test cases and applications are presented in this chapter.
- *Chapter 7: Conclusions.* A conclusive discussion as to the present research findings and achievements is given in this chapter, together with a series of suggested future steps in line with the existing results and research characteristics.
- *Appendixes:* reference information is presented in these addendum sections to extend on particular aspects that the reader may find useful. These comprise

an account of a *dual finite element discretization* proposed by Christiansen [3] and the description of the *residual force indicator* as proposed and used in the present work.

1.5 References

1. Jirásek M., Bazant Z., *Inelastic analysis of structures*, John Wiley a& Sons, Ltd, 2001.
2. Andersen K.D., Christiansen E., *Limit analysis with the dual affine scaling algorithm.* Journal of Computational and Applied Mathematics, Vol. 59 (1995) 233-243.
3. Christiansen, E. *Computation of limit loads.* International Journal for Numerical Methods in Engineering. Vol. 17 (1981) 1547-1570.
4. Liu Y.H., Cen Z.Z., Xu B.Y., *A numerical method for plastic limit analysis of 3-D structures*, Int. J. Solids & Structures, Vol. 32, No. 12 (1995) 1645-1658.
5. Zhang Y., Lu M., *An algorithm for plastic limit analysis*, Comput. Methods Appl. Engrg., Vol. 126 (1995) 333-341.
6. Sloan S.W., Kleeman P.W., *Upper bound limit analysis using discontinuous velocity fields.* Comput. Methods. Appl. Engrg., Vol 127 (1995) 293-314.
7. Yu H.S., Sloan S.W., Kleeman P.W., *A quadratic element for upper bound limit analysis.* Engrg. Comput., Vol 11 (1992) 195-212.
8. Hamilton R., Mackenzie D., Shi J., Boyle J.T., *Simplified lower bound limit analysis of pressurized cylinder/cylinder intersections using generalized yield criteria*, Int. J. Pres. Ves. & Piping, Vol. 67 (1996) 219-226.
9. Shi J., Boyle J.T., Mackenzie D., Hamilton R., *Approximate limit design of frames using elastic analysis*, Computers & Structures, Vol. 61, No.3 (1996) 495-501.
10. Borges L.A., Zouain N., Huespe A.E. *A nonlinear optimization procedure for limit analysis.* European Journal of Mechanics, A/Solids, Vol. 15, No. 3 (1996) 487-512.
11. Queiroz J.R., Ponter A.R.S., *A general approximate technique for the finite element shakedown and limit analysis of axisymmetrical shells.* Part 1: Theory and fundamental relations, Int. J. for Numerical Methods in Engineering, Vol. 40 (1997) 3495-3513.
12. Queiroz J.R., Ponter A.R.S., *A general approximate technique for the finite element shakedown and limit analysis of axisymmetrical shells.* Part 2: Numerical applications, Int. J. for Numerical Methods in Engineering, Vol. 40 (1997) 3515-3536.
13. Capsoni A., Corradi L., *A finite element formulation of the rigid-plastic limit analysis problem*, Int. J. for Numerical Methods in Engineering, Vol. 40 (1997) 2063-2086.
14. Damkilde L., Krenk S., *LIMITS – A system for limit state analysis and optimal material layout*, Computers & Structures, Vol. 64, No. 1-4 (1997) 709-718.
15. Pontes I.D.S., Borges L., Zouain N., Lopes F.R., *An approach to limit analysis with cone-shaped yield surfaces*, Int. J. for Numerical Methods in Engineering, Vol. 40 (1997) 4011-4032.

16. Ponter A.R.S., Carter K.F., *Limit state solutions, based upon linear elastic solutions with a spatially varying elastic modulus*, Comput. Methods Appl. Mech. Engrg. Vol. 140 (1997) 237-258.
17. Chen H.F., Liu Y.H., Cen Z.Z., Xu B.Y., *Numerical analysis of limit load and reference stress of defective pipelines under multi-loading systems*, Int. J. of Pres. Ves. & Piping, Vol. 75 (1998) 105-114.
18. Christiansen E., Andersen K.D. *Computation of collapse states with von Mises type yield condition.* International Journal for Numerical Methods in Engineering, Vol. 46 (1999) 1185-1202.
19. Capsoni A., *A mixed finite element model for plane strain limit analysis computations*, Communications in Numerical Methods in Engineering, Vol.15 (1999) 101-112.
20. Chen H.F., Liu Y.H., Cen Z.Z., Xu B.Y., *On the solution of limit load and reference stress of 3-D structures under multi-loading systems.* Engineering Structures, Vol. 21 (1999) 530-537.
21. Chen H.F., Shu D.W., *A numerical methods for lower bound limit analysis of 3-D structures with multi-loading systems*, Int. J. Pres. Ves. & Piping, Vol. 76 (1999) 105-112.
22. Heitzer M., Staat M., *FEM-computation of load carrying capacity of highly loaded passive component by direct methods*, Nuclear Engineering and Design , Vol. 193 (1999) 349-358.
23. Huh H., Lee C.H., Yang W.H., *A general algorithm for plastic flow simulation by finite element limit analysis*, Int. J. Solids & Structures, Vol. 36 (1999) 1193-1207.
24. Chen H.F., Shu D.W., *Lower and upper bound limit analysis for pipeline with multi-slots of various configurations*, Int. J. Pres. Ves. & Piping, Vol. 77 (2000) 17-25.
25. Liu Y.H., Cen Z.Z., Chen H.F., Xu B.Y., *Plastic collapse analysis of defective pipelines under multi-loading systems.* International Journal of Mechanical Sciences, Vol. 42 (2000) 1607-1622.
26. Lenci S., *An existence theorem for the limit analysis problem.* Mécanique des solides et des structures, C. R. Acad. Sci. Paris, t. 328, Série IIb (2000) 713-718.
27. Ponter A.R.S., Fuschi P., Engelhardt M., *Limit analysis for a general class of yield conditions*, Eur. J. Mech. A/Solids, Vol. 19 (2000) 401-421.
28. Poulsen P.N., Damkilde L., *Limit state analysis of reinforced concrete plates subjected to in-plane forces*, Int. J. Solids & Structures, Vol. 37 (2000) 6011-6029.
29. Capsoni A., Corradi L., Vena P., *Limit analysis of orthotropic structures based on Hill's yield condition*, Int. J. Solids & Structures, Vol. 38 (2001) 3945-3963.
30. Capsoni A., Corradi L., Vena P., *Limit analysis of anisotropic structures based on the kinematic theorem*, Int. J. of Plasticity, Vol. 17 (2001) 1531-1549.
31. Christiansen E., Pendersen O.S., *Automatic mesh refinement in limit analysis.* International Journal for Numerical Methods in Engineering, Vol. 50 (2001) 1331-1346.
32. Chen H.F., Ponter A.R.S., *Shakedown and limit analysis for 3-D structures using the linear matching method*, Int. J. Pres. Ves. & Piping, Vol. 78 (2001) 443-451.
33. Chen H.F., Shu D., *Simplified limit analysis of pipelines with multi-defects*, Engineering Structures, Vol. 23 (2001) 207-213.
34. Staat M., Heitzer M., *LISA- a European project for FEM-based limit and shakedown analysis*, Nuclear Engineering and Design, Vol. 206 (2001) 151-166.

35. Borges L., Zouain N., Costa C., Feijóo., *An adaptive approach to limit analysis.* International Journal of Solids and Structures, Vol. 38 (2001) 1707-1720.
36. Lyamin A.V., Sloan S.W., *Upper bound limit analysis using linear finite elements and nonlinear programming.* Research Report 199.01.2001, Dept. of Civil, Surveying and Environmental Engineering, The University of Newcastle, Australia, 2001.
37. Lyamin A.V., Sloan S.W., *Lower bound limit analysis using non-linear programming.* International Journal for Numerical Methods in Engineering, Vol. 55 (2002) 573-611.
38. Krabbenhoft K., Damkilde L., *A general non-linear optimisation algorithm for lower bound limit analysis.* International Journal for Numerical Methods in Engineering, Vol. 56 (2003) 165-184.
39. Ciria H., Peraire J., *Computation of upper and lower bounds in limit analysis using second-order cone programming and mesh adaptivity.* MSc Thesis, Massachusetts Institute of Technology, 2004.
40. Casciaro R., Cascini L., *A mixed formulation and mixed finite elements for limit analysis.* International Journal for Numerical Methods in Engineering, Vol. 18 (1982) 211-243.
41. Ladeveze P., Leguillon D., *Error estimate procedure in the finite element method and applications.* SIAM Journal on Numerical Analysis. Vol. 20, Issue 3 (1983) 485-509.

Chapter 2

Theory of Limit Analysis

2.1 Introduction

The theory of Limit Analysis although extensively studied, corresponds to a very specific area of the broad Plasticity Theory. Limit Analysis focuses on the special case of a structure or a generalized body in *state of impending collapse*, when subjected to a certain set of boundary conditions. Special considerations are made in order to make it possible to construct solution procedures that lead scientists and engineers to understand and evaluate the behaviour of structures in such a characteristic condition. One important idealization, or simplification, comes in the form of the one-dimensional constitutive material behaviour used as a basis for analysis, usually retrieved from a number of laboratory tests. Although plasticity theory resorts to a variety of material relations, in the case of limit analysis it is common to focus on relations that show *elastic-perfectly plastic* or *rigid-perfectly plastic* behaviour, as shown in figure 2.1, which rules out any consideration of work hardening or acute changes in geometry on the late phase of the curve. More specifically, the important *upper bound* and *lower bound* theorems of limit analysis are better formulated under the assumption of a *rigid-plastic* stress-strain relationship, as described later.

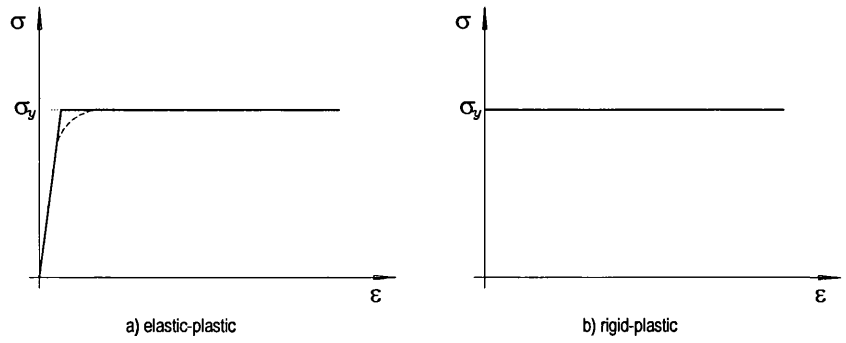

Figure 2.1 Elastic-plastic and rigid-plastic behaviour

As commented in the previous chapter, most engineering design codes encourage the use of limit analysis procedures for the attainment of a simpler design phase resulting in a more material efficient structure, however the use of such techniques is not an easy task when applied to complex structures.

The objectives set out in the present research work lie within a new approach to the application of the theorems of limit analysis to evaluate the collapse load multiplier of a structure in 2-dimensional space, so in what follows, we will emphasize the description of *rigid-plastic* material behaviour and related theory.

As set out by Chen and Liu [1], three conditions have to be met in the solution of a boundary value problem in the mechanics of deformable bodies: a) equilibrium equations, b) stress-strain relations, and c) compatibility equations. A number of stress fields would satisfy the stress boundary conditions, the equilibrium equations and the yield criterion, as well as a number of displacement fields would be compatible with a distortion of the continuum satisfying the displacement boundary conditions. We have to make sure these stress and displacement fields correspond and produce a unique solution.

In limit analysis, instead of travelling through a three stage development in a solution, namely the elastic response, the intermediate contained plastic flow and the uncontained plastic flow, one can make a definite statement about the collapse load without carrying out the step-by-step elastic-plastic analysis. The core of the limit analysis theory is built upon two theorems, namely the *upper bound theorem* and the *lower bound theorem*, which independent of each other, establish a set of conditions

that let us estimate a value close to the true collapse load of a generalized loaded body.

The conditions required to establish an upper or lower bound solution to the collapse load are essentially as follows:

Lower bound theorem: the loads, determined from a distribution of stress that satisfies a) the equilibrium equations, b) the stress boundary conditions, and c) nowhere violates the yield condition, cannot be greater than the actual (true) collapse load. As symbolically described later, this stress distribution is known as a *statically admissible stress field.* In other words, the lower bound theorem can be stated as: if a statically admissible stress field can be found, uncontained plastic flow cannot occur at a lower load. Note that no consideration is given to the kinematics of the body, it only takes equilibrium and yield into account.

Upper bound theorem: the loads, determined by equating the external work rate to the internal dissipation rate in an assumed velocity field that satisfies a) the velocity boundary conditions, and b) the compatibility conditions, cannot be less that the actual collapse load. The velocity field satisfying these conditions is known as a *kinematically admissible velocity field.* Hence, the upper bound theorem states that if a kinematically admissible velocity field can be found, uncontained plastic flow must have taken place previously. Note that it only considers velocity modes and energy dissipation, no equilibrium conditions are imposed over the stress distribution.

By a suitable choice of stress and velocity fields, the above theorems enable the required collapse load to be bracketed as closely as seems necessary for the problem under consideration.

Although the approximate nature of this solution seems to limit the power of these methods, the results obtained through this solution are neither worse nor better than the inherently uncertain results in all modern engineering problems. The real difficulty is the likely discrepancy between the plastic deformation properties of the ideal and the real material, which often shows some degree of work hardening or softening and may not follow the associated flow rule. A clear view of the

assumptions regarding the mechanical properties of the material under investigation, determine the range of validity of this theory.

Due to the particular requirements set out for this research work, in the following sections a theoretical description of those elements of plasticity theory that are essential to the thorough understanding of the progress and results of this work will be presented. Additionally, some basic aspects of the *dual approach* to limit analysis are discussed. Then a summary of approaches to the limit analysis problem is given, which let us position the present work within the currently known schemes.

2.2 Basic theory of Limit Analysis

As a means of introduction to the essential aspects of limit analysis theory in the context of the present research work, this section gives a description of the concepts and theory of limit analysis as presented by Chen and Liu [1], Hill [2], Lubliner [3], Shames and Cozzarelli [4] and Jirásek and Bazant [5].

2.2.1 The yield condition

It is always important to assess the behaviour of the body under a complex stress state, specially the conditions under which a change occurs from an elastic state to that of a plastic state, that is a flow state or yielding. Here we need a form of the condition that characterizes the transition of a material from an elastic state to a plastic flow state with a complex stress state. The condition, satisfied in the flow state, is called the perfect plasticity condition or the yield criterion. It is generally assumed that the plastic flow occurs when on any plane at any point in a portion of material, the set of stress components σ_{ij} reaches a yield surface which can be mathematically expressed as a yield function f in the stress space. That is, each element of a generalized body is assumed to be governed by a yield function f. For a perfectly plastic or rigid-plastic material, f depends only on the set of stress components σ_{ij} but not on the strain components ε_{ij}. Plastic flow can occur only when the yield function is satisfied:

$$f\left(\sigma_{ij}\right)=0 \tag{2.1}$$

The stress states for which $f(\sigma_{ij}) > 0$ are excluded, and $f(\sigma_{ij}) < 0$ correspond to elastic stress states. The fact that three or more components of stress σ_{ij} may be taken as coordinate axes leads to the construction of a *yield surface* in stress space. The yield surface is represented by a yield curve when two independent components of stress are studied. It is helpful to see a state of stress in a nine-dimensional stress as a point in the 2-dimensional picture shown in Figure 2.2, as a vector with nine components σ_{ij}. As shown later, the yield surface must be convex for materials satisfying Drucker's stability postulate.

Considering further the yield criterion, based on a description by Hill [2], if we suppose an isotropic material, we have that since plastic yielding can depend only on the magnitudes of the three principal applied stresses and not on their directions, any yield criterion is expressible in the form

$$f(J_1, J_2, J_3) = 0 \tag{2.2}$$

where J_1, J_2 and J_3 are the first three invariants of the stress tensor σ_{ij}. The stress can be either specified by the three principal components or by the three invariants.

The function f in metals is characteristic of the state of the element immediately before unloading, and hence depends on the whole mechanical and heat treatment of the metal since it was in the annealed condition.

An immediate simplification to (2.2) can be obtained taking into account the experimental fact that yielding of a metal is unaffected by a moderate hydrostatic pressure or tension, either applied alone or superposed on a state of combined stress. Assuming this to be strictly true for the ideal plastic body, yielding depends only on the principal components of the deviatoric stress tensor

$$s_{ij} = \sigma_{ij} - \sigma\delta_{ij} \tag{2.3}$$

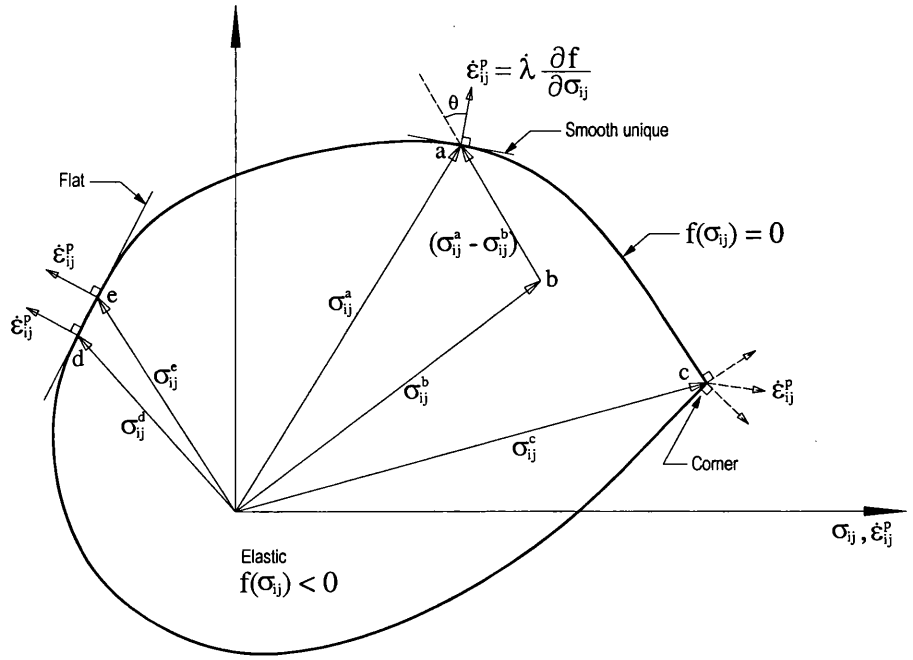

Figure 2.2 Yield surface and flow rule

where $\sigma = \frac{1}{3}\sigma_{ii}$ is the hydrostatic component of stress. Note the use of the summation convention. The principal components of the deviatoric stress tensor s_1, s_2, s_3 are not independent due to $s_1 + s_2 + s_3 \equiv 0$. The yield criterion reduces to

$$f\left(J_2', J_3'\right) = 0 \tag{2.4}$$

where

$$\begin{aligned} J_2' &= -\left(s_1 s_2 + s_2 s_3 + s_3 s_1\right) = \tfrac{1}{2}\left(s_1^{\,2} + s_2^{\,2} + s_3^{\,2}\right) = \tfrac{1}{2} s_{ij} s_{ij} \\ J_3' &= s_1 s_2 s_3 = \tfrac{1}{3}\left(s_1^{\,3} + s_2^{\,3} + s_3^{\,3}\right) = \tfrac{1}{3} s_{ij} s_{jk} s_{ki} \end{aligned} \tag{2.5}$$

When an element is unloaded from a plastic stress state σ_{ij} and then reloaded to the state $-\sigma_{ij}$, keeping the ratios of the stress components constant throughout, it is assumed that the body only deforms elastically and is finally again on the point of yielding. Since J_3' changes sign when the stresses are reversed, it follows that f must be an even function of J_3', i.e. $f\left(J_2', J_3'\right) = f\left(J_2', -J_3'\right)$.

von Mises suggested that yielding occurred when J_2' reached a critical value, implying that function f does not involve J_3'. This criterion can be written as

$$2J_2' = s_{ij}s_{ij} = s_1^2 + s_2^2 + s_3^2 = 2k^2 \tag{2.6}$$

Alternative expressions for this criterion are given later. In equation (2.6), k (yielding shear stress) is a parameter depending on the amount of pre-strain. A physical interpretation of von Mises's law was given by Hencky, which implies that yielding begins when the elastic energy of distortion reaches a critical value. Thus a hydrostatic pressure does not cause yielding since it produces only elastic volumetric energy on an isotropic material. The yield criterion of von Mises has been shown to be in excellent agreement with experimental data for many ductile metals, for example copper, nickel, aluminium, cold-worked mild steel, medium carbon and alloy steels. Independence of the yielding criterion from the hydrostatic component of stress, as a property of the ideal plastic body, implies that no plastic work is done by this hydrostatic component of the applied stress, so that there is no plastic or irrecoverable change in volume. In other words, changes in volume during plastic deformation are elastic so that for the ideal plastic body we have $d\varepsilon_{ii}^p = 0$.

2.2.2 The flow rule

For stable materials that comply with Drucker's postulate, as discussed in section 2.2.5 below, it can be shown that the vector representing the plastic strain-rate $\dot{\varepsilon}_{ij}^p$ has the direction of the outward normal to the yield surface $f(\sigma_{ij}) = 0$. This can be written in the general expression:

$$\dot{\varepsilon}_{ij}^p = \dot{\lambda}\frac{\partial f}{\partial \sigma_{ij}} \tag{2.7}$$

where $\dot{\lambda} > 0$ (when $f = 0$, according to the *Karush-Kuhn-Tucker conditions*; Jirásek and Bazant [5]) is a scalar proportionality factor. The expression above is known as the *associated flow rule*, because it is connected with the yield surface of the perfectly

plastic material in a clear manner. Note that if $\dot{\lambda}$ is known, $\dot{\varepsilon}_{ij}^{p}$ and thus $\dot{\varepsilon}_{ij}$ can easily be calculated, as described below in section 2.2.4.

The tensor function $\partial f / \partial \sigma_{ij}$ appearing in the flow equation (2.7), implies that function f defining the yield surface is itself a plastic potential. Thus the normality rule is also called a flow rule associated with the yield criterion. Materials obeying an associated flow rule are usually called *standard materials*. A flow rule coming from a plastic potential g different from f such that $\partial g / \partial \sigma_{ij}$ is not proportional to $\partial f / \partial \sigma_{ij}$, is called a *non-associated* flow rule.

An extended description of relation (2.7) can be drawn, based on a discussion by Hill [2] regarding the *plastic potential*. It seems that the consideration of f as a plastic potential has an especial significance in the mathematical theory of plasticity, since certain variational principles and uniqueness theorems can be formulated. Under this consideration the general plastic stress-strain relations can be written as

$$d\varepsilon_{ij}^{p} = d\lambda \frac{\partial f}{\partial \sigma_{ij}} \tag{2.8}$$

where f must be independent of a hydrostatic pressure, that is, $\partial f / \partial \sigma_{ii} = 0$ if the plastic volume change is to be zero. In addition, if f is an even function, i.e. no Bauschinger effect[1] is in place, relation (2.8) implies that a reversal of the sign of the stress merely reverses the sign of the strain increment. An instance of this can be found in the Lévy-Mises or Reuss equations, where $f = J_2' = \frac{1}{2} s_{ij} s_{ij}$ and

$$\partial f / \partial \sigma_{ij} = s_{ij} \tag{2.9}$$

Relation (2.8) can be derived as follows. Suppose that the plastic strain increment $d\varepsilon_{ij}^{p}$ is prescribed and that the corresponding stress determined from (2.8) and the yield criterion is σ_{ij}. Let σ_{ij}^{*} be any other plastic state of stress, so that

[1] During cyclic loading, even if the magnitudes of the yield stress in tension and compression are initially the same, this is not the case when the material has been preloaded into the plastic range and then unloaded. Jirásek and Bazant [5].

$$f\left(\sigma_{ij}^{*}\right)=f\left(\sigma_{ij}\right)=c \tag{2.10}$$

where c is the yield locus. The work done by σ_{ij}^{*} with the strain $d\varepsilon_{ij}^{p}$ would be $dW_{p}^{*}=\sigma_{ij}^{*}d\varepsilon_{ij}^{p}$. This has a stationary value for varying plastic states σ_{ij}^{*} when, by the method of Lagrange

$$\frac{\partial}{\partial\sigma_{ij}^{*}}\left\{\sigma_{ij}^{*}d\varepsilon_{ij}^{p}-f\left(\sigma_{ij}^{*}\right)d\lambda\right\}=0 \tag{2.11}$$

where a constant multiplier $d\lambda$ has been introduced.

Thus we can write

$$d\varepsilon_{ij}^{p}=d\lambda\frac{\partial f\left(\sigma_{ij}^{*}\right)}{\partial\sigma_{ij}^{*}} \tag{2.12}$$

This equation is satisfied when σ_{ij}^{*} is the actual stress σ_{ij} leading to expression (2.8). When relation (2.8) holds, the plastic work done in a given plastic strain increment has a stationary value in the actual state, with respect to varying stress systems satisfying the yield criterion. This theorem is due to von Mises. The yield locus c must be concave to the origin at all points if the stress corresponding to a given strain increment is to be unique, and in this case the work done is an absolute maximum, that is, a maximum for all plastic states of stress and not merely for infinitesimally near states.

Equation (2.7) can be derived from relation (2.12) due to the fact that strain increments can be evaluated with respect to time, that is, $d\varepsilon_{ij}^{p}/dt=\dot{\varepsilon}_{ij}^{p}$ so that the term *strain-rate* instead of strain-increment is commonly used at a state of impending collapse. This also applies to the scalar multiplier $d\lambda$ ($d\lambda/dt=\dot{\lambda}$). However, from Lubliner [3], for the case of *rigid-plastic* materials, where the yield locus is located at $f\left(\sigma_{ij}\right)=c=0$, plastic deformation occurs only if $\dot{f}=(\partial f/\partial\sigma_{ij})\dot{\sigma}_{ij}=0$. Parameter $\dot{\lambda}$ takes an indeterminate positive value when $f=0$ and $(\partial f/\partial\sigma_{ij})\dot{\sigma}_{ij}=0$, and zero otherwise.

Thus, $\dot{\lambda}$ and f obey the Karush-Kuhn-Tucker conditions of optimisation theory:

$$\dot{\lambda} f = 0, \quad \dot{\lambda} \geq 0, \quad f \leq 0$$

2.2.3 Von Mises yield criterion

In the present work, the *yield criterion* is based on the *Lévy flow rule* and the *von Mises yield criterion*, as described by Lubliner [3]. Lévy proposed a general form of a flow rule derived from the J_2 potential, written here for plastic strain as

$$\dot{\varepsilon}_{ij}^{p} = \dot{\lambda} s_{ij} \tag{2.13}$$

with $\dot{\lambda} = \left|\dot{\varepsilon}_1^p\right| + \left|\dot{\varepsilon}_2^p\right| + \left|\dot{\varepsilon}_3^p\right|$ and s_{ij} being the *deviator* stress (see relations (2.3) and (2.9)). The yield criterion with which this flow rule is associated is the *von Mises criterion*, represented by the yield function

$$f(\sigma) = J_2 - k^2 \tag{2.14}$$

where k is the yield stress in shear. Due to the relation between J_2 and the octahedral shear stresses, the von Mises criterion is also known as the *maximum-octahedral-shear-stress* criterion, also called *maximum-distortional-energy* criterion. Expresing J_2 in terms of the principal stresses we can write this criterion in the form

$$(\sigma_1 - \sigma_2)^2 + (\sigma_2 - \sigma_3)^2 + (\sigma_3 - \sigma_1)^2 = 6k^2 \tag{2.15}$$

As is generally known, the yield surface in plane stress, where $\sigma_3 = 0$ describes an elliptical shape in principal stress space with equation

$$\sigma_1^2 + \sigma_2^2 - \sigma_1\sigma_2 = 3k^2 \tag{2.16}$$

2.2.4 The kinematic assumption

It is known that plastic flow occurs when a stress point in stress space, represented by a vector drawn from the origin, reaches the perfectly plastic yield surface. When this condition occurs for *non-hardening materials* it is clear that nothing can be said about

the total plastic strain, denoted ε_{ij}^{p} because the magnitude of the plastic flow is unlimited. In this case we use strain rates $\dot{\varepsilon}_{ij}$, instead of strains. The total strain-rate $\dot{\varepsilon}_{ij}$ is composed of elastic and plastic parts:

$$\dot{\varepsilon}_{ij} = \dot{\varepsilon}_{ij}^{e} + \dot{\varepsilon}_{ij}^{p} \qquad \text{with} \quad \dot{\varepsilon}_{ij} = \tfrac{1}{2}\left(\frac{\partial \dot{u}_i}{\partial x_j} + \frac{\partial \dot{u}_j}{\partial x_i} \right) \tag{2.17}$$

The elastic part $\dot{\varepsilon}_{ij}^{e}$ is related to the $\dot{\sigma}_{ij}$ through Hooke's law[2] only, while the plastic part $\dot{\varepsilon}_{ij}^{p}$ depends on the state of stress through an appropriate kinematic assumption on the deformations. The second expression in (2.17) gives the kinematic strain rate-velocity relations, otherwise simply called the strain rate tensor.

The coordinate axes of the stress space already referred to for the yield surface can also be used to represent simultaneously plastic strain rates as well as stresses; each axis of σ_{ij} being an axis of the corresponding plastic strain component of $\dot{\varepsilon}_{ij}^{p}$. Figure 2.2 shows this combined stress and strain-rate plot. It is expected for isotropic materials, that the principal stress axes coincide with the principal strain-rate axes.

2.2.5 Drucker's postulate

A more restrictive definition for work-hardening materials was formulated by Drucker around 1950, by generalizing the characteristics of uniaxial stress-strain curves. Taking into account a single component σ, the conjugate plastic strain-rate $\dot{\varepsilon}^{p}$ clearly satisfies:

$$\dot{\sigma}\dot{\varepsilon}^{p} \begin{cases} \geq 0, & \text{hardening material} \\ = 0, & \text{perfectly plastic material} \\ \leq 0, & \text{softening material} \end{cases} \tag{2.18}$$

[2] In the generalized Hook's law, stress-strain relations are given by $\dot{\sigma}_{ij} = C_{ijkl}\dot{\varepsilon}_{kl}^{e}$, where C_{ijkl} is the elastic constitutive tensor. Thus, assuming C_{ijkl} to be invertible we have $\dot{\varepsilon}_{ij}^{e} = C_{ijkl}^{-1}\dot{\sigma}_{kl}$. Lubliner [3].

As shown in Figure 2.3, this definition describes three types of materials, shown here as three graphic phases.

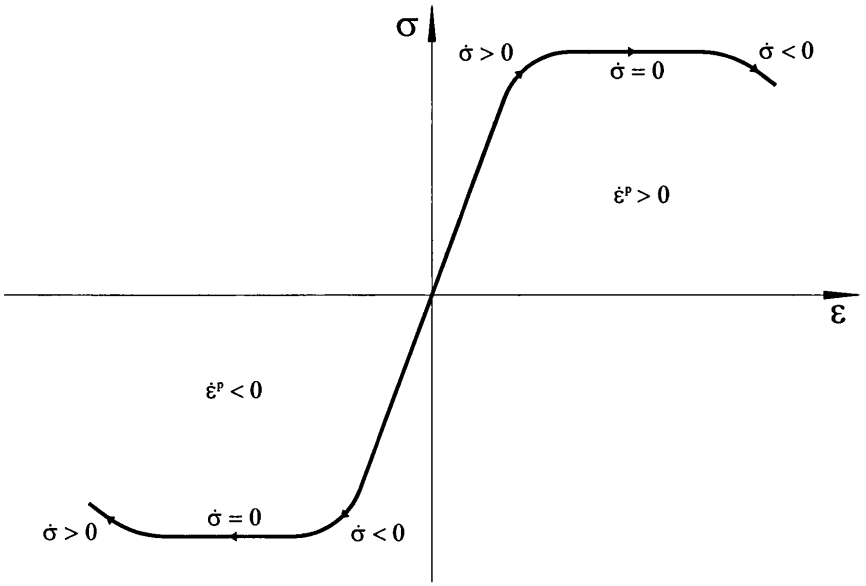

Figure 2.3 Illustration of Drucker's postulate in uniaxial stress-strain plane

The interpretation of this product by Drucker supposes an external agency that applies and then removes additional forces (independent from the current loads) to an already loaded body without any temperature change. For a stable material defined by Drucker's stability postulate, it should be that a) positive work is done by the external agency during the application of the added set of stresses on the changes in strains and b) nonnegative net work is done by the external agency over the cycle of application and removal. It should be clear that the work referred to is only the work done by the added set of stresses on the change in strains it produces, not the total stresses on strains, so although the product $\dot{\sigma}\dot{\varepsilon}$ is negative for a certain stress-strain development, the work done by the total stress is positive.

The inequalities are not changed if the stress and plastic strain rates are multiplied by dt, so that they hold equally well for $d\sigma d\varepsilon^p$, as a product that has dimensions of work per unit volume. Clearly, $d\sigma d\varepsilon = d\sigma\left(d\varepsilon^e + d\varepsilon^p\right)$ is the work done by the external agency in the course of incremental loading, and $d\sigma d\varepsilon^p$ is the work done in the course of the cycle consisting of the application and removal of the incremental stress. Since $d\sigma d\varepsilon^e$ is always positive, and for a work-hardening material

$d\sigma d\varepsilon^p \geq 0$, it follows that for such a material $d\sigma d\varepsilon > 0$. Thus, Drucker defines a work-hardening plastic material as one in which the work done during incremental loading is positive, and the work done in the loading-unloading cycle is nonnegative, a definition generally known as **Drucker's postulate**.

Having defined hardening in terms of work, Drucker naturally extends the definition to general three-dimensional stress and strain states, such that $d\sigma_{ij} d\varepsilon_{ij} > 0$ and $d\sigma_{ij} d\varepsilon_{ij}^p \geq 0$, the equality holding only for $d\varepsilon^p = 0$. For perfectly plastic materials Drucker's inequalities are $d\sigma_{ij} d\varepsilon_{ij} \geq 0$ and $d\sigma_{ij} d\varepsilon_{ij}^p = 0$. It can be seen that the inequality

$$\dot{\sigma}_{ij} \dot{\varepsilon}_{ij}^p \geq 0 \tag{2.19}$$

sometimes known simply as **Drucker's inequality**, is valid for both work-hardening and perfectly plastic materials. This inequality may also be interpreted without any consideration of incremental work, noting that the left-hand side represents the scalar product $\dot{\boldsymbol{\sigma}} \cdot \dot{\boldsymbol{\epsilon}}^p$, and the inequality therefore expresses the hypothesis that *the plastic strain-rate cannot oppose the stress rate.*

The additional stresses produced by the external agency as described above, need not be a small increment. For instance, the initial stress, let us say σ_{ij}^*, may be inside the elastic region, or at a point on the yield surface far from σ_{ij}, and the process followed by the external agency may consist of elastic loading to a stress σ_{ij} on the current yield surface, a small stress increment $d\sigma$ producing an incremental plastic strain $d\varepsilon$, and finally, elastic unloading back to σ_{ij}^*. With $d\sigma$ neglected alongside $\sigma_{ij} - \sigma_{ij}^*$, the work per unit volume done by the external agency is $\left(\sigma_{ij} - \sigma_{ij}^*\right) d\varepsilon_{ij}^p$. Drucker's postulate consequently implies

$$\left(\sigma_{ij} - \sigma_{ij}^*\right) \dot{\varepsilon}_{ij}^p \geq 0 \tag{2.20}$$

A derivation of relation (2.20) under the external agency assumption is given by Shames and Cozzarelli [4].

2.2.6 Maximum Plastic Dissipation postulate, normality and convexity

The validity of the inequality (2.20) is not limited to work-hardening materials in Drucker's sense. This would be better understood if we take its uniaxial counterpart

$$\left(\sigma-\sigma^{*}\right)\dot{\varepsilon}^{p}\geq 0 \tag{2.21}$$

This inequality expresses the property that the plastic strain-rate is positive only if the current stress σ is not less than any stress σ^{*} in the current elastic range, that is, if σ equals the current tensile yield stress. Work-softening and perfectly plastic materials clearly share this property as well, thus inequality (2.20) constitutes a postulate in its own right, called the *postulate of maximum plastic dissipation.*

Inequality (2.20) has important implications in plasticity theory. First, let us think of relation (2.20) as a vector scalar product, and suppose that the yield surface is everywhere smooth, so that a well-defined tangent hiperplane and normal direction exist at every point. It is clear from figure 2.4a) that if inequality (2.20) is to be valid for all σ^{*} inside the yield surface and on the inward side of the tangent, and $\left(\sigma-\sigma^{*}\right)$ describing a directed vector from σ^{*} to σ, then $\dot{\varepsilon}^{p}$ must be directed along the outward normal to the yield surface at σ, a restriction called *the normality rule.* On the other hand, as shown in figure 2.4b), if there are any σ^{*} lying to the outward side of the tangent, the inequality is violated, thus the entire elastic region must lie to one side of the tangent, as a result another restriction known as *convexity of the yield surface*, has to be met.

Let us define $D_{p}\left(\dot{\varepsilon}^{p}\right)$, namely the *plastic dissipation rate*, as

$$D_{p}\left(\dot{\varepsilon}^{p}\right)=\max_{\sigma^{*}}\ \sigma_{ij}^{*}\dot{\varepsilon}_{ij}^{p} \tag{2.22}$$

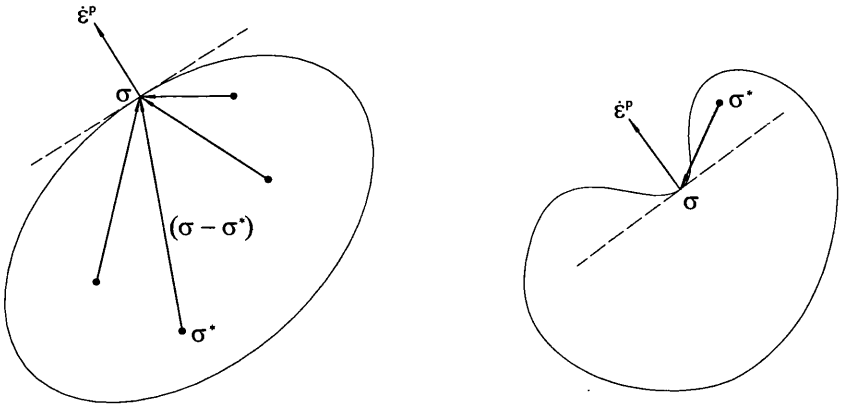

a) b)

Figure 2.4 Properties of flow associated yield surface, normality (a) and convexity (b)

the maximum being taken over all $\boldsymbol{\sigma}^*$ such that $f(\boldsymbol{\sigma}^*) \leq 0$, then from inequality (2.20) we have

$$\sigma_{ij}\dot{\varepsilon}_{ij}^p = D_p(\dot{\boldsymbol{\varepsilon}}^p) \tag{2.23}$$

Note that $D_p(\dot{\boldsymbol{\varepsilon}}^p)$ depends only on $\dot{\boldsymbol{\varepsilon}}^p$ and not on $\boldsymbol{\sigma}$, due to the fact that if the yield surface is strictly convex at $\boldsymbol{\sigma}$ then this is the only stress related to a normal direction in stress space and hence to a given $\dot{\boldsymbol{\varepsilon}}^p$. In the case of a flat segment on the surface, all points on the segment have the same normal, but the scalar product $\boldsymbol{\sigma} \cdot \dot{\boldsymbol{\epsilon}}^p = \sigma_{ij}\dot{\varepsilon}_{ij}^p$ is the same on all of them. $D_p(\dot{\boldsymbol{\varepsilon}}^p)$ will be called simply the *plastic dissipation*, and inequality (2.20) can be rewritten as

$$D_p(\dot{\boldsymbol{\varepsilon}}^p) \geq \sigma_{ij}^*\dot{\varepsilon}_{ij}^p \quad \text{for all } \boldsymbol{\sigma}^* \text{ such that } f(\boldsymbol{\sigma}^*) \leq 0 \tag{2.24}$$

giving explicit meaning to the *principle of maximum plastic dissipation.* This principle is defined here as a point-wise application, that is, per unit volume, further on it is extended as a sum over the whole domain.

If the yield surface has one or more singular points (corners) at which the normal direction is not unique, then at such a point $\dot{\boldsymbol{\varepsilon}}^p$ must lie in the cone formed by the

normal vectors meeting there, as shown by figure 2.2. Note that the convexity of the yield surface is not affected by this generalization.

2.2.7 Plastic dissipation for the von Mises criterion

The plastic dissipation for the von Mises criterion and associated flow rule is given by

$$D_p(\dot{\boldsymbol{\varepsilon}}^p) = \sigma_{ij}\dot{\varepsilon}_{ij}^p = \dot{\lambda}s_{ij}s_{ij} = \sqrt{2J_2}\sqrt{\dot{\varepsilon}_{ij}^p\dot{\varepsilon}_{ij}^p} = k\sqrt{2\dot{\varepsilon}_{ij}^p\dot{\varepsilon}_{ij}^p} \tag{2.25}$$

where s_{ij} is the *deviator* stress tensor. Equation (2.25) can be derived (based on Shames and Cozzarelli [4]) by first expressing the plastic dissipation in alternate forms *under the assumption of incompressibility*, as

$$D_p(\dot{\boldsymbol{\varepsilon}}^p) = \sigma_{ij}\dot{\varepsilon}_{ij}^p = \sigma_{ij}\dot{\varepsilon}_{ij}'^p = s_{ij}\dot{\varepsilon}_{ij}'^p = s_{ij}\dot{\varepsilon}_{ij}^p \tag{2.26}$$

with $\dot{\varepsilon}_{ij}'^p$ being the *strain-rate deviator tensor.*

From equation (2.13) and (2.26) we can rewrite equation (2.25) as

$$D_p(\dot{\boldsymbol{\varepsilon}}^p) = s_{ij}\dot{\varepsilon}_{ij}^p = \dot{\lambda}s_{ij}s_{ij} \tag{2.27}$$

Now using relation (2.13) again, i.e. $s_{ij} = \dot{\varepsilon}_{ij}^p / \dot{\lambda}$, the parameter $\dot{\lambda}$ can be determined as

$$\dot{\lambda} = \frac{\sqrt{\dot{\varepsilon}_{ij}^p\dot{\varepsilon}_{ij}^p}}{\sqrt{s_{ij}s_{ij}}} \tag{2.28}$$

With the expression for the *second invariant* of the deviator stress tensor $J_2 = \frac{1}{2}s_{ij}s_{ij}$ and using equation $f(\boldsymbol{\sigma}) = J_2 - k^2 = 0$ at the yield surface, we obtain expressions (2.25). An alternative form of the plastic dissipation in (2.25) can be derived as follows. Consider the yield stress in simple tension/compression $\sigma_y = \sqrt{3}k$ (with $k = \tau_y$, the yield stress in shear); we can rewrite expression (2.25) as

$$D_p(\dot{\varepsilon}^p) = \sigma_y \sqrt{\frac{2}{3}\dot{\varepsilon}_{ij}^p \dot{\varepsilon}_{ij}^p} = \sigma_y \dot{\bar{\varepsilon}} \tag{2.29}$$

where $\dot{\bar{\varepsilon}}$ is the *effective* or *equivalent strain-rate*, given by

$$\dot{\bar{\varepsilon}} = \sqrt{\frac{2}{3}\dot{\varepsilon}_{ij}^p \dot{\varepsilon}_{ij}^p} \tag{2.30}$$

In particular, equation (2.29) will be used as a core element in the computation of the *total plastic dissipation work* in the present solution procedures.

2.2.8 The assumption of small deformations and the Equation of Virtual Work

The theorems of limit analysis are based and proved by the use of the equation of virtual work. In limit analysis, it is assumed that the changes in geometry over the body that occur at impending collapse are small, so that the original undeformed dimensions will be used in the equilibrium equations. The equation of virtual work implies the description of an *equilibrium set* and a *compatible set*, independent of each other. This equation is due to the balance between the work done by the external forces and the work done by the internal forces as

$$\int_V b_i \dot{u}_i dV + \int_{S_t} t_i \dot{u}_i dS = \int_V \sigma_{ij} \dot{\varepsilon}_{ij} dV \tag{2.31}$$

where b_i, t_i and σ_{ij}, body forces, traction forces on the surface and an arbitrary set of stresses, respectively, constitute the equilibrium set in the sense that the stresses are in equilibrium with the body forces at the internal level and with the traction forces at the external level. Similarly, the strain-rate $\dot{\varepsilon}_{ij}$ represents any set of strains compatible with the boundary conditions, and real or virtual displacement rate $\dot{u}_i$ of the points of application of the external traction forces t_i and the body forces b_i, so that the a continuous distortion of the body compatible with an assumed displacement field must satisfy a strain-displacement rate compatibility relation. Note that neither the equilibrium set, nor the compatibility set need to describe the actual state, nor should they be related to each other, they are completely independent. Figure 2.5 depicts these two sets.

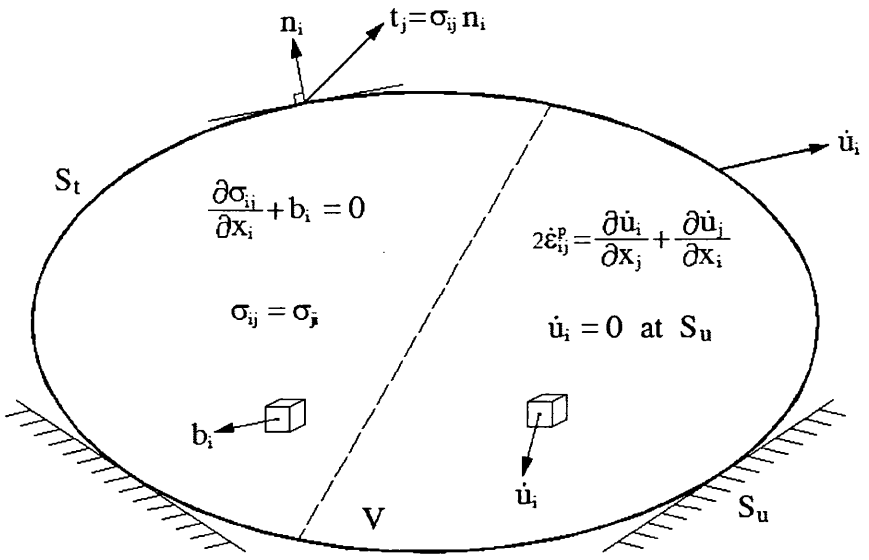

Figure 2.5 Independent sets in the equation of virtual work:
equilibrium set (left) and compatible set (right)

In Figure 2.5 the body boundary ∂V is composed of the two complementary sets $S_u \subseteq \partial V$ and $S_t \subseteq \partial V$, such that $\partial V = S_u \cup S_t$. Velocities are prescribed on S_u, whereas external loads are given on S_t.

The equation of virtual work may be written in rate form as

$$\int_V \dot{b}_i \dot{u}_i dV + \int_{S_t} \dot{t}_i \dot{u}_i dS = \int_V \dot{\sigma}_{ij} \dot{\varepsilon}_{ij} dV \tag{2.32}$$

as stated by Chen and Liu [1], due to the fact that any equilibrium set can be used in equation (2.31), in particular a rate of change of forces and interior stresses, namely $\dot{b}_i$, $\dot{t}_i$ and $\dot{\sigma}_{ij}$. It is useful to keep this special treatment in mind as some descriptions of the theorems of limit analysis often refer to this indistinctively (refer to section 2.2.10 below).

2.2.9 Uniqueness of the stress field

A discussion on *uniqueness of the stress field* due to Lubliner [3] follows, for the case of stress distribution over rigid-plastic material bodies.

Referring to expression (2.23) for the plastic dissipation defined previously

$$D_p(\dot{\epsilon}) = \sigma_{ij}\dot{\varepsilon}_{ij} \tag{2.33}$$

The *maximum plastic dissipation principle* can then be written as

$$(\sigma_{ij} - \sigma_{ij}^*)\dot{\varepsilon}_{ij} \geq 0 \tag{2.34}$$

If $\dot{\epsilon} \neq 0$, the equality holds only if σ_{ij} and σ_{ij}^* are *plastically equivalent*; in other words, if $\dot{\epsilon}$ is related to both stresses through the associated flow rule. In a von Mises material, two plastically equivalent stresses differ by at most a hydrostatic pressure. If we define two admissible states $\left(\sigma_{ij}^a, \dot{u}_i^a\right)$ and $\left(\sigma_{ij}^b, \dot{u}_i^b\right)$ for a rigid-plastic body, corresponding to the same body force and boundary conditions, then

$$n_j\left(\sigma_{ij}^a - \sigma_{ij}^b\right)\left(\dot{u}_i^a - \dot{u}_i^b\right) = 0 \quad \text{on } S \tag{2.35}$$

meaning that no work-rate difference is produced, and therefore, by summing over the boundary we have

$$\int_S n_j\left(\sigma_{ij}^a - \sigma_{ij}^b\right)\left(\dot{u}_i^a - \dot{u}_i^b\right)dS = \int_V \left(\sigma_{ij}^a - \sigma_{ij}^b\right)\left(\dot{\varepsilon}_{ij}^a - \dot{\varepsilon}_{ij}^b\right)dV = 0 \tag{2.36}$$

The last integrand may be written as

$$\left(\sigma_{ij}^a - \sigma_{ij}^b\right)\dot{\varepsilon}_{ij}^a + \left(\sigma_{ij}^b - \sigma_{ij}^a\right)\dot{\varepsilon}_{ij}^b \tag{2.37}$$

which is positive unless either $\dot{\varepsilon}_{ij}^a$ and $\dot{\varepsilon}_{ij}^b$ both vanish, or σ_{ij}^a and σ_{ij}^b are plastically equivalent. It can be concluded then, that two admissible stress fields σ_{ij}^a and σ_{ij}^b must be plastically equivalent everywhere except in their common rigid region, that is at points where $f(\boldsymbol{\sigma}) < 0$. If the body is made of a von Mises material or any material whose yield surface in stress-deviator space is strictly convex, and deforms plastically in its entirety, then the two stress fields can differ at most by a hydrostatic pressure field, which must be uniform in order to satisfy equilibrium, and must vanish if a surface traction is prescribed anywhere on S. Thus there is not more than one

admissible stress field for which the whole body is plastic, unless $S = S_u$ (where $\dot{u}$ are prescribed), in which case the stress field is determined only within a uniform hydrostatic pressure. In the words of Hill [2]: *in a plastic-rigid material there cannot be two distinct plastic states of stress satisfying the same boundary conditions.* On the other hand, as stated by Hill and Lubliner, uniqueness of the strain rate field or velocity field is not established.

2.2.10 The static/kinematic problem in Limit Analysis

The theorems of limit analysis can be established directly for a general body if the body possesses the following ideal properties:

1. The material exhibits perfect or ideal plasticity. This implies that the stress point cannot move outside the yield surface, so the vector $\dot{\sigma}_{ij}$ must be tangential to the yield surface whenever plastic strain rates are occurring.
2. The yield surface is convex and the plastic strain rates are derivable from the yield function through the associated flow rule. It follows from the perfect plasticity and the normality condition that $\dot{\sigma}_{ij}\dot{\varepsilon}^{p}_{ij} = 0$.
3. The changes in geometry of the body, which occur at the limit load are insignificant, hence the equation of virtual work at a fixed configuration can be applied.

Before describing the theorems of limit analysis it is necessary to clearly establish the basis to assume, in what follows, a *rigid-plastic* material behaviour. As stated by Chen and Liu [1]: *when the limit load is reached and the deformation proceeds under constant load, all stresses remain constant; only plastic (not elastic) increments of strain occur.* A direct proof is given by Lubliner [3] and Chen and Liu [1] by means of the equation of virtual work, and implies that the application of the *elastic-perfectly plastic* stress–strain rate relation becomes formally the same as the use of the *rigid-perfectly plastic* stress-strain rate relation. Note that in this case the elastic strain increments are proved to be zero, rather than being neglected. This was clearly proven by Lubliner by assuming that the equations of equilibrium and the traction boundary conditions can be differentiated with respect to time with no change in form, therefore the principle of virtual work is valid with $\boldsymbol{\sigma}$, $\mathbf{b}$ and $\mathbf{t}$ replaced by $\dot{\boldsymbol{\sigma}}$, $\dot{\mathbf{b}}$ and $\dot{\mathbf{t}}$. For a

virtual displacement field we take $\dot{\boldsymbol{u}}\delta t$, where $\dot{\boldsymbol{u}}$ is the actual velocity field and δt is a small time increment. The virtual strain field is then $\dot{\varepsilon}_{ij}\delta t$, with $2\dot{\varepsilon}_{ij} = \left(\dot{u}_{i,j} + \dot{u}_{j,i}\right)$ as defined before, so that at impending collapse

$$0 = \int_V \dot{\mathbf{b}} \cdot \dot{\boldsymbol{u}}\, dV + \int_{S_t} \dot{\mathbf{t}} \cdot \dot{\boldsymbol{u}}\, dS = \int_V \dot{\sigma}_{ij}\dot{\varepsilon}_{ij}\, dV = \int_V \dot{\sigma}_{ij}\left(\dot{\varepsilon}_{ij}^{p} + C_{ijkl}^{-1}\dot{\sigma}_{kl}\right) dV \qquad (2.38)$$

The positive definiteness of the elastic complementary energy implies $C_{ijkl}^{-1}\dot{\sigma}_{ij}\dot{\sigma}_{kl} \geq 0$ unless $\dot{\boldsymbol{\sigma}} = 0$. This fact and Drucker's inequality (equation (2.19)) imply that at impending collapse or incipient plastic flow the stress rates vanish, so that $\dot{\boldsymbol{\epsilon}}^{e} = 0$ and $\dot{\boldsymbol{\epsilon}} = \dot{\boldsymbol{\epsilon}}^{p}$, that is, a body in plastic collapse or flow behaves as if it were *rigid-plastic* rather than *elastic-plastic*, and this makes possible the rigorous application to elastic-plastic bodies of the theorems of limit analysis that had previously been defined for rigid-plastic bodies.

As described above, the equation of virtual work implies two independent sets, namely the equilibrium set and the compatible set, which in turn correspond directly to a *statically admissible state* and a *kinematically admissible state*, respectively. See figure 2.5. A detailed description of these states follows.

Following Jirásek and Bazant [5], let us specify the reference loading given by body forces, $\mathbf{b}$, and given surface tractions, $\mathbf{t}$. A *statically admissible state* is described by a stress field $\boldsymbol{\sigma}^{s}$ and a load multiplier γ^{s} such that

$$\begin{aligned} -div\ \boldsymbol{\sigma}^{s} &= \gamma^{s}\mathbf{b} \quad \text{in V} \\ \boldsymbol{\sigma}^{s}\mathbf{n} &= \gamma^{s}\mathbf{t} \quad \text{on } S_t \\ f(\boldsymbol{\sigma}^{s}) &\leq 0 \quad \text{in V} \end{aligned} \qquad (2.39)$$

Note that the superscript *s* only indicates statically admissible quantities. The above equations are the Cauchy equations of equilibrium, static boundary conditions and conditions of plastic admissibility. In the indicial notation these could be written as

$$
\begin{aligned}
-\frac{\partial \sigma_{ij}^{s}}{\partial x_j} &= \gamma^{s} b_i \quad \text{in V} \\
\sigma_{ij}^{s} n_j &= \gamma^{s} t_i \quad \text{on } S_t \\
f(\sigma_{ij}^{s}) &\le 0 \quad \text{in V}
\end{aligned}
\tag{2.40}
$$

Let us denote the set of all the plastically admissible stress fields by

$$
B = \{\boldsymbol{\sigma} \mid f(\boldsymbol{\sigma}(x)) \le 0, \forall x \in V\} \tag{2.41}
$$

so that the condition of plastic admissibility can be rewritten as $\boldsymbol{\sigma}^{s} \in B$.

On the other hand, a *kinematically admissible state* is described by a displacement rate field $\dot{\boldsymbol{u}}^{k}$ and a plastic strain-rate field $\dot{\boldsymbol{\varepsilon}}^{k}$ such that

$$
\begin{aligned}
\dot{\boldsymbol{\epsilon}}^{k} &= \tfrac{1}{2}\left[\nabla \dot{\boldsymbol{u}}^{k} + (\nabla \dot{\boldsymbol{u}}^{k})^{T}\right] \quad \text{in V} \\
\dot{\boldsymbol{u}}^{k} &= 0 \quad \text{on } S_u \\
\int_V \mathbf{b} \cdot \dot{\boldsymbol{u}}^{k} dV + \int_{S_t} \mathbf{t} \cdot \dot{\boldsymbol{u}}^{k} dS &> 0
\end{aligned}
\tag{2.42}
$$

Again, the superscript k refers only to the kinematical admissibility. The previous equations are the strain-displacement relations, kinematic boundary conditions, and condition of positive external power. In indicial notation these could be written as

$$
\begin{aligned}
\dot{\varepsilon}_{ij}^{k} &= \frac{1}{2}\left(\frac{\partial \dot{u}_i^{k}}{\partial x_j} + \frac{\partial \dot{u}_j^{k}}{\partial x_i}\right) \quad \text{in V} \\
\dot{u}_i^{k} &= 0 \quad \text{on } S_u \\
\int_V b_i \dot{u}_i^{k} dV + \int_{S_t} t_i \dot{u}_i^{k} dS &> 0
\end{aligned}
\tag{2.43}
$$

From the equation of virtual work in (2.31) a corresponding kinematically admissible multiplier can be given as

$$\gamma^k = \frac{\int_V D_p(\dot{\epsilon}^k)dV}{\int_V \mathbf{b}\cdot\dot{\boldsymbol{u}}^k dV + \int_{S_t} \mathbf{t}\cdot\dot{\boldsymbol{u}}^k dS} \tag{2.44}$$

The postulate of maximum plastic dissipation (section 2.2.6) is extended as a sum over the volume in the next section, leading to the relations between a load multiplier coming from a *static* analysis, i.e. one that yields a statically admissible stress field, and another resulting from a *kinematic* analysis, i.e. yielding a kinematically admissible velocity field.

2.2.11 Maximum Total Plastic Dissipation and the collapse multipliers

A discussion based on Jirásek and Bazant [5] on the *postulate of maximum plastic dissipation* and the steps leading to the determination of the static and kinematic collapse multipliers follows.

Consider an elastoplastic material with a convex yield surface and an associated flow rule. Let $\dot{\epsilon}^p$ *be a given plastic strain-rate field describing the flow induced by a certain stress field* $\boldsymbol{\sigma}$*. Then, the power that would be produced by an arbitrary plastically admissible stress field* $\boldsymbol{\sigma}^* \in B$ *cannot exceed the actual dissipation rate, that is*

$$\Pi_p(\dot{\boldsymbol{u}}) = \int_V D_p(\dot{\epsilon}^p)dV = \int_V \boldsymbol{\sigma} : \dot{\epsilon}^p dV = \max_{\boldsymbol{\sigma}^* \in B} \int_V \boldsymbol{\sigma}^* : \dot{\epsilon}^p dV \tag{2.45}$$

If we consider now an arbitrary statically admissible stress field $\boldsymbol{\sigma}^s$, and an arbitrary kinematically admissible displacement rate field $\dot{\boldsymbol{u}}^k$ (completely independent of each other). Since $\boldsymbol{\sigma}^s$ is plastically admissible, the postulate of maximum plastic dissipation (in which we set $\boldsymbol{\sigma}^* = \boldsymbol{\sigma}^s$ and $\dot{\epsilon}^p = \dot{\epsilon}^k$) yields

$$\int_V \boldsymbol{\sigma}^s : \dot{\epsilon}^k dV \le \int_V D_p(\dot{\epsilon}^k)dV \tag{2.46}$$

As $\boldsymbol{\sigma}^s$ is in equilibrium with body forces $\gamma^s\mathbf{b}$ and surface tractions $\gamma^s\mathbf{t}$, and $\dot{\epsilon}^k$ is compatible with $\dot{\boldsymbol{u}}^k$, the principle of virtual work lets us write the left expression in (2.46) as

$$\int_V \boldsymbol{\sigma}^s : \dot{\boldsymbol{\epsilon}}^k dV = \gamma^s \left(\int_V \mathbf{b} \cdot \dot{\boldsymbol{u}}^k dV + \int_{S_t} \mathbf{t} \cdot \dot{\boldsymbol{u}}^k dS \right) \tag{2.47}$$

The power represented by the sum of the integrals in the parenthesis is positive, as seen earlier. Combining the last two equations and using the definition of the kinematically admissible multiplier in (2.44), we obtain the inequality

$$\gamma^s \leq \frac{\int_V D_p(\dot{\boldsymbol{\epsilon}}^k) dV}{\int_V \mathbf{b} \cdot \dot{\boldsymbol{u}}^k dV + \int_{S_t} \mathbf{t} \cdot \dot{\boldsymbol{u}}^k dS} = \gamma^k \tag{2.48}$$

which shows the intrinsic relation between the theorems of limit analysis. As defined by Lubliner [3], the relation comes from similar definitions that are attached to the conditions of a *rigid–plastic* material. In the description of the St. Venant-Lévy-Mises flow rule it is considered that $\dot{\boldsymbol{\varepsilon}}$ is equal to $\dot{\boldsymbol{\varepsilon}}^p$, in fact, neglecting the effect of the elastic strain-rate as it vanishes at impending collapse. As discussed before, any solutions obtained on this basis are theoretically valid for idealized materials called *rigid-plastic.*

The *extremum principles* for standard rigid-plastic materials can be reformulated as the theorems of limit analysis, which give the upper and lower bounds on the loads under which a body that may be approximately modelled as elastic-perfectly plastic reaches a critical state, in which large increases in plastic deformation (considerably greater than the elastic deformation) become possible with little if any increase in load. In the case of perfectly plastic bodies this state is called *uncontained plastic flow* and the loading state at which it becomes possible is called *ultimate* or *limit loading*. It has been shown, that in a state of uncontained plastic flow, elasticity may be ignored and therefore a theory based on rigid-plastic behaviour is valid for elastic-plastic bodies. The proof of the limit analysis theorems is based on the principle of maximum plastic dissipation, and consequently they are valid only for standard materials (see section 2.2.2).

2.2.12 The Limit Analysis theorems

The limit analysis theorems are summarized in this section. Based on a description given by Lubliner [3], the theorems of limit analysis (the bounds theorems) can be established as follows.

Lower bound theorem

Suppose that at collapse the actual loads are $\mathbf{b}$ and $\mathbf{t}$, and the actual stress, velocity and strain-rate fields (in general unknown) are $\boldsymbol{\sigma}$, $\dot{\boldsymbol{u}}$ and $\dot{\boldsymbol{\epsilon}}$. Suppose further that we have somehow determined a stress field $\boldsymbol{\sigma}^*$, which does not violate the yield criterion anywhere and which is in equilibrium with the loads $\mathbf{b}^* = \gamma^s \mathbf{b}$ and $\mathbf{t}^* = \gamma^s \mathbf{t}$ where γ^s is a scalar factor. By virtual work we have

$$\int_V \sigma_{ij}^* \dot{\varepsilon}_{ij} \, dV = \gamma^s \left(\int_V \mathbf{b} \cdot \dot{\boldsymbol{u}} \, dV + \int_{S_t} \mathbf{t} \cdot \dot{\boldsymbol{u}} \, dS \right) = \gamma^s \int_V \sigma_{ij} \dot{\varepsilon}_{ij} \, dV \tag{2.49}$$

where $\int_V \sigma_{ij} \dot{\varepsilon}_{ij} \, dV$ is the internal work-rate corresponding to the nominal loads $\mathbf{b}$ and $\mathbf{t}$, that is

$$\int_V \sigma_{ij}^* \dot{\varepsilon}_{ij} \, dV = \gamma^s \int_V D_p(\dot{\boldsymbol{\epsilon}}) \, dV \tag{2.50}$$

By the principle of maximum plastic dissipation, $D_p(\dot{\boldsymbol{\epsilon}}) \geq \sigma_{ij}^* \dot{\varepsilon}_{ij}$, thus we have $\gamma^s \leq 1$, corresponding to a *safety factor* (static multiplier).

Upper bound theorem

Suppose that instead of $\boldsymbol{\sigma}^*$, we somehow determine a velocity field $\dot{\boldsymbol{u}}^*$ (a *collapse mechanism*) with the corresponding strain-rate field $\dot{\boldsymbol{\epsilon}}^*$, and loads $\mathbf{b}^* = \gamma^k \mathbf{b}$ and $\mathbf{t}^* = \gamma^k \mathbf{t}$ that satisfy

$$\int_V \mathbf{b}^* \cdot \dot{\boldsymbol{u}}^* dV + \int_{S_t} \mathbf{t}^* \cdot \dot{\boldsymbol{u}}^* dS = \int_V D_p(\dot{\boldsymbol{\epsilon}}^*) dV \tag{2.51}$$

provided the total plastic dissipation on the right-hand side is positive; here again by virtual work

$$\int_V D_p(\dot{\epsilon}^*)dV = \gamma^k \int_V \sigma_{ij}\dot{\varepsilon}_{ij}^* dV \tag{2.52}$$

where $\boldsymbol{\sigma}$ is the actual stress field at collapse, and $\int_V \sigma_{ij}\dot{\varepsilon}_{ij}\, dV$ is again the internal work-rate compatible with nominal loads. The principle of maximum plastic dissipation, however, also implies $D_p(\dot{\epsilon}^*) \geq \sigma_{ij}\dot{\varepsilon}_{ij}^*$. Consequently $\gamma^k \geq 1$, that means that γ^k is an *overload factor* (kinematic multiplier).

Form the previous descriptions, we can summarize, as defined in words by Jirásek and Bazant [5]:

i. **Fundamental theorem of limit analysis**: *No statically admissible multiplier is larger than any kinematically admissible multiplier.*
ii. **Lower Bound Theorem**: *The safety factor is the largest statically admissible multiplier.*
iii. **Upper Bound Theorem**: *The overload factor is the smallest kinematically admissible multiplier.*

The essential theory presented here constitutes the base upon which the present research work is founded. A brief discussion on the duality in limit analysis follows, to help construct, along with the theory presented up to this point, a better picture of the main approaches on which authors have been working recently.

2.3 Duality approach to Limit State Analysis

A very important aspect of the theory of limit analysis is that of the *duality property* between the *static principle* and the *kinematic principle* to the determination of the collapse load. This property permits to develop solutions based on optimisation tools that range from linear programming to semi-definite programming to exploit duality properties inherent to this formulations. Here a brief description of this property is presented based on the work of Christiansen [6] and Christiansen and Andersen [7], although the approach followed in the present research does not exploit duality, it is worth a review here as a sound theoretical reference, as it supports certain aspects of the formulation proposed in this research work. It serves also several other comparison purposes, specifically related to a recent work by Ciria and Peraire [8]

based on the duality approach, as well as earlier work by Casciaro and Cascini [9] where a mixed formulation is used, and another proposal by Borges, Zouain and Huespe[10] where a solution by optimality conditions is given.

2.3.1 Duality theory in Limit Analysis

Bearing in mind that the collapse problem for a plastic continuum is stated as follows: *given a load distribution acting on a body find the limit multiple of this load that the body can carry without collapsing*. Let V be the volume in space occupied by the material.

Part of the surface, $S_u \subseteq \partial V$ is fixed

$$\dot{\boldsymbol{u}} = 0 \quad \text{on} \quad S_{\mathrm{u}} \subseteq \partial V \tag{2.53}$$

where $\dot{\boldsymbol{u}}$ is the plastic displacement rate. The remaining surface, $S_{\mathrm{t}} \subseteq \partial V$, is free and subject to surface forces $\mathbf{t}$, while the volume is subject to body forces $\mathbf{b}$.

The work rate for the external forces $(\mathbf{t},\mathbf{b})$ with the plastic displacement rate $\dot{\boldsymbol{u}}$ is given by

$$F(\dot{\boldsymbol{u}}) = \int_V \mathbf{b}\cdot\dot{\boldsymbol{u}}\, dV + \int_{S_t} \mathbf{t}\cdot\dot{\boldsymbol{u}}\, dS \tag{2.54}$$

The work rate for the internal forces, given by the stress tensor $\boldsymbol{\sigma}$, and $\dot{\boldsymbol{u}}$ is

$$a(\boldsymbol{\sigma},\dot{\boldsymbol{u}}) = \int_V \sigma_{ij}\dot{\varepsilon}_{ij}\, dV = \int_V \sigma_{ij}\frac{\partial \dot{u}_j}{\partial x_i}\, dV \tag{2.55}$$

$$= -\int_V (div\ \boldsymbol{\sigma})\cdot\dot{\boldsymbol{u}}\, dV + \int_{S_t} (\boldsymbol{\sigma}\mathbf{n})\cdot\dot{\boldsymbol{u}}\, dS$$

where we have considered that $\dot{\boldsymbol{u}} = 0$ on S_u and assumed that Green's formula hold. With the strain-rate tensor $\dot{\epsilon} = (\dot{\varepsilon}_{ij})$

$$\dot{\varepsilon}_{ij} = \frac{1}{2}\left(\frac{\partial \dot{u}_i}{\partial x_j} + \frac{\partial \dot{u}_j}{\partial x_i} \right) \tag{2.56}$$

The equilibrium equation for the stress tensor $\boldsymbol{\sigma}$ (virtual work) is

$$a(\boldsymbol{\sigma}, \dot{\boldsymbol{u}}) = F(\dot{\boldsymbol{u}}) \quad \forall \dot{\boldsymbol{u}} \tag{2.57}$$

where $\boldsymbol{\sigma}$ must satisfy the yield condition, that is $\boldsymbol{\sigma} \in B$, where B, as defined in expression (2.41), is the convex set of *plastically admissible* stresses for the material.

The static principle of limit analysis states that the collapse multiplier γ^c is given by

$$\gamma^c = sup\left\{ \gamma \mid \exists \boldsymbol{\sigma} \in B : \; a(\boldsymbol{\sigma}, \dot{\boldsymbol{u}}) = \gamma F(\dot{\boldsymbol{u}}), \forall \dot{\boldsymbol{u}} \right\} \tag{2.58}$$

and, as established by Christiansen [6], it can be rewritten as

$$\gamma^c = \sup_{\boldsymbol{\sigma} \in B} \inf_{\dot{\boldsymbol{u}} \in C} a(\boldsymbol{\sigma}, \dot{\boldsymbol{u}}) \tag{2.59}$$

where the inner infimum in (2.59) equals $-\infty$, unless the function $a(\boldsymbol{\sigma}, \cdot)$ of $\dot{\boldsymbol{u}}$ is constant on the affine hyperplane

$$C = \left\{ \dot{\boldsymbol{u}} \mid F(\dot{\boldsymbol{u}}) = 1 \right\} \tag{2.60}$$

in which case $a(\boldsymbol{\sigma}, \cdot)$ and F are proportional. Hence, (2.58) is equivalent to the purely variational problem in (2.59).

The dual problem of (2.59) is, with the use of (2.60):

$$\gamma^c = \inf_{\dot{\boldsymbol{u}} \in C} \sup_{\boldsymbol{\sigma} \in B} a(\boldsymbol{\sigma}, \dot{\boldsymbol{u}}) = \inf_{\dot{\boldsymbol{u}} \in C} \Pi_p(\dot{\boldsymbol{u}}) \tag{2.61}$$

where

$$\Pi_p(\dot{\boldsymbol{u}}) = \sup_{\boldsymbol{\sigma} \in B} a(\boldsymbol{\sigma}, \dot{\boldsymbol{u}}) \tag{2.62}$$

is the total energy dissipation rate associated with $\dot{\boldsymbol{u}}$. Note that this corresponds directly with the plastic dissipation rate defined in previous sections, that is $\Pi_p(\dot{\boldsymbol{u}}) = \int_V D_p\left(\dot{\varepsilon}^p(\dot{\boldsymbol{u}})\right)dV$. The kinematic principle of limit analysis states that also the dual problem in (2.61), gives the collapse multiplier γ^c.

It can be shown under weak conditions that the duality between (2.59) and (2.61) holds with $\boldsymbol{\sigma}$ and $\dot{\boldsymbol{u}}$ varying in appropiate spaces:

$$\sup_{\boldsymbol{\sigma}\in B}\ \inf_{\dot{\boldsymbol{u}}\in C} a(\boldsymbol{\sigma},\dot{\boldsymbol{u}}) = \inf_{\dot{\boldsymbol{u}}\in C}\ \sup_{\boldsymbol{\sigma}\in B} a(\boldsymbol{\sigma},\dot{\boldsymbol{u}}) \tag{2.63}$$

It can also be shown that the collapse fields $\boldsymbol{\sigma}^c$, the solution to the *primal* problem and $\dot{\boldsymbol{u}}^c$, the solution to the *dual* problem, exist and form a saddle point for the internal energy $a(\boldsymbol{\sigma},\dot{\boldsymbol{u}})$ on $B\times C$. The saddle point is a pair of collapse fields for stress and velocity. More precisely, if $\boldsymbol{\sigma}^c$ and $\dot{\boldsymbol{u}}^c$ are solutions to (2.58) and (2.61) respectively, then for all $\boldsymbol{\sigma}\in B$ and $\dot{\boldsymbol{u}}\in C$ we have

$$a(\boldsymbol{\sigma},\dot{\boldsymbol{u}}^c) \le \gamma^c = a(\boldsymbol{\sigma}^c,\dot{\boldsymbol{u}}^c) \le a(\boldsymbol{\sigma}^c,\dot{\boldsymbol{u}}) \tag{2.64}$$

where $\boldsymbol{\sigma}^c$ is bounded, while $\dot{\boldsymbol{u}}^c$ has first-order derivatives, which are bounded measures in V, thus $\dot{\boldsymbol{u}}^c$ is of bounded variation. Neither $\boldsymbol{\sigma}^c$ nor $\dot{\boldsymbol{u}}^c$ need to be continuous, but the internal work in the collapse state is well defined and finite.

In his work, Christiansen [6] used a family of discretizations of the mixed form in (2.63) to solve the continuous duality problem in expressions (2.58) to (2.63). The approximation is made by a finite element approach. The finite element discretization is given in Appendix A. Refer to this addendum if an extended recount of such discretization is required. Additionally, Christiansen sets forth a pair of definitions which state the characteristics of the discretization, namely a *purely static* discretization, or a *purely kinematic* discretization; and also provides a pair of theorems leading to conclude that these static and kinematic discretizations yield a lower bound and an upper bound to the collapse multiplier, respectively. This definitions and theorems are also detailed in appendix A.

2.4 Limit Analysis solution approaches

In a paper by Borges, Zouain and Huespe [10], it is stated that all the discretized versions of limit analysis formulations lead to a single type of finite dimensional problem, which can be cast in four strictly equivalent forms, namely the *static*, *mixed*, *kinematic* and the set of discrete *optimality conditions*. In this way, a particular finite element discretization of the mixed principle in (2.63) gives rise to a discrete model which can be stated in four dual forms as described in Ciria and Peraire [8], all having exactly the same solution, in this case referred to as a *mixed* solution.

Then the discrete limit analysis problem consists of finding a load factor γ^c, a stress field $\boldsymbol{\sigma}$, a velocity field $\dot{\boldsymbol{u}}$ and a plastic multiplier $\dot{\lambda}$ such that the system represented by a strain-rate field (flow) $\dot{\boldsymbol{\epsilon}} = (\nabla \dot{\boldsymbol{u}})_{sym}$ and a convex function $f(\boldsymbol{\sigma})$ undergoes plastic collapse for some load proportional to a given force $\mathbf{t}$ and body forces $\mathbf{b}$. It is assumed that all rigid motions are ruled out by prescribed kinematic constraints, so that the kernel of the matrix produced from the strain rate-velocity relations contains only the null vector.

The four formulations below are equivalent statements of the discrete limit analysis problem in view of the convexity of $f(\boldsymbol{\sigma})$:

i. Static formulation

$$\gamma^c = \max_{\substack{\gamma \in \mathbb{R} \\ \sigma \in B}} \gamma \;\Bigg|\; \begin{array}{l} -div\ \boldsymbol{\sigma} = \gamma \mathbf{b} \\ \boldsymbol{\sigma}\,\mathbf{n} = \gamma \mathbf{t} \\ f(\boldsymbol{\sigma}) \le 0 \end{array} \tag{2.65}$$

ii. Mixed formulation

$$\gamma^c = \min_{\dot{u} \in C} \max_{\sigma \in B} a(\boldsymbol{\sigma}, \dot{\boldsymbol{u}}) \;\Bigg|\; \begin{array}{l} F(\dot{\boldsymbol{u}}) = 1 \\ f(\boldsymbol{\sigma}) \le 0 \end{array} \tag{2.66}$$

iii. Kinematic formulation

$$\gamma^c = \min_{\dot{u} \in C} \Pi_p(\dot{u}) \;\Big|\; F(\dot{u}) = 1 \tag{2.67}$$

where

$$\Pi_p(\dot{u}) = \max_{\sigma \in B} a(\sigma, \dot{u}) \;\Big|\; f(\sigma) \leq 0$$

iv. Optimality conditions

$$\begin{aligned}
&\dot{\varepsilon} - \nabla f(\sigma)\dot{\lambda} = 0 \\
&-div\ \sigma - \gamma \mathbf{b} = 0 \\
&\sigma\, \mathbf{n} - \gamma \mathbf{t} = 0 \\
&F(\dot{u}) = 1 \\
&f_i(\sigma)\dot{\lambda}_i = 0 \;\; ; \;\; i = 1, \ldots, m \\
&f(\sigma) \leq 0 \\
&\dot{\lambda} \geq 0
\end{aligned} \tag{2.68}$$

In this last approach, the equations are: the flow rule, two equilibrium equations, the condition of unitary external force work rate, and the last three, the *Karush-Kuhn-Tucker conditions*. The rest of the approaches are explained on the basis of duality theory.

In Christiansen and Andersen [7], an application of the theory described above is presented, for solving plane strain problems. The problem of limit analysis with quadratic yield condition is developed and tested, using the exact yielding condition and the general case of unbounded yield set is treated, which corresponds to unrestricted hydrostatic pressure. The finite element discretization is based on the duality between the static and the kinematic principle of limit analysis, and the solution method exploits this duality computing simultaneously approximations to the stress field and flow (velocity field) in the collapse state. Two examples in plane strain are presented, and the use of this approach in combiation with adaptive mesh refinement in limit analysis is suggested as for future research work.

A recent work by Ciria and Peraire [8] has produced excellent results in the implementation of both the *static* and *kinematic* formulations based on duality aspects set out by Christiansen [6], to be solved by a large-scale optimisation technique, namely an *interior point method* using Second-Order Cone Programming. An adaptive mesh refinement procedure has been implemented in their work, in line with the adaptive approach followed in the present work.

Casciaro and Cascini [9] presented an ample set of solutions to problems in *plane stress* and *plane strain*, resolved through a mixed formulation approach where stress and velocity fields are obtained from the stationary condition for a suitable defined functional, leading to an unconstrained minimization solution procedure. Mixed finite elements with independent interpolation of stress and velocity fields are used.

2.5 Proposed solution approach

The previous description (section 2.4) lets us locate the present research work within the suggested frameworks just depicted for the solution of the limit analysis problem. All our efforts have been concentrated in producing an accurate and reliable application of the *kinematic formulation*, so that as will be clear later, a first stage in the development is devoted to the formulation and implementation of the *upper bound theorem* (approach iii. above). A second stage has been dedicated to formulating, implementing and proving computationally, a new proposed approach to the computation of a *lower bound* to the collapse multiplier. Although this new approach is not derived or resolved through the direct application of the limit analysis theorem, it is based on it in the sense that a series of localized problems are resolved over the domain, providing equilibrium conditions within local discrete volumes (elements) of the domain, as well as assuring stress continuity conditions along the edge of each discrete volume. Plastic admissibility conditions for the stress distribution inside the volume domain is complied with by resolving the local problem, at each discrete volume, by a local application of the *kinematic* solution, taking the stress distribution to the plastic limit at the local level and obtaining a local kinematic multiplier for each volume domain. A summation of the local piecewise contributions to the lower bound can then be computed to achieve a convergent progression of the lower collapse multiplier. Both this stages and their formulation are described in Chapter 3 and

Chapter 4. Implementation details are dealt with in Chapter 5, and then validation and application examples are discussed in Chapter 6.

The theoretical framework presented here on the duality property is based mainly on the work of Edmund Christiansen for the *static* and *kinematic* principles, as set out by A. Charnes, H. J. Greenberg, C.E. Lemke and O. C. Zienkiewicz. In addition, a discussion based on Borges, Zouain and Huespe [10] has led us to define four different approaches to the solution of the Limit Analysis problem. Although our approach is neither based on a mixed finite element formulation, nor on an approach which exploits duality, the concepts are brought here due to the requirement of a framework that serves as a foundation reference in some parts of the theoretical development for the present research and as a comparative reference to some of the results obtained in the application of this particular modern approach to limit analysis. Specifically, a recent work using Ciria & Peraire [8], in which an implementation of the discrete duality problem, based on a bounds formulation (*static* and *kinematic* approaches), has been solved through the use of Second-Order Cone Programming. This technique is one of the most recent *interior point* solvers for grand-scale non-linear optimisation problems. Another important reference, as described above, is the work of Casciaro and Cascini [9]. These last three references will be used thoroughly specially in the comparison of the results of the present proposal, as discussed in Chapter 6.

2.6 References

1. Chen W.F., Liu X.L. *Limit analysis in soil mechanics*. Elsevier Science Publishers, Amsterdam, 1990.
2. Hill R. *The mathematical theory of plasticity*. Oxford University Press, London, 1950.
3. Lubliner J. *Plasticity theory*. Macmillan Publishing Company, New York, 1990.
4. Shames I.H., Cozzarelli F.A. *Elastic and inelastic stress analysis*. Prentice-Hall, Inc., New Jersey, 1991.
5. Jirazek M., Bazant Z. *Inelastic analysis of structures*. John Wiley & Sons, Ltd., Chichester, 2001.
6. Christiansen, E. *Computation of limit loads*. International Journal for Numerical Methods in Engineering. Vol. 17, 1981, p.1547-1570.
7. Christiansen E., Andersen K.D. *Computation of collapse states with von Mises type yield condition*. International Journal for Numerical Methods in Engineering. Vol. 46, 1999, p.1185-1202.

8. Ciria H., Peraire J. *Computation of upper and lower bounds in limit analysis using second-order cone programming and mesh adaptivity*. MSc Thesis, Massachusetts Institute of Technology, 2004.
9. Casciaro R., Cascini L. *A mixed formulation and mixed finite elements for limit analysis*. International Journal for Numerical Methods in Engineering. Vol. 18, 1982, p.211-243.
10. Borges L.A., Zouain N., Huespe A.E. *A nonlinear optimization procedure for limit analysis*. European Journal of Mechanics, A/Solids, Vol. 15, No. 3, 1996, p.487-512.

Chapter 3

Finite element upper bound evaluation

3.1 Introduction

In the present section a kinematic approach to the limit analysis problem is formulated. As described in sections 2.2.10 to 2.2.12 through the establishment of the limit analysis theorems, and in view of the discussion in section 2.3.1 based on the duality property, an *upper bound* to the collapse multiplier can be found through a *kinematic* discrete solution. The following sections deal with the construction of a *finite element* discrete formulation leading to a robust limit analysis solution package for *plane stress* problems. A multiplier approaching the true collapse load multiplier from above, that is, an upper bound, is found from this analysis along with a corresponding failure *mechanism*, or failure *mode* defined by the collapse velocity field. Secondary data can be drawn out of this implementation, in the form of stress distributions, and the plastic dissipation distribution based on a piecewise evaluation of the *equivalent strain-rate*. The kinematic approach described here, although through a different formulation and solution procedures, is in line with the approach taken by Ponter and Carter [1], based on similar principles to the *elastic compensation* and reformulated as a non-linear programming method. A generalisation of these principles is presented in a paper by Ponter, Fuschi and Engelhardt [2], coinciding with some of the aspects described in the next sections.

3.2 Plastic Potential for Plane Stress

The constitutive elements for the *plane stress limit analysis solution,* leading to the construction of the *tangent system matrix*, after an assembling process in the traditional finite element sense, is discussed in the following paragraphs.

Consider a simple rigid-plastic von Mises material in plane stress. The *rate of plastic dissipation* for a given *Eulerian strain-rate* tensor defined by

$$\dot{\boldsymbol{\epsilon}} = \tfrac{1}{2}\left(\nabla \dot{\boldsymbol{u}} + \nabla \dot{\boldsymbol{u}}^T\right) \tag{3.1}$$

as described by Lubliner [3], can be written as:

$$D_p\left(\dot{\boldsymbol{\epsilon}}\right) = \boldsymbol{\sigma}\left(\dot{\boldsymbol{\epsilon}}\right) : \dot{\boldsymbol{\epsilon}} = \sigma_y \dot{\bar{\varepsilon}} \tag{3.2}$$

in line with definition (2.25). Note that $\boldsymbol{\sigma}\left(\dot{\boldsymbol{\epsilon}}\right)$ is the pointwise definition of the stress tensor in space, i.e. a nine-component tensor, with $\dot{\boldsymbol{\epsilon}}$ being its work conjugate, the strain-rate tensor. The scalars σ_y and $\dot{\bar{\varepsilon}}$ are the uniaxial yield stress and the *equivalent strain-rate*, respectively; the latter being defined in equation (2.30) and expressed conveniently here by

$$\dot{\bar{\varepsilon}} = \sqrt{\frac{2}{3}\left(\dot{\boldsymbol{\epsilon}} : \dot{\boldsymbol{\epsilon}}\right)} \tag{3.3}$$

The strain-rate tensor for the case of *plane stress* in nine-component form is given by

$$\dot{\boldsymbol{\epsilon}} = \begin{bmatrix} \dot{\varepsilon}_{11} & \dot{\varepsilon}_{12} & 0 \\ \dot{\varepsilon}_{21} & \dot{\varepsilon}_{22} & 0 \\ 0 & 0 & \dot{\varepsilon}_{33} \end{bmatrix} \tag{3.4}$$

so that the incompressibility condition for the plastic flow implies:

$$tr(\dot{\boldsymbol{\epsilon}}) = \dot{\varepsilon}_{11} + \dot{\varepsilon}_{22} + \dot{\varepsilon}_{33} = 0 \tag{3.5}$$

therefore the off-plane stretching component is given by

$$\dot{\varepsilon}_{33} = -(\dot{\varepsilon}_{11} + \dot{\varepsilon}_{22}) = -I_d = -tr(\boldsymbol{d}) \tag{3.6}$$

with

$$\boldsymbol{d} = \begin{bmatrix} d_{11} & d_{12} \\ d_{21} & d_{22} \end{bmatrix} = \begin{bmatrix} \dot{\varepsilon}_{11} & \dot{\varepsilon}_{12} \\ \dot{\varepsilon}_{21} & \dot{\varepsilon}_{22} \end{bmatrix} \tag{3.7}$$

where matrix $\boldsymbol{d}$ represents the 2-dimensional tensor of in-plane components, and $I_d = d_{11} + d_{22}$ its trace. So that from condition (3.5) we have

$$\dot{\boldsymbol{\epsilon}} : \dot{\boldsymbol{\epsilon}} = \boldsymbol{d} : \boldsymbol{d} + d_{33}^2 \tag{3.8}$$

Hence equation (3.3) in incompressible plane stress becomes

$$\dot{\bar{\varepsilon}} = \sqrt{\frac{2}{3}\left(\boldsymbol{d} : \boldsymbol{d} + I_d^2\right)} \tag{3.9}$$

Thus the plastic dissipation can be expressed as in (3.2) for plane stress, complying with incompressibility conditions, by the product

$$D_p(\boldsymbol{d}) = \sigma_y \dot{\bar{\varepsilon}} = \sigma_y \sqrt{\frac{2}{3}\left(\boldsymbol{d} : \boldsymbol{d} + I_d^2\right)} \tag{3.10}$$

Note that D_p is order-one homogeneous, that is $D_p(\alpha \boldsymbol{d}) = \alpha D_p(\boldsymbol{d})$. In view of equation (3.2), given also as $D_p(\boldsymbol{d}) = \boldsymbol{\sigma} : \boldsymbol{d}$, with the stress and strain-rate tensor now given in four-component form for plane stress, the convexity of the yield surface and the normality rule for the plastic flow (see section 2.2.6) imply

$$D_p(\boldsymbol{d}) = \boldsymbol{\sigma} : \boldsymbol{d} \geq \boldsymbol{\sigma}^* : \boldsymbol{d} \tag{3.11}$$

for any $\boldsymbol{\sigma}^*$ inside the yield surface, as shown in figure 3.1, where P is the space of stresses that satisfy the yield criterion.

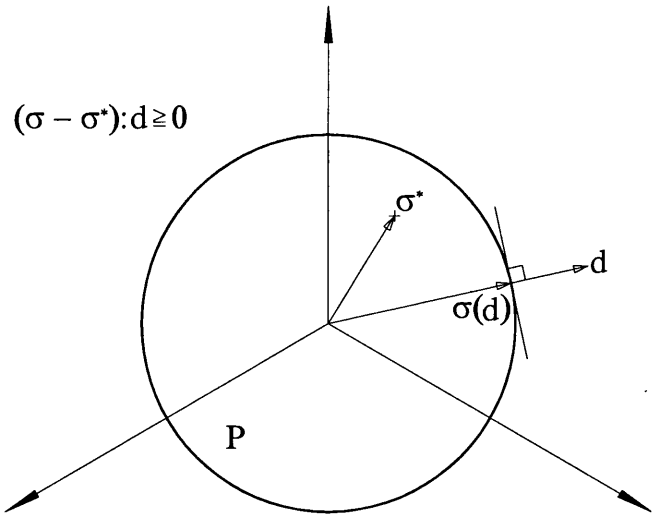

Figure 3.1 Von Mises yield surface

3.3 Constitutive relations

In order to define piecewise constitutive components let us consider the plastic dissipation as in definition (3.2). Note that since D_p is order-one homogeneous in $\boldsymbol{d}$ then

$$\frac{\partial D_p}{\partial \boldsymbol{d}} : \boldsymbol{d} = D_p = \boldsymbol{\sigma} : \boldsymbol{d} \tag{3.12}$$

and therefore D_p represents a strain-rate potential (see section 2.2.2) from which stresses can be evaluated as

$$\boldsymbol{\sigma} = \frac{\partial D_p}{\partial \boldsymbol{d}} \tag{3.13}$$

thus, by considering definition (3.10), stresses can be obtained from the derivative of expression (3.10) to give

$$\boldsymbol{\sigma} = \frac{1}{2}\frac{\sigma_y}{\dot{\bar{\varepsilon}}}\frac{\partial \dot{\bar{\varepsilon}}^2}{\partial \boldsymbol{d}} = \frac{2}{3}\frac{\sigma_y}{\dot{\bar{\varepsilon}}}(\boldsymbol{d} + I_d \mathbf{I}) \tag{3.14}$$

where $\mathbf{I} = \left[\delta_{ij}\right]$, $i, j = 1,2$, is the second-order identity tensor. By defining the *strain-rate dependent, viscosity type* parameter μ as

$$\mu = \frac{\sigma_y}{3\dot{\bar{\varepsilon}}}, \tag{3.15}$$

a parameter which is similar to the one used by Ponter, Fuschi and Engelhardt [2], the stress can be written as

$$\boldsymbol{\sigma} = 2\mu(\boldsymbol{d} + I_d\mathbf{I}) \tag{3.16}$$

From these relations we can clearly define the *tangent plastic moduli* as

$$\frac{\partial^2 D_p}{\partial \boldsymbol{d}\partial \boldsymbol{d}} = \frac{\partial \boldsymbol{\sigma}}{\partial \boldsymbol{d}} = 2\mu(\mathbf{I}\otimes\mathbf{I} + \mathbb{I}) + \frac{\boldsymbol{\sigma}}{\mu}\otimes\frac{\partial \mu}{\partial \boldsymbol{d}} \tag{3.17}$$

with $\mathbb{I}$ being the fourth-order unit tensor $\mathbb{I}_{ijkl} = \frac{1}{2}(\delta_{ik}\delta_{jl} + \delta_{il}\delta_{jk})$ and $\mathbf{I}\otimes\mathbf{I} = \delta_{ij}\delta_{kl}$. With the help of relation (3.16) and after some algebra, it is shown that

$$\frac{\partial \mu}{\partial \boldsymbol{d}} = -\frac{1}{3\dot{\bar{\varepsilon}}^2}2\mu\left(\boldsymbol{d} + I_d\mathbf{I}\right) = -\frac{1}{3\dot{\bar{\varepsilon}}^2}\boldsymbol{\sigma} \tag{3.18}$$

hence, the tangent plastic modulus components can be computed from

$$\mathbb{C}_p = \frac{\partial^2 D_p}{\partial \boldsymbol{d}\partial \boldsymbol{d}} = 2\mu\left(\mathbf{I}\otimes\mathbf{I} + \mathbb{I}\right) - \frac{1}{\sigma_y\dot{\bar{\varepsilon}}}\boldsymbol{\sigma}\otimes\boldsymbol{\sigma} \tag{3.19}$$

Note that the first term in expression (3.19) resembles that of *plane stress linear elasticity,* except that μ is a parameter depending on the strain-rate and behaving asymthotically in the vicinity of $\dot{\bar{\varepsilon}} = 0$ and $\dot{\bar{\varepsilon}} = +\infty$. Also note that the denominator in the second term is actually the piecewise plastic dissipation per unit volume. An infinite value of the modulus component can be obtained when the strain-rate approaches zero, that is when piecewise rigid motion is in place. Numerically, this condition can lead to divergent behaviour, depending on the geometry and load configuration of the problem to be solved, specifically dependent on the number of discrete volumes subject to an infinite value of μ and the order at which the infinite value and operations upon it can be represented digitally. A convenient treatment to solve this problem is described in Chapter 5, where implementation issues are

discussed. The parameter μ can be interpreted as a piecewise tangent material modulus, as in Ponter, Fuschi and Engelhardt [2].

3.4 The Limit Analysis Upper Bound theorem revisited

Consider a body in *plane stress* occupying a volume V with boundary $S = \partial V = S_t \cup S_u$. The body in figure 3.2 is under the action of surface forces $\gamma \mathbf{t}$ on S_t and under some fixity condition on S_u, where γ is the load multiplier and $\mathbf{t}$ the nominal load.

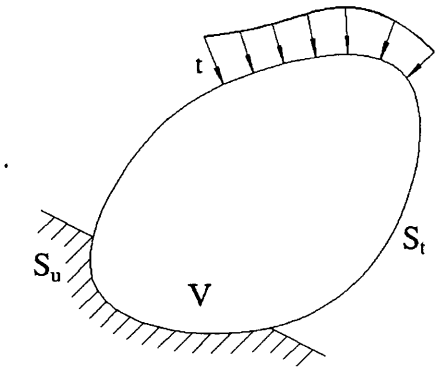

Figure 3.2 Generalized body subject to boundary conditions

Assuming that the body is rigid-plastic with plastic potential D_p, uncontained plastic flow will be initiated for a collapse multiplier γ^c and will lead to a statically admissible stress field $\boldsymbol{\sigma}^c$ inside the body. Neglecting body forces, as will be done in the rest of this work, the equilibrium at this collapse state implies:

$$\gamma^c \int_{S_t} \mathbf{t} \cdot \dot{\boldsymbol{u}}\, ds = \int_V \boldsymbol{\sigma}^c : \boldsymbol{d}\, dV \qquad \forall\, \dot{\boldsymbol{u}} \in Y \tag{3.20}$$

where Y is the space of motions compatible with boundary conditions, and $\boldsymbol{d}$ is the strain-rate tensor defined in (3.7) and associated with velocities $\dot{\boldsymbol{u}}$.

The work rate done by the external forces will be conveniently denoted as $\Pi_t(\dot{\boldsymbol{u}})$ neglecting body forces, and defined as

$$\Pi_t(\dot{\boldsymbol{u}}) = \int_{S_t} \mathbf{t} \cdot \dot{\boldsymbol{u}}\, ds \tag{3.21}$$

The principle of maximum plastic dissipation implies

$$\boldsymbol{\sigma}^c : \boldsymbol{d} \le D_p(\boldsymbol{d}) \tag{3.22}$$

consequently,

$$\gamma^c \Pi_t(\dot{\boldsymbol{u}}) \le \int_V D_p(\boldsymbol{d})\, dV \tag{3.23}$$

and, by defining the *total plastic work* $\Pi_p(\dot{\boldsymbol{u}})$ as

$$\Pi_p(\dot{\boldsymbol{u}}) = \int_V D_p(\boldsymbol{d})\, dV \tag{3.24}$$

the following inequality, known as the *upper bound theorem*, is obtained:

$$\gamma^c \le \gamma^k \equiv \frac{\Pi_p(\dot{\boldsymbol{u}})}{\Pi_t(\dot{\boldsymbol{u}})} \quad \forall\, \dot{\boldsymbol{u}} \in Y \tag{3.25}$$

which is a particular instance of the more general form in relation (2.48) given by Jirásek and Bazant [4]. Note the use of a *volume differential* in expressions (3.23) and (3.24); in plane analysis with constant unit thickness $dV = dA$ is implied.

In particular, for the collapse mechanism $\boldsymbol{v}^c$, we can write

$$\gamma^c = \frac{\Pi_p(\boldsymbol{v}^c)}{\Pi_t(\boldsymbol{v}^c)} = \min_{\dot{\boldsymbol{u}} \in Y} \frac{\Pi_p(\dot{\boldsymbol{u}})}{\Pi_t(\dot{\boldsymbol{u}})} \tag{3.26}$$

Where it is assumed that $\gamma^s \le \gamma^c \le \gamma^k$ in the context of sections 2.2.10 to 2.2.12, and that a sufficiently fine dicretization is in place. Note however, that both Π_p and Π_t are first-order homogeneous, that is $\Pi(\alpha\dot{\boldsymbol{u}}) = \alpha\Pi(\dot{\boldsymbol{u}})$, where $\alpha \in \mathbb{R}$. Hence $\dot{\boldsymbol{u}}$ is only defined in direction but not in magnitude by (3.26) as pointed out in section 2.3.1. To remove this indeterminancy, we define the *reduced* space $\overline{Y}$ as

$$\overline{Y} = \left\{ \dot{\boldsymbol{u}} \in Y \;\middle|\; \Pi_t(\dot{\boldsymbol{u}}) = 1 \right\} \tag{3.27}$$

which defines a hyperplane, as defined by Christiansen [5] in which the external work rate is set constant with respect to $\dot{\boldsymbol{u}}$, as similarly restricted in definition (2.60). Therefore (3.26) becomes

$$\gamma^c = \min_{\dot{\boldsymbol{u}} \in \overline{Y}} \Pi_p(\dot{\boldsymbol{u}}) \tag{3.28}$$

The next section describes the finite element discretization based on the theoretical elements described in the previous and present sections, and in section 2.3.1.

3.5 Finite Element Upper Bound solution

In this section, three key elements in the construction of the kinematic solution procedure are dealt with, providing a setting for the proposed solution in the context of the finite element discretization. The present description follows, at many steps, the discretization and linearization developments found in Bonet and Wood [6].

3.5.1 The discrete kinematic Limit Analysis problem

Consider a finite element discrete model of the body, and using the notation set by Christiansen [5] (see section 2.3.1) for the velocity space, let Y_H denote the corresponding solution space, as shown in figure 3.3:

$$Y_H = \left\{ \dot{\boldsymbol{u}} \in Y \;\middle|\; \dot{\boldsymbol{u}} = \sum_{a=1}^{N} \dot{\mathbf{u}}_a N_a \right\} \tag{3.29}$$

for a given set of finite element shape functions N_a over a mesh with N nodes. It is worth noting subscript H in definition (3.29), which will be used to indicate a *coarse mesh* definition further on; however in the ongoing discussion it is regarded as a conventional nominal element size parameter.

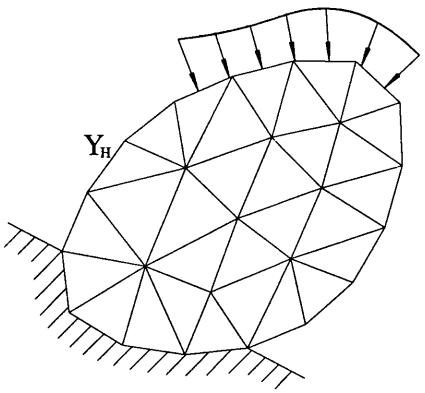

Figure 3.3 Discrete kinematic solution space

Consider also the *reduced* space $\overline{Y}_H$

$$\overline{Y}_H = \left\{ \dot{\boldsymbol{u}} \in Y_H \,\middle|\, \Pi_t(\dot{\boldsymbol{u}}) = 1 \right\} \tag{3.30}$$

under this conditions, the minimization is now written as

$$\gamma_H \equiv \Pi_p(\boldsymbol{v}_H) = \min_{\dot{\boldsymbol{u}} \in \overline{Y}_H} \Pi_p(\dot{\boldsymbol{u}}) \tag{3.31}$$

where $\boldsymbol{v}_H \in \overline{Y}_H$. Field $\boldsymbol{v}_H$ corresponds to a kinematically admissible velocity field that minimizes the plastic potential and describes an approximate collapse mechanism, defined over a finite element mesh with nominal element size H.

Recall that $\overline{Y}_H \subset \overline{Y}$, therefore we have an upper bound of the solution:

$$\gamma^c \leq \gamma_H \tag{3.32}$$

as stated by Christiansen [5] in definition A.2 and theorem A.2 in appendix A.

The solution space Y_H implies the discrete interpolation

$$\dot{\boldsymbol{u}} = \sum_{a=1}^{N} \dot{\boldsymbol{u}}_a N_a \tag{3.33}$$

where N is the number of nodes in the discretized space, $N_a(\xi,\eta)$ are the standard isoparametric shape functions for a linear triangular (3-noded) element; and also the nodal velocity is

$$\dot{\boldsymbol{u}}_a = \left[\dot{u}_a^x \quad \dot{u}_a^y\right]^T \tag{3.34}$$

so that the interpolation can be written as

$$\dot{\boldsymbol{u}}^e = \sum_{a=1}^{3} \dot{\boldsymbol{u}}_a N_a \tag{3.35}$$

within element e. Index a is used to indicate a generalized node defined within the body, so that the global vector of nodal velocities (unknowns) can be defined as

$$\dot{\mathbf{u}} = \left[\dot{u}_1^x \quad \dot{u}_1^y \quad \dot{u}_2^x \quad \dot{u}_2^y \quad \cdots \quad \dot{u}_N^x \quad \dot{u}_N^y\right]^T \tag{3.36}$$

With this setting the minimisation (3.31) can be rewritten in discrete form as

$$\gamma_H = \Pi_p(\mathbf{v}_H) = \min_{\dot{\mathbf{u}}} \frac{\Pi_p(\dot{\mathbf{u}})}{\Pi_f(\dot{\mathbf{u}})} \tag{3.37}$$

where $\mathbf{v}_H$ is the vector of nodal velocities pertaining to the collapse state. The discretized form of the work done by the external forces over node a of element e is given by

$$\Pi_f(N_a\dot{\boldsymbol{u}}_a)\Big|_a^e = \int_{S_t^e} \mathbf{t}\cdot(N_a\dot{\boldsymbol{u}}_a)\, ds = \left(\int_{S_t^e} \mathbf{t}\, N_a\, ds\right)\cdot\dot{\boldsymbol{u}}_a = \boldsymbol{F}_a^e\cdot\dot{\boldsymbol{u}}_a \tag{3.38}$$

so that the external forces acting on node a are given by the assemblage

$$\boldsymbol{F}_a = \sum_{\substack{e=1 \\ e\ni a}}^{M} \boldsymbol{F}_a^e \quad ; \quad \boldsymbol{F}_a^e = \int_{S_t^e} \mathbf{t}\, N_a\, ds \tag{3.39}$$

which sums the contributions from elements containing node a. Index M is the number of elements in the discretized space. When contributions from all the nodes in the discretized space are accounted for, the global vector of external forces is given as

$$\mathbf{F} = \begin{bmatrix} \boldsymbol{F}_1 & \boldsymbol{F}_2 & \cdots & \boldsymbol{F}_N \end{bmatrix}^T \tag{3.40}$$

These are a collection of two-component sub-vectors, one per each node, arranged to form the global external force vector.

Thus, from (3.30) and (3.38), the condition imposed over the reduced space implies:

$$\Pi_f(\dot{\boldsymbol{u}}) = \mathbf{F}^T \dot{\mathbf{u}} = 1 \tag{3.41}$$

So that the minimisation now reads

$$\gamma_H = \Pi_p(\mathbf{v}_H) = \min_{\dot{\mathbf{u}} | \mathbf{F}^T \dot{\mathbf{u}} = 1} \Pi_p(\dot{\mathbf{u}}) \tag{3.42}$$

Given the notation used herein, it is illustrative to write the following steps of the discretization, and later the linearization, in the more familiar matrix-vector notation. So that, for the plane-stress case at hand the stress tensor given in four-component form, takes the reduced form

$$\boldsymbol{\sigma} = \begin{bmatrix} \sigma_{11} & \sigma_{22} & \sigma_{12} \end{bmatrix}^T \tag{3.43}$$

Accordingly, the strain-rate tensor can be expressed as

$$\mathbf{d} = \begin{bmatrix} d_{11} & d_{22} & 2d_{12} \end{bmatrix}^T \tag{3.44}$$

The factor 2 at the last component is necessary to produce the correct internal energy, that is:

$$\int_V \boldsymbol{\sigma} : \boldsymbol{d} \, dV = \int_V \mathbf{d}^T \boldsymbol{\sigma} \, dV \tag{3.45}$$

With this notation, the strain-rate tensor can be rewritten in a corresponding form, departing from the conventional matrix form

$$\boldsymbol{d} = \nabla^{sym} \dot{\boldsymbol{u}} = \tfrac{1}{2} \sum_{a=1}^{3} \left(\dot{\boldsymbol{u}}_a \otimes \nabla N_a + \nabla N_a \otimes \dot{\boldsymbol{u}}_a \right) \tag{3.46}$$

where the Cartesian derivatives $\nabla N_a = \partial N_a / \partial \boldsymbol{x}$ can be computed from expressions:

$$\frac{\partial N_a}{\partial \boldsymbol{x}} = \left(\frac{\partial \boldsymbol{x}}{\partial \boldsymbol{\xi}} \right)^{-T} \frac{\partial N_a}{\partial \boldsymbol{\xi}} \quad ; \quad \frac{\partial \boldsymbol{x}}{\partial \boldsymbol{\xi}} = \sum_{a=1}^{3} \boldsymbol{x}_a \otimes \nabla_{\xi} N_a \tag{3.47}$$

Expanding (3.46) and equating components we arrive at

$$\mathbf{d} = \begin{bmatrix} d_{11} \\ d_{22} \\ 2d_{12} \end{bmatrix} = \sum_{a=1}^{3} \mathbf{B}_a \dot{\boldsymbol{u}}_a \tag{3.48}$$

with the Cartesian derivatives matrix defined as usual

$$\mathbf{B}_a = \begin{bmatrix} \partial N_a/\partial x & 0 & \partial N_a/\partial y \\ 0 & \partial N_a/\partial y & \partial N_a/\partial x \end{bmatrix}^T \tag{3.49}$$

Similarly, the symmetric stress tensor is defined using (3.46) in four-component form as in definition (3.16):

$$\boldsymbol{\sigma} = 2\mu \left(\boldsymbol{d} + I_d \mathbf{I} \right) \tag{3.50}$$

that is, the components given by $\sigma_{ij} = 2\mu \left(d_{ij} + I_d \delta_{ij} \right)$, $i, j = 1,2$ where μ and I_d are given in (3.15) and (3.6), respectively. Matrix $\mathbf{I}$ is the second-order identity tensor. Note that in expression (3.50) the tensor $\boldsymbol{d}$ is defined by (3.7). The stress vector in (3.43) can easily be rearranged from the stress tensor in (3.50).

An alternative approach to solve the minimization is that of the *secant* method, where instead of a tangent matrix, a material secant matrix is derived, leading to a relation of the form

$$\boldsymbol{\sigma} = D_{secant}(\mu)\mathbf{d} \tag{3.51}$$

This approach is similar to that used by Carter and Ponter [1], and it has been found to yield a larger convergence path (i.e. more iterations are needed to converge) than that of the Newton-Raphson procedure.

3.5.2 Solving the minimization problem

Now, returning to the constrained minimization stated previously:

$$\gamma_H = \min_{\dot{\mathbf{u}}|\mathbf{F}^T\mathbf{u}=1} \Pi_p(\dot{\mathbf{u}}) \tag{3.52}$$

the problem can be solved by means of a Lagrange multiplier λ defining a discrete functional L as

$$L(\dot{\mathbf{u}},\lambda) = \Pi_p(\dot{\mathbf{u}}) - \lambda\left(\mathbf{F}^T\mathbf{u} - 1\right) \tag{3.53}$$

From (3.53) a minimum can be obtained by the following conditions

$$\frac{\partial L(\dot{\mathbf{u}},\lambda)}{\partial \dot{\mathbf{u}}} = \frac{\partial \Pi_p(\dot{\mathbf{u}})}{\partial \dot{\mathbf{u}}} - \lambda\mathbf{F} = 0 \tag{3.54}$$

and

$$\frac{\partial L(\dot{\mathbf{u}},\lambda)}{\partial \lambda} = \mathbf{F}^T\dot{\mathbf{u}} - 1 = 0 \tag{3.55}$$

Clearly, condition (3.55) yields the vector form of the constraint set in the space definition (3.27). In order to establish condition (3.54) in matrix-vector notation, we resort here to the minimisation in terms of the velocity field $\dot{\boldsymbol{u}}$, thus the Lagrangian is now given by

$$L(\dot{\boldsymbol{u}},\lambda) = \Pi_p(\dot{\boldsymbol{u}}) - \lambda\left(\Pi_t(\dot{\boldsymbol{u}}) - 1\right) \tag{3.56}$$

with conditions given by the following equations

$$D_1 L(\dot{\boldsymbol{u}},\lambda)[\delta\dot{\boldsymbol{u}}] = D\Pi_p(\dot{\boldsymbol{u}})[\delta\dot{\boldsymbol{u}}] - \lambda D\Pi_t(\dot{\boldsymbol{u}})[\delta\dot{\boldsymbol{u}}] = 0 \tag{3.57}$$

or similarly

$$D_1 L(\dot{\boldsymbol{u}},\lambda)[\delta\dot{\boldsymbol{u}}] = T(\dot{\boldsymbol{u}};\delta\dot{\boldsymbol{u}}) - \lambda F(\dot{\boldsymbol{u}};\delta\dot{\boldsymbol{u}}) = 0 \tag{3.58}$$

and also

$$D_2 L(\dot{\boldsymbol{u}}, \lambda)[\delta\lambda] = \delta\lambda\left(\Pi_t(\dot{\boldsymbol{u}}) - 1\right) = 0 \tag{3.59}$$

The operator $D(\bullet)[\bullet]$ is the well-known *directional derivative,* as defined in Bonet and Wood [6]. Conditions (3.55) and (3.59) correspond to the unit external load work-rate imposed before.

Given that in condition (3.54) the second term is clearly defined in vector form, we first turn our attention to the internal work-rate term in condition (3.57), that is the work done by the internal forces on a set of virtual velocities $\delta\dot{\boldsymbol{u}}$:

$$T(\dot{\boldsymbol{u}}; \delta\dot{\boldsymbol{u}}) = D\Pi_p(\dot{\boldsymbol{u}})[\delta\dot{\boldsymbol{u}}] \tag{3.60}$$

It is convenient, however, to first determine the nodal contribution by each element to the internal work-rate in order to construct a global value by summation over the nodes.

Thus we start from the definition of the internal work-rate for element e:

$$\Pi_p^e(\dot{\boldsymbol{u}}) = \int_{V_e} D_p(\boldsymbol{d})\, dV \tag{3.61}$$

so that we can write (3.60) as

$$D\Pi_p^e(\dot{\boldsymbol{u}})[\delta\dot{\boldsymbol{u}}] = D\left(\int_{V_e} D_p(\boldsymbol{d})\, dV\right)[\delta\dot{\boldsymbol{u}}] = \int_{V_e} \frac{\partial D_p}{\partial \boldsymbol{d}} : \delta\boldsymbol{d}\, dV \tag{3.62}$$

otherwise as

$$D\Pi_p^e(\dot{\boldsymbol{u}})[\delta\dot{\boldsymbol{u}}] = \int_{V_e} \boldsymbol{\sigma} : \delta\boldsymbol{d}\, dV \tag{3.63}$$

The discretized form of expression (3.63) for element e at node a is given by

$$D\Pi_p^e(\dot{\boldsymbol{u}})[N_a \delta\dot{\boldsymbol{u}}_a] = \int_{V_e} \boldsymbol{\sigma} : (\delta\dot{\boldsymbol{u}}_a \otimes \nabla N_a)\, dV \tag{3.64}$$

which, given that integration is independent of virtual nodal velocities, and using property: $\boldsymbol{\sigma} : (\boldsymbol{u} \otimes \boldsymbol{v}) = \boldsymbol{u} \cdot \boldsymbol{\sigma v}$; $\forall \boldsymbol{u}, \boldsymbol{v}$, we can rewrite (3.64) as

$$D\Pi_p^e(\dot{\boldsymbol{u}})[N_a \delta \dot{\boldsymbol{u}}_a] = \delta \dot{\boldsymbol{u}}_a \cdot \int_{V_e} \boldsymbol{\sigma} \, \nabla N_a \, dV \tag{3.65}$$

Now, if we define the internal force per element per node, in vector form and in indicial form, respectively as

$$\boldsymbol{T}_a^e = \int_{V_e} \boldsymbol{\sigma} \, \nabla N_a \, dV \;\; ; \;\; T_{a,i}^e = \sum_{j=1}^{3} \int_{V_e} \sigma_{ij} \frac{\partial N_a}{\partial x_j} \, dV \tag{3.66}$$

thus the derivative can be posed in vector form as

$$D\Pi_p^e(\dot{\boldsymbol{u}})[N_a \delta \dot{\boldsymbol{u}}_a] = \delta \dot{\boldsymbol{u}}_a \cdot \boldsymbol{T}_a^e \tag{3.67}$$

In a similar manner, the second term of equation (3.57) can be developed as

$$F(\dot{\boldsymbol{u}}; \delta \dot{\boldsymbol{u}}) = D\Pi_t(\dot{\boldsymbol{u}})[\delta \dot{\boldsymbol{u}}] = \int_{S_t} \boldsymbol{t} \cdot \delta \dot{\boldsymbol{u}} \, ds \tag{3.68}$$

so that, for element e the discretized expression (3.68) can be written as

$$D\Pi_t^e(\dot{\boldsymbol{u}})[N_a \delta \dot{\boldsymbol{u}}_a] = \int_{S_t^e} \boldsymbol{t} \cdot (N_a \delta \dot{\boldsymbol{u}}_a) \, ds \tag{3.69}$$

or similarly, as in the previous development (see (3.65) and (3.67)) we can write

$$D\Pi_t^e(\dot{\boldsymbol{u}})[N_a \delta \dot{\boldsymbol{u}}_a] = \delta \dot{\boldsymbol{u}}_a \cdot \int_{S_t^e} N_a \boldsymbol{t} \, ds = \delta \dot{\boldsymbol{u}}_a \cdot \boldsymbol{F}_a^e \tag{3.70}$$

so that the contribution of all elements in the discretized domain containing node a can be given for both the internal and external forces as

$$\boldsymbol{T}_a = \sum_{\substack{e=1 \\ e \ni a}}^{M} \boldsymbol{T}_a^e \;\; ; \;\; \boldsymbol{F}_a = \sum_{\substack{e=1 \\ e \ni a}}^{M} \boldsymbol{F}_a^e \tag{3.71}$$

Finally, the global internal and external work-rate values for these two forces, can be assembled by summing all nodal contributions as

$$T(\dot{\boldsymbol{u}};\delta\dot{\boldsymbol{u}}) = \sum_{a=1}^{N} \delta\dot{\boldsymbol{u}}_a \cdot \boldsymbol{T}_a = \delta\dot{\mathbf{u}}^T\mathbf{T} \tag{3.72}$$

and also

$$F(\dot{\boldsymbol{u}};\delta\dot{\boldsymbol{u}}) = \sum_{a=1}^{N} \delta\dot{\boldsymbol{u}}_a \cdot \boldsymbol{F}_a = \delta\dot{\mathbf{u}}^T\mathbf{F} \tag{3.73}$$

where clearly:

$$\mathbf{T} = [\boldsymbol{T}_1, \boldsymbol{T}_2, \cdots, \boldsymbol{T}_N]^T \quad ; \quad \mathbf{F} = [\boldsymbol{F}_1, \boldsymbol{F}_2, \cdots, \boldsymbol{F}_N]^T \tag{3.74}$$

With these at hand, equation (3.57) can be rewritten in discrete form as

$$\delta\dot{\mathbf{u}}^T(\mathbf{T} - \lambda\mathbf{F}) = 0 \tag{3.75}$$

thus, noting that the stress is a non-linear function of the velocity field, in this case the velocity vector $\dot{\mathbf{u}}$, equation (3.75) leads to the equilibrium equation:

$$\mathbf{T}(\dot{\mathbf{u}}) - \lambda\mathbf{F} = 0 \tag{3.76}$$

for a constant external equivalent force vector $\mathbf{F}$.

3.5.3 Constructing a Newtonian solution

In order to solve equation (3.76) consider a Newton-Raphson process, as in Bonet and Wood [6], starting from an initial guess, which in order to ensure compliance with the reduced space $\overline{Y}_H$ can be taken as

$$\dot{\mathbf{u}}_{(0)} = \frac{\mathbf{F}}{\mathbf{F}^T\mathbf{F}} \quad \text{with} \quad \dot{\mathbf{u}}_{(0)} \in \overline{Y}_H \tag{3.77}$$

implying $\mathbf{F}^T\dot{\mathbf{u}}_{(0)} = 1$. It should be noted here that an alternative way of stating an initial velocity vector comes in the form of a conventional *elastic finite element analysis* of the problem. The displacement vector resulting from such an analysis can be cast to fall into the hyperplane defined by (3.27). This is the preferred method used in this implementation, as described in Chapter 5.

At this point we seek the state at which the velocity field, a vector at this stage, produces a zero value for the residual force, to comply with equilibrium conditions. The Newton-Raphson method is used here to achieve this. Recall that expression (3.76) can be used to assess the state of equilibrium, that is, by evaluating the residual force vector at the k-th iteration in the Newtonian procedure, so that we can write the vector form

$$\mathbf{R}(\dot{\mathbf{u}}_k, \lambda_k) = \mathbf{T}(\dot{\mathbf{u}}_k) - \lambda_k \mathbf{F} \tag{3.78}$$

Thus, the linearization of the residual in the direction of a velocity increment $\Delta\dot{\mathbf{u}}$ and of a multiplier increment $\Delta\lambda$, calls for a Taylor expansion as follows

$$\mathbf{R}(\dot{\mathbf{u}}_k + \Delta\dot{\mathbf{u}}, \lambda_k + \Delta\lambda) \simeq \mathbf{R}(\dot{\mathbf{u}}_k, \lambda_k) + D\mathbf{T}(\dot{\mathbf{u}}_k)[\Delta\dot{\mathbf{u}}] - D(\lambda_k \mathbf{F})[\Delta\lambda] \tag{3.79}$$

The derivative in the direction of $\Delta\lambda$ can be directly resolved as

$$D(\lambda_k \mathbf{F})[\Delta\lambda] = \frac{d}{d\in}\bigg|_{\in=0} (\lambda_k + \in \Delta\lambda)\mathbf{F} = \Delta\lambda\mathbf{F} = (\lambda_{k+1} - \lambda_k)\mathbf{F} \tag{3.80}$$

To resolve the derivative in the direction of $\Delta\dot{\mathbf{u}}$, we recall the internal work as

$$D\Pi_p(\dot{\boldsymbol{u}})[\delta\boldsymbol{v}] = \int_V \boldsymbol{\sigma} : \delta\boldsymbol{d}\, dV = \delta\mathbf{v}^T \mathbf{T}(\dot{\mathbf{u}}) \tag{3.81}$$

therefore we can find the pending term in equation (3.79), i.e. the derivative in the direction of $\Delta\dot{\boldsymbol{u}}$, from expression

$$D^2\Pi_p(\dot{\boldsymbol{u}})[\delta\boldsymbol{v}, \Delta\dot{\boldsymbol{u}}] = \delta\mathbf{v}^T D\mathbf{T}(\dot{\mathbf{u}})[\Delta\dot{\mathbf{u}}] \tag{3.82}$$

leading to

$$\begin{aligned} D^2\Pi_p(\dot{\boldsymbol{u}})[\delta\boldsymbol{v}, \Delta\dot{\boldsymbol{u}}] &= \int_V \delta\boldsymbol{d} : \frac{\partial\boldsymbol{\sigma}}{\partial\boldsymbol{d}} : D\boldsymbol{d}(\dot{\boldsymbol{u}})[\Delta\dot{\boldsymbol{u}}]\, dV \\ &= \int_V \delta\boldsymbol{d} : \mathbb{C}_p : \nabla_{sym}\Delta\dot{\boldsymbol{u}}\, dV \end{aligned} \tag{3.83}$$

where $\mathbb{C}_p$ is the fourth order plastic constitutive tensor.

If we compute (3.83) for element e, its contribution to the discretized virtual work is given by

$$\begin{aligned} &D^2\Pi_p^e(\dot{\boldsymbol{u}})[N_a\delta\boldsymbol{v}_a, N_b\Delta\dot{\boldsymbol{u}}_b] = \\ &\int_{V_e} \tfrac{1}{2}(\delta\boldsymbol{v}_a \otimes \nabla N_a + \nabla N_a \otimes \delta\boldsymbol{v}_a) : \mathbb{C}_p : \tfrac{1}{2}(\Delta\dot{\boldsymbol{u}}_b \otimes \nabla N_b + \nabla N_b \otimes \Delta\dot{\boldsymbol{u}}_b)\, dV \end{aligned} \tag{3.84}$$

In order to avoid large matrix expressions, and given that code execution is expedited by using expressions in indicial notation, expression (3.84) can be written as in Bonet and Wood [6]:

$$\begin{aligned} &D^2\Pi_p^e(\dot{\boldsymbol{u}})[N_a\delta\boldsymbol{v}_a, N_b\Delta\dot{\boldsymbol{u}}_b] \\ &= \sum_{i,j,k,l=1}^{3} \int_{V_e} \tfrac{1}{2}\left(\delta v_{a,i}\frac{\partial N_a}{\partial x_j} + \delta v_{a,j}\frac{\partial N_a}{\partial x_i}\right) : \mathbb{C}_{p,ijkl} : \tfrac{1}{2}\left(\Delta\dot{u}_{b,k}\frac{\partial N_b}{\partial x_l} + \Delta\dot{u}_{b,l}\frac{\partial N_b}{\partial x_k}\right) dV \\ &= \sum_{i,j,k,l=1}^{3} \delta v_{a,i}\left(\int_{V_e} \frac{\partial N_a}{\partial x_j}\mathbb{C}_{p,ijkl}\frac{\partial N_b}{\partial x_l} dV\right)\Delta\dot{u}_{b,k} \end{aligned} \tag{3.85}$$

where all the symmetries of the tangent plastic modulus $\mathbb{C}_p$ have been exploited to the full.

The above expression can be written in matrix-vector form as

$$D^2\Pi_p^e(\dot{\boldsymbol{u}})[N_a\delta\boldsymbol{v}_a, N_b\Delta\dot{\boldsymbol{u}}_b] = \delta\boldsymbol{v}_a \cdot \boldsymbol{K}_{ab}^e \Delta\dot{\boldsymbol{u}}_b \tag{3.86}$$

where the component of the tangent matrix relating node a and node b for element e, is given by

$$\left[\boldsymbol{K}_{ab}^e\right]_{ij} = \int_{V_e} \sum_{k,l=1}^{2} \frac{\partial N_a}{\partial x_k}\mathbb{C}_{p,ijkl}^{sym}\frac{\partial N_b}{\partial x_l} dV \quad ; \quad i,j = 1,2 \tag{3.87}$$

The component contribution to the total linearized virtual work, for every element containing nodes a and b, can be determined by using expression:

$$D^2\Pi_p(\dot{\boldsymbol{u}})[N_a\delta\boldsymbol{v}_a, N_b\Delta\dot{\boldsymbol{u}}_b] = \sum_{\substack{e=1 \\ e\ni a,b}}^{M_{ab}} D^2\Pi_p^e(\dot{\boldsymbol{u}})[N_a\delta\boldsymbol{v}_a, N_b\Delta\dot{\boldsymbol{u}}_b] \tag{3.88}$$

where M_{ab} is the number of elements containing node a and node b.

A standard finite element assembly procedure can be used to sum all the node-to-node contributions into the global assembled tangent matrix $\mathbf{K}$, leading to a matrix of the form

$$\mathbf{K} = \begin{bmatrix} \boldsymbol{K}_{11} & \boldsymbol{K}_{12} & \cdots & \boldsymbol{K}_{1N} \\ \boldsymbol{K}_{21} & \boldsymbol{K}_{22} & \cdots & \boldsymbol{K}_{2N} \\ \vdots & \vdots & & \vdots \\ \boldsymbol{K}_{N1} & \boldsymbol{K}_{N2} & \cdots & \boldsymbol{K}_{NN} \end{bmatrix} \tag{3.89}$$

With this last definition, the total internal work can be obtained using the global matrix and vectors, as

$$D^2\Pi_p(\dot{\boldsymbol{u}})[\delta\boldsymbol{v}, \Delta\dot{\boldsymbol{u}}] = \delta\mathbf{v}^T\mathbf{K}\Delta\dot{\mathbf{u}} \tag{3.90}$$

where $\Delta\dot{\mathbf{u}}$ has the same structure as that defined in (3.36).

Returning to equation (3.82) we can equate terms:

$$D^2\Pi_p(\dot{\boldsymbol{u}})[\delta\boldsymbol{v}, \Delta\dot{\boldsymbol{u}}] = \delta\mathbf{v}^T D\mathbf{T}(\dot{\mathbf{u}})[\Delta\dot{\mathbf{u}}] = \delta\mathbf{v}^T\mathbf{K}\Delta\dot{\mathbf{u}} \tag{3.91}$$

Thus, the directional derivative of $\mathbf{T}(\dot{\mathbf{u}})$ in the direction of $\Delta\dot{\mathbf{u}}$ is given by the matrix-vector product:

$$D\mathbf{T}(\dot{\mathbf{u}})[\Delta\dot{\mathbf{u}}] = \mathbf{K}\Delta\dot{\mathbf{u}} \tag{3.92}$$

Now, rewriting expression (3.79) so that the new residual becomes zero, we obtain the equation

$$\mathbf{R}(\dot{\mathbf{u}}_k, \lambda_k) + D\mathbf{T}(\dot{\mathbf{u}}_k)[\Delta\dot{\mathbf{u}}] - D(\lambda_k\mathbf{F})[\Delta\lambda] = 0 \tag{3.93}$$

we have

$$\mathbf{T}(\dot{\mathbf{u}}_k) - \lambda_k \mathbf{F} + \mathbf{K}_k \Delta\dot{\mathbf{u}} - (\lambda_{k+1} - \lambda_k)\mathbf{F} = 0 \tag{3.94}$$

reducing to the incremental equilibrium equation

$$\mathbf{K}_k \Delta\dot{\mathbf{u}} = \lambda_{k+1}\mathbf{F} - \mathbf{T}(\dot{\mathbf{u}}_k) \tag{3.95}$$

This last expression constitutes the iterative form of the Newton-Raphson procedure; however, the conditions of the present problem yield a modified iterative form for the solution procedure, as described below.

3.5.4 Terms of the equilibrium equation in vector-matrix notation

In order to provide a more familiar description of the discretization process, in this section the terms of the equilibrium equation, defined in the iterative expression (3.95), are given in a vector-matrix format typically used for plane analysis. Note that some basic elements of this vector-matrix format have been given in section 3.5.1. Special attention is given here to the definition of nodal internal forces and the constitutive component of the tangent matrix.

We start by recalling the expression of the internal work for element e:

$$\Pi_p^e(\dot{\boldsymbol{u}}) = \int_{V_e} \boldsymbol{\sigma} : \boldsymbol{d}\, dV = \int_{V_e} \mathbf{d}^T \boldsymbol{\sigma}\, dV \tag{3.96}$$

so that the discretized virtual internal work is given by

$$D\Pi_p^e(\dot{\boldsymbol{u}})[N_a \delta \boldsymbol{v}_a] = \int_{V^e} (\mathbf{B}_a \delta \boldsymbol{v}_a)^T \boldsymbol{\sigma}\, dV \tag{3.97}$$

where

$$\mathbf{d} = \sum_{a=1}^{N} \mathbf{B}_a \boldsymbol{v}_a \tag{3.98}$$

and

$$\mathbf{B}_a = \begin{bmatrix} \partial N_a/\partial x & 0 & \partial N_a/\partial y \\ 0 & \partial N_a/\partial y & \partial N_a/\partial x \end{bmatrix}^T \tag{3.99}$$

Thus, we write the internal virtual work as in (3.81) for element e in the form

$$D\Pi_p^e(\dot{\boldsymbol{u}})[N_a\delta\boldsymbol{v}_a] = \delta\boldsymbol{v}_a \cdot \int_{V^e} \mathbf{B}_a^T\boldsymbol{\sigma}\, dV = \delta\mathbf{v}_a \cdot \boldsymbol{T}_a^e \tag{3.100}$$

from which clearly the element equivalent nodal forces at node a are given by

$$\boldsymbol{T}_a^e = \int_{V_e} \mathbf{B}_a^T\boldsymbol{\sigma}\, dV \tag{3.101}$$

Finally, the contribution to the linearized virtual work in matrix notation can be defined by using the vector in (3.44):

$$\mathbf{d} = [d_{11}, d_{22}, 2d_{12}]^T \tag{3.102}$$

so that the constitutive component of the linearized internal virtual work can be written as

$$D\Pi_p^e(\dot{\boldsymbol{u}})[\delta\boldsymbol{v},\dot{\boldsymbol{u}}] = \int_{V_e} \delta\boldsymbol{d}(\delta\boldsymbol{v}) : \mathbb{C}_p : \boldsymbol{d}(\dot{\boldsymbol{u}})\, dV = \int_{V_e} \delta\mathbf{d}^T\mathbf{D}_p\mathbf{d}\, dV \tag{3.103}$$

where $\mathbf{D}_p$ is the nine-component material matrix for plane analysis, and the fourth-order constitutive tensor $\mathbb{C}_p$ is defined by

$$\mathbb{C}_p = 2\mu(\mathbf{I}\otimes\mathbf{I} + \mathbb{I}) + \nu\underline{\underline{\boldsymbol{\sigma}}}\otimes\underline{\underline{\boldsymbol{\sigma}}} \tag{3.104}$$

where $\mathbf{I}\otimes\mathbf{I} = \delta_{ij}\delta_{kl}$ and $\mathbb{I}_{ijkl} = \frac{1}{2}(\delta_{ik}\delta_{jl} + \delta_{il}\delta_{jk})$, and δ_{ij} is the Kronecher delta. Note that in order to avoid confusion we adopt notation $\underline{\underline{\boldsymbol{\sigma}}}$ to indicate a stress tensor in space, i.e. a tensor given in nine components. Also, the symbols μ and ν are defined as before

$$\mu = \frac{\sigma_y}{3\dot{\bar{\varepsilon}}} \quad ; \quad \nu = -\frac{1}{\sigma_y \dot{\bar{\varepsilon}}} \tag{3.105}$$

now, by equating the products $\delta \boldsymbol{d} : \mathbb{C}_p : \boldsymbol{d} = \delta \mathbf{d}^T \mathbf{D}_p \mathbf{d}$ the components of the constitutive matrix $\mathbf{D}_p$ can be defined from tensor $\mathbb{C}_p$, as

$$\mathbf{D}_p = \frac{1}{2}\begin{bmatrix} 2\mathbb{C}_{p,1111} & 2\mathbb{C}_{p,1122} & \mathbb{C}_{p,1112} + \mathbb{C}_{p,1121} \\ & 2\mathbb{C}_{p,2222} & \mathbb{C}_{p,2212} + \mathbb{C}_{p,2221} \\ Sym & & \mathbb{C}_{p,1212} + \mathbb{C}_{p,1221} \end{bmatrix} \tag{3.106}$$

thus, for the rigid-plastic plane-stress case at hand, matrix (3.106) can be rewritten as

$$\mathbf{D}_p = \begin{bmatrix} \lambda' + 2\mu' + \nu'\sigma_{11}^2 & \lambda' + \nu'\sigma_{11}\sigma_{22} & \nu'\sigma_{11}\sigma_{12} \\ & \lambda' + 2\mu' + \nu'\sigma_{22}^2 & \nu'\sigma_{12}\sigma_{22} \\ Sym & & \mu' + \nu'\sigma_{12}^2 \end{bmatrix} \tag{3.107}$$

where the values λ', μ' and ν' are now given as

$$\lambda' = 2\mu \;\; ; \;\; \mu' = \mu \;\; ; \;\; \nu' = -\frac{1}{\sigma_y \dot{\bar{\varepsilon}}} \tag{3.108}$$

From the linearized internal work for element e, we obtain the discrete form:

$$\begin{aligned} D\Pi_p^e(\dot{\boldsymbol{u}})[N_a \delta \boldsymbol{v}_a, N_b \dot{\boldsymbol{u}}_b] &= \int_{V^e} \delta \mathbf{d}^T \mathbf{D}_p \mathbf{d} \, dV \\ &= \int_{V^e} (\mathbf{B}_a \delta \boldsymbol{v}_a)^T \mathbf{D}_p (\mathbf{B}_a \dot{\boldsymbol{u}}_b) \, dV = \delta \boldsymbol{v}_a \cdot \left(\int_{V^e} \mathbf{B}_a^T \mathbf{D}_p \mathbf{B}_a \, dV \right) \dot{\boldsymbol{u}}_b \end{aligned} \tag{3.109}$$

after substituting $\delta \mathbf{d}$ and $\mathbf{d}$; therefore the constitutive component of the plastic tangent matrix relating node a to node b for element e, in matrix-vector notation is given as

$$\boldsymbol{K}_{ab}^e = \int_{V^e} \mathbf{B}_a^T \mathbf{D}_p \mathbf{B}_a \, dV \tag{3.110}$$

The previous definitions, given in terms of matrix-vector expressions, provide a clear structure of the solution in the context of the finite element method, resembling conventional data structures, which may help construct a coded solution. In the

solution code developed in the present work, however, the indicial expressions have been used in order to cater for better efficiency when executed on the computer.

3.5.5 Singularity of the tangent matrix and the iterative form

Note that given the order-one homogeneous nature of the internal work-rate, $\Pi_p(\dot{\boldsymbol{u}})$, i.e. $\Pi_p(\alpha\dot{\boldsymbol{u}}) = \alpha\Pi_p(\dot{\boldsymbol{u}})$, by using expression $\Pi_p(\mathbf{v}) = \mathbf{v}^T\mathbf{T}(\mathbf{v})$ (derived from expression (3.81)), we have $(\alpha\mathbf{v})^T\mathbf{T}(\alpha\mathbf{v}) = \alpha(\mathbf{v}^T\mathbf{T}(\mathbf{v}))$, and the following equation is in order

$$\mathbf{T}(\alpha\mathbf{v}) = \mathbf{T}(\mathbf{v}) \quad ; \quad \forall\mathbf{v} \tag{3.111}$$

where $\mathbf{T}$ is the internal force field, for which there exist a constant value α for the equation to be valid. With this in mind, the rate of change with respect to constant α yields

$$\frac{d\mathbf{T}(\alpha\mathbf{v})}{d\alpha} = 0 \tag{3.112}$$

thus expanding equation (3.112) by the chain rule, we have

$$\frac{\partial\mathbf{T}}{\partial\mathbf{v}}\frac{d(\alpha\mathbf{v})}{d\mathbf{v}} = \mathbf{K}(\mathbf{v})\mathbf{v} = 0 \quad ; \quad \forall\mathbf{v} \tag{3.113}$$

implying a *non-positive definiteness* of $\mathbf{K}$, i.e. $\mathbf{v}^T\mathbf{K}\mathbf{v} = 0$, thus indicating a *singular* global tangent matrix. This then also implies that, within the iterative Newtonian process at the *k-th* step, we have

$$\mathbf{K}(\dot{\mathbf{u}}_k)\dot{\mathbf{u}}_k = \mathbf{K}_k\dot{\mathbf{u}}_k = 0 \tag{3.114}$$

Therefore, the plastic tangent matrix is singular in the direction of $\dot{\mathbf{u}}_k$. Note that the field $\dot{\boldsymbol{u}}$ implies a global vector $\dot{\mathbf{u}}$ produced after Dirichlet boundary conditions have been applied. The singularity condition has an effect over the iterative form of the Newton method, as follows. Let us take the iterative form in expression (3.95):

$$\mathbf{K}_k \Delta \dot{\mathbf{u}} = \lambda_{k+1}\mathbf{F} - \mathbf{T}(\dot{\mathbf{u}}_k) \tag{3.115}$$

Now, using the singularity condition of the tangent matrix $\mathbf{K}_k \dot{\mathbf{u}}_k = 0$ we have

$$\mathbf{K}_k(\dot{\mathbf{u}}_{k+1} - \dot{\mathbf{u}}_k) = \mathbf{K}_k \dot{\mathbf{u}}_{k+1} \tag{3.116}$$

thus a modified iterative form is obtained:

$$\mathbf{K}_k \dot{\mathbf{u}}_{k+1} = \lambda_{k+1}\mathbf{F} - \mathbf{T}(\dot{\mathbf{u}}_k) \tag{3.117}$$

From equation (3.117) and condition $\dot{\mathbf{u}}_k{}^T\mathbf{F} = 1$ (from definition (3.41)), we arrive at

$$\dot{\mathbf{u}}_k^T \mathbf{K}_k \dot{\mathbf{u}}_{k+1} = \lambda_{k+1} - \dot{\mathbf{u}}_k^T \mathbf{T}(\dot{\mathbf{u}}_k) \tag{3.118}$$

so that, by substituting $\dot{\mathbf{u}}_k^T \mathbf{K}_k = 0$, the *inner product* form of the plastic dissipation, the multiplier can be determined by

$$\lambda_{k+1} = \dot{\mathbf{u}}_k^T \mathbf{T}(\dot{\mathbf{u}}_k) \tag{3.119}$$

Note that from relation (3.81) we can also write

$$\lambda_{k+1} = \Pi_p(\dot{\boldsymbol{u}}_k) = \int_V D_p(\boldsymbol{d})\, dV = \int_V \boldsymbol{\sigma} : \boldsymbol{d}\, dV = \dot{\mathbf{u}}_k^T \mathbf{T}(\dot{\mathbf{u}}_k) \tag{3.120}$$

The developments presented in these sub-sections describe the data components and operations carried out by the programmed algorithms to find a solution to the kinematic problem in limit analysis, i.e. the upper bound problem. In chapter 5, a description of the algorithms is presented along with relevant coding and implementation issues. In the following chapter, the elements of the solution to the static problem, i.e. the lower bound problem, are described. The results of the application of these solutions to test cases and common applications are given in chapter 6, for both the upper and lower bound problems set in an adaptive scheme approach.

In section 3.6, a discussion is given on the line search technique used here to attain a convergent path in the Newtonian procedure.

3.5.6 Treatment of the singularity of the tangent matrix

Given the singularity property of the tangent matrix $\mathbf{K}$, as

$$\mathbf{K}_k \dot{\mathbf{u}}_k = 0 \tag{3.121}$$

we revisit the iterative expression in terms of a singular value of matrix $\mathbf{K}$:

$$\mathbf{K}_k \dot{\mathbf{u}}_{k+1} = \lambda_{k+1}\mathbf{F} - \mathbf{T}(\dot{\mathbf{u}}_k) \tag{3.122}$$

To convert the problem into a definite solution, we express $\dot{\mathbf{u}}_{k+1}$ as

$$\dot{\mathbf{u}}_{k+1} = \dot{\tilde{\mathbf{u}}}_{k+1} + \beta \dot{\mathbf{u}}_k \tag{3.123}$$

where $\dot{\tilde{\mathbf{u}}}_{k+1}$ is obtained by solving equation (3.122) combined with an arbitrary additional condition, for instance that the displacement-rate of the Cartesian component i at node a vanishes, that is

$$\left[\dot{\tilde{\mathbf{u}}}_{k+1}\right]_a^i = 0 \tag{3.124}$$

This condition removes one row and one column from matrix $\mathbf{K}$ and renders it non-singular.

The reduced vector $\dot{\tilde{\mathbf{u}}}_{k+1}$ can be determined with the help of the reduced tangent matrix $\tilde{\mathbf{K}}_k$ as

$$\dot{\tilde{\mathbf{u}}}_{k+1} = (\tilde{\mathbf{K}}_k)^{-1}\left[\lambda_{k+1}\tilde{\mathbf{F}} - \tilde{\mathbf{T}}(\dot{\mathbf{u}}_k)\right] \tag{3.125}$$

Note that clearly $\left[\lambda_{k+1}\tilde{\mathbf{F}} - \tilde{\mathbf{T}}(\dot{\mathbf{u}}_k)\right]$ denotes the consistently reduced residual vector. We can rewrite equation (3.123) as

$$\mathbf{F}^T\dot{\mathbf{u}}_{k+1} = \mathbf{F}^T\dot{\tilde{\mathbf{u}}}_{k+1} + \beta\mathbf{F}^T\dot{\mathbf{u}}_k \tag{3.126}$$

from which the scalar β can be computed as

$$\beta + \mathbf{F}^T\dot{\tilde{\mathbf{u}}}_{k+1} = 1 \quad \therefore \quad \beta = 1 - \mathbf{F}^T\dot{\tilde{\mathbf{u}}}_{k+1} \tag{3.127}$$

to retrieve the actual velocity vector using relation (3.123).

3.6 The Line Search technique

The standard form of the Newton-Raphson method, implemented originally in the present work as the solution procedure, soon proved to be in need of a better selection of the velocity increment vector. As stated by Bonet & Wood [6], in the course of complex deformation processes, conditions may be given to cause the method to prove insufficient in its standard form.

Different enhancements to the Newton-Raphson method are available in the literature in order to accelerate convergence, or even to produce a convergent path which otherwise would not be attainable. Under the present conditions the *line search method* stands out as a powerful solution technique.

In this section, the *line search* technique is discussed, as it is not only used to enhance, but rather to convert a non-convergent Newton procedure into a convergent one, that is, in the context of the present solution.

The main element of the line search technique is the parameter η sometimes called the *damping* parameter. The parameter value η is a scaling factor that controls the fraction of the increment $\Delta\dot{\mathbf{u}}$ to be applied to evaluate the subsequent iteration within the procedure, and is usually chosen so that the potential energy $\Pi(\eta) = \Pi(\dot{\mathbf{u}}_k + \eta\Delta\dot{\mathbf{u}})$ is minimized in the direction of $\Delta\dot{\mathbf{u}}$, as described in the following paragraphs.

To implement this technique we let the velocity increment $\Delta\dot{\mathbf{u}} = \dot{\mathbf{u}}_{k+1} - \dot{\mathbf{u}}_k$ to be re-evaluated by introducing a scaling factor η as in

$$\dot{\mathbf{u}}_{k+1} = \dot{\mathbf{u}}_k + \eta\Delta\dot{\mathbf{u}} \tag{3.128}$$

where $\eta \in [0.0,1.0]$. The value of η is determined so that it produces the minimum value for the potential energy, expressed as a function of η, that is

$$\Pi_p(\eta) = \Pi_p(\dot{\mathbf{u}}_k + \eta\Delta\dot{\mathbf{u}}) \tag{3.129}$$

in the direction of $\Delta\dot{\mathbf{u}}$. Differentiating with respect to η and recalling from equation (3.120) that $\partial\Pi_p/\partial\dot{\mathbf{u}} = \mathbf{T}(\dot{\mathbf{u}})$, shows that the minimality condition with respect to η is equivalent to the requirement that the internal force $\mathbf{T}(\dot{\mathbf{u}}_k + \eta\Delta\dot{\mathbf{u}})$ be orthogonal to the direction of advance $\Delta\dot{\mathbf{u}}$. This leads to the scalar expression

$$R(\eta) = \Delta\dot{\mathbf{u}}^T\mathbf{T}(\dot{\mathbf{u}}_k + \eta\Delta\dot{\mathbf{u}}) = 0 \tag{3.130}$$

Note that although the system in equation (3.117) yields a velocity vector, the difference $\Delta\dot{\mathbf{u}}$ is computed from vectors $\dot{\mathbf{u}}_k$ and $\dot{\mathbf{u}}_{k+1}$, taken from the *previous* and the *current* values of the velocity vector.

A classical solution at this point would be constructed through a quadratic approximation for the value of $R(\eta)$ and solved to locate the proper value of η, given the values of $R(0)$, $R(1)$ and $dR/d\eta$. This is illustrated in figure 3.4a) and works well with continuous functions. In this implementation, however, a different approach, rather simpler, has been used due to the discontinuous nature of function $R(\eta)$.

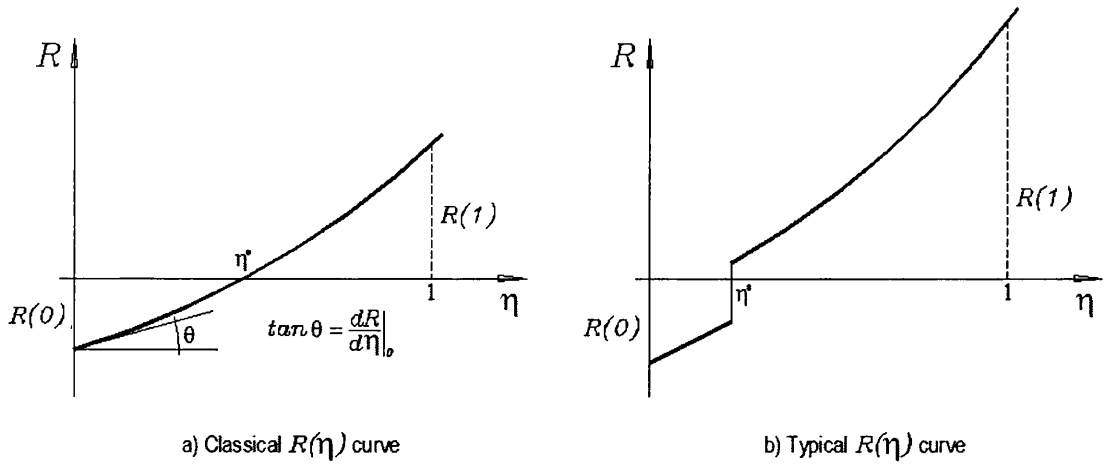

Figure 3.4 a) Expected $R(\eta)$ curve; b) Typical $R(\eta)$ curve in this implementation.

Given the nature of the rigid-plastic potential, the minimizing value for η typically occurs on a jump along the $R(\eta)$ curve, as shown in figure 3.4b), and not as it is normally expected, as in figure 3.4a). This condition leads to the use of a basic root-finding *midpoint* or *bisection* method, which has proved to produce robust results. The case of having a curve which does not produce a change of sign in $R(\eta)$ over the domain $\eta \in [0.0,1.0]$ is resolved by taking $\eta = 1$, and proceeding with the Newton-Raphson iteration process. This iterative procedure has been implemented to use a very low order of magnitude tolerance in the root-finding process, a typical value being the *machine epsilon* number. Although the use of this procedure with such a stringent condition seems to be inefficient, tests show that only a reasonable amount of time is consumed in the process. In chapter 5, an additional discussion over the convergent nature of the Newton-Raphson method and the line search technique is given.

3.7 References

1. Ponter A.R.S., Carter K.F. *Limit state solutions, based upon linear elastic solutions with a spatially varying elastic modulus*. Computer Methods in Applied Mechanics and Engineering. Vol. 140, 1997, p.237-258.
2. Ponter A.R.S., Fuschi P., Engelhardt M. *Limit analysis for a general class of yield conditions*. European Journal of Mechanics A/Solids. Vol. 19, 2000, p.401-421.
3. Lubliner J. *Plasticity theory*. Macmillan Publishing Company, New York, 1990.

4. Jirazek M., Bazant Z. *Inelastic analysis of structures*. John Wiley & Sons, Ltd., Chichester, 2001.
5. Christiansen, E. *Computation of limit loads*. International Journal for Numerical Methods in Engineering. Vol. 17, 1981, p.1547-1570.
6. Bonet J., Wood D.R. *Nonlinear continuum mechanics for finite element analysis*. Cambridge University Press, 1997.

Chapter 4

Lower bound evaluation

4.1 Introduction

In this chapter, a procedure for the evaluation of a *lower bound* to the collapse load multiplier is constructed. A general solution based on a Lagrangian optimization, in a sense similar to that used in the upper bound solution is defined. The solution takes shape by considering a set of inter-element edge force definitions to comply with *equilibrium* conditions at the element level, and also meet *continuity* conditions along inter-element edges. This solution considers the evaluation of equilibrated inter-element edge forces to produce a series of *local problems*, each of which yielding a local macro-element plastic carrying capacity. These local collapse multipliers are used to evaluate a lower bound to the collapse multiplier, in a procedure defined in terms of piecewise macro-element contributions. The discussions that follow are given in order to provide the essential components of the present solution proposal to attain a lower bound to the collapse load.

4.2 Elements of the Lower Bound solution

Consider a coarse mesh definition Y_H as shown in figure 4.1, over which a kinematic problem has been solved, i.e. by the upper bound procedure described in chapter 3. Consider now, a very fine mesh Y_h as that of figure 4.2, obtained by enriching the space Y_H, by higher order polynomials or *element subdivision*. By construction

$Y_H \subset Y_h$ and we will assume that the solution in Y_h is sufficiently accurate to be considered exact, that is

$$\gamma^c \simeq \gamma_h \equiv \Pi_p(\boldsymbol{v}_h) = \min_{\dot{\boldsymbol{u}} \in \overline{Y}_h} \Pi_p(\dot{\boldsymbol{u}}) \tag{4.1}$$

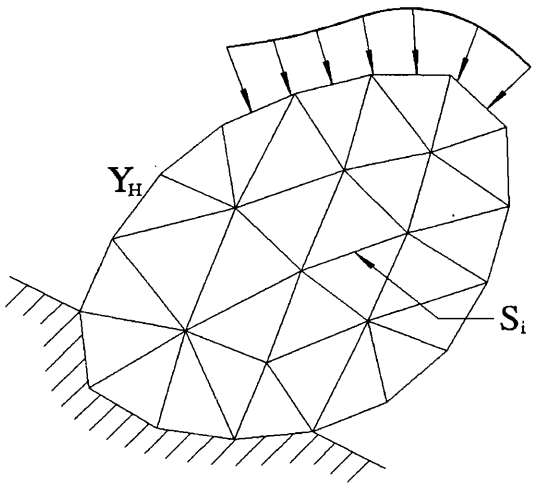

Figure 4.1 Body drawn by a coarse mesh describing space Y_H

where γ^c is the exact collapse multiplier. The reduced space $\overline{Y}_h$ is, as previously defined in chapter 3:

$$\overline{Y}_h = \left\{ \dot{\boldsymbol{u}} \in Y_h \;\middle|\; \Pi_i(\dot{\boldsymbol{u}}) = 1 \right\} \tag{4.2}$$

The interpolation space Y_h is known as the *reference mesh*, or in other contexts as the "*truth*" *mesh* [9,10]. It is supposed to be fine enough to deliver a solution practically indistinguishable from the analytical solution.

Definition 4.1.

A mesh defined over the space Y_h corresponding to the lowest nominal element size h for a given problem, that is, the finest mesh assumed in the course of a limit analysis solution as proposed herein, is referred to as the *reference mesh.*

The term *relative nominal element size* will be sometimes used to indicate the ratio h/L_m, where h is the nominal element size (either based on an edge length measure

or on a diameter measure), and L_m is the minimum characteristic length in a geometric body. In general, it indicates the relative element size in the mesh, and in the present development it is based on the nominal edge length of a triangular finite element.

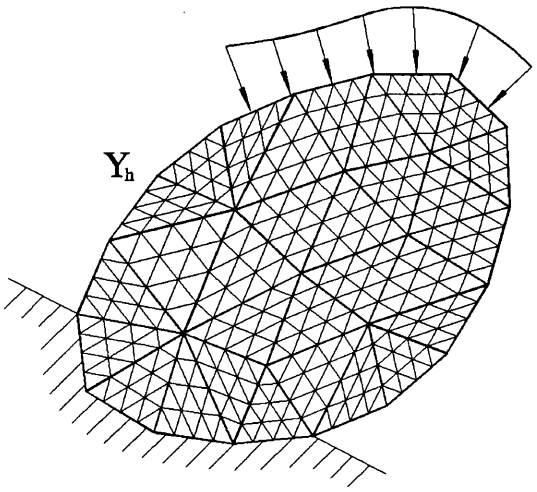

Figure 4.2 Body discretized by a very fine mesh Y_h, to be considered the reference mesh

In the present discussion it is assumed that a kinematic solution exists, that is, an *upper bound* solution over the fine space Y_h, or over a space similar to that of the reference mesh, so that a *lower bound* solution can be consistently found, according to the ongoing proposal.

In addition to the fine space Y_h of figure 4.2, consider also the *broken* space $\hat{Y}_h$ in figure 4.3, where continuity across the edges of the macro-elements defined by Y_H is not enforced.

Note that $Y_h \subset \hat{Y}_h$, that is, all solutions belonging to Y_h also belong to $\hat{Y}_h$; of course the reverse is not true as interpolations in $\hat{Y}_h$ which are not continuous across element edges do not belong to Y_h. To restore continuity we introduce the edge forces $\boldsymbol{q}$ so that for all velocity fields $\dot{\boldsymbol{u}}$ a boundary work-rate function $b(\boldsymbol{q},\dot{\boldsymbol{u}})$ is defined as

$$b(\boldsymbol{q},\dot{\boldsymbol{u}}) = \int_{S_i} \boldsymbol{q} \cdot [\![\dot{\boldsymbol{u}}]\!]\, dl \tag{4.3}$$

where $[\![\dot{\boldsymbol{u}}]\!]$ denotes the jump of $\dot{\boldsymbol{u}}$ across the internal edges S_i, that is $[\![\dot{\boldsymbol{u}}]\!] = \dot{\boldsymbol{u}}_{S_i}^{left} - \dot{\boldsymbol{u}}_{S_i}^{right}$ where *left* and *right* are defined arbitrarily but uniquely, by for instance the numbering of nodes a,b defining S_i, so that *left* and *right* refer to the sides as seen when travelling from the lower node number to the higher one.

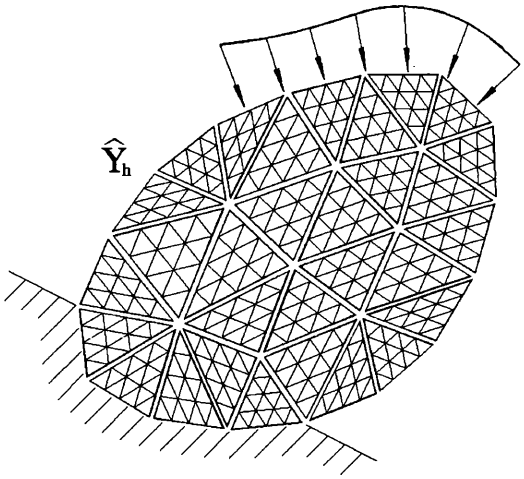

Figure 4.3 Body discretized by means of the broken space $\hat{Y}_h$

Then the original fine mesh interpolation space can be recovered by enforcing continuity on $\hat{Y}_h$ as

$$Y_h = \left\{ \dot{\boldsymbol{u}} \in \hat{Y}_h \;\middle|\; b(\boldsymbol{q}, \dot{\boldsymbol{u}}) = 0 \;, \forall \boldsymbol{q} \right\} \tag{4.4}$$

Similarly, the reduced space $\overline{Y}_h$ is now obtained by enforcing continuity and unit work-rate by external forces as

$$\overline{Y}_h = \left\{ \dot{\boldsymbol{u}} \in \hat{Y}_h \;\middle|\; \Pi_t(\dot{\boldsymbol{u}}) + b(\boldsymbol{q}, \dot{\boldsymbol{u}}) = 1 \;, \forall \boldsymbol{q} \right\} \tag{4.5}$$

Note that condition $\Pi_t(\dot{\boldsymbol{u}}) = 1$ is obtained by simply taking $\boldsymbol{q} = 0$. The minimization in (4.1) is now rewritten in terms of the Lagrangian functional:

$$L_h(\dot{\boldsymbol{u}}, \boldsymbol{q}, \lambda_h) = \Pi_p(\dot{\boldsymbol{u}}) + \lambda_h \left[\Pi_t(\dot{\boldsymbol{u}}) + b(\boldsymbol{q}, \dot{\boldsymbol{u}}) - 1 \right] \tag{4.6}$$

Recalling the line of reasoning in Christiansen [1], the dual problem can be expressed as

$$\gamma_h = \min_{\dot{\boldsymbol{u}} \in \hat{Y}_h} \max_{\lambda_h, \boldsymbol{q}} L_h(\dot{\boldsymbol{u}}, \boldsymbol{q}, \lambda_h) \tag{4.7}$$

duality now enables this expression to be rearranged as

$$\gamma_h = \max_{\boldsymbol{q}} \min_{\dot{\boldsymbol{u}} \in \hat{Y}_h} \max_{\lambda_h} L_h(\dot{\boldsymbol{u}}, \boldsymbol{q}, \lambda_h) \geq \min_{\dot{\boldsymbol{u}} \in \hat{Y}_h} \max_{\lambda_h} L_h(\dot{\boldsymbol{u}}, \boldsymbol{p}_H, \lambda_h) \tag{4.8}$$

The first relation in expression (4.8) implies that variations in $\boldsymbol{q}$ will at most produce the solution obtained in (4.7) over the fine space $\hat{Y}_h$. On the other hand, the term $\boldsymbol{p}_H$ represents any particular choice of the edge tractions $\boldsymbol{q}$ to be evaluated, for instance, in the coarse space Y_H. This last assumption renders the second relation in (4.8) true, with the last *min-max* solution clearly leading to a lower value. The last term in inequality (4.8) actually represents a lower bound to the collapse multiplier γ^c. The stress distribution denoted by $\boldsymbol{p}_H$ can be determined following a procedure outlined in section 4.2.1 below. However, a *flux equilibration* procedure is implemented in the present solution proposal. This procedure is detailed in section 4.4.

With these elements at hand, a *lower bound solution* can be attained based upon the broken space expression in (4.8) as

$$\hat{\gamma}_h = \min_{\dot{\boldsymbol{u}} \in \hat{Y}_h} \max_{\lambda_h} L_h(\dot{\boldsymbol{u}}, \boldsymbol{p}_H, \lambda_h) \tag{4.9}$$

A simpler expression for the *broken space lower bound* $\hat{\gamma}_h$ in (4.9) is found by first defining the *augmented* external work-rate term

$$\hat{\Pi}_t(\dot{\boldsymbol{u}}) = \Pi_t(\dot{\boldsymbol{u}}) + b(\boldsymbol{p}_H, \dot{\boldsymbol{u}}) \tag{4.10}$$

Now, the condition of unit external work rate that defines the reduced broken space $\hat{\bar{Y}}_h$ is given by

$$\hat{\bar{Y}}_h = \left\{ \dot{\boldsymbol{u}} \in \hat{Y} \;\middle|\; \hat{\Pi}_t(\dot{\boldsymbol{u}}) = 1 \right\} \tag{4.11}$$

Thus the minimisation can be carried out over the broken space to find $\hat{\gamma}_h$ as

$$\hat{\gamma}_h \equiv \Pi_p(\hat{\boldsymbol{v}}_h) = \min_{\dot{\boldsymbol{u}} \in \hat{\bar{Y}}_h} \Pi_p(\dot{\boldsymbol{u}}) \tag{4.12}$$

Note that the velocity field $\hat{\boldsymbol{v}}_h$ denotes a collapse mechanism in the broken space $\hat{\bar{Y}}_h$. The lower bound solution in (4.12) implies a tight coupling of the macro-elements defining the broken space, with the key assumption of the existence of inter-element tractions complying with local equilibrium and continuity conditions along edges S_i, as well as meeting Dirichlet and Neumann boundary conditions at the nodes. Figure 4.4 shows a set of equilibrated tractions acting on element e, and by reaction on adjacent elements f, g, h. In the next section, a procedure is brought forward that permits the definition of inter-element tractions $\boldsymbol{p}_H$.

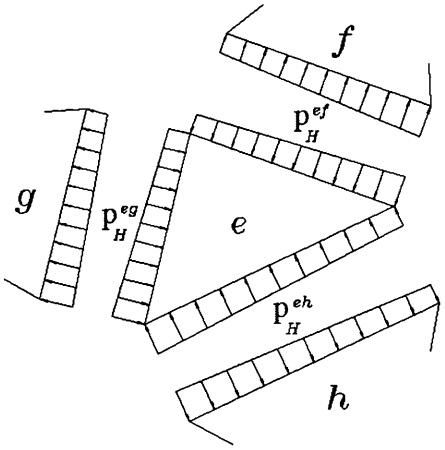

Figure 4.4 An element with adjacent elements showing equilibrated tractions $\left(\mathrm{p}_H^{ef}, \mathrm{p}_H^{eg}, \mathrm{p}_H^{eh}\right) \subset \boldsymbol{p}_H$.

4.2.1 Evaluation of inter-element tractions

The problem of finding inter-element edge tractions $\boldsymbol{p}_H$, as suggested in the previous section is addressed in this section. The proposed solution is given here as a general approach to the problem at hand, however other existing procedures within the

category of *stress recovering methods* can be used seamlessly to attain the same purpose. The particular stress recovering method, actually used in the present implementation, is described briefly at the end of this section. A more detailed description of the method used herein is given in section 4.4.

It is important to note that tractions $\boldsymbol{p}_H$ must verify two important properties. On the one hand, they must be uniquely defined for a given side S_i, that is, the *left* and *right* hand tractions must be the same. In addition, the tractions defined for a given macro-element must be in equilibrium with the external forces. Failing to comply with this last requirement would make the solution in the reference mesh impossible.

The most common procedure for the evaluation of tractions $\boldsymbol{p}_H$ that satisfies the above requirements is based on solving the broken problem in the coarse mesh. For this purpose, consider the broken coarse mesh $\hat{Y}_H$ shown in figure 4.5. The reduced space $\overline{Y}_H$ is recovered imposing continuity through the work done by arbitrary tractions $\boldsymbol{q}$, as

$$\overline{Y}_H = \left\{ \dot{\boldsymbol{u}} \in \hat{Y}_H \;\middle|\; \Pi_t(\dot{\boldsymbol{u}}) + b(\boldsymbol{q}, \dot{\boldsymbol{u}}) = 1 \;, \forall \boldsymbol{q} \right\} \tag{4.13}$$

Defining the Lagrangian

$$L_H(\dot{\boldsymbol{u}}, \boldsymbol{q}, \lambda_H) = \Pi_p(\dot{\boldsymbol{u}}) + \lambda_H \left[\Pi_t(\dot{\boldsymbol{u}}) + b(\boldsymbol{q}, \dot{\boldsymbol{u}}) - 1 \right] \tag{4.14}$$

The solution in the coarse space is expressed as follows

$$\gamma_H = \min_{\dot{\boldsymbol{u}} \in \hat{Y}_H} \max_{\lambda_H, \boldsymbol{q}} L_H(\dot{\boldsymbol{u}}, \boldsymbol{q}, \lambda_H) \tag{4.15}$$

The corresponding equilibrium equation for the velocity field $\boldsymbol{v}_H$ and inter-element tractions $\boldsymbol{p}_H$ is

$$T(\boldsymbol{v}_H; \delta\dot{\boldsymbol{u}}) - \lambda_H \Pi_t(\delta\dot{\boldsymbol{u}}) - \lambda_H b(\boldsymbol{p}_H; \delta\dot{\boldsymbol{u}}) = 0 \quad \forall \delta\dot{\boldsymbol{u}} \tag{4.16}$$

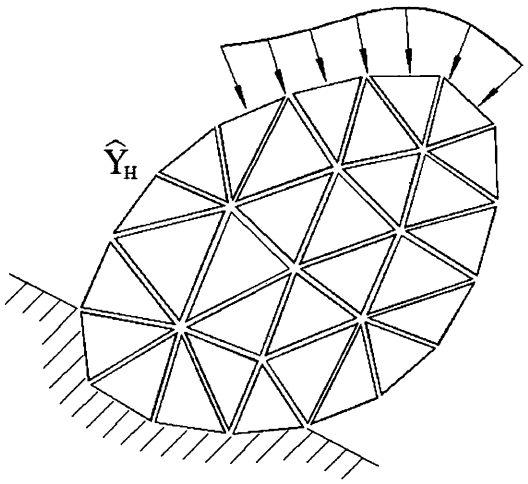

Figure 4.5 Body drawn by the coarse broken space $\hat{Y}_H$

Note that the velocity field $\boldsymbol{v}_H$ in the coarse mesh is already known, hence the only unknown in equation (4.16) is the inter-element load field $\boldsymbol{p}_H$. Note also that if $\delta\dot{\boldsymbol{u}}$ is chosen as a rigid body field $\delta\dot{\boldsymbol{u}}_R$, then $T(\boldsymbol{v}_H;\delta\dot{\boldsymbol{u}}_R)=0$ since the internal forces do not produce work during rigid body motion, and the expression $\Pi_t(\delta\dot{\boldsymbol{u}}_R)=b(\boldsymbol{p}_H;\delta\dot{\boldsymbol{u}}_R)$ implies that tractions $\boldsymbol{p}_H$ are in static equilibrium with the external forces.

This equation can be solved for $\boldsymbol{p}_H$ in a global manner, although the number of unknowns in the system is larger than the number of equations; that is, there are many sets of $\boldsymbol{p}_H$ tractions that satisfy this system of equations. However, as described in the next section, a solution to problem (4.9) can be found by solving a series of *local problems*, whose setting requires the definition of the stress distribution acting along the contour of a local volume, i.e. an element e.

This kind of distribution can be found by well known methods which have been used in the theory of *error estimation* to recover continuous and equilibrated stress distributions along the edges of elements in a typical finite element discretization. These techniques have been used for many years and in different applications, mostly in error estimation solutions. Two of the proposed *flux equilibration* methods, one by Ladeveze and Leguillon [2] and another by Ainsworth and Oden [3], represent appropriate alternatives to this intermediate step in the present proposal. It is fair here

to comment that this step represents an important, articulating element in the present solution. In the present implementation, a *Ladeveze constant flux equilibration* method has been used. Details of this method are given in section 4.4 below.

4.2.2 Solution of the local problem

Despite the fact that condition (4.11) seems to tie up the solution of the local problems, they can in fact be solved individually. To show this consider each macro-element $e = 1 \,..\, m_H$ in turn, where m_H is the number of elements in the coarse mesh. Consider the corresponding *local reduced* space $\overline{Z}_h^e$ defined for each element as

$$\overline{Z}_h^e = \left\{ \dot{\boldsymbol{u}}^e \in Z_h^e \;\middle|\; \hat{\Pi}_t^e\left(\dot{\boldsymbol{u}}^e\right) = 1 \right\} \tag{4.17}$$

Where $\hat{\Pi}_t^e\left(\dot{\boldsymbol{u}}^e\right)$ denotes the work done by the forces acting on the edges of e (either coming from the nominal load $\mathbf{t}$ or from tractions $\boldsymbol{p}_H$). An isolated local e element is shown in figure 4.6, acted upon by the equilibrated tractions.

We now define the local *minimum* $\hat{\gamma}_h^e$ as

$$\hat{\gamma}_h^e \equiv \min_{\dot{\boldsymbol{u}}_h^e \in \overline{Z}_h^e} \Pi_p^e\left(\dot{\boldsymbol{u}}_h^e\right) = \Pi_p^e\left(\hat{\dot{\boldsymbol{v}}}_h^e\right) \tag{4.18}$$

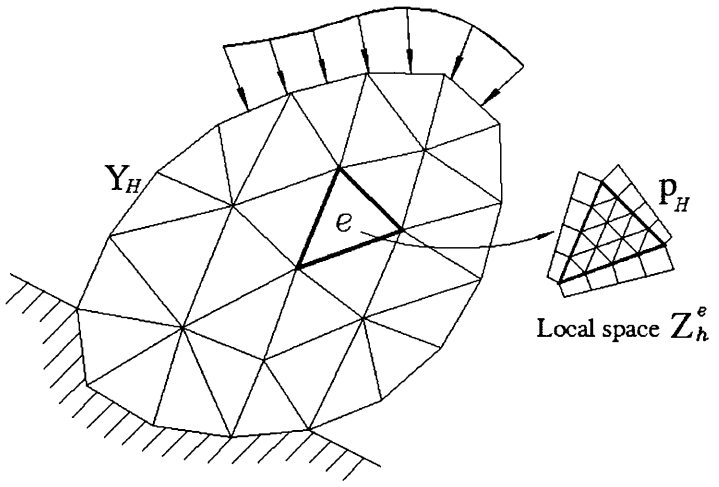

Figure 4.6 Macro-element drawn by a fine mesh describing space Z_h^e

Note that $\Pi_p^e\left(\hat{\dot{v}}_h^e\right)$ in equation (4.18) represents a collapse multiplier obtained by solving the local problem under kinematic conditions, over the space $\overline{Z}_h^e$. In other words, the problem expressed in equation (4.18) is in fact a *local upper bound problem*, which is resolved using exactly the same procedure as that described in section 3.5 (see equation 3.31). However, to construct the local problem over space $\overline{Z}_h^e$, the local volume (element) is subject to a load configuration drawn by the equilibrated (and continuous) tractions along the macro-element edges, and also subject to consistent support conditions. This procedure yields a local collapse capacity.

4.2.3. A Lower bound evaluation

As implied by equation (4.18), the local collapse multipliers play an important role in the evaluation of the lower bound to the true collapse multiplier in the present context. A first approach suggests that the whole structure will fail at a point where, given the stress and strain-rate fields acting over a differential body volume, the *static* and *kinematic* conditions would cause a sharp reduction of the load carrying capacity at the local volume. This assumption requires the identification of a local volume at which these conditions take place, as reflected in the following proposition.

Proposition 4.1

The *minimizer* $\hat{\gamma}_h$ is given by

$$\hat{\gamma}_h = \min_{e=1..m_H} \hat{\gamma}_h^e \equiv \hat{\gamma}_h^E \tag{4.19}$$

where m_H is the number of elements in the coarse mesh.

Proof: In order to prove (4.19), it suffices to prove that

$$\Pi_p\left(\dot{\boldsymbol{u}}_h\right) \geq \hat{\gamma}_h^E \quad ; \quad \forall \dot{\boldsymbol{u}}_h \in \hat{\overline{Y}}_h \tag{4.20}$$

showing that $\hat{\gamma}_h^E$ cannot be greater than the internal work rate produced over the reference space Y_h, thus yielding a lower bound to the collapse multiplier.

Consider any velocity field $\dot{\boldsymbol{u}}_h \in \hat{\bar{Y}}_h$ and let $\dot{\boldsymbol{u}}_h^e$ denote its restriction to macro-element e, that is $\dot{\boldsymbol{u}}_h^e \in Z_h^e$, a velocity field pertaining to the space defined within the element volume. The total plastic potential can be given by its macro-elemental contributions as

$$\Pi_p\left(\dot{\boldsymbol{u}}_h\right) = \sum_e \Pi_p^e\left(\dot{\boldsymbol{u}}_h^e\right) \tag{4.21}$$

and the external load work-rate can also be defined in terms of the local shares of the total unit:

$$\hat{\Pi}_t\left(\dot{\boldsymbol{u}}_h\right) = \sum_e \hat{\Pi}_t^e\left(\dot{\boldsymbol{u}}_h^e\right) = 1 \tag{4.22}$$

Starting from the minimal plastic potential, found by the kinematic solution on $\bar{Y}_h$ and given here as a sum of elemental contributions, as in (4.21), and noting that the plastic potential Π_p is order one homogeneous, that is $\Pi_p\left(\alpha\dot{\boldsymbol{u}}\right) = \alpha\Pi_p\left(\dot{\boldsymbol{u}}\right)$, we can rewrite

$$\Pi_p\left(\dot{\boldsymbol{u}}_h\right) = \sum_e \Pi_p^e\left(\dot{\boldsymbol{u}}_h^e\right) = \sum_e \hat{\Pi}_t^e\left(\dot{\boldsymbol{u}}_h^e\right)\ \Pi_p^e\left[\dot{\boldsymbol{u}}_h^e / \hat{\Pi}_t^e\left(\dot{\boldsymbol{u}}_h^e\right)\right] \tag{4.23}$$

Noting that definition (4.18) implies

$$\Pi_p^e\left(\boldsymbol{v}_h^e\right) \geq \Pi_p^e\left(\hat{\boldsymbol{v}}_h^e\right) \quad \forall \boldsymbol{v}_h^e \in \bar{Z}_h^e \tag{4.24}$$

meeting the equality only for $\boldsymbol{v}_h^e = \hat{\boldsymbol{v}}_h^e$, thus we clearly arrive at the following inequality

$$\sum_e \hat{\Pi}_t^e\left(\dot{\boldsymbol{u}}_h^e\right)\,\Pi_p^e\left[\dot{\boldsymbol{u}}_h^e/\hat{\Pi}_t^e\left(\dot{\boldsymbol{u}}_h^e\right)\right] \geq \sum_e \hat{\Pi}_t^e\left(\dot{\boldsymbol{u}}_h^e\right)\,\Pi_p^e\left(\hat{\boldsymbol{v}}_h^e\right) \quad \forall \dot{\boldsymbol{u}}_h^e \tag{4.25}$$

Now, using the definition of multiplier $\hat{\gamma}_h^E$ as the smallest of all multipliers $\hat{\gamma}_h^e$ over the whole domain, we can write

$$\sum_e \hat{\Pi}_t^e\left(\dot{\boldsymbol{u}}_h^e\right)\,\Pi_p^e\left(\hat{\boldsymbol{v}}_h^e\right) \geq \sum_e \hat{\Pi}_t^e\left(\dot{\boldsymbol{u}}_h^e\right)\,\hat{\gamma}_h^E \tag{4.26}$$

Finally, in view of equation (4.22), a load multiplier approaching from below is clear, thus from relations (4.23) to (4.26) we arrive at:

$$\Pi_p\left(\dot{\boldsymbol{u}}_h\right) \geq \hat{\gamma}_h^E \sum_e \hat{\Pi}_t^e\left(\dot{\boldsymbol{u}}_h^e\right) \geq \hat{\gamma}_h^E \quad \forall \dot{\boldsymbol{u}}_h^e \tag{4.27}$$

The previous proof is particularly clear if we take $\dot{\boldsymbol{u}}_h$ as a kinematically admissible collapse velocity field, i.e. resulting from an upper bound solution, defined over a given reference mesh $\overline{Y}_h$.

The assumption of local solutions implies that in the broken problem the deformation localises at the weakest element (under the conditions described above), which is intuitively logical. Note that this line of reasoning leads to

$$\hat{\boldsymbol{v}}_h^e = 0 \text{ if } e \neq E \text{ and } \hat{\boldsymbol{v}}_h^E = \hat{\boldsymbol{v}}_h^E \tag{4.28}$$

which indicates that the solution of the local problem given by the minimizer in (4.19) depends only on the velocity field within the macro-element E (refer to minimization in (4.12)).

In contrast with the *minimizer* solution above, a second approach to obtain a more accurate lower bound can be constructed from relation (4.25), which implies a solution based in the contribution of each macro-element given by the local collapse multipliers and the distribution of the unit external work rate. It is worth noting at this

point, that the minimizer solution (4.19) can lead to a localized volume of extreme plastic dissipation producing low stress carrying capacity levels, which can fail to represent a broader plastic volume (not necessarily contiguous) within the whole domain. On the other hand, an alternative integrated approach accounts for the contribution of every local volume, covering the whole domain, which provides a better estimate as demonstrated in the numerical results presented in Chapter 6. This alternative approach is detailed in the next section.

4.2.4 An integrated approach to the Lower Bound

In accordance with the developments and reasoning in section 4.2.3, an *integrated approach* to the evaluation of the lower bound can be established. In contrast with the *minimizer approach*, this alternative procedure calls for the determination of the load multiplier given by local (elemental) contributions, as proposed next.

Proposition 4.2

A lower bound to the collapse load multiplier $\hat{\gamma}_h$ is given by

$$\hat{\gamma}_h = \sum_e \hat{\Pi}_t^e\left(\boldsymbol{v}_H^e\right)\, \Pi_p^e\left(\hat{\boldsymbol{v}}_h^e\right) \tag{4.29}$$

Proof. Assuming that a kinematic solution exists on the coarse space $\overline{Y}_H$, for which a collapse mechanism is defined by $\boldsymbol{v}_H \in \overline{Y}_H$. The elemental factor $\hat{\Pi}_t^e\left(\dot{\boldsymbol{u}}_h^e\right)$ in (4.25) dependent on a fine space velocity field, can be determined by using the coarse space velocity field $\boldsymbol{v}_H^e$, that is as $\hat{\Pi}_t^e\left(\boldsymbol{v}_H^e\right)$ (see figure 4.7). The external forces implied in the determination of factor $\hat{\Pi}_t^e\left(\boldsymbol{v}_H^e\right)$ come from equilibrated tractions applied on the edges of macro-element e, over the discretized space Z_h^e.

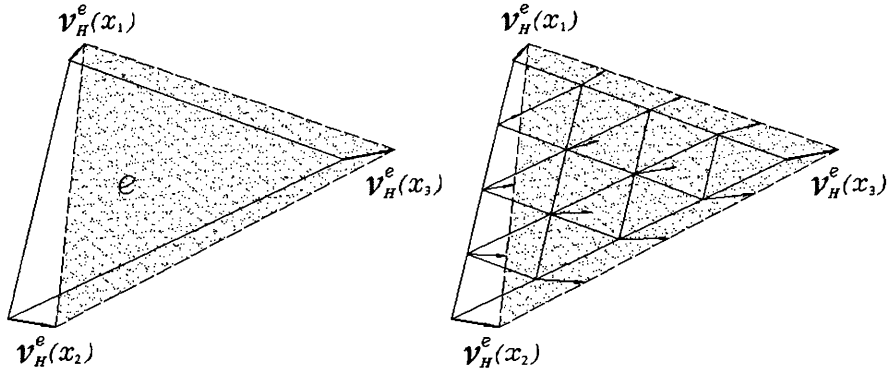

a) b)

Figure 4.7 Macro-element e showing the velocity field over: a) the coarse space; b) the fine space.

Now, consider any $\dot{u}_h \in \hat{\bar{Y}}_h$ and $\dot{u}_h^e \in Z_h^e$, as in proposition 4.1. Similarly as in expressions (4.23) and (4.25), it is proved that definition (4.29) leads to an expression yielding a collapse multiplier approaching from below, that is

$$\Pi_p(\dot{u}_h) = \sum_e \Pi_p^e(\dot{u}_h^e) = \sum_e \hat{\Pi}_t^e(v_H^e)\ \Pi_p^e\left[\dot{u}_h^e / \hat{\Pi}_t^e(v_H^e)\right] \tag{4.30}$$

and abiding again by relation (4.24), we arrive at

$$\Pi_p(\dot{u}_h) \geq \sum_e \hat{\Pi}_t^e(v_H^e)\ \Pi_p^e(\hat{v}_h^e) \tag{4.31}$$

This integrated approach to the lower bound evaluation will be emphasized from this point on in the present research work, although some numerical results regarding the minimizer approach will be presented in Chapter 6 to show a contrasting behaviour between both solution schemes.

Proposition (4.29) corresponds to a fundamental element of the proposed solution in the present research, and is used in the implementation and test stages as described in Chapter 5 and 6. It is also an articulating element in the *adaptive mesh refinement* strategy, which is an important component of the original research objectives. The implementation aspects of the adaptive approach are discussed in Chapter 5, however in the next section an important definition, namely the *bound gap*, is presented. This

bound gap corresponds to the error parameter upon which the adaptive procedure is constructed.

4.3 Adaptivity indicator

The adaptive mesh refinement used in this thesis, requires the determination of an *adaptivity control parameter,* or *adaptivity indicator,* as discussed in Haegland and Skaflestad [4], to set up a refining criteria, normally in the form of a parameter threshold beyond which an element is refined using one of various refinement schemes. In the present work the proposed control parameter is derived from the difference between an upper and a lower bound value, interpreted as an error indicator and referred to as the *bound gap* as in Ciria and Peraire [5]. In the present implementation the so-called *total bound gap* is produced by the bound values at a given iteration within the refinement progression. Consequently, an *elemental bound gap* can be defined as the control parameter for the adaptive refinement procedure, as described next.

The *total bound gap*, between lower and upper bounds, is given by

$$g = \gamma_H - \hat{\gamma}_h \tag{4.32}$$

In order to express (4.32) as the sum of positive element contributions note that the following piecewise bounds definitions are in order

$$\gamma_H = \sum_e \Pi_p^e\left(\boldsymbol{v}_H^e\right) \text{ and } \hat{\gamma}_h = \sum_e \hat{\Pi}_t^e\left(\boldsymbol{v}_H^e\right)\, \Pi_p^e\left(\hat{\boldsymbol{v}}_h^e\right) \tag{4.33}$$

given expression (4.21) over the coarse space Y_H, and proposition (4.29). Hence the total gap is now

$$g = \sum_e \left\{ \Pi_p^e\left(\boldsymbol{v}_H^e\right) - \hat{\Pi}_t^e\left(\boldsymbol{v}_H^e\right) \Pi_p^e\left(\hat{\boldsymbol{v}}_h^e\right) \right\} \tag{4.34}$$

where clearly, the elemental contribution to this total bound gap is given by

$$g_e = \Pi_p^e\left(\boldsymbol{v}_H^e\right) - \hat{\Pi}_t^e\left(\boldsymbol{v}_H^e\right)\,\Pi_p^e\left(\hat{\hat{\boldsymbol{v}}}_h^e\right) \tag{4.35}$$

To prove that the gap is everywhere positive, note that from relation (4.24), rewritten conveniently here as

$$\Pi_p^e\left(\boldsymbol{v}_h^e\right) \geq \Pi_p^e\left(\hat{\hat{\boldsymbol{v}}}_h^e\right) \quad \forall \boldsymbol{v}_h^e \in \overline{Z}_h^e \tag{4.36}$$

we arrive at

$$\Pi_p^e\left(\boldsymbol{v}_H^e\right) = \hat{\Pi}_t^e\left(\boldsymbol{v}_H^e\right)\Pi_p^e\left[\boldsymbol{v}_H^e / \hat{\Pi}_t^e\left(\boldsymbol{v}_H^e\right)\right] \geq \hat{\Pi}_t^e\left(\boldsymbol{v}_H^e\right)\Pi_p^e\left(\hat{\hat{\boldsymbol{v}}}_h^e\right),\ \forall e \in Y_H \tag{4.37}$$

for which Y_H is typically a coarser mesh definition relative to Y_h, except for $H = h$. Relation (4.37) suffices to prove the positiveness of the elemental gap in (4.35).

These tools will prove effective in producing an appropriate adaptive mesh refinement procedure. In Chapter 5, important aspects of the adaptive scheme are discussed. Results coming from this implementation are also reviewed in Chapter 6.

4.4 Flux equilibration method

Owing its name to classical thermodynamics finite element analysis, *flux equilibration techniques* are among the most commonly used methods for recovering tractions at inter-element edges in a variety of applications. The flux equilibration procedure is typically found in error estimation applications, from which it emerged. In order to present a coherent description of this procedure, it is necessary to locate it within the context of the *error estimation techniques*. A brief primer to error estimates is given below, which is of a general application in the finite element context, and then an approach to *residual based error estimators* is given, leading to a detailed description of the *flux equilibration technique* applied in this work. However, we need to bear in mind that in the present application no error estimates in the traditional manner are produced, instead an error evaluation based on the total bound gap is proposed here, specifically when dealing with the *adaptive refinement scheme*,

as discussed in chapter 5. We believe that this is a far better alternative in the context of limit state analysis where the aim is to obtain the collapse load to within a given precision. Thus the flux equilibration procedure is of key interest in the present context, and it corresponds to the main subject of the discussion that follows.

4.4.1 Residual based error estimators

In an ideal world an exact solution would be attainable for any problem. Unfortunately experience shows that for practical problems this is not the case, and approximate solutions are aimed at to produce convenient practical solutions. If we denote the exact solution of a problem by $\dot{\boldsymbol{u}}$, in the context of the present solution, and the finite element approximation by $\dot{\boldsymbol{u}}_h$ the error is defined as

$$\mathbf{e} = \dot{\boldsymbol{u}} - \dot{\boldsymbol{u}}_h \tag{4.38}$$

In general, the quality of an approximate solution is not equal at all points in space, especially near singularities, so we usually consider some appropriate norm of the error $\|\mathbf{e}\|$. In order to control the quality of the approximate solution the error is required to be less than some prescribed limit. The need for an error estimator comes from the approximate nature of the solution at hand. Some applications require only special qualities of the solution to be emphasised. In these cases a set of appropriate *indicators* to measure the solution quality can be used. Various approaches have been proposed to cater for the error estimation requirements, from which *recovery methods, residual based methods* and *goal oriented methods* are typical applications. In what follows, a description of a *residual based method* proposed by Ladeveze & Leguillon [2], is presented in accordance with the requirement of a flux equilibration procedure in the present research work. This procedure falls within the set of tools used to construct the so-called *a posteriori error estimation methods.* It is imperative to keep in mind that the conventional procedures for error estimation differ from the aims of the present work in form, but not in essence: both aim to determine an extension to a given admissible stress field. In this research, flux equilibration is used to retrieve local contributions to the total bound gap, i.e. the difference between lower and upper bounds to the collapse load multiplier, which in essence, resemble the local

contributions to the *global error* aimed by conventional finite element error estimation procedures. In that sense, the bounds evaluation, particularly the total bound gap proposed herein corresponds to an *error estimation-type* procedure. Details on the definition of the bound gap are given in section 4.3 above. Adaptivity implementation issues are discussed in chapter 5.

A large class of error estimators use the residuals of the finite element approximation, commonly known as the *residual error estimators*. In a paper by Babuska [6], it is concluded that element-residual estimators should only be used with equilibration. These are known as *equilibrated element residual estimators* and are the most robust among the class. Our main interest here is the description of a method to attain an extension to an admissible stress field given the present requirements, thus a description of the flux equilibration method is given in the following sections.

4.4.2 Determination of equilibrated fluxes on element edges

The following descriptions are based on the work of Ladeveze & Leguillon [2], Ladeveze, Pelle & Rougeot [7], and Coorevits, Ladeveze & Pelle [8].

Let S_u be the part of the boundary S where the velocities are prescribed:

$$\dot{\boldsymbol{u}} = \dot{\boldsymbol{u}}_0 \quad \text{on } S_u \tag{4.39}$$

and let S_t be the complementary part of S. On S_t the tractions are given:

$$\boldsymbol{\sigma}\mathbf{n} = \mathbf{t} \quad \text{on } S_t \tag{4.40}$$

where $\mathbf{n}$ is the unit outward normal. Let e denote any triangular element of the mesh. Obviously, it is assumed that S_u and S_t are unions of element boundaries.

On each element boundary ∂V_e, where V_e is the volume of element e, we define the scalar function η_e such that $\eta_e = 1$ for the edges where element e is on the *right* and $\eta_e = -1$ if e is on the *left* as seen from the edge.

Then the equilibrated traction for an element e is given by $\tilde{\mathbf{q}}$, which for a specific edge is defined in vector form as

$$\tilde{\mathbf{q}}_{ef} = \boldsymbol{\alpha}_{ef} + \bar{\mathbf{q}}_{ef} \tag{4.41}$$

where, if $S_{ef} \not\subset \partial S$ then an average traction distribution $\bar{\mathbf{q}}_{ef} = \frac{1}{2}\eta_e\left(\boldsymbol{\sigma}_H^e + \boldsymbol{\sigma}_H^f\right)\mathbf{n}_e$ is defined, and $\bar{\mathbf{q}}_{ef} = \eta_e \boldsymbol{\sigma}_H^e \mathbf{n}_e$ otherwise (for boundary edges); that is, an average stress projection is considered for any inter-element edge, and a single element projection when the edge belongs to the boundary. Notation $\boldsymbol{\sigma}_H^e$ indicates the stress tensor pertaining to element e, resulting from the finite element solution. We will use $\tilde{\mathbf{q}}$ to denote the equilibrated tractions for the present description, but note that these are assumed to be vector equivalents of $\boldsymbol{p}_H$ ($= \tilde{\mathbf{q}}$). The parameter of interest, stress α_{ef}, can be fully determined in component form by

$$\varphi_{ef}^i(a) = \int_{S_{ef}} \alpha_{ef}^i \omega_{Ha} dS \;\; ; \;\; a = 1,2 \tag{4.42}$$

with nodes at x_1 and x_2 (thus x_a, a=1,2) being the extreme points of S_{ef} (one of these is x_a itself). The index i denotes the Cartesian direction x or y. Scalar ω_{Ha} is defined by Ladeveze & Leguillon as $\omega_{Hb}(x_a) = \delta_{ab}$, with x_a being the position of node a and δ_{ab} being the Kronecker delta. Alongside, a linear interpolating expression is defined over S_{ef}, and given in component form by

$$\alpha_{ef}^i\Big|_{x_a} = \frac{2}{|S_{ef}|}\left\{\left[2\varphi_{ef}^i(1) - \varphi_{ef}^i(2)\right]\omega_{H1}(x_a) + \left[2\varphi_{ef}^i(2) - \varphi_{ef}^i(1)\right]\omega_{H2}(x_a)\right\} \tag{4.43}$$

so that $\tilde{\mathbf{q}}$ is also determined on S_{ef} using (4.43). Clearly $|S_{ef}|$ denotes the length of edge S_{ef}.

A stress field $\tilde{\boldsymbol{\sigma}}$, interpreted as an equilibrated extension of the finite element solution, i.e. corresponding to a state of equilibrated tractions, is statically admissible if:

$$\int_V \tilde{\boldsymbol{\sigma}} : \dot{\boldsymbol{\epsilon}}\left(\dot{\boldsymbol{u}}^*\right) dV = \int_V \mathbf{b} \cdot \dot{\boldsymbol{u}}^* dV + \int_{S_t} \mathbf{t} \cdot \dot{\boldsymbol{u}}^* dS \tag{4.44}$$

for every displacement field $\dot{\boldsymbol{u}}^*$ such that $\dot{\boldsymbol{u}}^* = 0$ on S_u.

From the internal force expression for element e at node a, the following consideration is in order:

$$\int_{V_e} \left(\tilde{\boldsymbol{\sigma}} - \boldsymbol{\sigma}_H\right) \nabla N_a \, dV = 0 \tag{4.45}$$

for every element (volume) V_e on mesh Y_H, and for every finite element shape function N_a defined over the element. Note that this condition entails the requirement of a zero value for the *residual forces* within each element. From the discretized form of equation (4.44) and condition (4.45), it follows

$$\int_{\partial V_e} \tilde{\mathbf{q}} N_a \, dS = \mathbf{Q}_e(a) \tag{4.46}$$

where

$$\mathbf{Q}_e(a) = -\int_{V_e} \mathbf{b} N_a \, dV + \int_{V_e} \boldsymbol{\sigma}_H \nabla N_a \, dV \tag{4.47}$$

for every shape function N_a and every element e. The quantity $\mathbf{Q}_e(a)$ is explicitly defined in terms of the data and the finite element solution $\boldsymbol{\sigma}_H$. Equation (4.46), written for every element e connected to a given node a, leads to a small linear system of equations between projections $\int_S \tilde{\mathbf{q}} N_a \, dS$ for each element on its edge S connected to the node a.

Let us consider an internal node a, as shown in figure 4.8, where the element volumes and edges are indicated.

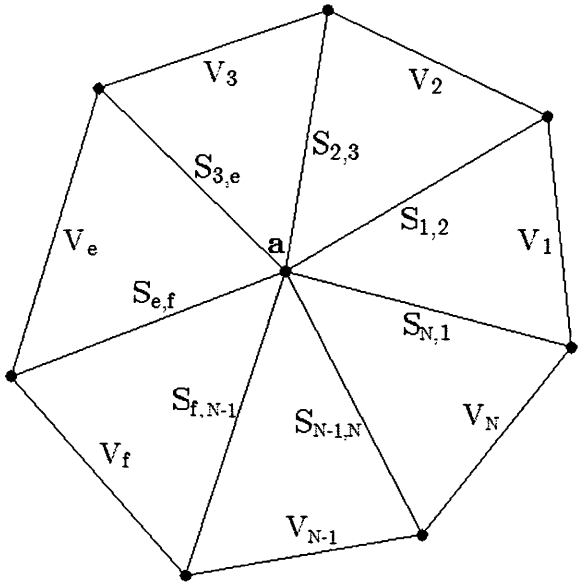

Figure 4.8 Equilibration over an internal node a.

Let us define $\mathbf{g}_{e,f} = \int_{S_{ef}} \tilde{\mathbf{q}}_{ef} N_a \, dS$ for $e = 1,2,\ldots,N$; $f = e+1$, with N being the number of elements converging at node a. Then from (4.46) we can write

$$\left.\begin{aligned} \mathbf{g}_{N,1} - \mathbf{g}_{1,2} &= \mathbf{Q}_1(a) \\ \mathbf{g}_{1,2} - \mathbf{g}_{2,3} &= \mathbf{Q}_2(a) \\ &\cdots \\ \mathbf{g}_{N-1,N} - \mathbf{g}_{N,1} &= \mathbf{Q}_N(a) \end{aligned}\right\} \tag{4.48}$$

As $\boldsymbol{\sigma}_H$ is in equilibrium in the finite element sense, we have:

$$\int_V \boldsymbol{\sigma}_H \nabla N_a \, dV = \int_V \mathbf{b} N_a \, dV + \int_{S_t} \mathbf{t} N_a \, dS \tag{4.49}$$

Then, for an internal node a, equation (4.49) leads to $\sum_{e=1}^{N} \mathbf{Q}_e(a) = 0$ and equation (4.48) admits at least one solution, which is not unique. System (4.48) can be solved through the *singular value decomposition* technique, as briefly described at the end of the next section.

4.4.3 Construction of a typical nodal system of equations for flux equilibration

A brief extension to the developments in the flux equilibration method is given here, to clarify some of the steps in the construction of the system of equations defined in (4.48). Expressions in component form are used (no vector variables are used, unless noted), so the following computations are to be made for each space direction (x and y). To indicate this clearly, we use index i, for $i=1,2$ as components x and y, respectively.

Departing from the system of equations in (4.48), an expansion of $g^i_{e,f}$ is needed, thus recalling the definition of $g^i_{e,f} = \int_{S_{ef}} \tilde{q}^i_{e,f} N_a \, dS$, we can write

$$g^i_{e,f} = \int_{S_{ef}} \alpha^i_{ef} N_a \, dS + \int_{S_{ef}} \overline{q}^i_{ef} N_a \, dS \tag{4.50}$$

after substituting equation (4.41). Now, noting that the first term $\int_{S_{ef}} \alpha^i_{ef} N_a \, dS$ can actually be defined as in (4.42), by considering a *constant shape* function along S_{ef}, as suggested by Ladeveze and Leguillon, we have

$$g^i_{e,f} = \int_{S_{ef}} \alpha^i_{ef} \omega_{Ha} \, dS + \int_{S_{ef}} \overline{q}^i_{ef} N_a \, dS \tag{4.51}$$

leading to

$$g^i_{e,f} = \alpha^i_{ef} L_{ef} + \tfrac{1}{2} \overline{q}^i_{ef} L_{ef} \tag{4.52}$$

with $L_{ef} = |S_{ef}|$, so that for element f and with $\mathbf{Q}_f(a) = \int_{V_f} \boldsymbol{\sigma}_H \nabla N_a \, dV$ given in vector form, after neglecting body forces, the equation for element f in the system of equations for node a leads to

$$g^i_{e,f} - g^i_{f,h} = Q^i_f(a) \tag{4.53}$$

for adjacent elements e and h, equation (4.53) can be written as

$$\alpha^i_{ef} L_{ef} + \tfrac{1}{2}\bar{q}^i_{ef} L_{ef} - \alpha^i_{fh} L_{fh} - \tfrac{1}{2}\bar{q}^i_{fh} L_{fh} = Q^i_f(a) \tag{4.54}$$

In the same fashion, the rest of the equations can be written to form the complete local nodal system in (4.48) as

$$\begin{aligned}
\alpha^i_{N,1} L_{N,1} + \tfrac{1}{2}\bar{q}^i_{N,1} L_{N,1} - \alpha^i_{1,2} L_{1,2} - \tfrac{1}{2}\bar{q}^i_{1,2} L_{1,2} &= Q^i_1(a) \\
\alpha^i_{1,2} L_{1,2} + \tfrac{1}{2}\bar{q}^i_{1,2} L_{1,2} - \alpha^i_{2,3} L_{2,3} - \tfrac{1}{2}\bar{q}^i_{2,3} L_{2,3} &= Q^i_2(a) \\
&\cdots \\
\alpha^i_{N-1,N} L_{N-1,N} + \tfrac{1}{2}\bar{q}^i_{N-1,N} L_{N-1,N} - \alpha^i_{N,1} L_{N,1} - \tfrac{1}{2}\bar{q}^i_{N,1} L_{N,1} &= Q^i_N(a)
\end{aligned} \tag{4.55}$$

This system is solved for coefficients α_{ef} and used in the interpolating expression (4.43) to obtain equilibrated external stress distributions through the component expression $\tilde{q}^i_{ef} = \alpha^i_{ef} + \bar{q}^i_{ef}$. The next section focuses on the derivation of the interpolating expression (4.43). Note that a nodal system like the one in (4.55) is constructed for every node, varying in size depending on the number of elements sharing the node; one equation is defined per element.

The case of boundary nodes is resolved by using $\bar{\mathbf{q}}_{ef} = \eta_e \boldsymbol{\sigma}^e_H \mathbf{n}_e$ at the corresponding edge; the rest of the equation for the related element remains the same.

The solution to (4.48) (or (4.55)) can be obtained through a *singular value decomposition* generic linear equations solver, as implemented in the present work by using the `DLVSRR` routine of the IMSL Mathematical Library Subroutines.

4.4.4 Inter-element edge flux interpolation

Again, general component *i* is used in the following expressions, so that these must be computed for each Cartesian direction *x* and *y*.

After solving for constant stresses α_{ef}^{i}, as described in the exercise above, a stress value at the extreme nodes on edge S_{ef} is yet to be computed in order to define a stress distribution along the edge. This can be done in terms of the equivalent forces

$$\varphi_{ef}^{i}(a) = \int_{S_{ef}} \alpha_{ef}^{i} \omega_{Ha} \, dS \;\; ; \;\; a = 1,2 \tag{4.56}$$

occurring at each node a of the edge. Note that the scalar α_{ef}^{i} stands for a constant stress distribution component along edge S_{ef}. Note also that forces $\varphi_{ef}^{i}(1)$ and $\varphi_{ef}^{i}(2)$ are defined in terms of distributions α_{ef}^{i} resulting from two different nodal equation systems, one for each node defining edge S_{ef}, and generalized conveniently here as nodes 1 and 2. The interpolation expression can be written as

$$\alpha_{ef}^{i}(x) = \varphi_{ef}^{i}(1)\phi_1(x) + \varphi_{ef}^{i}(2)\phi_2(x) \tag{4.57}$$

noting that x runs along edge S_{ef}. Note that $\varphi_{ef}^{i}(1)$ and $\varphi_{ef}^{i}(2)$ remain constant. Furthermore, the linear interpolating functions are defined as

$$\phi_1(x) = a_1 x + b_1 \quad ; \quad \phi_2(x) = a_2 x + b_2 \tag{4.58}$$

Simplifying notation, expression (4.57) can be written as

$$\alpha_{ef}^{i} = \varphi_{ef}^{i}(1)\phi_1 + \varphi_{ef}^{i}(2)\phi_2 \tag{4.59}$$

In order to produce an equivalent force over node 1 and 2, the following equations arise from expression (4.59):

$$\begin{aligned} \int_{S_{ef}} \alpha_{ef}^{i}\psi_1 \, dS &= \varphi_{ef}^{i}(1) \int_{S_{ef}} \phi_1\psi_1 \, dS + \varphi_{ef}^{i}(2) \int_{S_{ef}} \phi_2\psi_1 \, dS \\ \int_{S_{ef}} \alpha_{ef}^{i}\psi_2 \, dS &= \varphi_{ef}^{i}(1) \int_{S_{ef}} \phi_1\psi_2 \, dS + \varphi_{ef}^{i}(2) \int_{S_{ef}} \phi_2\psi_2 \, dS \end{aligned} \tag{4.60}$$

where $\psi_1 = 1 - x/L$ and $\psi_2 = x/L$, with $L = L_{ef} = |S_{ef}|$ as before. Applying consistent node conditions for these equations, the following requirements are arrived at

$$\int_{S_{ef}} \phi_1 \psi_1 \, dS = 1 \quad ; \quad \int_{S_{ef}} \phi_2 \psi_1 \, dS = 0 \tag{4.61}$$

$$\int_{S_{ef}} \phi_1 \psi_2 \, dS = 0 \quad ; \quad \int_{S_{ef}} \phi_2 \psi_2 \, dS = 1 \tag{4.62}$$

Conditions (4.61) lead to a linear system from which a_1 and b_1 can be determined. Similarly, coefficients a_2 and b_2 can be solved from (4.62). Their solution yields the following forms for the interpolation functions

$$\phi_1 = 4/L - 6x/L^2 \quad ; \quad \phi_2 = 6x/L^2 - 2/L \tag{4.63}$$

so that, at the nodes these functions take the values

$$\begin{aligned} \phi_1|_{x_1} &= 4/L \quad ; \quad \phi_1|_{x_2} = -2/L \\ \phi_2|_{x_1} &= -2/L \quad ; \quad \phi_2|_{x_2} = 4/L \end{aligned} \tag{4.64}$$

leading to expressions

$$\begin{aligned} \alpha_{ef}^i|_{x_1} &= 4\varphi_{ef}^i(1)/L - 2\varphi_{ef}^i(2)/L \\ \alpha_{ef}^i|_{x_2} &= 4\varphi_{ef}^i(2)/L - 2\varphi_{ef}^i(1)/L \end{aligned} \tag{4.65}$$

These results are clearly consistent with expression (4.43), as proposed by Ladeveze and Leguillon [2].

4.5 References

1. Christiansen, E. *Computation of limit loads*. International Journal for Numerical Methods in Engineering. Vol. 17, 1981, p.1547-1570.
2. Ladeveze P., Leguillon D. *Error estimate procedure in the finite element method and applications*. SIAM Journal on Numerical Analysis. Vol. 20, Issue 3, 1983, p.485-509.
3. Ainsworth M., Oden J.T. *A posteriori error estimation in finite element analysis*. John wiley & Sons, Inc., New York, 2000.
4. Haegland B., Skaflestad B. *A survey of some methods for moving grid and grid adaptation.* Numerics No.2, Norwegian University of science and Technology, 2002.

5. Ciria H., Peraire J. *Computation of upper and lower bounds in limit analysis using second-order cone programming and mesh adaptivity*. MSc Thesis, Massachusetts Institute of Technology, 2004.
6. Babuska I. *Validation of a posteriori error estimators by numerical approach.* International Journal for Numerical Methods in Engineering, Vol. 37, 1994, p.1073-1123.
7. Ladeveze P., Pelle J.-P., Rougeot Ph. *Error estimation and mesh optimisation for classical finite elements.* Engineering Computations, Vol. 8, 1991, p.69-80.
8. Coorevits P., Ladeveze P., Pelle J.-P. *An automatic procedure with control of accuracy for finite element analysis in 2D elasticity.* Journal of Computational Methods in Applied Mechanics and Engineering, Vol. 121, 1995, p.91-120.
9. Paraschivoiu M., Patera A.T. *A posteriori bounds for linear functional outputs of Crouzeix-Raviart finite element discretizations of the incompressible Stokes problem.* International Journal for Numerical Methods in Fluids, Vol. 32, 2000, p.823-849.
10. Paraschivoiu M., Peraire J., Patera A.T. *A posteriori finite element bounds for linear-functional outputs of elliptic partial differential equations.* Comput. Methods Appl. Mech. Engrg. Vol 150, 1997, p.289-312.

Chapter 5

Implementation and adaptivity

5.1 Introduction

In the present chapter a general algorithm is presented for each phase of the solution process, namely the evaluation of the *upper bound* and the *lower bound*, as these naturally stand out in the foundation theory, and finally the *adaptive refinement* procedure. A brief description is given for each step within the algorithm, where appropriate, and a reference to a broader discussion is given for the relevant issues. Departing from a specific step, the relevant aspects of the solution procedures are further developed or otherwise referenced to clearly convey the necessary components of the proposed solution. It is imperative to point out here that the solution procedures produced in this research work are all based in the use of a *constant strain 3-noded triangular finite element* which complies with the requirements for an appropriate implementation, as suggested by Christiansen [1], where *constant-linear* functions are suggested for the pair $(\boldsymbol{\sigma}, \dot{\boldsymbol{u}})$, $\boldsymbol{\sigma}$ being defined by *constant element functions* and $\dot{\boldsymbol{u}}$ having bounded first order derivatives (see section 2.3). We first present the upper bound solution, followed by the lower bound evaluation, closing the chapter with a review of adaptivity aspects in the context of the present solution leading to the adaptive procedure algorithm.

5.2 Upper bound solution implementation

In the following sections the *upper bound solution* is presented, describing the most important aspects within the computer algorithms employed in its implementation, as

well as the necessary references to the theoretical elements upon which the solution is constructed. A similar set of sections will be devoted to the *lower bound solution* later in this chapter (see section 5.2). Details of the test cases and the analysis of the results are discussed in chapter 6.

5.2.1 The upper bound algorithm

The minimization requirements over the upper bound theorem in the present context are met through the use of the Newton-Raphson method, using a Lagrangian optimizing procedure as described in section 3.5.2. The main steps of the solution algorithm to attain the upper bound to the collapse multiplier, using the finite element method, are described in the following pseudocode. Each of the steps are described in more detail below.

Upper Bound algorithm

1. INPUT DATA - read geometry, boundary conditions, material properties, and solution control parameters
2. ASSEMBLE the nominal load vector – use $\mathbf{F}_a^n = \int_{S_n} \mathbf{t}^n N_a \, dS$ to assemble $\mathbf{F}$
3. COMPUTE INITIAL VELOCITY VECTOR
   3.1. SOLVE ELASTIC F.E. PROBLEM - solve $\mathbf{K}_{\text{elastic}}\mathbf{u} = \mathbf{F}$
   3.2. COMPUTE $\dot{\mathbf{u}}_0$ - use $\dot{\mathbf{u}}_0 = \mathbf{u}/\mathbf{F}^T\mathbf{u}$ to comply with condition $\mathbf{F}^T\dot{\mathbf{u}}_0 = 1$
4. SET $k = 0$
5. LOOP
   5.1. COMPUTE RESIDUAL VECTOR - use $\mathbf{R}(\dot{\mathbf{u}}_k, \lambda_{k+1}) = \lambda_{k+1}\mathbf{F} - \mathbf{T}(\dot{\mathbf{u}}_k)$ with
   $\lambda_{k+1} = \dot{\mathbf{u}}_k^T\mathbf{T}(\dot{\mathbf{u}}_k)$; use $\mathbf{T}^e(\dot{\mathbf{u}}_k) = \int_{V_e} \mathbf{B}^T\boldsymbol{\sigma}(\dot{\mathbf{u}}_k) \, dV$ to assemble $\mathbf{T}(\dot{\mathbf{u}}_k)$
   5.2. IF $\left(\left\|\mathbf{R}(\dot{\mathbf{u}}_k, \lambda_{k+1})\right\| / \left\|\lambda_{k+1}\mathbf{F}\right\| < tol\right)$ TERMINATE LOOP
   5.3. COMPUTE TANGENT MATRIX - use elemental matrix $\mathbf{K}_k^e = \int_{V_e} \mathbf{B}^T\mathbf{D}_p(\dot{\mathbf{u}}_k)\mathbf{B} \, dV$ to assemble tangent matrix $\mathbf{K}_k$
   5.4. COMPUTE VELOCITY VECTOR - solve $\mathbf{K}_k\dot{\mathbf{u}}_{k+1} = \lambda_{k+1}\mathbf{F} - \mathbf{T}(\dot{\mathbf{u}}_k)$
   5.5. APPLY LINE SEARCH - solve $R(\eta) = \Delta\dot{\mathbf{u}}^T\mathbf{T}(\dot{\mathbf{u}}_k + \eta\Delta\dot{\mathbf{u}}) = 0$ with $\Delta\dot{\mathbf{u}} = \dot{\mathbf{u}}_{k+1} - \dot{\mathbf{u}}_k$

5.6. UPDATE VELOCITY VECTOR - use $\dot{\mathbf{u}}_{k+1} = \dot{\mathbf{u}}_k + \eta \Delta \dot{\mathbf{u}}$

5.7. SET $k = k + 1$

6. END LOOP

7. COMPUTE kinematic load multiplier – use $\gamma_H = \sum_e \Pi_p^e \left(\mathbf{v}_H^e \right)$ with $\Pi_p^e \left(\mathbf{v}_H^e \right) = \int_{V_e} \sigma_y \dot{\bar{\varepsilon}}_H^e \, dV$

8. OUTPUT DATA - minimum collapse load multiplier γ_H, velocity field $\mathbf{v}_H$, stress field $\boldsymbol{\sigma}$

Relevant comments follow, and details are referred to appropriate sections in this or other chapters.

Step 1: is the entry point of the problem data block: the geometry of the body, the load and support conditions, the material properties and the solution parameters, as described briefly in section 5.5. This step is repeated in the main block in section 5.4.4 for convenience.

Step 2: uses expression $\mathbf{F}_a^n = \int_{\bar{s}_n} \mathbf{t}^n N_a \, dS$, which denotes the equivalent force vector applied over node a on the edge of the linearized face n with surface $\bar{s}_n$, as shown on figure 5.1. Note that this expression differs slightly from the one given in equation (3.39), that is $\mathbf{F}_a^e$, due to implementation convenience, as it is more practical to identify boundary element edges as independent entities, thus leading to independent data structures in the code. Customary finite element expressions for the equivalent force vector are obtained. It should be noted here that loads are limited to constant face-stress distributions in the present implementation. Vector $\mathbf{F}$ is constructed by using the assembling procedure described in expression (3.40).

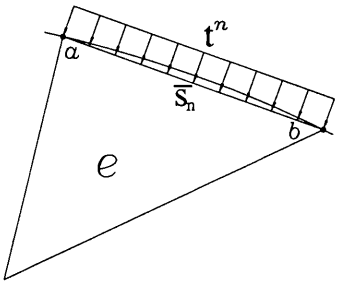

Figure 5.1 Linearized boundary face

Step 3: computes an initial value for the velocity vector, and its form is clearly different from the expression (3.77). Instead of the initial value given before, a typical elastic finite element solution is used to determine an initial velocity vector. The velocity field so obtained resembles the deformation mode of the elastic solution, determined after a scaling operation to maintain the velocity field on the affine hyperplane that meets the condition $\mathbf{F}^T\dot{\mathbf{u}}_{(0)}=1$, where $\mathbf{F}$ is the external equivalent force vector, as above. In fact, the proposed expression (3.77) was used initially with unconvincing results as it produces a longer convergence path to the solution than using an "*elastic*" velocity distribution.

Step 5.1: implies the computation of the internal force vector $\mathbf{T}(\dot{\mathbf{u}}_k)$ and the *multiplier* λ_{k+1}, leading to the residual vector $\mathbf{R}(\dot{\mathbf{u}}_k,\lambda_{k+1})$. The elemental expression $\mathbf{T}^e(\dot{\mathbf{u}}_k)$ can be computed by using $\mathbf{B}$ and $\boldsymbol{\sigma}$ as defined in (3.101). An important aspect in the construction of $\mathbf{T}(\dot{\mathbf{u}}_k)$ and $\mathbf{K}_k^e$ (step 5.3) at the element level is the use of a special parameter defined in section 5.2.2; called the *strain-rate offset* and denoted as $\dot{\bar{\varepsilon}}_{offset}$. This parameter is used to avoid the limit case of an infinite value of $\mathbb{C}_p$ in expression (3.19), that is

$$\mathbb{C}_p=\frac{2}{3}\frac{\sigma_y}{\dot{\bar{\varepsilon}}}\left(\mathbf{I}\otimes\mathbf{I}+\mathbb{I}\right)-\frac{1}{\sigma_y\dot{\bar{\varepsilon}}}\boldsymbol{\sigma}\otimes\boldsymbol{\sigma} \tag{5.1}$$

when the *equivalent strain rate* $\dot{\bar{\varepsilon}}$ approaches zero. This condition directly affects the convergence of the method, thus a solution is proposed which deserves an extended discussion as given in section 5.2.2.

Step 5.2: is the termination condition, in which a *tolerance* is set to provide a relative error bound. Although the terminating condition shown in step 5.2 is the main condition in the context of the Newton-Raphson method, two additional criteria are actually implemented. The second criterion is the relative error over the value of the collapse load multiplier itself

$$\frac{\|\lambda_{k+1} - \lambda_k\|}{\|\lambda_{k+1}\|} < tol \tag{5.2}$$

which is typically met in a lower number of iterations than the condition shown in step 5.2. Note that the condition in step 5.2 is required to actually guarantee compliance with equilibrium conditions over the whole discretized domain. The same value of *tol* is used in the first and second conditions. The third termination criterion only sets a maximum number of iterations as a common safety net addition.

Step 5.3: summarizes the computation of the tangent matrix $\mathbf{K}_k$ after an assembling procedure, which requires the determination of the components of the elemental tangent matrix $\mathbf{K}_k^e$ for the case at hand. These are given in expressions (3.87) and (3.110).

Step 5.4: calls for a typical linear equation system solver, in this case a *sparse symmetric matrix factorisation method* is used. The method is based on the $\boldsymbol{LDL}^T$ decomposition as described in Zienkiewicz and Taylor [2], and implemented in Bonet and Wood [3] with the Cuthill-McKee algorithm to minimize the length of the off-diagonal array. Note also that in this step, a special treatment is given to the solution of the system of equations due to the singularity of the tangent matrix. Refer to section 3.5.6 for more details.

Step 5.5: indicates the application of the line search technique by solving $R(\eta) = 0$. Details of the line search technique in the context of the Newton-Raphson method are discussed in section 3.6. Behavioural aspects of the line search device are treated briefly treated in section 5.2.3

Step 5.6: simply adds the velocity vector *increment* $\eta\Delta\dot{\mathbf{u}}$ to the previously computed vector $\dot{\mathbf{u}}_k$, after determination of scalar factor η by the line search technique.

Step 7: uses the summation expression to compute the kinematic multiplier given by the elemental contributions to the *total plastic dissipation*. Note that notation $\dot{\bar{\varepsilon}}_H^e$

indicates the equivalent strain-rate at the Gauss point for element e, obtained from elemental velocities given by the solution coarse space, that is $\dot{\mathbf{u}}_H^e \in \overline{Y}_H$.

Step 8: indicates the main set of output data drawn out as a result of the execution of the algorithm. A brief description of the software tools used to visualize the output data is given in section 5.5, namely the *pre-post graphical processing software* and the MS Excel 2000.

5.2.2 The Equivalent Strain Rate Offset

Given the nature of the behaviour of a uniaxial ideal stress-strain rate test for rigid-plastic materials, as shown in figure 5.2, a simple but practical solution has been used to avoid the problem of infinite values of the parameter μ when the *equivalent strain-rate* $\dot{\bar{\varepsilon}}$ takes a near-zero value, in the computation of the constitutive components used in step 5.3.

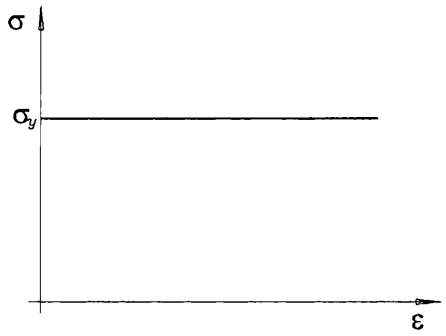

Figure 5.2 Rigid-plastic ideal uniaxial stress-strain curve

A solution was originally proposed in the form of expression:

$$\dot{\bar{\varepsilon}} = \sqrt{\frac{2}{3}\left(\boldsymbol{d} : \boldsymbol{d} + I_d^2\right) + e^2} \tag{5.3}$$

where an offsetting parameter e is introduced to avoid a mere null value for $\dot{\bar{\varepsilon}}$; however, a different approach has eventually been used. A modified value $\dot{\bar{\varepsilon}}_m$ of the equivalent strain rate given by

$$\dot{\bar{\varepsilon}}_m = \dot{\bar{\varepsilon}} + \dot{\bar{\varepsilon}}_{offset} \tag{5.4}$$

is used. This proposal showed a smoother behaviour in the near-zero region, therefore leading to a better transition between positive and negative $\dot{\bar{\varepsilon}}$ values. Of course, the parameter e above or $\dot{\bar{\varepsilon}}_m$ should have a low order of magnitude, when compared to a typical value of $\dot{\bar{\varepsilon}}$. The smooth transition in this region has a regularising effect on the convergence of the solution procedure in terms of the numerical implementation, going from a divergent behaviour to a well-behaved convergent solution depending on a proper selection of the parameter $\dot{\bar{\varepsilon}}_{offset}$. The effect of this simple solution is difficult to visualise in the case of a multi-component velocity vector, but it is made clearer if we consider the curve for the parameter μ (see figure 5.3) for a rigid-plastic uniaxial state of stress, along with the stress-strain rate graph and its related plastic potential curve.

First, let us recall expression (3.15) for the parameter μ for a uniaxial stress state:

$$\mu = \frac{\sigma_y}{3\dot{\bar{\varepsilon}}} = \frac{\sigma_y}{3|\dot{\varepsilon}|} \tag{5.5}$$

and its corresponding *offsetting* form

$$\mu_m = \frac{\sigma_y}{3\dot{\bar{\varepsilon}}_m} = \frac{\sigma_y}{3\left(\dot{\bar{\varepsilon}} + \dot{\bar{\varepsilon}}_{offset}\right)} = \frac{\sigma_y}{3\left(|\dot{\varepsilon}| + \dot{\bar{\varepsilon}}_{offset}\right)} \tag{5.6}$$

denoted μ_m, as the *modified* form of μ.

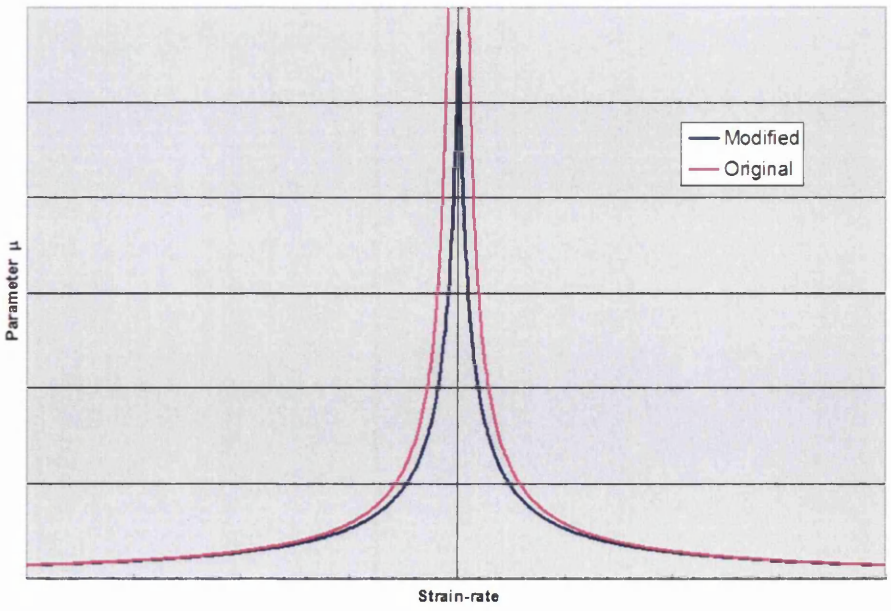

Figure 5.3 Curves for parameters μ (original) and μ_m (modified)

Note that for the uniaxial case we have $\dot{\bar{\varepsilon}} = \sqrt{\dot{\varepsilon}^2} = |\dot{\varepsilon}|$. These relations are plotted in figure 5.3 in which the effect of the offsetting term is evident. While the original expression yields infinite values when the equivalent strain-rate approaches zero, the modified version provides a clearly definite value at the limit, giving way to a convergent path. Note that the curves in figure 5.3 are given as μ versus $\dot{\varepsilon}$ and μ_m versus $\dot{\varepsilon}$ to let the abscissa run along the negative and positive regions ($\dot{\bar{\varepsilon}}$ is non-negative).

The use of the offsetting term implies a modified curve for both the stress and the plastic potential. For the uniaxial case, the *modified* form of the stress is given by

$$\sigma_m = \frac{\sigma_y \dot{\varepsilon}}{|\dot{\varepsilon}| + \dot{\bar{\varepsilon}}_{offset}} \tag{5.7}$$

which is plotted in figure 5.4 in contrast with a constant value of $\pm\sigma_y$ as originally assumed for a rigid-plastic material (see figure 5.2). A clear smoothing of the *jump* region around the zero strain-rate value is observed. It should be noted that the degree of smoothness clearly decreases with a reduction of the offset $\dot{\bar{\varepsilon}}_{offset}$ value, that is, as it tends to zero.

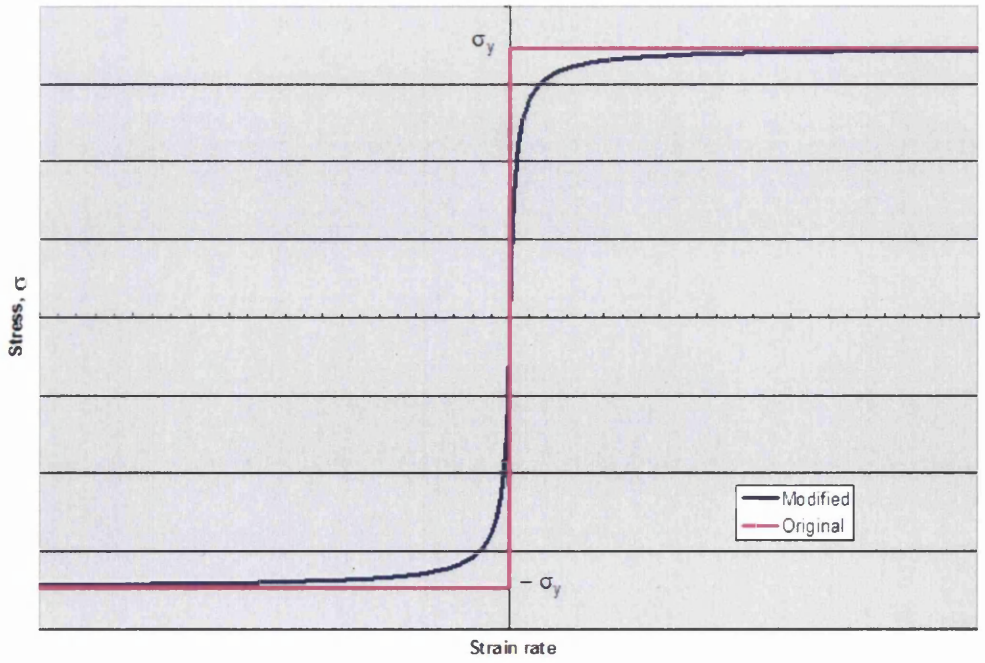

Figure 5.4 Original and smoothed equivalent stress-strain rate curve

The plastic potential shows also a smoothing effect by the use of the parameter $\dot{\bar{\varepsilon}}_{offset}$. As a consequence, the original expression for the plastic potential in equation (3.2) given by

$$D_p = \sigma_y \dot{\bar{\varepsilon}} = \sigma_y |\dot{\varepsilon}| \tag{5.8}$$

now, in terms of the strain-rate, takes the modified form

$$D_{p,m} = \sigma_y (|\dot{\varepsilon}| - \dot{\bar{\varepsilon}}_{offset} \ln(|\dot{\varepsilon}| + \dot{\bar{\varepsilon}}_{offset})) \tag{5.9}$$

These curves are depicted in figure 5.5a). As shown in the figure, an offset value for the potential (the ordinate) is observed, which increases as the value of $\dot{\bar{\varepsilon}}_{offset}$ increases. The sharp corner occurring at the origin of the plastic potential curve in equation (5.8) indicates a high jump in the stress values (from negative to positive, or the inverse) with no apparent change in strain rate. This poses a tremendous burden over the numerical otherwise convergent solution procedure, leading to a sudden convergence or to a divergent behaviour, especially for the Newton-Raphson method which is sensitive to the selection of the initial velocity vector.

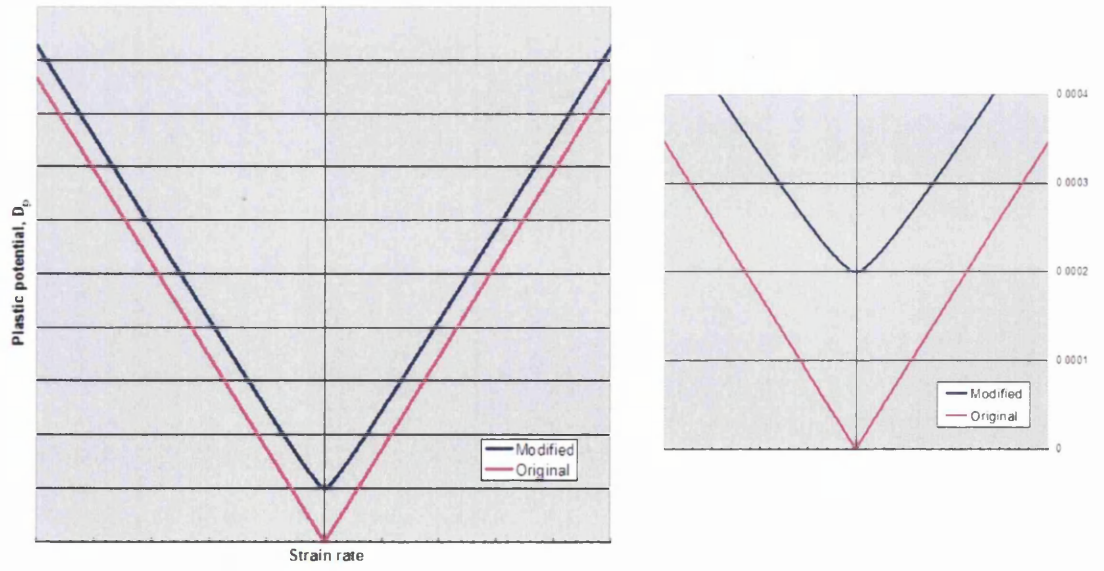

a) b)

Figure 5.5 a) Original and smoothed plastic potential curve; b) Detail near the origin

The smoothing effect of the offsetting parameter is better shown in figure 5.5b) where a detail around the origin shows the contrast between both curves. This evidently implies a better transition for near-zero values and it has shown to play an important role in the convergence of the solution procedure. Note that the scale in this detailed graph is given for the ordinate axis, showing the discrepancy between the original and the modified potential. This discrepancy is typically of a low order of magnitude, close to the magnitude of the offsetting parameter $\dot{\bar{\varepsilon}}_{offset}$.

5.2.3 Convergence of the kinematic solution

We now turn our attention to some of the aspects of the upper bound solution, in particular to the convergence issues regarding the present kinematic solution. If we consider a general refinement process, as proposed herein, a series of refinement steps will yield both upper and lower bounds approaching the true collapsing load multiplier. At each of these steps, due to the non-linear nature of the optimisation process in the computation of the upper bound, a series of Newtonian iterations are carried out to deliver an approximated final *kinematically admissible velocity field.* Convergence comes into the scene, but we now focus our attention on the convergence of the Newton-Raphson method itself (refer to section 3.5.3). In non-linear applications it is customary to use one of many techniques to avoid excessive velocity increments. In this case, the *line search* is the technique of choice, as described in section 3.6. In the Newton procedure implemented here, at the *termination criterion* (step 5.2), two parameters are monitored: a) a relative error computed as the ratio of the Euclidean norm of the residual and the norm of the scaled equivalent load vector; b) a relative error given by the ratio of the difference in the Lagrange multiplier between the current and previous iteration to the current multiplier value. Both this errors have to comply with the prescribed tolerance. These error forms are given as follows

a) Residual error:

$$E_k^R = \frac{\|\mathbf{R}_k\|}{\|\lambda_k \mathbf{F}\|} = \frac{\|\lambda_k \mathbf{F} - \mathbf{T}_k\|}{\|\lambda_k \mathbf{F}\|} \tag{5.10}$$

b) Multiplier error:

$$E_k^{\lambda} = \left| \frac{\lambda_k - \lambda_{k-1}}{\lambda_k} \right| \tag{5.11}$$

Refer to sections 3.5.1 and 3.5.2 where definitions of the terms used in these expressions are given. Note that expression (5.10) ensures that within a prescribed tolerance, the equilibrium is guaranteed. With these in mind, a plot of typical progression curves for each of these errors is given in figure 5.6. This plot corresponds to the solution of a beam with uniform loading and fixed-ends resolved by symmetry conditions.

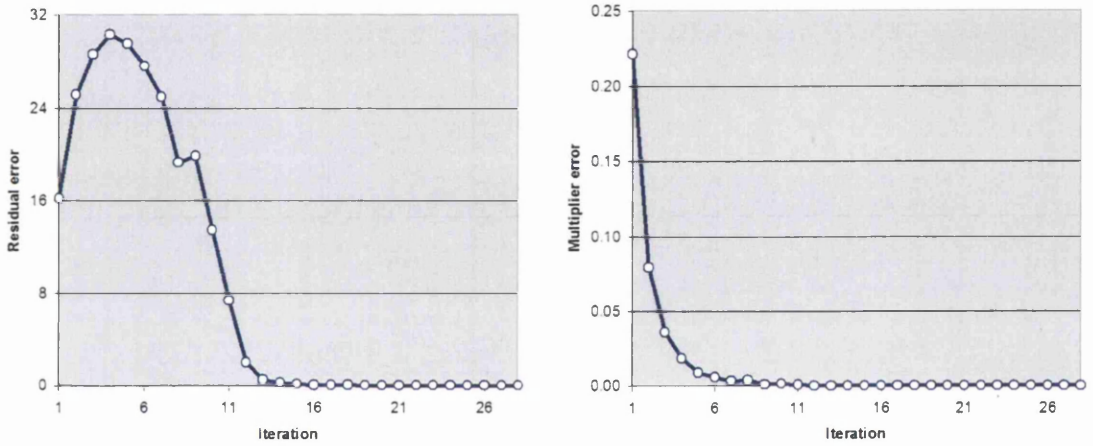

a) b)

Figure 5.6 Iteration versus: a) the residual error E_k^R; b) the multiplier error E_k^{λ}.

An immediate observation can be made, as the multiplier error E^{λ} converges more rapidly and with a slightly erratic but clearly convergent behaviour. On the other hand, in the graph of figure 5.6a) for the residual error E^R, one can identify two phases: the first phase is marked by an initial erratic behaviour in the sense that a sequence of error increments is shown, up to an apex value from which the error starts to fall in a clear but sometimes erratic descent (this erratic behaviour is worse in other cases), until it meets the second phase, in which a neat convergent curve can be observed. The threshold in this case is at iteration 13 in the residual error curve for the present case. Starting at this iteration a monotonic descendent behaviour is observed. In figure 5.6b) for the multiplier error on the other hand, a descendent curve with one

out of line point is observed again for the first 12 iterations, after which a second smooth descendant phase can be seen, although producing lower order values than the residual error. This two-phase behaviour of the Newton-Raphson procedure is observed to coincide with the trace of parameter η in the line search technique, as shown in figure 5.7. Note how the erratic behaviour of η in the first 12 iterations is shared with the previous curves. The effect of the contained step increment over the velocity vector is clearly illustrated, as a value of $\eta < 1$ is shown for the first 12 iterations. From the figure it is clear that the containment of the Newton direction prevents it from falling into a divergent non-recoverable state within the first set of iterations.

The parameter value $\eta = 1$ clearly indicates that a region of smooth convergence has been reached starting at iteration 13, so that a smooth convergent behaviour is observed from this point onwards.

Considering the last 16 monotonically convergent error observations, from iteration 13 to 28, a quadratic convergence rate is expected for this sequence. However, a *linear convergence rate* is observed here following the relation

$$E_{i+1}^R \leq rE_i^R \tag{5.12}$$

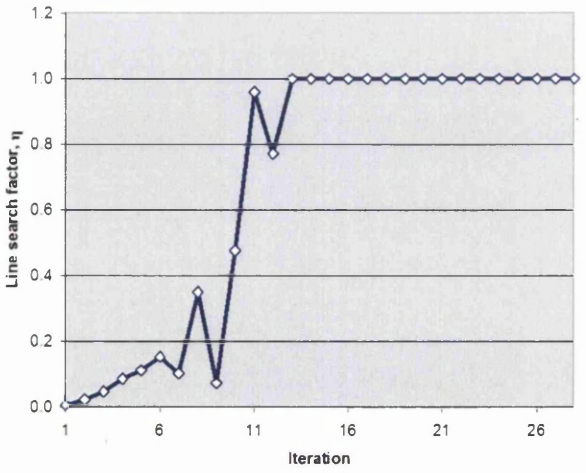

Figure 5.7 Iteration versus η factor in line search.

with $r \approx \frac{1}{2}$, for the case of the residual error E^R, which is of main interest in the present application. Similar conclusions can be drawn for the multiplier error.

Now, independently of the convergence rate, which is normally assessed near the solution, the Newton method is typically sensitive to the selection of the initial guess direction, i.e. this behaviour would be divergent if the line search technique were not in use. So, the question of whether the *elastic displacements field* serves well as an initial guess comes in naturally. We can only set forth that the iterative process herein suggests both a searching sequence in the first phase, and a smooth convergent sequence in the second phase.

With respect to the linear convergence observed in the Newtonian procedure just described, it seems that the effect of the operation used to render the tangent matrix non-singular, results in the delivery of a *linear convergent* procedure, instead of the expected quadratic convergence. Refer to section 3.5.6 for details on this procedure.

As a corollary, the Newton-Raphson method implemented in the present work takes as initial guess an elastic displacement field translated to the affine plane of velocities which produce a unit external work rate, resulting in a vector located outside of a convergence region, over a *multi-dimensional space*. Thus, the process is marked by a searching phase to locate a smooth convergence region in the neighbourhood of the solution, followed by a second phase describing a *linear convergent* sequence.

5.3 Lower bound solution implementation

In this section a description of the lower bound implementation is given, corresponding to the second main component in the present solution. We depart from a general algorithm in the same spirit of the description made in the previous presentation for the upper bound. The most important aspects of the methods used in this implementation are described, by means of an extended discussion, or else referred to related chapters. Details of the test cases are found in Chapter 6.

5.3.1 The lower bound algorithm

We give below a sequence of pseudocode instructions describing the evaluation of a lower bound to the collapse multiplier for a rigid-plastic, plane stress generalized problem. In this algorithm, a more general approach is used due to the nature of the solution, in favour of a more detailed description of relevant aspects in subsequent sections.

Lower Bound algorithm

1. APPLY FLUX EQUILIBRATION – use Ladeveze Constant Flux Equilibration Method
2. FOR EACH ELEMENT e DO
   - 2.1. CONSTRUCT A LOCAL PROBLEM
     - 2.1.1. GENERATE ELEMENT SUB-MESH – use sub-meshing procedure to generate mesh within the isolated element e, creating space denoted by Z_h^e
     - 2.1.2. APPLY SUPPORT CONDITIONS – impose fixing conditions on element boundary S_u^e
     - 2.1.3. APPLY LOCAL PROBLEM LOAD – use equilibrated flux $\tilde{\mathbf{q}}^e$ to build a local loading configuration
   - 2.2. SOLVE LOCAL PROBLEM – use upper bound procedure to compute the collapse multiplier by attaining the local minimum $\hat{\gamma}_h^e \equiv \min_{\dot{u}^e \in \bar{Z}_h^e} \Pi_p^e\left(\dot{u}^e\right) = \Pi_p^e\left(\hat{\dot{v}}_h^e\right)$
   - 2.3. COMPUTE LOCAL EXTERNAL LOAD WORK-RATE – use $\hat{\Pi}_t^e\left(\mathbf{v}_H^e\right) = \left[\tilde{\mathbf{Q}}_{h/H}^e\right]^T \mathbf{v}_{h/H}^e$
   - 2.4. STORE DATA – store $\Pi_p^e\left(\hat{\dot{\mathbf{v}}}_h^e\right)$, store $\hat{\Pi}_t^e\left(\mathbf{v}_H^e\right)$, and store additional element-wise data to be used in the adaptive procedure and in the solution output.
3. END DO

4. COMPUTE LOWER BOUND COLLAPSE MULTIPLIER – use $\hat{\gamma}_h = \sum_e \hat{\Pi}_t^e\left(\boldsymbol{\nu}_H^e\right)\ \Pi_p^e\left(\hat{\boldsymbol{\nu}}_h^e\right)$

5. OUTPUT DATA – deliver the lower bound multiplier $\hat{\gamma}_h$ and related numerical and graphical information

---

A more detailed description of each step is given below, with corresponding references to sections in this chapter or in previous chapters.

Step 1: is a key component of the *lower bound* implementation, as it provides us with a reliable method to attain the stress (flux) field over the element faces complying with *equilibrium* within the localized element volume and *continuity* conditions along the inter-element surfaces. Under such conditions, it is possible to isolate an element to construct the local problem and evaluate the element capacity to withstand a collapse state, that is the estimation of a *local collapse multiplier* as shown in subsequent steps. A detailed description of the flux equilibration method is given in section 4.4. Refer to Ladeveze and Leguillon [4], Ladeveze, Pelle and Rougeot [5] and Coorevits, Ladeveze and Pelle [6] for a complete description and use of flux equilibration methods in *error estimation* applications.

Step 2.1: depicts the creation of a local problem to be treated as an isolated kinematic problem, resolved at the element level. Certainly, the setting of a local problem requires the definition of the procedures to generate geometric, load, support and material properties data. The relevant aspects of these procedures are described in section 5.3.2.

Step 2.2: implies the application of the upper bound (kinematic) solution to the local problem. This procedure is applied to every element in the mesh, as indicated by the element-wise loop in the algorithm. A brief description of the aspects involved in solving the local problem is given in section 5.3.3, and extended theoretical elements are referred to in section 4.2.2.

Step 2.3: computes the work-rate produced by the equilibrated forces when applied over an element (local domain). Refer to sections 4.2.4 and 5.3.4 for definitions and implementation details.

Step 2.4: is intended to indicate the need for the recollection of data at this point to be used on a subsequent stage (at step 4) for the computation of the lower bound to the collapse multiplier.

Step 4: actually computes the value of the *lower bound* as the summation of the element-wise contributions to the collapse multiplier given in *integral form,* as defined in section 4.2.4.

Step 5: explains by itself, but it is important to point out the storage of data at this stage to be used in the adaptive procedures, as described in section 5.4 below.

5.3.2 Construction of the local problem

In this section we briefly describe the process of constructing the local problem as carried out in this implementation. The present description is made to clarify procedural aspects of the encoded solution, its assumptions and specific considerations.

Element sub-meshing

When isolating an element a set of rules has to be followed with respect to the re-meshing strategy to be applied, either through a *telescopic (uniform) meshing* scheme or by an *adaptive meshing* scheme, so we begin by defining some of the terms used herein for this purpose:

- *Mesh configuration:* definition of the mesh geometry - nodes and element definitions.
- *Coarse mesh*: the mesh defined over the whole domain, on which the problem is originally defined.

- *Fine mesh*: the mesh defined over the whole domain, generated as the result of a sequence of refinement stages.
- *Reference mesh*: the finest mesh for a given problem (see definition 4.1 and related comments).
- *Refinement*: the process of going from one mesh configuration to a finer one over the whole domain.
- *Sub-meshing*: the process of refining within an element domain, going from one to m elements within the same volume.
- *i-th level sub-meshing:* uniform sub-meshing by subsequent triangulation connecting mid-face nodes.

The *sub-meshing* process refers to the uniform refinement of an element needed to construct the local problem, keeping in mind that the final mesh for the local problem has to comply with that of the reference mesh. So the every local problem *sub-mesh* should reflect the reference mesh configuration at the element (local) sub-domain.

The sub-meshing used in this implementation is quite straight forward as it is made out of a sequence of telescopic triangulations, that is, an original three sided triangle will be split into four sub-elements using the three mid-point nodes generated in the process, as shown in figure 5.8. The so called *sub-meshing level* will only indicate the number of times this basic splitting step is applied to the original element in a recursive down-chained splitting procedure.

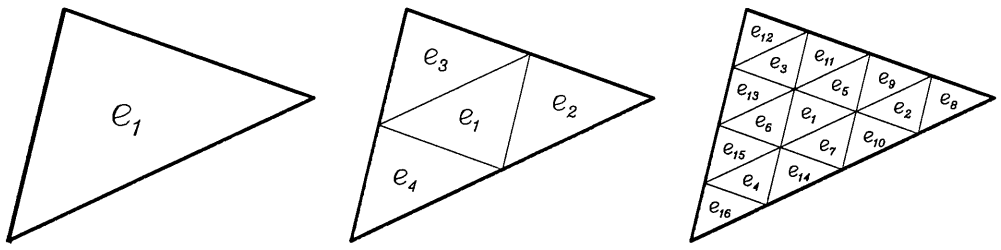

Figure 5.8 Sub-meshing of an element

This sub-meshing procedure is applied every time a local problem is to be solved, and the final sub-mesh corresponds to the new solution space for the local problem, i.e.

Z_h^e as defined in chapter 4. A constant nominal sub-element size is procured to enforce compliance with the reference mesh, i.e. through the relative nominal element size. Note that in order to reach the reference mesh, several levels of refinement may be needed. Element conformity, that is, the resolution of transition elements and hanging nodes is attained through a series of steps as described in section 5.4.6.

Support conditions for the local problem

Once we have the solution space for the local problem, as described in the previous section, a set of support conditions can be defined, so the question arises as to what fixing conditions are needed to solve the new problem. The answer is fairly simple, considering that the element has been isolated and that necessary equilibrium conditions have been met before hand. Two simple conditions are to be found: a) for an internal element: none of its faces is part of a boundary edge; b) for an external element: one or two of its faces are part of a boundary edge. The first case requires the application of the minimal support conditions to render the problem stable. Figure 5.9 shows the typical application of support conditions for both unstable and stable configurations. Note that in either case, the boundary conditions applied to attain rigid-body stability, i.e. the support conditions, do not produce reactions due to the equilibrated condition of the local load configuration, that is, the external loads to which the local body is subject to are in equilibrium in the local problem setting.

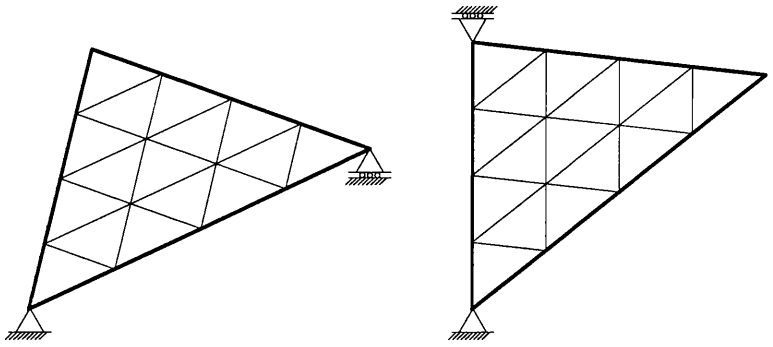

a) Stable b) Unstable

Figure 5.9 A typical support condition for an internal element

The second case requires the direct application of the original boundary conditions over the corresponding boundary edges in the element. This application should

typically be enough to render the problem stable, otherwise an additional condition has to be applied. In figure 5.10a) an external element has been locally restricted in the x direction but released in the y direction along a boundary face, producing an unstable condition. On the other hand in figure 5.10b) an additional fixing condition has been applied to render the problem stable. This description gives a general idea of the support condition checking encoded in this implementation.

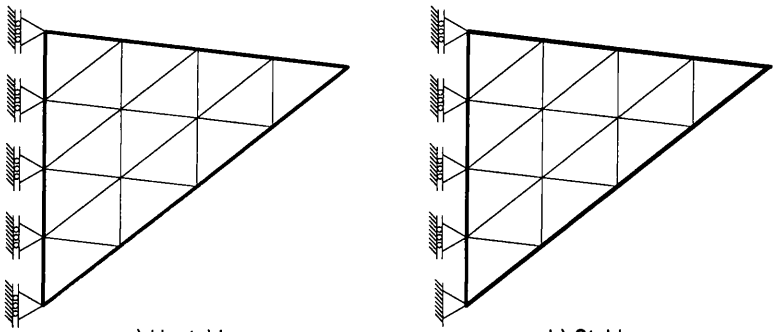

Figure 5.10 Support conditions for boundary elements

Note that undefined local boundary conditions can always be resolved by applying the simplest support conditions for an internal element (as in figure 5.9a). Note that again, no reactions are generated in any case.

Local problem load configuration

As a result of the application of the *flux equilibration procedure* a new stress distribution along the inter-element surfaces is at hand, as described in section 4.4. Two properties of the equilibrated distributions have to be recalled here:

a) The equilibrated stress distribution complies with *equilibrium* conditions within the isolated element domain upon its application over the element faces.
b) The face equilibrated stress distributions comply with *continuity* conditions along the inter-element face, that is, a stress distribution acting along an element face produces the same distribution along the opposite face on the adjacent element, of the same magnitude but opposite direction.

These conditions are depicted in figure 5.11 which show how the equilibrated *linear* stress distributions also provide point-wise stress continuity along the element faces. Under these conditions, the *loading configuration* for the local problem is given by directly applying these load distributions to the corresponding sub-mesh configuration. Figure 5.12 below, shows the typical local problem to be solved.

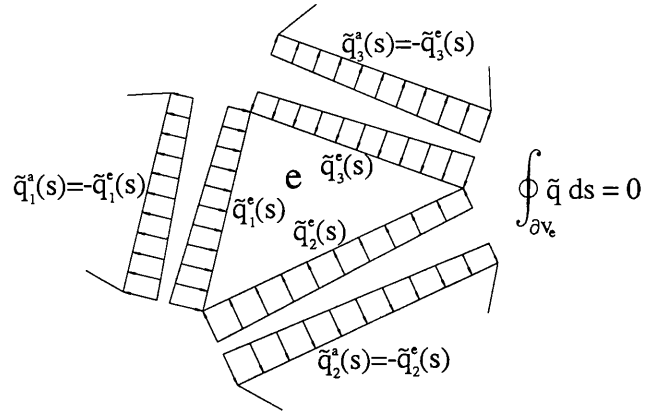

Figure 5.11 Equilibrium and stress continuity along the element boundary

It is important to note that this implementation uses only the stress distributions obtained from flux equilibration to set up the loading configurations over the isolated element, and no distinction is made between internal or boundary (external) elements. That is, no external or reactive stress distributions are used for the loading configuration, instead only equilibrated stress distributions are used. This last assumption is based on the fact that equilibrium conditions are met by the equilibrated stress distributions at the node level in the same way that these are met by the original finite element discontinuous stress distribution.

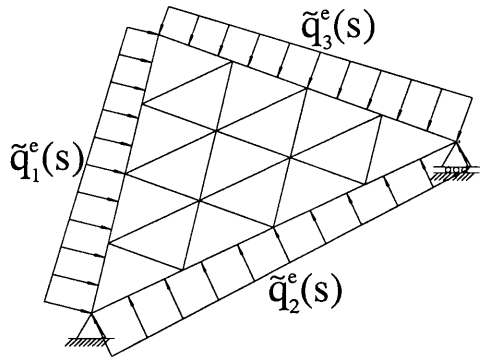

Figure 5.12 Graphical description of the local problem

5.3.3 Solution of the local problem

Once the local problem has been composed, as described in the previous sections and summarized in figure 5.12, the solution is found by applying the upper bound solution procedure to the new problem. In effect, a *lower bound* solution is constructed as a result of finding *upper bound* solutions of every isolated element in the domain, in accordance with the present proposal (see expression (4.29)). At this step of the process, the problem is solved by the well know kinematic theorem, which establishes the following conditions

$$\begin{aligned} &\dot{\boldsymbol{\epsilon}}^e = (\nabla \dot{\boldsymbol{u}}_h^e)_{sym} \quad \text{in } V_e \\ &\dot{\boldsymbol{u}}_h^e = 0 \qquad\qquad \text{on } S_u^e \\ &\int_{S_t^e} \tilde{\boldsymbol{q}} \cdot \dot{\boldsymbol{u}}_h^e dS > 0 \end{aligned} \tag{5.13}$$

applied over the new local problem, to find a kinematically admissible velocity field. The process leading to the solution described in proposition 4.2, involves the solution of a series of local (elemental) problems to assess the collapse multiplier, or *local minimum*

$$\hat{\gamma}_h^e \equiv \min_{\dot{\mathbf{u}}_h^e \in \overline{Z}_h^e} \Pi_p^e \left(\dot{\boldsymbol{u}}_h^e \right) = \Pi_p^e \left(\hat{\dot{\boldsymbol{v}}}_h^e \right) \tag{5.14}$$

as defined in equation 4.18. These local values provide a key component in the evaluation of the lower (bound) multiplier, along with the local external load work-rate, as described in the next section.

5.3.4 Computation of the lower bound

After a series of extensive tests it was clear that the lower bound found using the minimizer approach in proposition 4.1 failed to depict a bound sequence close to the actual *static* carrying capacity of the structure at collapse. Therefore, we turn our attention to the solution method to compute the lower bound implemented in this work, as defined by the expression

$$\hat{\gamma}_h = \sum_e \hat{\Pi}_t^e\left(\boldsymbol{v}_H^e\right)\, \Pi_p^e\left(\hat{\boldsymbol{v}}_h^e\right) \tag{5.15}$$

corresponding to the approach set forth in proposition 4.2. As shown by the test results, this procedure provides a compact and elegant solution and yields satisfactory results when compared to data obtained by methods proposed previously by various other authors, without the high demand of resources that is typical when solving this limit state problem, for instance by the use of large-scale optimisation tools. The solution in (5.15) implies the key factor $\Pi_p^e\left(\hat{\boldsymbol{v}}_h^e\right)$ representing a local collapse multiplier, as described in the previous section.

Another important parameter in this step is the *local external load work-rate,* as given by:

$$\hat{\Pi}_t^e\left(\boldsymbol{v}_H^e\right) = \int_{S_t^e} \tilde{\boldsymbol{q}}^e \cdot \boldsymbol{v}_H^e \, ds = \left[\tilde{\mathbf{Q}}_{h/H}^e\right]^T \mathbf{v}_{h/H}^e \tag{5.16}$$

where $\mathbf{v}_{h/H}^e$ is computed by interpolation from the velocities at each node of the three-noded macro-element defining the local volume, which complies with

$$\hat{\Pi}_t\left(\boldsymbol{v}_h\right) = \sum_e \hat{\Pi}_t^e\left(\boldsymbol{v}_H^e\right) = \sum_e \left[\tilde{\mathbf{Q}}_{h/H}^e\right]^T \mathbf{v}_{h/H}^e = 1 \tag{5.17}$$

This last expression is readily explained if we consider the global condition $\Pi_t\left(\dot{\boldsymbol{u}}\right) = \mathbf{F}^T\dot{\mathbf{u}} = 1$ and the local equilibrium, so that the local work-rate contribution to unity by the isolated local region (element e) $\hat{\Pi}_t^e\left(\boldsymbol{v}_H^e\right)$ must also comply with condition (5.17).

The linear interpolation at node b is carried out using the expression

$$\mathbf{v}_{h/H}^{e,b}\left(\mathbf{x}_b\right) = \sum_{a=1}^{3} \mathbf{v}_H^{e,a} N_a\left(\mathbf{x}_b\right) \tag{5.18}$$

where $\mathbf{v}_{h/H}^{e,b}(\mathbf{x}_b)$ is the velocity vector (two component vector, for x and y Cartesian directions) for the node b located at point $\mathbf{x}_b$ within element e, i.e. defined in the local fine space Z_h^e as stated in section 4.2.4. Note that node a belongs to space Y_H, but in expression (5.18) it is restricted to nodes within element e, as $\mathbf{v}_H^{e,a}$.

If we expand the nodal vector $\mathbf{v}_{h/H}^{e,b}(\mathbf{x}_b)$ by its components, for each node in space Z_h^e, we arrive at vector

$$\mathbf{v}_{h/H}^e = \left[(v_x)_{h/H}^{e,1}, (v_y)_{h/H}^{e,1}, (v_x)_{h/H}^{e,2}, (v_y)_{h/H}^{e,2}, \cdots, (v_x)_{h/H}^{e,N_h}, (v_y)_{h/H}^{e,N_h} \right]^T \tag{5.19}$$

where N_h denotes the number of nodes in space Z_h^e.

Now, vector $\tilde{\mathbf{Q}}_{h/H}^e$ is determined from the nodal equivalent force components computed from equilibrated tractions, as $\tilde{\mathbf{Q}}_{h/H}^{e,b} = \int_{S_e} \tilde{\mathbf{q}}^e N_a(\mathbf{x}_b)\, dS$, so that we have

$$\tilde{\mathbf{Q}}_{h/H}^e = \left[(\tilde{Q}_x)_{h/H}^{e,1}, (\tilde{Q}_y)_{h/H}^{e,1}, (\tilde{Q}_x)_{h/H}^{e,2}, (\tilde{Q}_y)_{h/H}^{e,2}, \cdots, (\tilde{Q}_x)_{h/H}^{e,N_h}, (\tilde{Q}_y)_{h/H}^{e,N_h} \right]^T \tag{5.20}$$

Clearly, expression (5.17) shows the nature of the external load work-rate $\hat{\Pi}_t^e(\boldsymbol{v}_H^e)$ as a normalized elemental indicator of the plastic dissipation distribution over the whole domain.

Figure 5.13 shows the local external load distribution $\tilde{\mathbf{q}}^e$ and the nodal velocities $\mathbf{v}_{h/H}^e$ used in the computation of $\hat{\Pi}_t^e(\boldsymbol{v}_H^e)$.

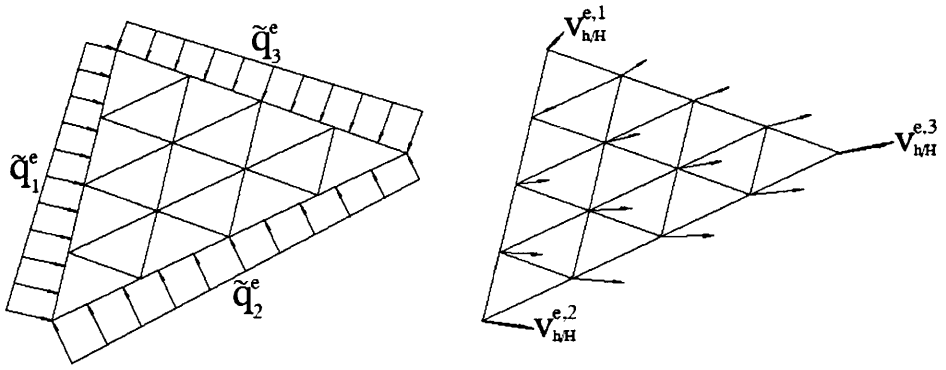

Figure 5.13 Elements used to compute the *local external load work*

Finally, the product $\hat{\Pi}_t^e\left(\boldsymbol{v}_H^e\right)\Pi_p^e\left(\hat{\hat{\boldsymbol{v}}}_h^e\right)$ gives the elemental contribution to the multiplier approaching from below (lower bound) as established in proposition 4.2. These elemental products are stored at this stage for posterior use in the element-wise loop to compute the lower bound in *Step 4* of the algorithm in section 5.3.1. This information is also used to compute the element gap in the adaptive refinement procedure. Additional data are stored in this step for graphical purposes.

5.4 Adaptive refinement procedure

Before the presentation of the main component (main program) of the coded solution, that is, the adaptive refinement algorithm, an introductory review of adaptivity and refinement issues is given in the following sections. The algorithm and related implementation details are described thereafter.

5.4.1 Relevant adaptivity aspects

In this section, a brief description of certain aspects of the general concept of *adaptive refinement* relevant to the present research work is given. This discussion aims to provide the necessary insight into the elements of adaptivity, which have been used to construct a solution to the *limit state analysis* problem, as proposed herein.

From the many approaches on adaptive mesh methods in the literature, all of them base the *mesh adaptation* on a series of indicators, which Haeglan & Skaflestad [7] classify in three types:

1. *r*-refinement methods: keep the total number of nodes constant and adjusts their positions in order to get the best possible approximation.
2. *h*-refinement methods: a first variant is to keep an initial mesh as basis and either refine or coarsen the individual elements as needed, but the initial mesh is always kept as the basis. This approach can be called *element subdivision.* The second approach is to completely *regenerate* the mesh in which new element sizes are predicted for the whole domain and a totally new mesh is created upon this information.
3. *p*-refinement methods: keep the element size but instead increase the order of the polynomial used to represent the solution within each element.

Combination of this types of refinement methods are possible to create specialised methods, for instance, an efficient *hp*-method can use *h*-refinement to achieve a final mesh and then use *p*-refinement. The present research work uses the first variant of the *h*-refinement method, as described above, i.e. by element subdivision, as can clearly be seen in section 5.3.2.

5.4.2 *h*-adaptive methods and the elemental bound gap

h-refinement methods alter the mesh iteratively either by regenerating or refining the mesh at each step until the user specifications are met. The most usual way to accomplish this is to procure an error estimate or some indicator of interest to be equally distributed among the elements. The *elemental bound gap* as defined in section 4.3 can be used as an adaptive indicator, as it shows similar aggregate characteristics as those of the typical error estimator. The total bound gap can be decomposed into elemental gap contributions so that by evenly distributing the elemental bound gap across the domain, a more efficient solution is attained for each subsequent adaptive stage.

5.4.3 Mesh refinement technique

Several grid procedures for mesh regeneration have been developed. In what follows, emphasis is made on the method used in the present implementation. Instead of

regenerating the mesh, the coarse mesh can be retained and refined by subdividing its elements. Generally this will result in a greater number of degrees of freedom compared to a complete regeneration. However, the simplicity of the approach matches well the present requirements for a mesh refinement procedure. So, if the objective is to distribute the estimated error (i.e. the elemental *bound gap*) evenly among the elements, the strategy to be used here reads:

Among all the elements, let us select the one with the greatest bound gap g_e and denote it $g_{\max} = \max_e g_e$. A direct technique is to refine those elements where $g_e \geq \kappa g_{\max}$ for some $0 < \kappa < 1$ chosen by the user.

When using a reasonable mesh generator it will make sure that the elements are regular in shape and well suited for finite element computation. It is important to maintain this shape regularity during the refinement process. A common strategy for the two-dimensional case is to refine an element by joining the midpoints of the edges. See figure 5.8b. From the computational point of view it is cheaper to refine only in the areas most needed, so a final mesh is refined only locally. Subdividing an element produces *hanging nodes* on its edges, which introduces an additional problem. If we intend to retain regularity across the mesh we are forced to introduce additional rules for subdividing the neighbour elements as well. Refer to the technique to refine triangular regions suitable for adaptive techniques in 2D presented by Cecilia Rivara [8] for an alternative refinement procedure. In the present research work, a simpler set of rules is defined in order to manage the hanging nodes, to convert non-conforming elements into regions of regular refined triangular elements, as much as this is possible. The so-called *transition elements* are produced in the process of element sub-meshing. The set of rules defining the adaptive procedure are given in section 5.4.6 below.

5.4.4 Adaptive refinement algorithm

In this section we review the implementation of the adaptive procedure used in the present proposal.

Adaptive refinement block algorithm (main routine)

1. INPUT *refinement_mode* – select from *adaptive/uniform*
2. INPUT PROBLEM PARAMETERS – geometry, material properties, boundary conditions and solution control parameters
3. FOR *stage_1* TO *stage_k* DO
   3.1. APPLY SUPPORT CONDITIONS to *current_mesh*
   3.2. APPLY LOAD CONFIGURATION to *current_mesh*
   3.3. SET STAGE PARAMETERS – update relevant parameters
   3.4. PERFORM Upper Bound Block – compute $\gamma_H = \Pi_p(\boldsymbol{v}_H) = \sum_e \Pi_p^e(\boldsymbol{v}_H^e)$
   3.5. PERFORM Lower Bound Block – compute $\hat{\gamma}_h = \sum_e \hat{\Pi}_t^e(\boldsymbol{v}_H^e)\ \Pi_p^e(\hat{\boldsymbol{v}}_h^e)$
   3.6. OUTPUT RELEVANT DATA – print γ_H, $\hat{\gamma}_h$ and related text and graphic data
   3.7. IF (*refinement_mode* = *adaptive*) THEN
      3.7.1. COMPUTE *adaptivity indicator* – use elemental bound gap expression
      $g_e = \Pi_p^e(\boldsymbol{v}_H^e) - \hat{\Pi}_t^e(\boldsymbol{v}_H^e)\ \Pi_p^e(\hat{\boldsymbol{v}}_h^e)$ where $g = \sum_e g_e = \gamma_H - \hat{\gamma}_h$
      3.7.2. APPLY *adaptive refinement* – use refinement procedure based on indicator g_e to generate a refined space
   3.8. ELSE
      3.8.1. APPLY *uniform refinement* – use telescopic refinement procedure to generate a refined space
   3.9. ENDIF
   3.10. MAKE *refinement_space* THE *current_mesh*
4. END DO

Relevant comments follow, and details are referred to sections in this or other chapters.

Step 1 and 2: are self-descriptive. It corresponds to the input data block on the main program.

Steps 3.1, 3.2 and 3.3: also explain by themselves, although it is important at this point to recall that these steps are actually implemented through the use of a *pre/post-processor* software, using the *pre-processing* feature, which can be programmed as a

front end to host a typical Finite Element application, similar to the programming code developed along with this research work. The software used in this case is *GiD The personal pre and postprocessor Version 7.1*, developed and supported by CIMNE (International Center for Numerical Methods in Engineering), Barcelona, Spain. A brief description of the software tools used is given in section 5.5.

Step 3.4: constitutes a major processing block to compute the *upper bound* to the collapse multiplier described in section 5.2.1, refer to this section for details.

Step 3.5: refers to a major processing block to compute the *lower bound* to the collapse multiplier described in section 5.3.1, refer to this section for details.

Step 3.6: indicates data delivery, in this case the most important *data pair* $(\gamma_H, \hat{\gamma}_h)$, along with related relevant information, in the form of text values (ASCII file), some of which are used to produce graphical representations of the results. These are presented in the tests and results presented in Chapter 6. It is useful to recall that some of the graphical data output at this stage is processed through the *post-processing* feature of the GiD package, and at the same time some of this information is processed and presented in graphical form through Microsoft Office Excel 2000.

Step 3.7.1: implies an important step in the adaptive scheme, where an *adaptivity indicator* is required to control the refinement process. Refer to section 5.4.5 for details on the adaptivity indicator.

Step 3.7.2: applies the adaptive refinement procedure, implemented in this programming package to produce a stage-wise finer mesh using an *adaptive indicator controlled* refinement strategy. The rules applied in this process are discussed in section 5.4.6.

Step 3.8.1: refers to the option of applying a uniform refinement strategy at every stage of the solution process; some behavioural descriptions are based on this refinement mode for comparison, which will be discussed briefly in Chapter 6. A brief description of this refinement option is given in section 5.4.6.

5.4.5 The adaptivity indicator

In the application of an adaptive refinement scheme a control index and a re-meshing criteria have to be set up to define the final refinement configuration. In section 4.3 a control index called the *adaptivity indicator* is defined as

$$g_e = \Pi_p^e\left(\boldsymbol{v}_H^e\right) - \hat{\Pi}_t^e\left(\boldsymbol{v}_H^e\right)\,\Pi_p^e\left(\hat{\boldsymbol{v}}_h^e\right) \tag{5.21}$$

The important point to make at this stage is that the elemental contribution to the bound gap, g_e, is naturally the parameter to be used as an indicator of the error bound distribution over the solution domain, and can be used as the *adaptivity indicator*, as described in Chapter 4. On an elemental basis, it reflects the difference in energy dissipation produced by the application of a *kinematic* approach and a *static* one, understood as proposed in the present context, i.e. the difference between an upper (bound) multiplier and a lower (bound) multiplier. This adaptivity indicator is used thereafter in the refining procedure. Refer to section 4.3 for details on the bound gap and related comments.

5.4.6 Refining strategies: *adaptive/uniform*

Adaptive refinement

The adaptive refinement technique is best described by defining a set of rules to be applied on an element-by-element basis, starting with the general refinement criteria and ending with the refinement of *non-conforming* elements. A series of *passes* over the whole set of elements τ_H has to be considered on applying these rules. These rules are limited to *triangular linear* finite elements, and no mixed elements definitions are considered, as no other type of elements is used in this implementation. In addition to the definitions in section 5.3.2, some additional definitions are required:

- *Transition element*: an element that does not meet sub-meshing criteria and shares one or more faces with a sub-meshed element. See figure 5.14a).

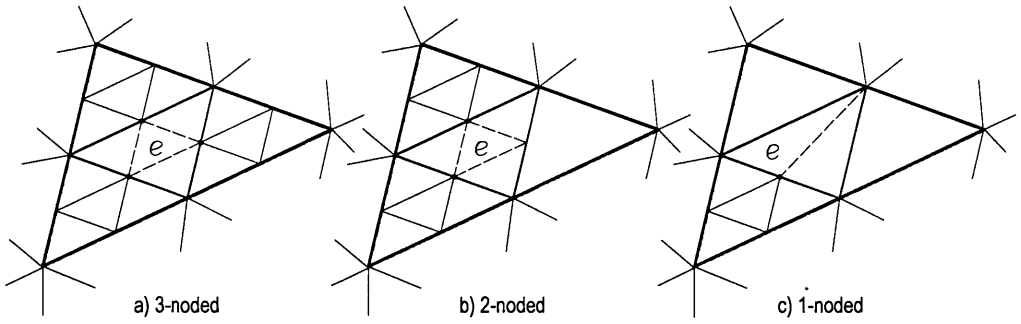

Figure 5.14 Transition elements

- *Non-conforming element:* a transition element sharing one or two faces with sub-meshed elements. See figures 5.14b) and 5.14c).
- *Bisected element:* an element sub-meshed into two new element definitions. See figure 5.14c).

With these definitions in mind, the set of refining rules is as follows:

a) An element e meeting $g_e \geq \kappa g_{\max}$ where $g_{\max} = \max_e(g_e)$ and $0 < \kappa \leq 1$, is applied *first level sub-meshing*, generating 3 mid-face nodes and 4 new element definitions.
b) A transition element having 3 mid-face nodes is applied *first level sub-meshing*, generating 4 new element definitions.
c) A non-conforming element having 2 mid-face nodes is applied *first level sub-meshing*, generating a third mid-face node and 4 new element definitions.
d) A non-conforming element having 1 mid-face node is *bisected*, generating 2 new element definitions.
e) An element (son) created by bisection, which at any time requires a subsequent bisection triggers a *first level sub-meshing* of the original bisected element (father). See figure 5.15.

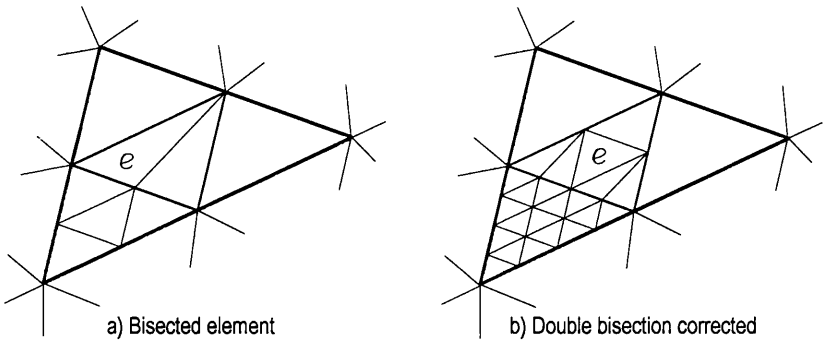

Figure 5.15 Double bisection correction

The repeated application of the previous rules over a sequence of passes constitutes the *refinement* process, and takes one mesh configuration (starting from the coarse mesh) to a *first level refined* configuration (either adaptive or uniform, recall that $\kappa = 0$ leads to uniform refinement) in a single stage after a certain number of passes, so that the *finest refined mesh* (user definable by the number of refinement stages) is attained after completion of the last stage in the refining algorithm (section 5.4.4). Refer to the tests and results in Chapter 6 for a graphical depiction of the adaptive refinement process.

Uniform refinement

From the previous section the uniform refinement procedure is clearly described by a simple modification to the first rule:

- An element is applied *first level sub-meshing*, generating 3 mid-face nodes and 4 new element definitions.

The application of this rule on every element produces a natural telescopic refinement at each stage. The generation of three nodes in each application only produces temporary transition elements, none of which being non-conforming. Refer to the tests and results in Chapter 6 where comparative results for uniform versus adaptive refinement are given for one test case.

5.5 Development software tools

The software employed and produced along the solution development includes the following resources:

i). The program LSA-ULB (Limit State Analysis – Upper Lower Bound), a Fortran 90 code corresponding to the core of the solution implementation from the numerical processing perspective. This software incorporates an adapted Fortran subroutine for the computation of *equilibrated fluxes* kindly made available by Professor Jaume Peraire, from the MIT, Boston, Massachussets. It also employs some numerical subroutines from the IMSL Mathematical Library Subroutines. The rest of the programming modules have been developed by Professor Javier Bonet and Raymundo Cordero.

ii). Compaq Visual Fortran, Edition 6.6, a Fortran 90/95 language compiler.

iii). GiD Version 7.1, by CIMNE, International Center for Numerical Methods in Engineering, Barcelona, Spain. This component corresponds to the *pre-post processing* software used throughout the development with excellent performance. The processor provides the tools to construct a *problem type* within the interface to cater for tailored applications, as required by the engineer or researcher. The software *hosts* the application program (in this case the LSA-ULB program) to provide a front-end in order for the user to define a finite element *problem* of the specified type, and also provides the back-end to graphically represent the resulting output after the processing of the problem.

iv). Microsoft Excel 2000, has been used to produce a series of graphical results out of the tests cases studied in the present work. Production tools for typical scattered plane graphics are the main resources provided by this software.

These resources have been used to run the test cases and applications on an Intel Pentium 4 PC with speed of 2.8 Ghz and 1.0Gb of RAM, running under Windows XP Professional Edition.

From all the software components used in the development of the present solution package, perhaps the one deserving an extended description is the *problem type* constructed within the pre/post-processor GiD 7.1. Following is a sequence of computer user-interface steps taken on the standard GiD 7.1 software to construct and solve a given limit analysis problem by the method proposed here.

In figure 5.16, the main window of the pre-processing session is shown. The step given here corresponds to the definition of the boundary conditions, i.e. support and load conditions.

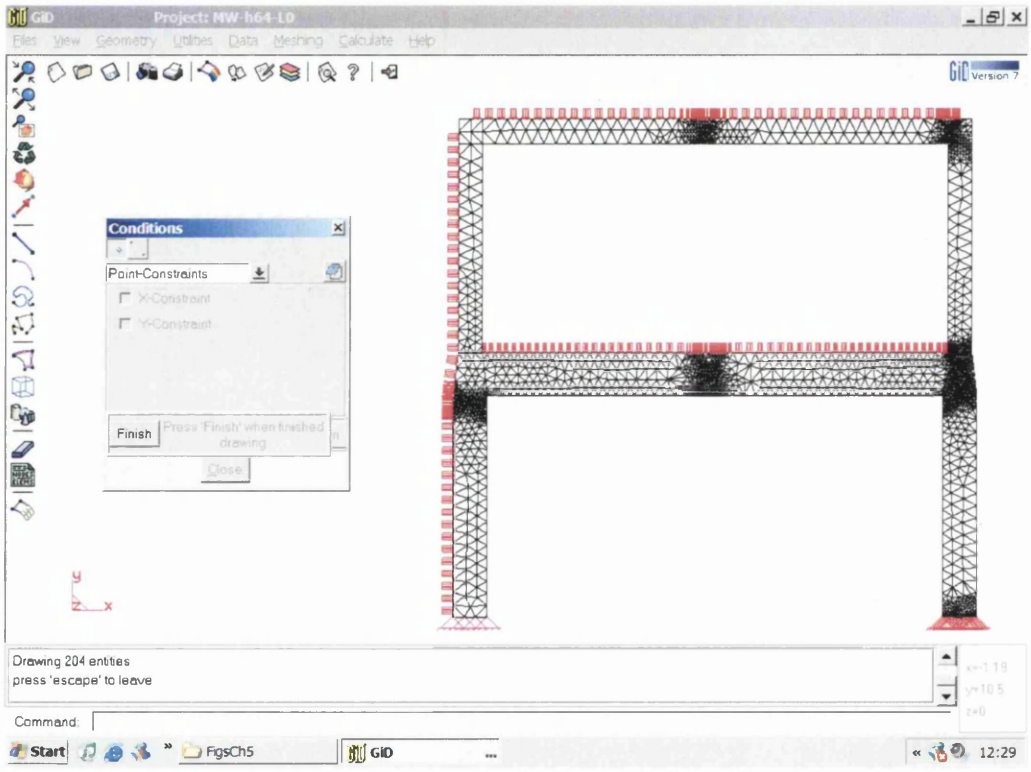

Figure 5.16 Pre-processor user interface: defining boundary conditions.

When the geometry and mesh of a given problem are defined, as shown in the figure above, the boundary conditions are given through the input windows shown in figure 5.17.

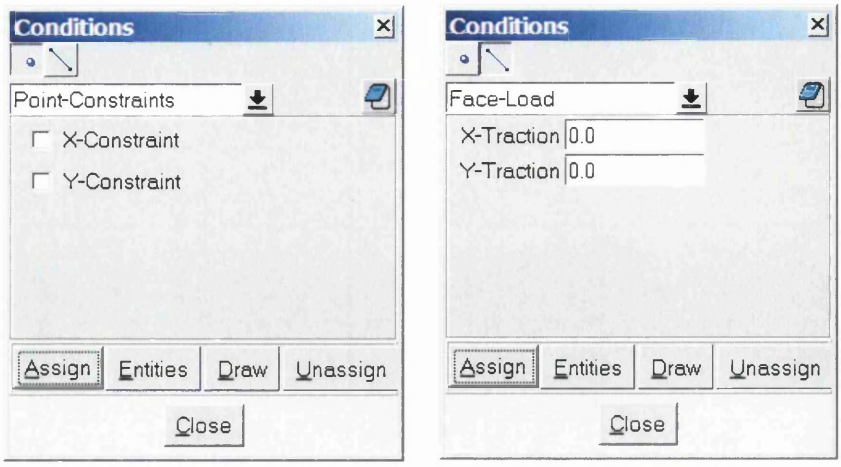

a) b)

Figure 5.17 Boundary conditions input: a) point constraints; b) face load.

Once the geometrical and boundary conditions data are given, a series of material properties are assigned to the elements. This is done in the input form in figure 5.18.

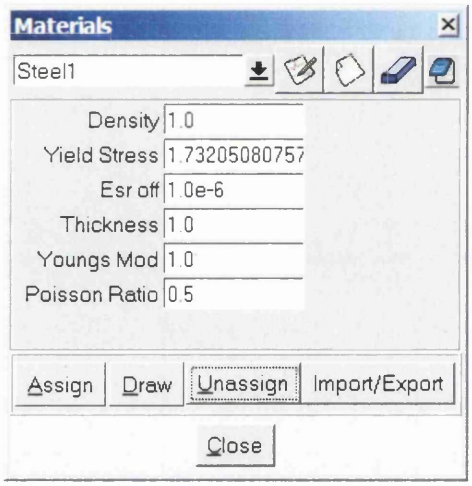

Figure 5.18 Material properties input window.

The following properties are given:

a) Density: the material density parameter typically denoted ρ. Note: not used in the present implementation.

b) Yield Stress: the limit uniaxial stress value σ_y.

c) Esr off: the equivalent strain-rate offset $\dot{\bar{\varepsilon}}_{offset}$.

d) Thickness: off-plane thickness of the body, often denoted as b.

e) Youngs Mod: Young's modulus, typically denoted E.

f) Poisson Ratio: Poisson's modulus, typically denoted ν.

Note that the density in not used in the present implementation, as body forces are neglected. On the other hand, Young's and Poisson's modulus are used in computing an initial velocity field, from an elastic analysis. Finally, the problem parameters are shown in figure 5.19

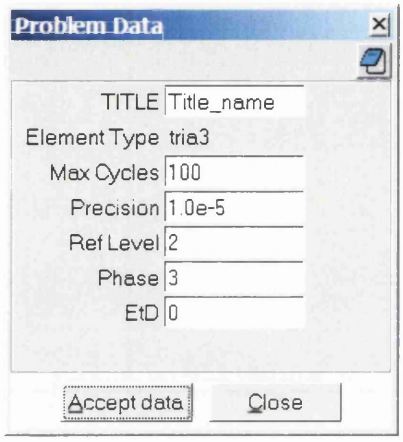

Figure 5.19 Problem parameters input window.

In this input form the following parameters are given:

a) TITLE: a given name to the problem case.

b) Element Type: the element type, in this case for tria3 only, i.e. a 3-noded triangle.

c) Max Cycles: a safety-net provision to limit the of iterations in the Newtonian procedure.

d) Precision: the accuracy required for the results. This corresponds to the variable *tol* (tolerance) in the upper bound algorithm (section 5.2.1).

e) Ref Level: the level of sub-meshing to be carried out over the local volume. This is overridden in the adaptive procedure by internal data, but is useful when uniform refinement is sought.

f) Phase: the number of phases the solution is to cover:

i. Phase 1: perform *upper bound sequence.*

ii. Phase 2: perform i. and the *lower bound sequence.*

iii. Phase 3: perform ii. and apply *adaptive refinement.*

g) EtD: the element to display. This permits to post-process only the results (failure mode, stresses, etc.) of a specific element (local volume).

The post-processing user interface is shown in figure 5.20, depicting the original and deformed mesh of the frame problem.

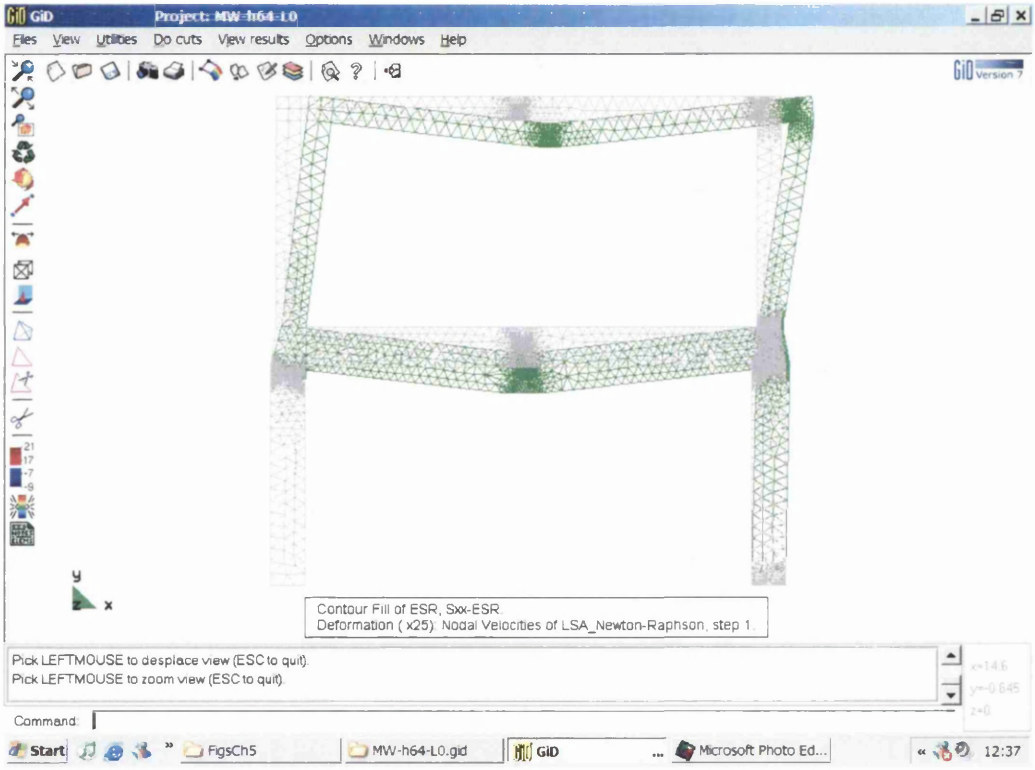

Figure 5.20 Post-processor user interface: displaying the collapse mechanism.

Many other results can be visualized at the post-processing session. Some of these are presented in chapter 6, where results for test cases and applications are given.

5.6 References

1. Christiansen, E. *Computation of limit loads*. International Journal for Numerical Methods in Engineering. Vol. 17, 1981, p.1547-1570.
2. Zienkiewicz O.C., Taylor R.L. *The Finite Element Method*, 4th Ed., Vol.1. McGraw-Hill, 1989.
3. Bonet J., Wood D.R. *Nonlinear continuum mechanics for finite element analysis*. Cambridge University Press, 1997.
4. Ladeveze P., Leguillon D. *Error estimate procedure in the finite element method and applications*. SIAM Journal on Numerical Analysis. Vol. 20, Issue 3, 1983, p.485-509.
5. Ladeveze P., Pelle J.-P., Rougeot Ph. *Error estimation and mesh optimisation for classical finite elements*. Engineering Computations, Vol. 8, 1991, p.69-80.
6. Coorevits P., Ladeveze P., Pelle J.-P. *An automatic procedure with control of accuracy for finite element analysis in 2D elasticity*. Journal of Computational Methods in Applied Mechanics and Engineering, Vol. 121, 1995, p.91-120.
7. Haegland B., Skaflestad B. *A survey of some methods for moving grid and grid adaptation*. Numerics No.2, Norwegian University of science and Technology, 2002.
8. Rivara M.C. *algorithms for refining triangular grids suitable for adaptive and multigrid techniques*. International Journal for Numerical Methods in Engineering, Vol. 20, 1984, p.745-756.

Chapter 6

Test cases and applications

6.1 Introduction

In the present chapter, a set of numerical examples is presented in three stages intended to describe different steps in the testing phase of the research work. The first stage is presented as a *validation* phase to provide a sense of correctness of the solution proposed. This stage is based on comparative analysis with numerical results obtained previously by different researchers using various approaches. The reference results provide a good comparative framework to the numerical results obtained by the present solution procedure. The examples solved at this stage constitute conventional, rather simple problems for which an analytical solution may be available in some cases. Given the diversity of approaches to the solution, we may only get a sense of closeness between the different numerical solutions. In some other cases, however we may be able to locate our solution within a valid interval, for example when a lower and upper bound value are available. A second stage in the testing phase is intended to provide a close comparison with a similar lower/upper bounds adaptive approach recently achieved by a group of researchers using *Second-Order Cone Programming*. Considering that although the solution procedure is essentially different, the bounds and adaptive approach is also essentially similar, so that we are able to compare almost all aspects of the solution presented in this research work. A third stage in the testing phase comes in the form of a series of solutions to practical problems, in this case with emphasis on beam and frame analysis. This is an immediate consequence of the availability of results for beam and

frame cases coming from classical limit analysis methods, in which a load multiplier and a failure mode is obtained for comparison.

It is important within this framework to emphasize the use of the adaptive approach in most of the numerical examples herein, with some references to *uniform refinement* in selected examples.

A Newton-Raphson convergence tolerance $tol = 1 \times 10^{-5}$, and the parameter $\dot{\bar{\varepsilon}}_{offset} = 1 \times 10^{-5}$ are used throughout the test cases reviewed in this chapter.

6.2 General validation test cases

6.2.1 *Square plate with a circular hole*

The case of a square plate with a circular hole is a classical plane stress problem and has been treated through an analytical approach by Gaydon & McCrum [1], in which a lower and upper bound is found for different hole diameter values. This problem has been also addressed by Casciaro & Cascini [4] through a mixed formulation and mixed finite elements, as part of a large list of examples in plane stress and plane strain. More recently, Borges, Zouain & Huespe [3] proposed a nonlinear optimization procedure to solve limit analysis problems, and they also present their results for the square plate in comparison to the results in [1] and [4]. We adhere to this comparative list of numerical results by presenting the adaptive procedure proposed in this research work, plotted against the analytical bounds found by Gaydon & McCrum [1], along with the numerical results by Casciaro & Cascini [4], and by Borges, Zouain & Huespe [3].

Consider the square plate with a circular hole in part *i*) of figure 6.1, which can be reduced to the quarter plate shown in part *ii*) of figure 6.1 due to its double symmetry. The plate has sides of length L and a circular hole of radius $d/2$. Uniform normal stresses are applied along the outside edges in the plane of the plate and the edge of the hole is unstressed.

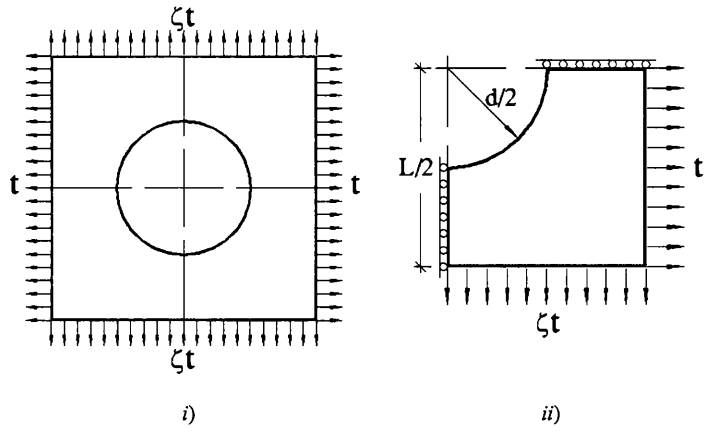

Figure 6.1 Square plate with circular hole

The problem is therefore in plane stress with all stress and strain components assumed constant through the thickness of the plate. The plate is assumed as constrained against out of plane buckling when compressive loads are applied. The material is rigid-plastic under the von Mises yield criterion. In their paper, Gaydon & McCrum [1], evaluate yield-point loads either exactly, or upper and lower bounds are obtained by means of the extremum principles for a rigid-plastic body. They analyse three cases of the constant ζ, the ratio between loads at adjacent sides of the plate, as shown in figure 6.1. In order to keep these comparisons within a reasonable number, an extended review is made for the case with $\zeta = 0$ only. A non-dimensional approach in the numerical values is used to cater for a direct comparison with the reference values.

This example is presented in three parts. *Part I* is intended to show an extended sequence of test results for $d/L = 0.2$ in graphical form. *Part II* presents complementary results for this same test case with a varying d/L relation ($d/L = 0.4, 0.6, 0.8$). Note that these problems use the case for $\zeta = 0$, i.e. only horizontal load is applied (see figure 6.1). All cases consider a unitary thickness in the off-plane direction.

Part I. Consider the square plate with a circular hole for $\zeta = 0$ corresponding to *uniaxial* stress with $L = 2.0$ and ratio $d/L = 0.2$. A unit stress distribution in the

positive x direction is applied as external nominal load, as shown in figure 6.2. It is also worth to observe that in this case of $d/L = 0.2$, the analytical solution $\gamma \mathbf{t}/\sigma_y = 0.8$, obtained by Gaydon and McCrum yields the same value for the upper and lower bound, so that the value computed is considered to be the exact solution. A yield stress of $\sigma_y = \sqrt{3}$ is used throughout the test cases.

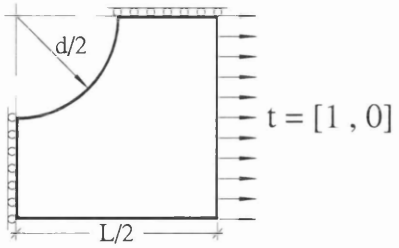

Figure 6.2 Problem setting for Part I and Part II

Uniform refinement

When using uniform refinement, the proposed solution procedure generates a series of refined meshes by element subdivision. These are drawn in figure 6.3a. for the first four refinement steps.

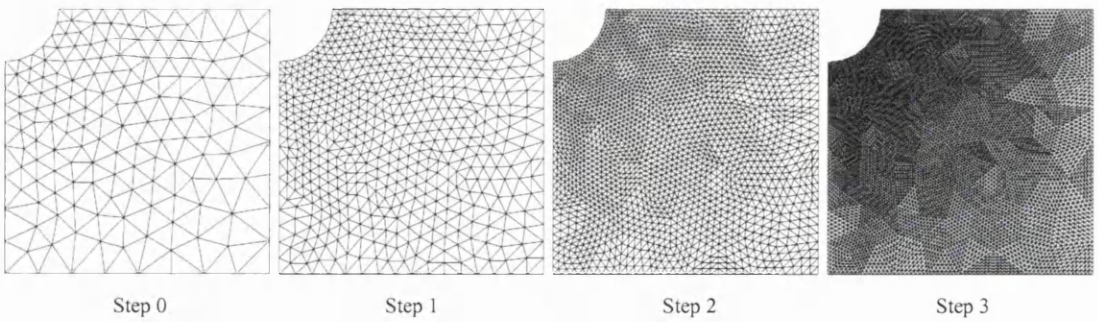

Figure 6.3a. A sequence of uniformly refined meshes for the hollow square plate $(d/L = 0.2)$

One of the most descriptive graphical results in this sequence is the plot showing the progression of the upper bound and lower bound to the collapse load, as well as the *predictor,* computed as $p = mean(\gamma_H, \hat{\gamma}_h)$. Recall from chapter 4 that the pair

$(\gamma_H, \hat{\gamma}_h)$ holds the upper and lower bound values obtained by the proposed procedure at a given refinement step. Figure 6.3b. depicts this result for the case under discussion, for uniform refinement. This plot is constructed as a graph of nominal element size in logarithmic scale versus upper/lower bound.

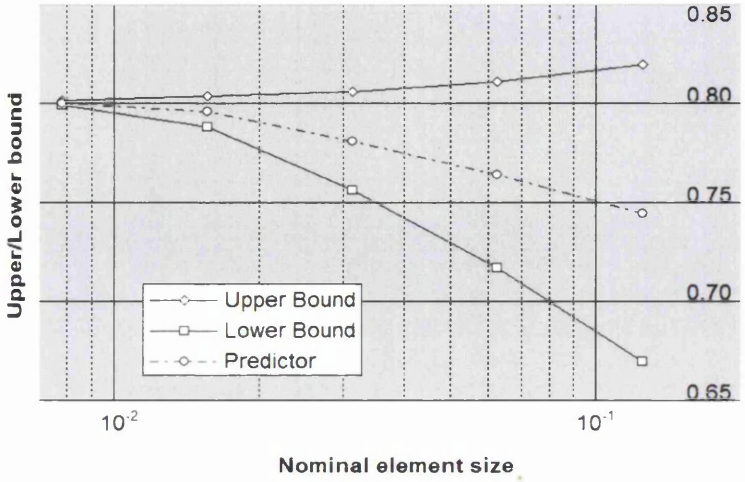

Figure 6.3b. Upper/Lower bound and the predictor for the hollow plate - *uniform refinement*

Table 6.1 lists the numerical results for the bound progression plotted in figure 6.3b. A true error of 0.05% is observed by taking the predictor in *step 4* in table 6.1 as the value attained by the present solution, under uniform refinement.

Square plate with a circular hole, d/L=0.2 / Uniform refinement						
Step i	Number of Elements	Upper Bound γ_H	Lower Bound $\hat{\gamma}_h$	Predictor p_i	Bound Gap g_i	Deviation δ_i (%)
0	288	0.8200	0.6694	0.7447	0.1505	10.1077
1	1152	0.8112	0.7172	0.7642	0.0940	6.1513
2	4608	0.8060	0.7563	0.7811	0.0497	3.1830
3	18432	0.8038	0.7885	0.7961	0.0153	0.9605
4	73728	0.8014	0.7993	0.8004	0.0021	0.1312

Table 6.1 Bound progression table

The last column in the table shows the deviation δ defined as:

$$\delta = \frac{g/2}{p}$$

Adaptive refinement

When the proposed adaptive refinement procedure is applied to this problem, a sequence of refined meshes are generated, each corresponding to a refinement step. These are drawn in figures 6.4a. and 6.4b. These refined meshes show zones of high plastic dissipation. As the adaptive sequence progresses, the high plastic zones become evident.

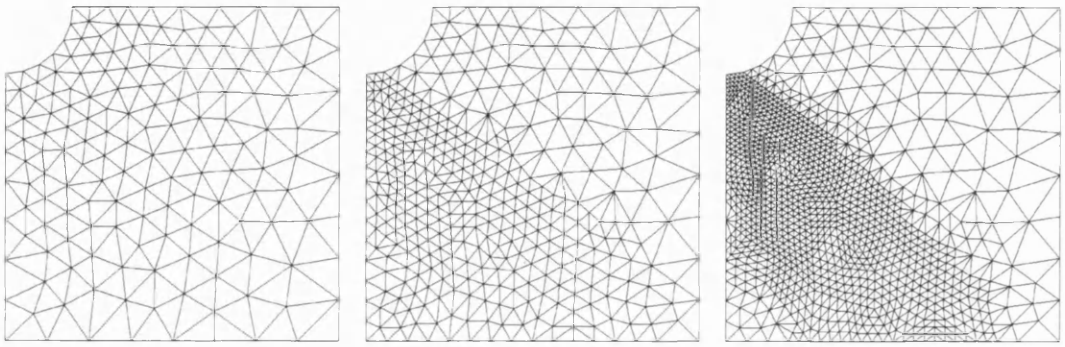

Figure 6.4a. A sequence of refined meshes for the hollow square plate ($d / L = 0.2$)

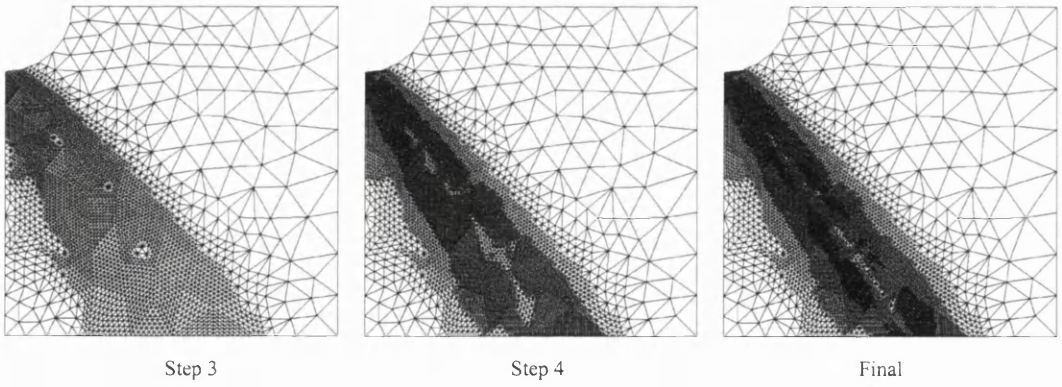

Figure 6.4b. A sequence of refined meshes for the hollow square plate ($d / L = 0.2$) (continued)

Note that the last refined mesh in figure 6.4b. indicated as the *final* mesh in the sequence, is produced when solving the problem using the mesh at the previous step (step 4) and requesting the mesh to be refined one final time. However, no solution procedure is carried out based on the final mesh, thus no bound values are computed for this mesh.

In figure 6.5, a plot similar to figure 6.3b. is shown for the case of adaptive refinement, but in a simpler format, a plot of Refinement step versus Upper/Lower bound which shows the same behaviour and information, so that throughout the rest of the chapter this type of plot will be used.

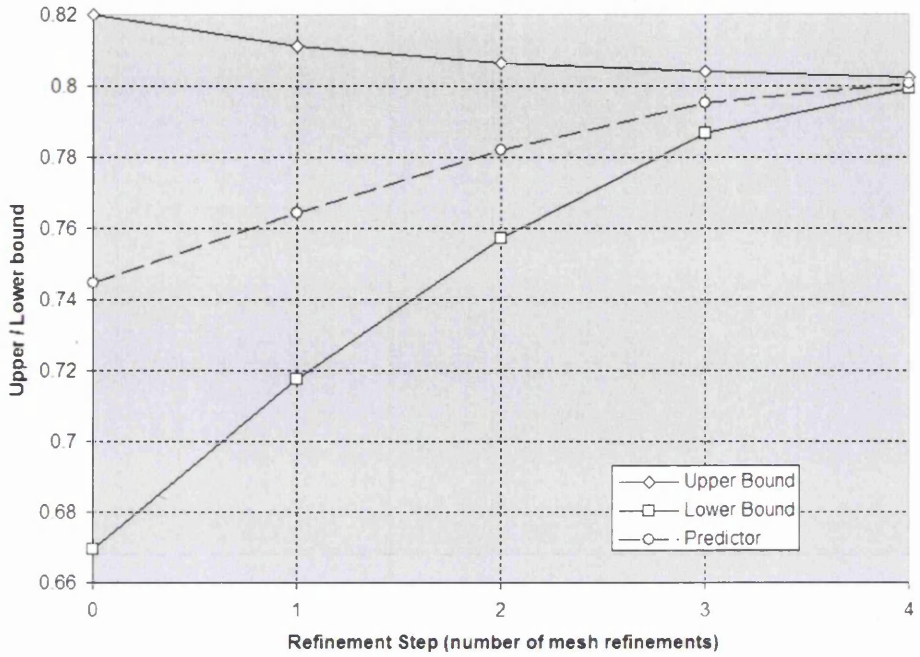

Figure 6.5 Upper/Lower bound and the predictor for the hollow plate - *adaptive refinement*

In Table 6.2 the data listing for the adaptive progression in figure 6.5 is given.

Square plate with a circular hole, d/L=0.2 / Adaptive refinement						
Step i	Number of Elements	Upper Bound γ_H	Lower Bound γ_h	Predictor p_i	Bound Gap g_i	Deviation δ_i (%)
0	288	0.8200	0.6694	0.7447	0.1505	10.1077
1	715	0.8113	0.7175	0.7644	0.0939	6.1400
2	2163	0.8066	0.7573	0.7819	0.0493	3.1532
3	6469	0.8039	0.7867	0.7953	0.0173	1.0848
4	16706	0.8023	0.7993	0.8008	0.0030	0.1877

Table 6.2 Adaptive bound progression table for d/L=0.2

A true error of 0.1% is observed in table 6.2, using again the predictor in *step 4*, for the present solution. Note that this result suggests that the discrepancy with respect to the uniform refinement predictor is due to the difference in the number of elements of both meshes; a finer mesh, that is the mesh generated by uniform refinement shows

improved accuracy in the results. This is in line with the concept of the *truth mesh*, i.e. the reference mesh defined in chapter 4.

A value of $\kappa = 0.01$ has been used for the refinement criteria, as described in section 5.4.6. As can be seen from these graphs, there are no significant differences between the results on a point-by-point basis, but a radical difference is clear when we plot these same results against the number of elements used to define the solution space. These results are shown in figure 6.6. Clearly, the adaptive refinement strategy reduces the problem size in a noticeable manner. A lower number of unknowns are defined, thus less data storage and less processing time are required by this approach.

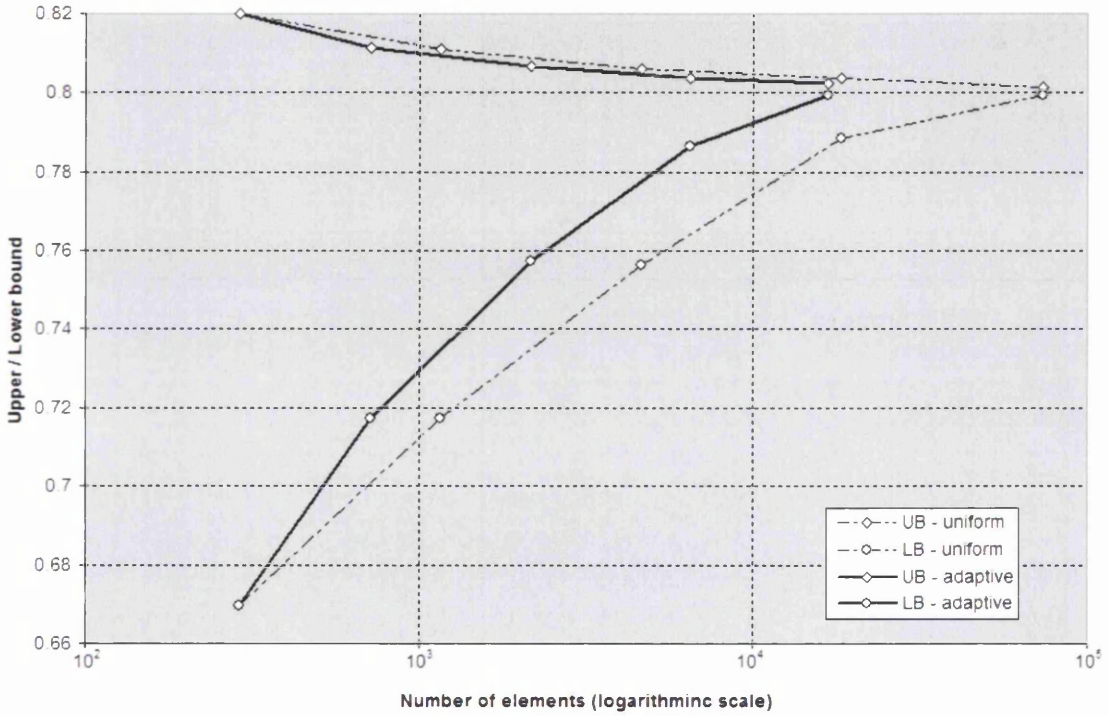

Figure 6.6 Upper/Lower bound for uniform and adaptive refinement versus the number of elements

Another interesting plot is that of the convergence rate, which shows the rate of convergence in terms of the *gap* reduction rate, as well as the rate of reduction of the error between the upper and lower bound and the *true value* for the load multiplier. This *true value* can be obtained by solving the problem over a *very fine* mesh definition, or by assuming the predictor of the last step of a uniform or adaptive

refinement sequence as the reference true value. In the present case, an exact value is available, so the error graphed is a true error.

Figure 6.7 shows a varying convergence rate which starts in a near $\mathcal{O}(h)$ (actually less-than-linear) value and ends with a rate of $\mathcal{O}(h^2)$ for the gap, where h is the nominal element size. Similar results are observed for the lower bound values, but a less-than-linear convergence is observed for the upper bound values. It should be noted that these values are plotted against the *nominal element size* in logarithmic scale.

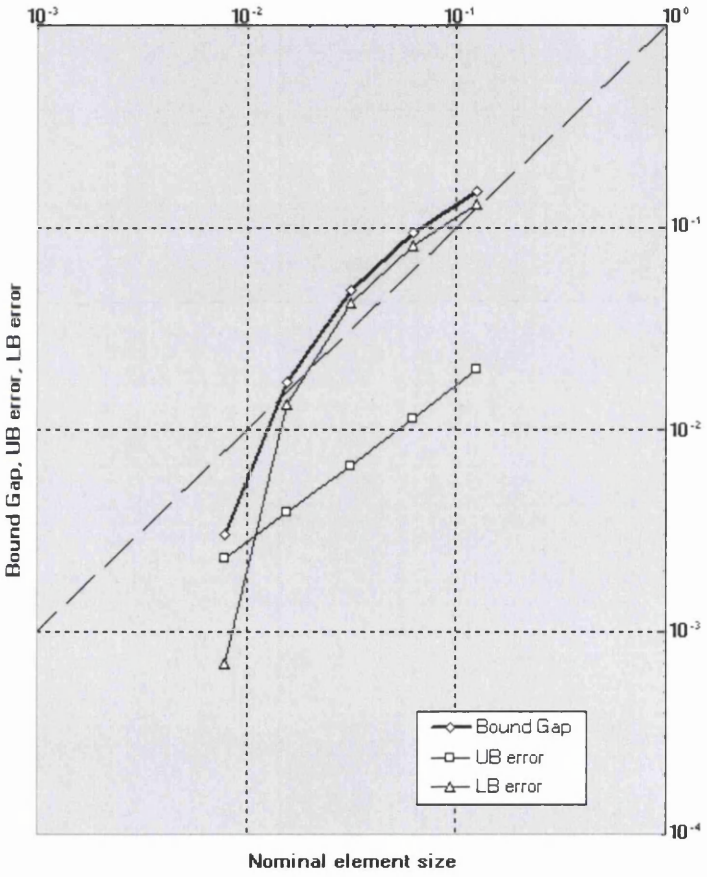

Figure 6.7 Gap and error convergence rate

The distribution of stresses in the x and y direction, as well as the shear stresses are plotted in figures 6.8a. and 6.8b., based on a fine uniform mesh. This set of figures also shows the velocity distribution resulting from the analysis, over a coarse deformed mesh (see figure 6.8b.).

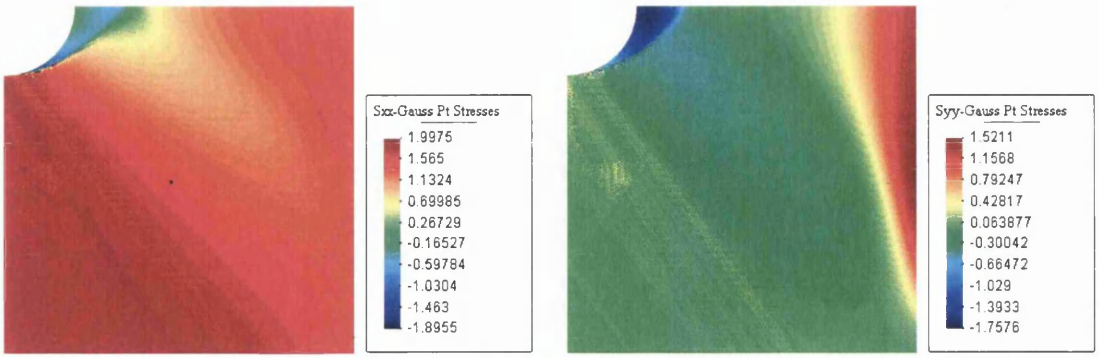

Figure 6.8a. Stress distributions for the hollow square plate (σ_{xx}, σ_{yy} respectively and $\sigma_y = \sqrt{3}$)

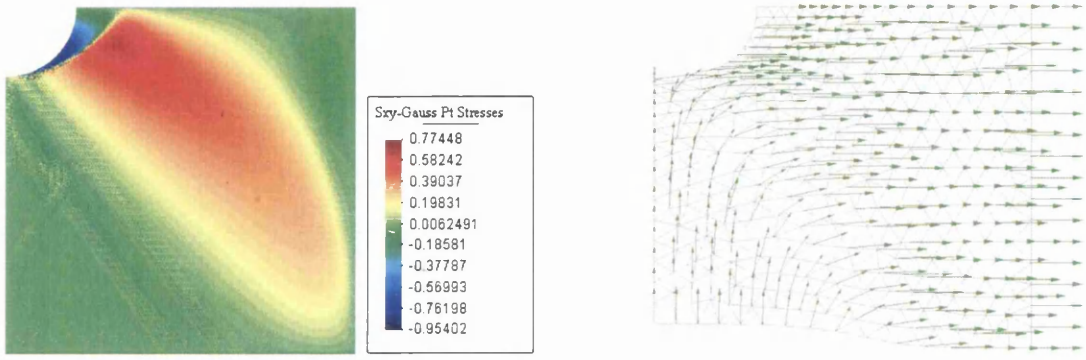

Figure 6.8b. Stress distribution for the hollow square plate (σ_{xy})

and velocity distribution over the deformed mesh

Also important to the present limit analysis solution are plots of the *equivalent strain rate* distribution, as well as the distribution of the von Mises stress computed at every element, both displayed in figure 6.9a. Velocity distributions in the x and y direction over the deformed body shape are shown in figure 6.9b. All these results are given for a fine uniform mesh.

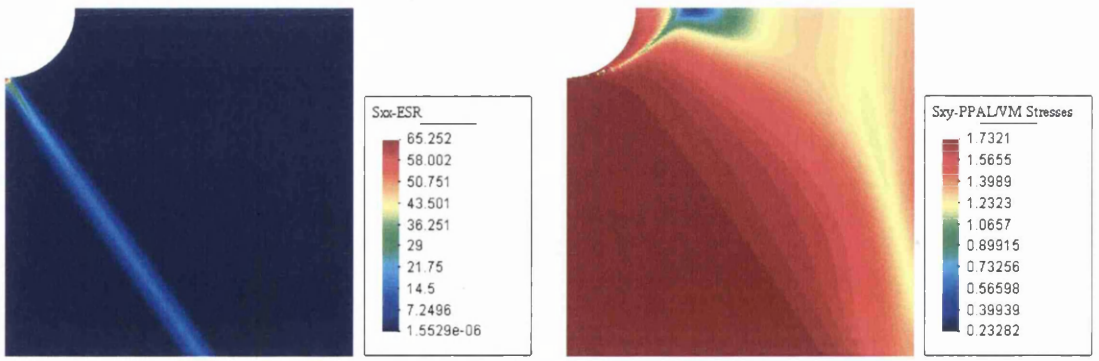

Figure 6.9a. Equivalent strain-rate and von Mises stresses, for the hollow square plate

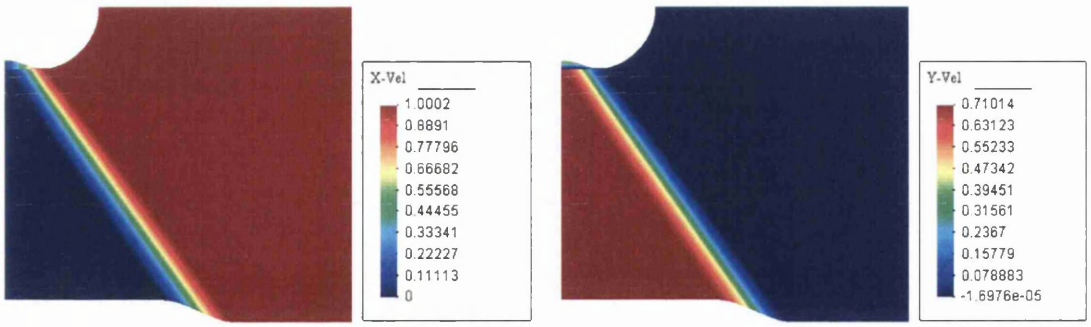

Figure 6.9b. Velocity distribution in x and y direction, for the hollow square plate over the deformed shape

It is worth to comment here that the distribution of von Mises stresses does not show a constant *yield stress* value as would be expected from the stress-strain relation for a rigid-plastic material. In fact, the are regions where the material remains below the yield limit. These regions, however, exhibit very small strain-rate values, as shown in figure 6.9a., and therefore do not contribute to the energy dissipation.

Part II. The same hollow plate problem is revisited now to compare the results obtained in this research with the results of other researchers, starting with an analytical approach presented by Gaydon & McCrum [1] and Gaydon [2], in which upper and lower bounds are found for the case of the hollow plate. Another comparison comes from the work of Casciaro & Cascini [4], who present a mixed finite element method and a series of tests in plane stress and plane strain for different cases, one of which is the hollow plate considered here, as well as other cases that will be described and compared later on in this chapter. A third source of comparison comes from another mixed formulation approach by Borges, Zouain & Hespe [3], where numerical results are obtained for the present case.

A series of graphical results obtained by the present solution procedure for a varying d / L ratio, are given in the following figures with accompanying bound progression tables. First, a set of adaptively refined meshes for each step is presented. Then, a figure showing the upper/lower bound progression for each ratio in the format of figure 6.5 is given. This plot is drawn to compare the analytical upper and lower

bounds by Gaydon & McCrum [1] and Gaydon [2], and the mixed FE solutions by Borges, Zouain and Huespe [3] and by Casciaro and Cascini [4].

The sequence of meshes generated by the adaptive refinement steps for ratio $d/L = 0.2$ is given in figures 6.4a. and 6.4b., above. In figure 6.10, a comparative plot of the bound progression is given for the same case. In this figure a multiplier value in red is drawn which corresponds to the exact solution. A closing interval containing the exact solution is produced on each refinement step by the present solution procedure.

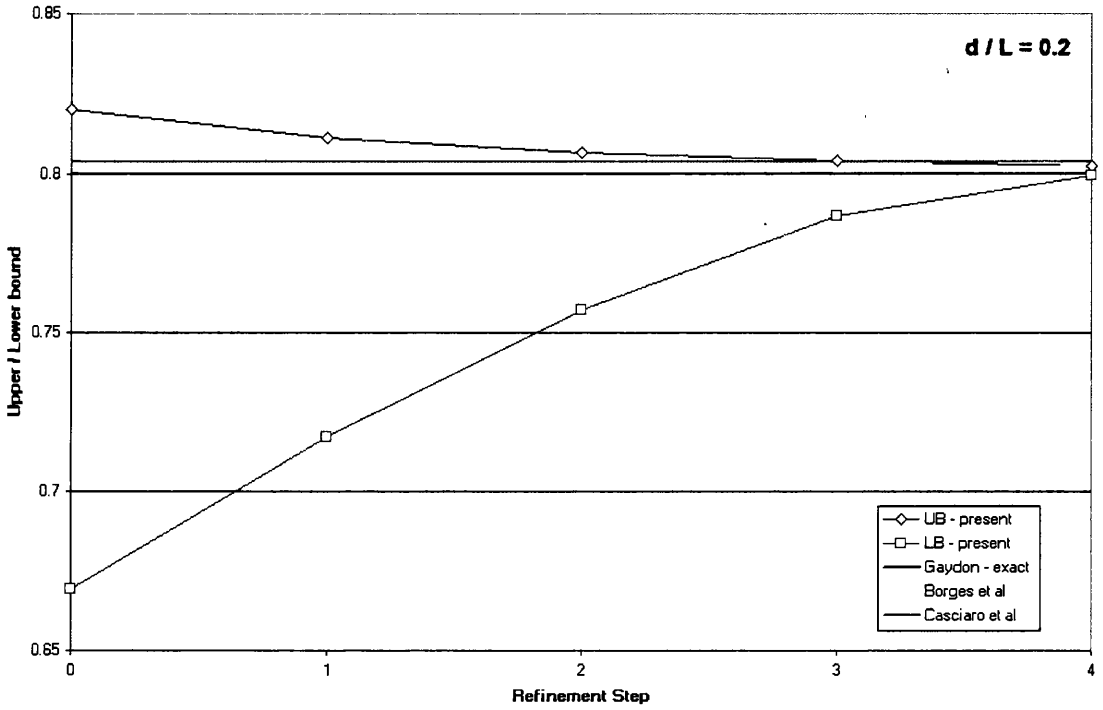

Figure 6.10 Bound progression plot for hollow plate with d/L=0.2

The sequence of refined meshes for ratio $d/L = 0.4$ is given in figures 6.11a. and 6.11b. These refined meshes emphasize regions of high plastic dissipation, and typically show areas running along the neighbourhood of the slip-lines.

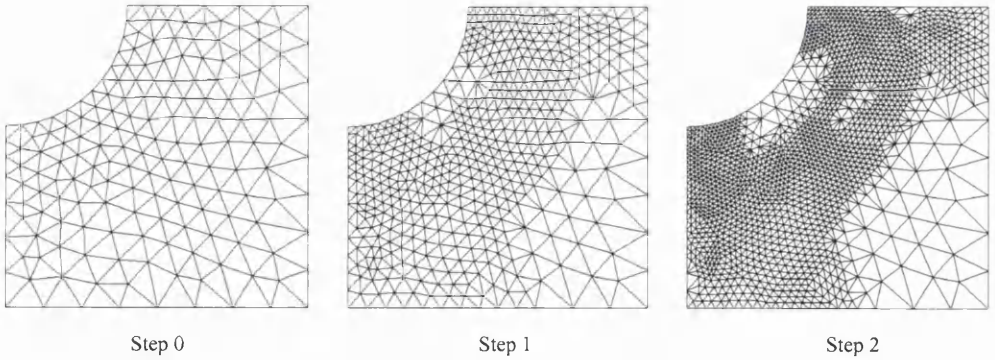

Step 0 Step 1 Step 2

Figure 6.11a. A sequence of refined meshes for the hollow square plate ($d / L = 0.4$)

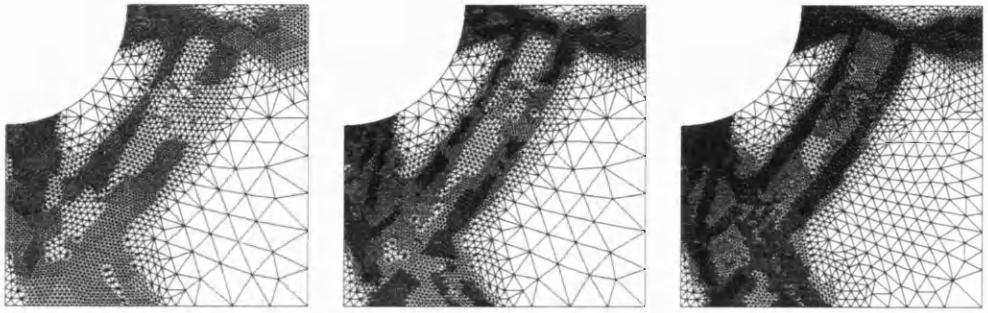

Step 3 Step 4 Final

Figure 6.11b. A sequence of refined meshes for the hollow square plate ($d / L = 0.4$) (continued)

The corresponding bound progression plot is given for this case in figure 6.12, in which a comparison is made against the reference results, as indicated in the chart.

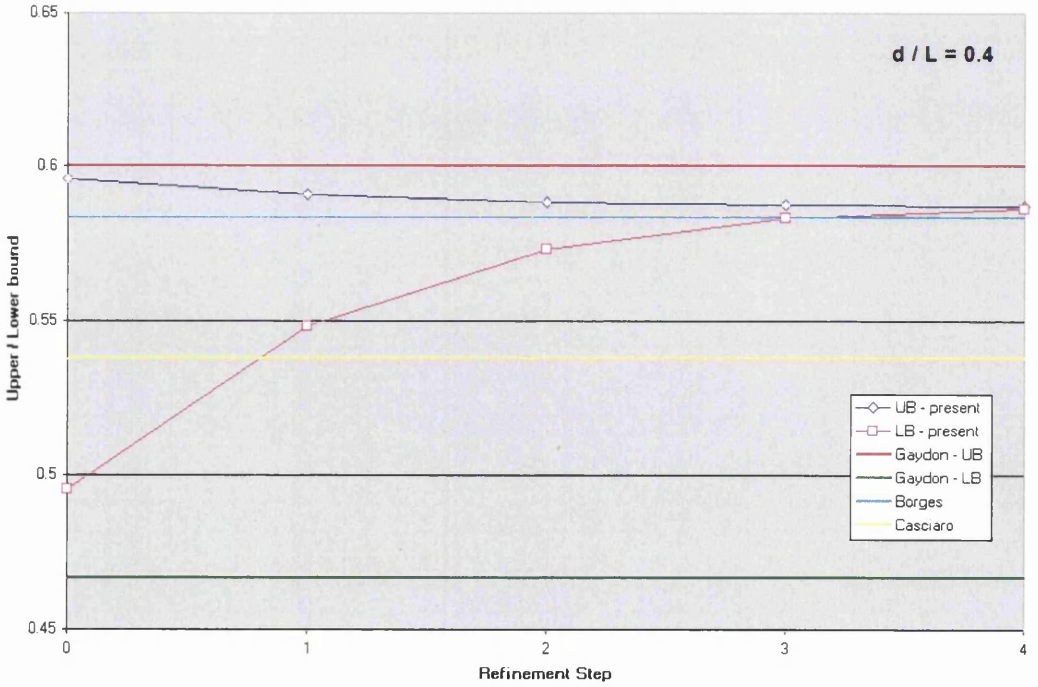

Figure 6.12 Bound progression for hollow plate with d/L=0.4

Notice the close value of the estimation made by Borges *et al.* to the predictor produced by the present solution. The value obtained by Casciaro *et al.* shows a substantial discrepancy from the value found through the present proposal, when compared to that of Borges *et al.*

Table 6.3 lists the numerical results obtained from the present solution for the bound progression in figure 6.12.

Square plate with a circular hole, d/L=0.4 / Adaptive refinement						
Step i	Number of Elements	Upper Bound γ_H	Lower Bound $\hat{\gamma}_h$	Predictor p_i	Bound Gap g_i	Deviation δ_i (%)
0	306	0.5959	0.4951	0.5455	0.1008	9.2390
1	975	0.5909	0.5481	0.5695	0.0427	3.7529
2	3334	0.5882	0.5732	0.5807	0.0150	1.2894
3	9324	0.5873	0.5832	0.5853	0.0041	0.3514
4	20666	0.5870	0.5860	0.5865	0.0010	0.0814

Table 6.3 Bound progression table for d/L=0.4

Next, the sequence of refined meshes for the ratio $d / L = 0.6$ is given in figures 6.13a. and 6.13b.

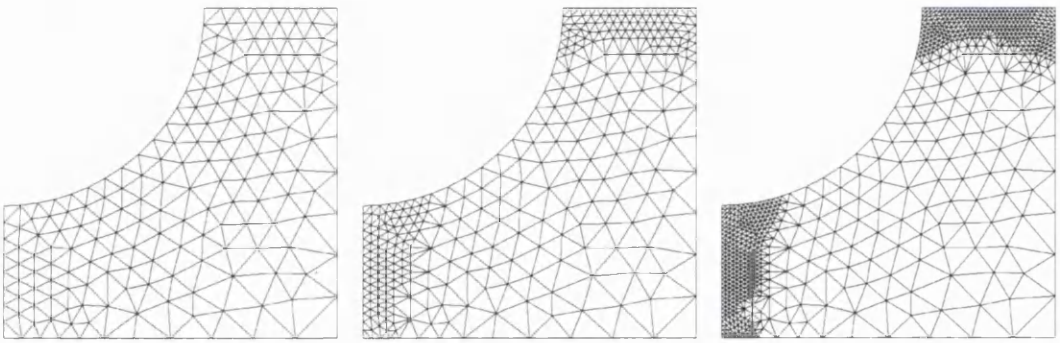

Step 0 Step 1 Step 2

Figure 6.13a. A sequence of refined meshes for the hollow square plate $(d / L = 0.6)$

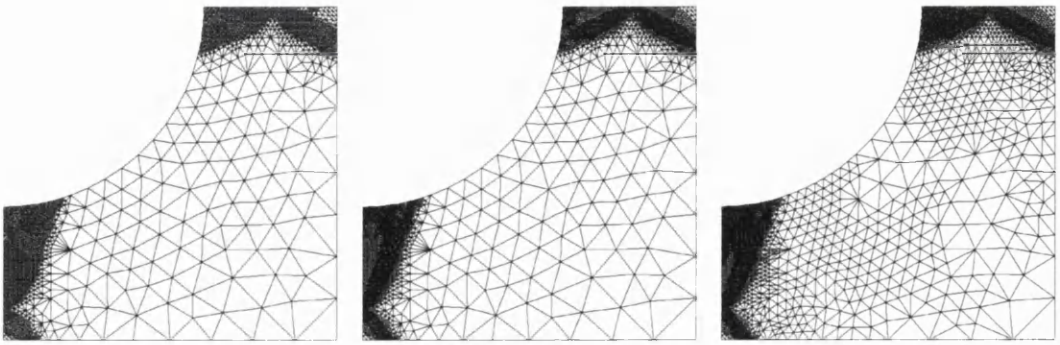

Step 3 Step 4 Final

Figure 6.13b. A sequence of refined meshes for the hollow square plate $(d / L = 0.6)$ (continued)

The bound progression graph for $d/L = 0.6$ is drawn in figure 6.14.

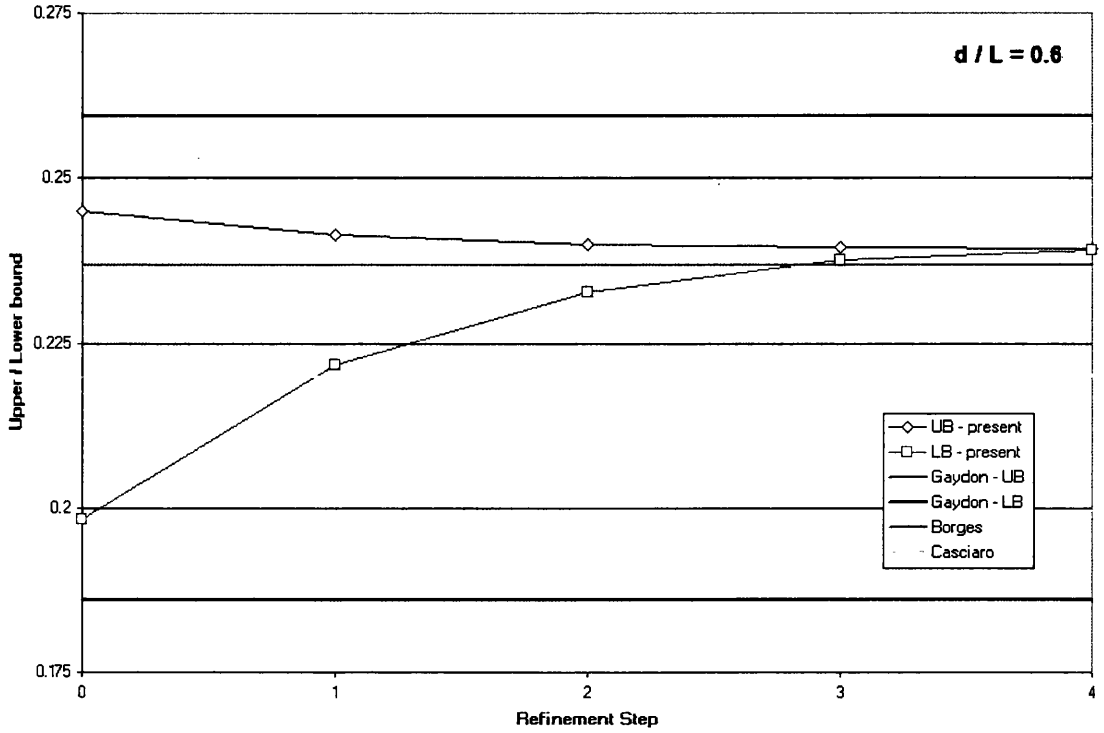

Figure 6.14 Bound progression and final mesh for *d/L*=0.6

Notice again that the value by Borges *et al.* is closer to the present solution. The value obtained by Casciaro *et al.* keeps a significant discrepancy to both, Borges *et al.* an the present solution. The numerical bound values are listed in table 6.4 for the case of ratio $d/L = 0.6$.

Square plate with a circular hole, d/L=0.6 / Adaptive refinement						
Step i	Number of Elements	Upper Bound γ_H	Lower Bound $\hat{\gamma}_h$	Predictor p_i	Bound Gap g_i	Deviation δ_i (%)
0	329	0.2450	0.1983	0.2216	0.0467	10.5443
1	589	0.2413	0.2217	0.2315	0.0196	4.2319
2	1548	0.2400	0.2328	0.2364	0.0071	1.5117
3	4571	0.2394	0.2375	0.2385	0.0019	0.3989
4	12133	0.2392	0.2390	0.2391	0.0003	0.0581

Table 6.4 Bound progression table for *d/L*=0.6

Finally, the set of refined meshes for the ratio $d/L = 0.8$ is presented in figures 6.15a. and 6.15b.

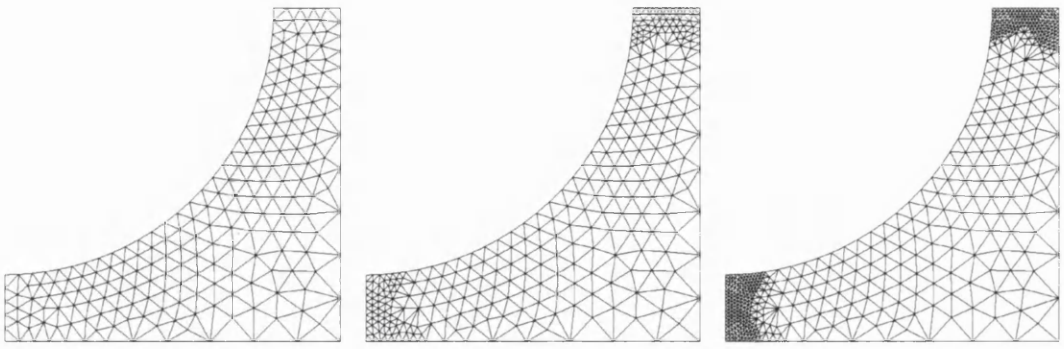

Step 0 Step 1 Step 2

Figure 6.15a. A sequence of refined meshes for the hollow square plate ($d / L = 0.8$)

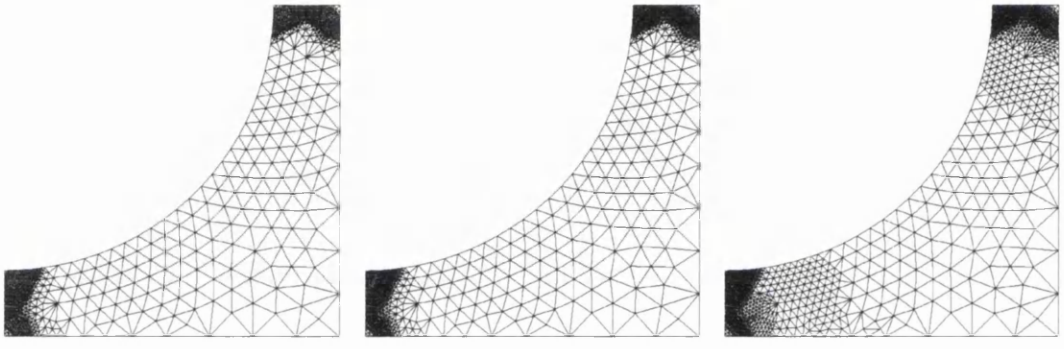

Step 3 Step 4 Final

Figure 6.15b. A sequence of refined meshes for the hollow square plate ($d / L = 0.8$) (continued)

The corresponding bound progression plot is given in figure 6.16, along with the reference results.

Notice also the value of the predictor in this case, clearly closer to that of Borges *et al.* and farther from the estimation by Casciaro *et al.* The numerical bound list is given in table 6.5, for this last ratio.

Recalling the problem setting of figure 6.2, a summary table is presented in table 6.6, which contains the four groups of load multipliers attained by the reference authors, and compared against the present solution. These are given for each ratio d / L, i.e. for ratios 0.2, 0.4, 0.6 and 0.8. Load multipliers are given in non-dimensional form.

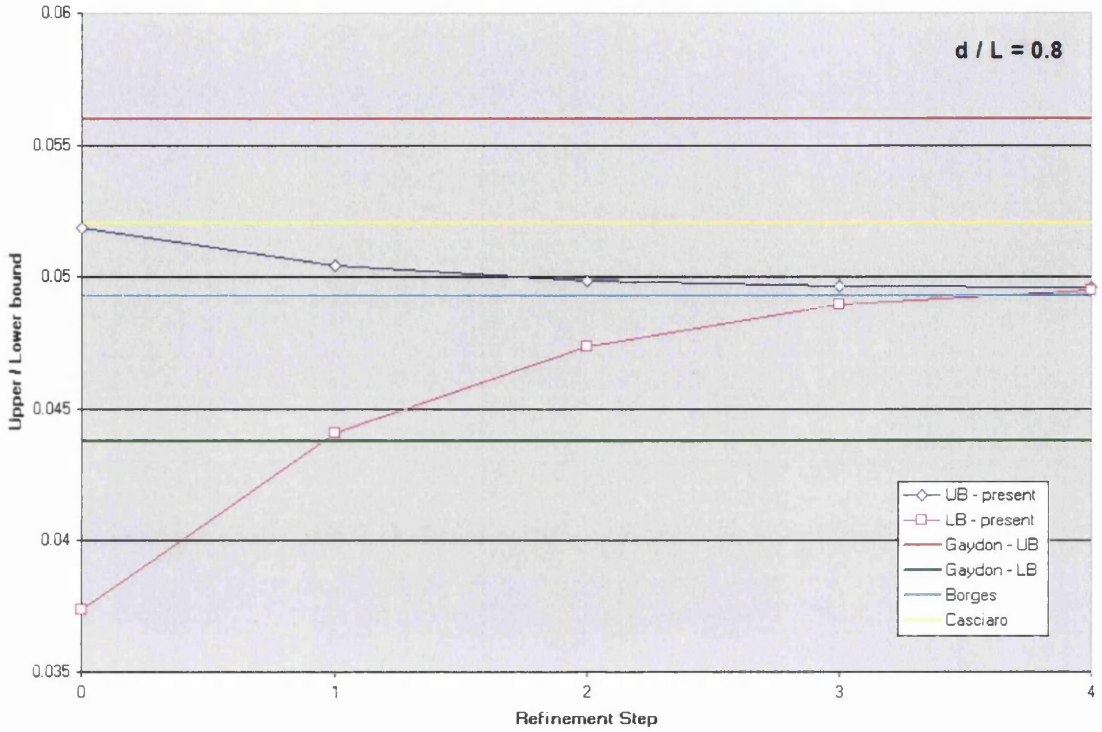

Figure 6.16 Bound progression and final mesh for d/L=0.8

Square plate with a circular hole, d/L=0.8 / Adaptive refinement						
Step i	Number of Elements	Upper Bound γ_H	Lower Bound $\hat{\gamma}_h$	Predictor p_i	Bound Gap g_i	Deviation δ_i (%)
0	379	0.0518	0.0374	0.0446	0.0145	16.2108
1	540	0.0504	0.0441	0.0473	0.0063	6.6807
2	1112	0.0499	0.0474	0.0486	0.0025	2.5848
3	2848	0.0497	0.0490	0.0493	0.0007	0.7157
4	7589	0.0496	0.0495	0.0495	0.0001	0.0935

Table 6.5 Bound progression table for d/L=0.8

In table 6.6, the value computed through the present procedure, in the form of the predictor, is typed in bold in the fourth column. In the case of the data coming from the work of Borges, Zouain & Huespe, the value for the finest mesh is used. The data taken from the work of Casciaro & Cascini comes from a single mesh configuration.

d/L	Method	Research	p/σ_y	Discrepancy %
0.2	Exact	Gaydon & McCrum, 1954	0.8000	0.1015
	Mixed FE	Borges, Zouain & Huespe, 1996	0.8004	0.0516
	Predictor	Present	**0.8008**	-
	Mixed FE	Casciaro & Cascini, 1982	0.8035	0.3355
0.4	Lower Bound	Gaydon & McCrum, 1954	0.4664	20.4774
	Mixed FE	Casciaro & Cascini, 1982	0.5375	8.3546
	Mixed FE	Borges, Zouain & Huespe, 1996	0.5834	0.5286
	Predictor	Present	**0.5865**	-
	Upper Bound	Gaydon & McCrum, 1954	0.6000	2.3018
0.6	Lower Bound	Gaydon, 1954	0.1859	22.2507
	Mixed FE	Casciaro & Cascini, 1982	0.2199	8.0308
	Mixed FE	Borges, Zouain & Huespe, 1996	0.2367	1.0045
	Predictor	Present	**0.2391**	-
	Upper Bound	Gaydon & McCrum, 1954	0.2594	8.4894
0.8	Lower Bound	Gaydon, 1954	0.0438	11.5823
	Mixed FE	Borges, Zouain & Huespe, 1996	0.0493	0.4999
	Predictor	Present	**0.0495**	-
	Mixed FE	Casciaro & Cascini, 1982	0.0520	4.9707
	Upper Bound	Gaydon & McCrum, 1954	0.0560	13.0454

Table 6.6 Comparative table for different collapse load multiplier estimations for problem in figure 6.2 ($\zeta = 0$). Discrepancy is computed relative to the present solution.

Note that no true *error* can be computed in this chapter, as no exact solution is available, except for the first case presented. However we use the term *discrepancy* in table 6.6, which is computed relative to the present solution, to indicate the level of coincidence between the present results and the reference results.

In summary, a good performance can be drawn out of this sequence of tests, starting with the comparison of the exact value for the case with ratio $d/L = 0.2$ which shows only a discrepancy of one-thousandth. The rest of the reference values show higher discrepancies, but the results obtained by Borges *et al.* seem to be closer to the results obtained through the present solution.

6.2.2 *Additional plate cases*

6.2.2a) *Square plate with various linear carvings*

In this section we are concerned with the problems defined in figure 6.17. These problems are presented by Casciaro and Cascini [4] and are given here to complement the test cases of section 6.2.1.

The first problem *i)* in figure 6.17 corresponds to a *square plate with a square hole* subject to uniaxial unit stress.

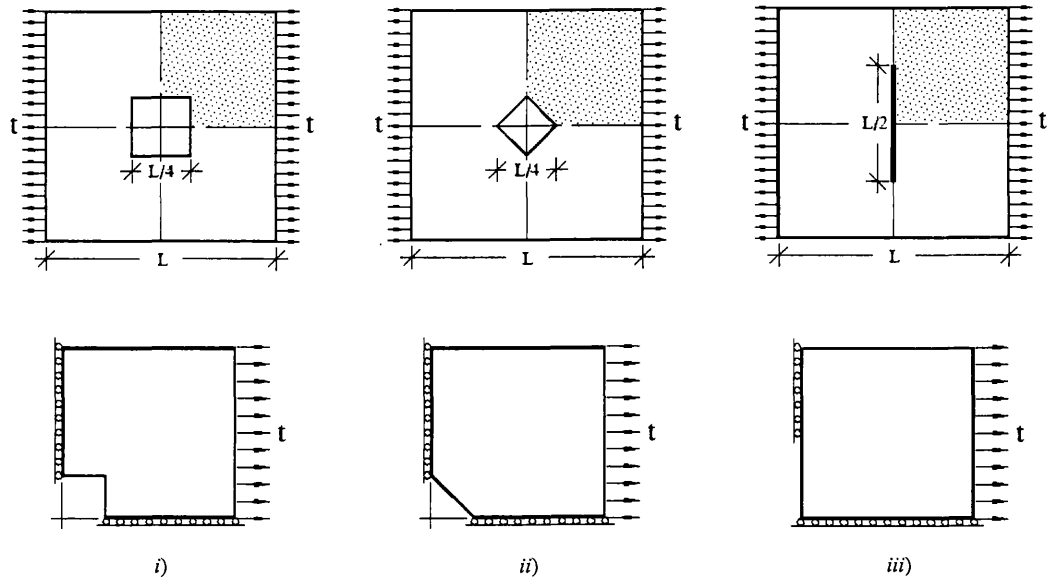

Figure 6.17 Problem settings for the square plate with linear carvings

The sequence of adaptively refined meshes for this problem is presented in figures 6.18a, 6.18b and 6.18c.

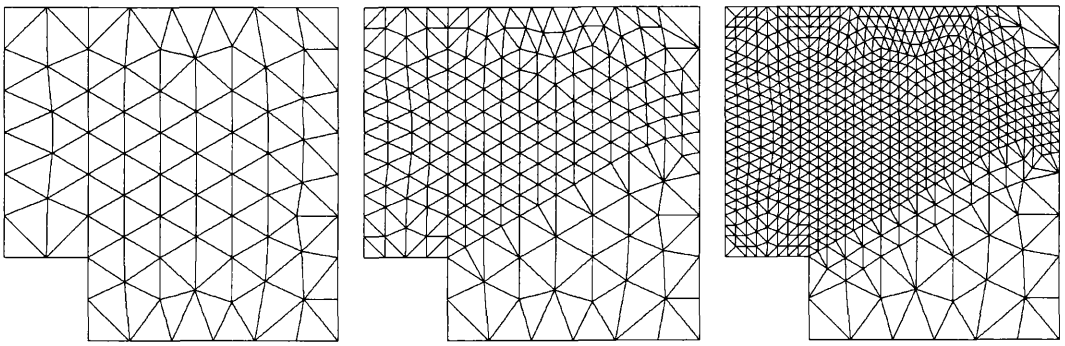

Step 0 Step 1 Step 2

Figure 6.18a. A sequence of refined meshes for the square hole plate

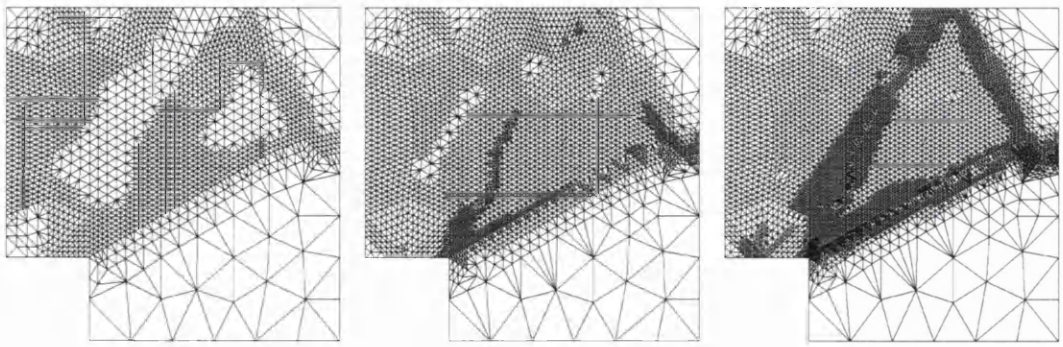

Step 3 Step 4 Step 5

Figure 6.18b. A sequence of refined meshes for the square hole plate (continued)

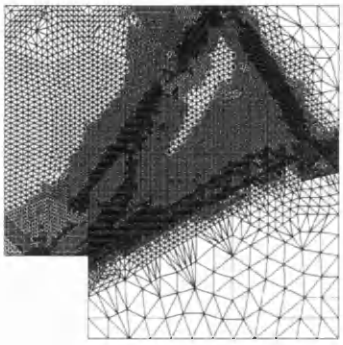

Final

Figure 6.18c. The final refined mesh for the square hole plate (continued)

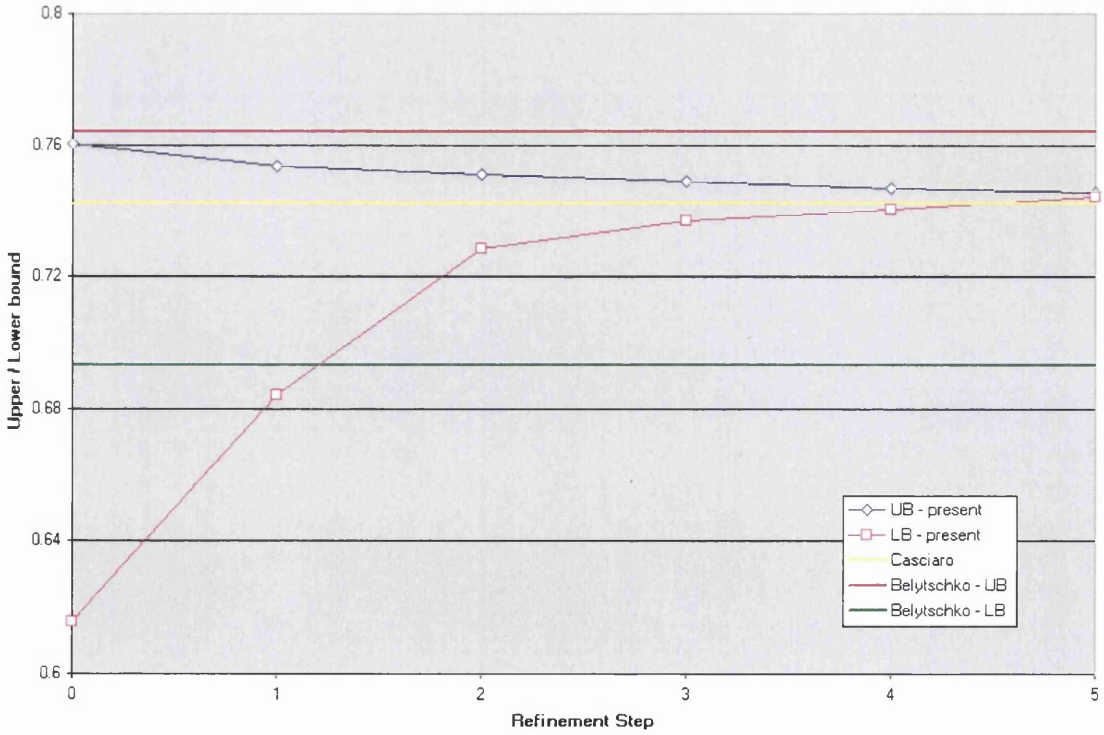

Figure 6.19 Bound progression for plate with square hole

The bound progression for problem *i*) in figure 6.17, corresponding to the previous mesh sequence, is given in figure 6.19. Reference values are also shown in this plot.

The bound progression table for this problem is given in table 6.7 as follows.

Square plate with a square hole / Adaptive refinement						
Step i	Number of Elements	Upper Bound γ_H	Lower Bound $\hat{\gamma}_h$	Predictor p_i	Bound Gap g_i	Deviation δ_i (%)
0	126	0.7601	0.6155	0.6878	0.1446	10.5104
1	363	0.7536	0.6840	0.7188	0.0695	4.8371
2	1302	0.7508	0.7287	0.7397	0.0222	1.4991
3	3666	0.7486	0.7369	0.7428	0.0117	0.7901
4	6090	0.7466	0.7403	0.7435	0.0064	0.4274
5	10612	0.7456	0.7442	0.7449	0.0014	0.0962

Table 6.7 Bound progression table for plate with square hole

The second problem *ii*) in figure 6.17 is a *square plate with an oblique square hole*, and the corresponding set of refined meshes is given in figures 6.20a, 6.20b and 6.20c.

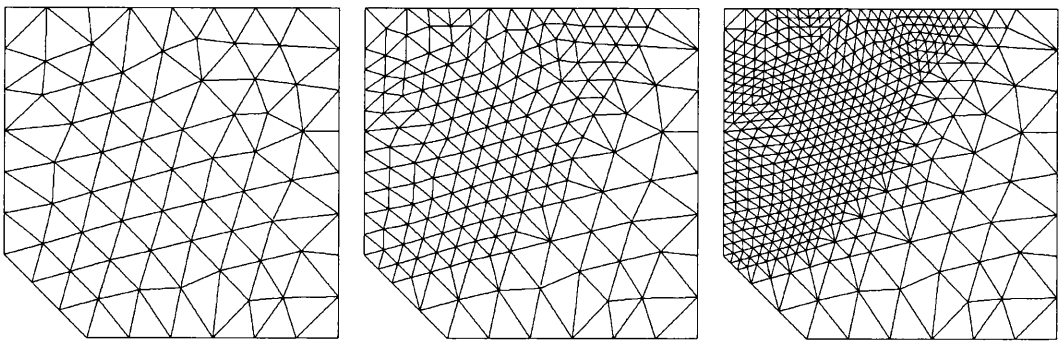

Step 0 Step 1 Step 2

Figure 6.20a. A sequence of refined meshes for the oblique square hole plate

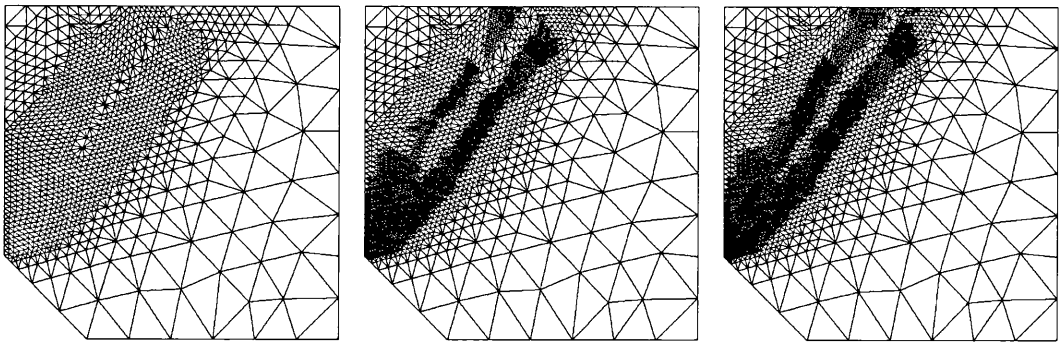

Step 3 Step 4 Step 5

Figure 6.20b. A sequence of refined meshes for the oblique square hole plate (continued)

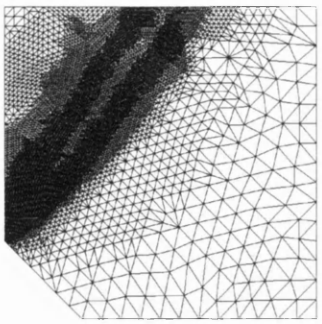

Final

Figure 6.20c. The final refined mesh for the oblique square hole plate (continued)

These meshes correspond to the progression bound plot of figure 6.21, presented against the reference values.

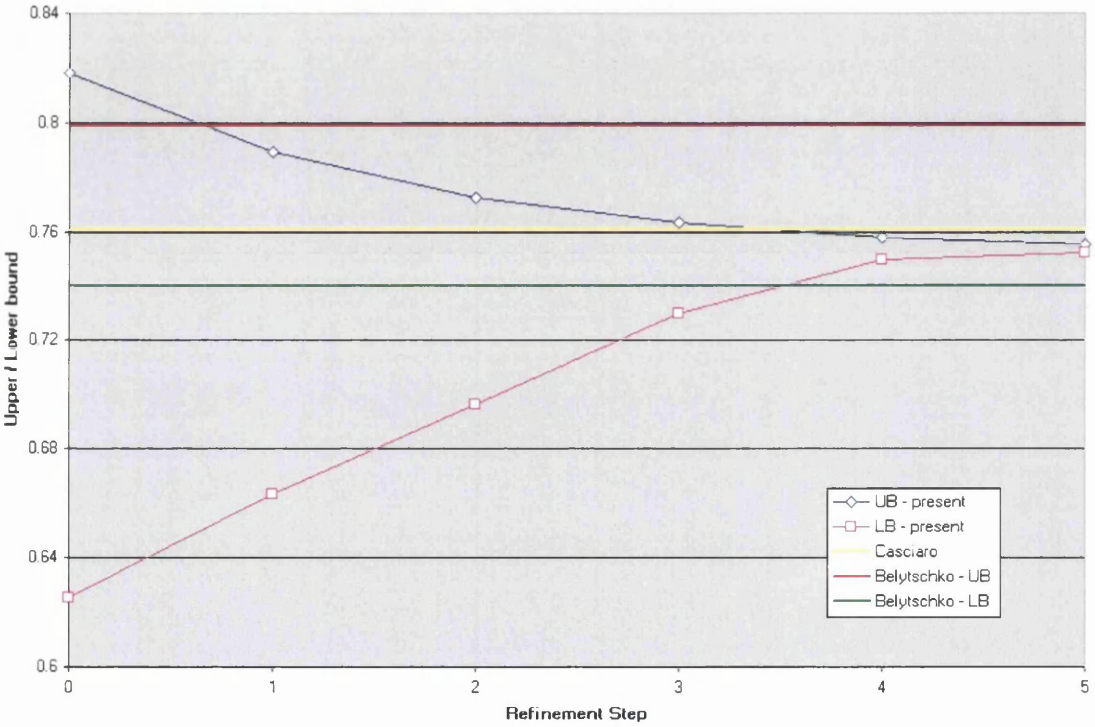

Figure 6.21 Bound progression for plate with oblique square hole

Square plate with an oblique square hole / Adaptive refinement						
Step i	Number of Elements	Upper Bound γ_H	Lower Bound $\hat{\gamma}_h$	Predictor p_i	Bound Gap g_i	Deviation δ_i (%)
0	127	0.8180	0.6256	0.7218	0.1924	13.3262
1	339	0.7891	0.6633	0.7262	0.1257	8.6577
2	970	0.7727	0.6964	0.7345	0.0763	5.1952
3	2508	0.7632	0.7297	0.7465	0.0335	2.2431
4	5410	0.7578	0.7495	0.7536	0.0083	0.5515
5	7134	0.7555	0.7520	0.7537	0.0035	0.2309

Table 6.8 Bound progression table for plate with oblique square hole

Numeric data for this case are given in table 6.8. The last problem *iii*) in figure 6.17 is a *square plate with a transversal slit*. The adaptive refinement steps for this problem are shown in figures 6.22a, 6.22b and 6.22c.

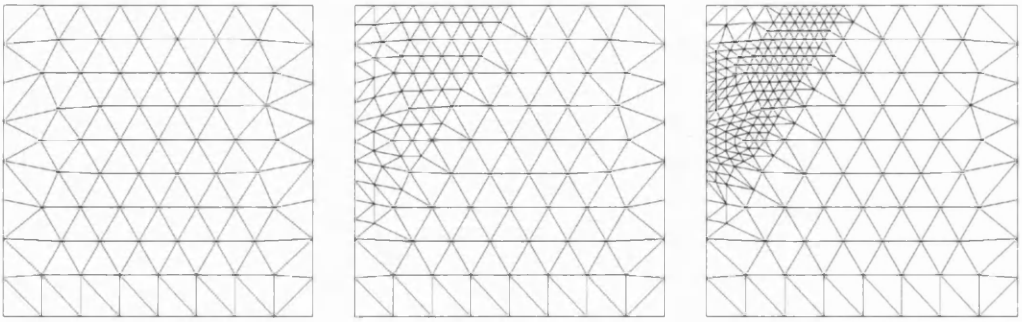

Step 0 Step 1 Step 2

Figure 6.22a. A sequence of refined meshes for plate with a transversal slit

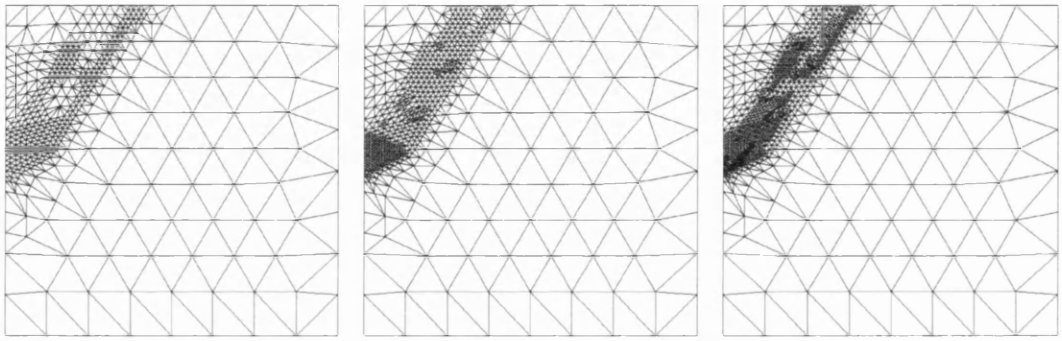

Step 3 Step 4 Step 5

Figure 6.22b. A sequence of refined meshes for plate with a transversal slit (continued)

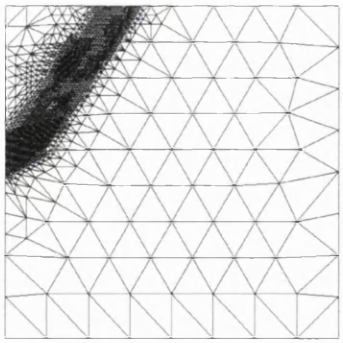

Final

Figure 6.22c. The final refined mesh for plate with a transversal slit (continued)

The bound progression graph along with reference results is drawn in figure 6.23. Table 6.9 list the numeric data for this problem.

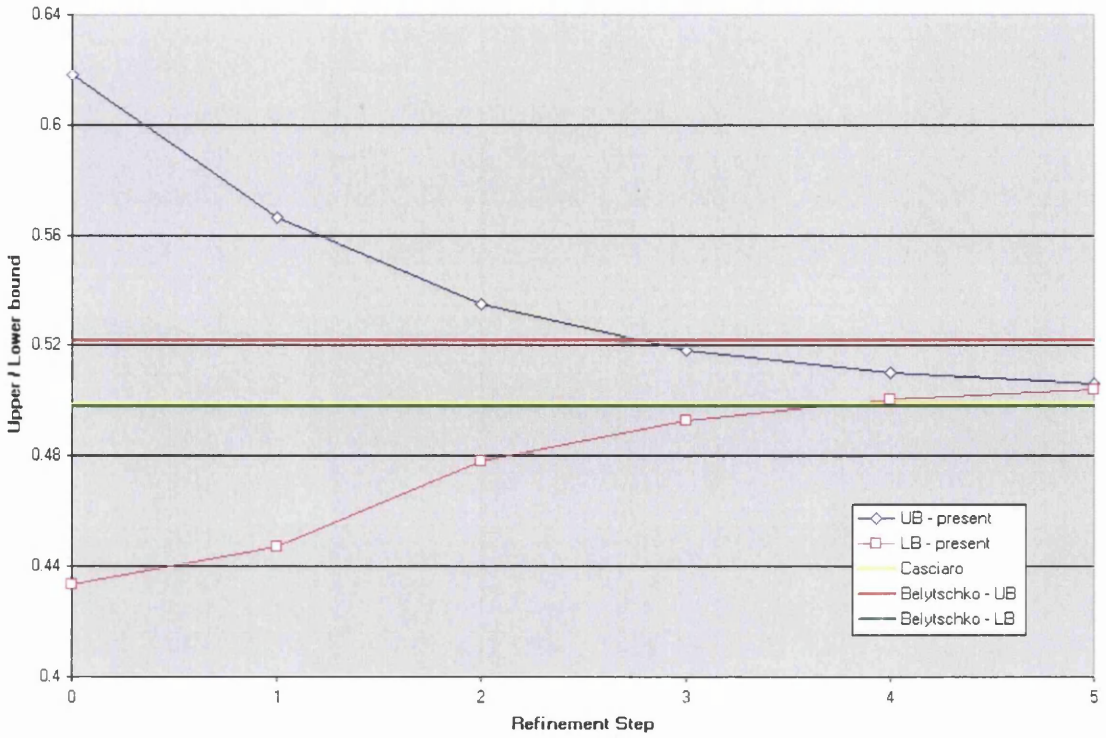

Figure 6.23 Bound progression for plate with a transversal slit

Square plate with a transversal slit / Adaptive refinement						
Step i	Number of Elements	Upper Bound γ_H	Lower Bound $\hat{\gamma}_h$	Predictor p_i	Bound Gap g_i	Deviation δ_i (%)
0	134	0.6180	0.4336	0.5258	0.1844	17.5343
1	222	0.5664	0.4471	0.5067	0.1193	11.7685
2	436	0.5349	0.4783	0.5066	0.0566	5.5816
3	816	0.5184	0.4928	0.5056	0.0256	2.5315
4	1307	0.5101	0.5006	0.5053	0.0096	0.9461
5	2343	0.5058	0.5040	0.5049	0.0018	0.1809

Table 6.9 Bound progression table for plate with a transversal slit

A summary table including these three last cases along with the next case is presented at the end of the present section, in which the discrepancy of the reference results with respect to the present solution is given (see table 6.11).

6.2.2b) *Rectangular plate with semicircular edge notches*

The last case in this third validation step corresponds to the case of a *rectangular plate with semicircular edge notches*, as shown in figure 6.24.

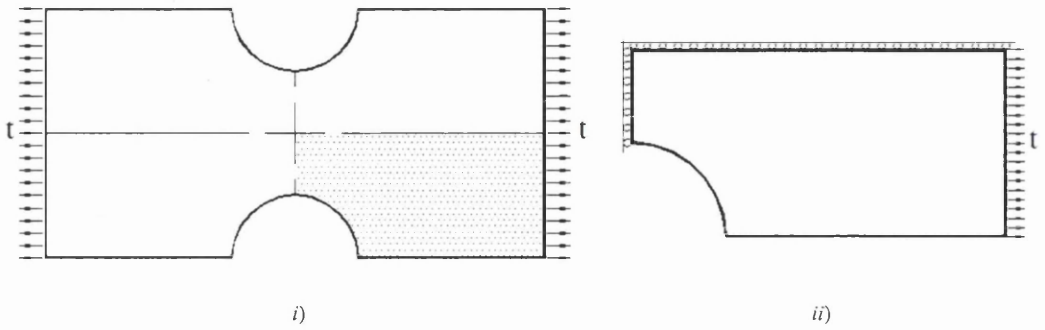

Figure 6.24 Rectangular plate with semicircular edge notches

The dimensions of this plate are L in width and $2L$ in length, and a carving radius of $L/4$. For the present test a value of $L = 2$ and a uniaxial unit stress have been used.

The mesh set resulting from the adaptive refinement scheme for this problem is depicted in figures 6.25a to 6.25d, next.

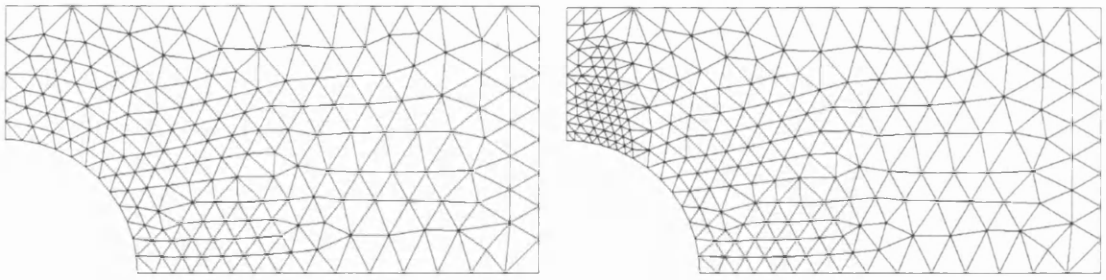

Figure 6.25a. A sequence of refined meshes for plate with semicircular edge notches

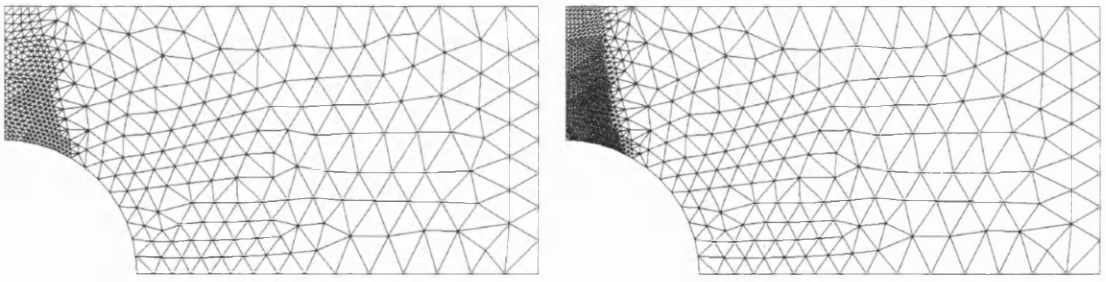

Figure 6.25b. A sequence of refined meshes for plate with semicircular edge notches (continued)

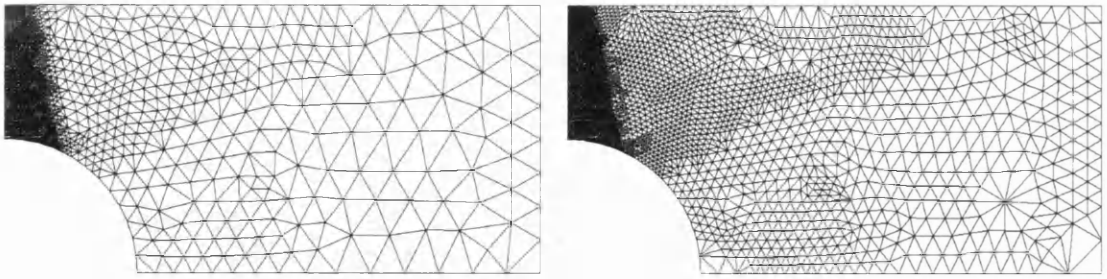

Step 4 Step 5

Figure 6.25c. A sequence of refined meshes for plate with semicircular edge notches (continued)

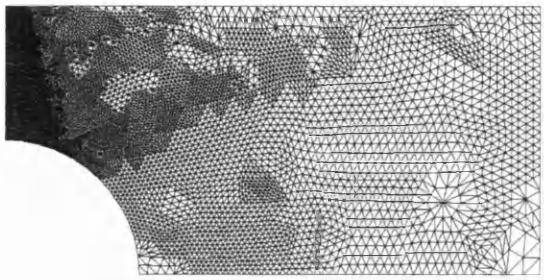

Final

Figure 6.25d. The final refined mesh for plate with semicircular edge notches (continued)

The bound progression plot for this problem is given in figure 6.26, along with a result obtained from Casciaro and Cascini [4].

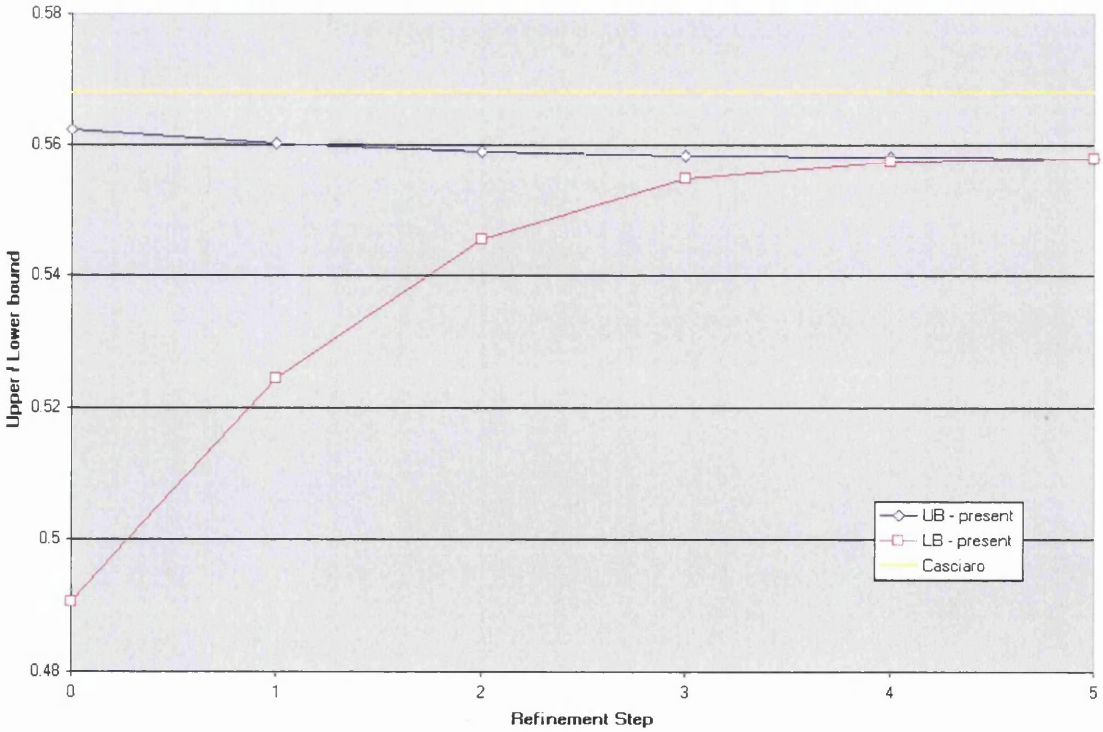

Figure 6.26 Bound progression for plate with semicircular edge notches

Note that a clear gap occurs between the reference value by Casciaro and Cascini [4] and the value obtained through the present solution. The list containing the bound sequence is given in table 6.10.

Plate with semicircular edge notches / Adaptive refinement						
Step i	Number of Elements	Upper Bound γ_H	Lower Bound $\hat{\gamma}_h$	Predictor p_i	Bound Gap g_i	Deviation δ_i (%)
0	370	0.5622	0.4906	0.5264	0.0716	6.7974
1	470	0.5600	0.5245	0.5422	0.0356	3.2812
2	843	0.5589	0.5455	0.5522	0.0133	1.2073
3	2000	0.5582	0.5548	0.5565	0.0035	0.3139
4	6106	0.5580	0.5575	0.5577	0.0005	0.0445
5	18771	0.5578	0.5578	0.5578	0.0000	0.0028

Table 6.10 Bound progression table for plate with semicircular edge notches

6.2.2c) *A summary of results*

The comparative evaluation of the reference results presented in this section with respect to the results obtained through the present solution scheme can be summarized in table 6.11. Recall that the discrepancy is computed relative to the present findings.

Case	Method	Research	$\gamma t/\sigma_y$	Discrepancy %
Square plate with square hole	FE Lower bound	Belytschko & Hodge, 1970	0.6930	6.9651
	Mixed FE	Casciaro & Cascini, 1982	0.7420	0.3869
	Predictor	Present	**0.7449**	-
	FE Upper bound	Belytschko & Hodge, 1970	0.7640	2.5666
Square plate with oblique hole	FE Lower bound	Belytschko & Hodge, 1970	0.7400	1.8201
	Predictor	Present	**0.7537**	-
	Mixed FE	Casciaro & Cascini, 1982	0.7610	0.9661
	FE Upper bound	Belytschko & Hodge, 1970	0.7990	6.0077
Square plate with transversal slit	FE Lower bound	Belytschko & Hodge, 1970	0.4980	1.3659
	Mixed FE	Casciaro & Cascini, 1982	0.4990	1.1679
	Predictor	Present	**0.5049**	-
	FE Upper bound	Belytschko & Hodge, 1970	0.5220	3.3875
Plate with semicircular edge notches	Predictor	Present	**0.5578**	-
	Mixed FE	Casciaro & Cascini, 1982	0.5680	1.8267

Table 6.11 Comparative summary table for plate problems with different carvings. Discrepancy is computed relative to the present solution.

Again, as in table 6.6 the value attained by the present solution is given in bold type in the fourth column. These results show a good level of closeness, which can be considered appropriate for the present applications.

6.3 Comparison with a strict upper and lower bound solution

A very important and recent limit analysis research work is due to Ciria and Peraire [5], in which a *purely static finite element solution space* is defined for the solution through the *static principle* leading to a *lower bound*, along with the definition of a *purely kinematic finite element solution space* for the solution through the *kinamatic principle* to obtain an *upper bound*. Interior-point optimisation tools in the form of *second-order cone programming* were used to maximize a specific *static* functional to attain a lower bound, as well as in order to minimize a *kinematic* functional to obtain an upper bound to the collapse multiplier. An adaptive refinement strategy in line with the procedure originally proposed in the present research was also used in their work with impressive results for *plane stress* and *plane strain* modelling. This adaptive scheme is based on a local *bound gap* contribution, which is used as the adaptivity control parameter or *adaptive indicator*, as in the present proposal.

This section is devoted to comparing the results attained by Ciria and Peraire in the case of *plane stress* modelling, for which they present a couple of test cases as will be described in what follows.

The results out of this investigation are of crucial importance to the present work because they provide an excellent set of reference numerical results covering two important aspects permitting a reliable comparison:

i). Purely discretized static and kinematic spaces are defined to capture strict upper and lower bounds.

ii). The same adaptivity strategy as the one proposed in the present work is used.

6.3.1 *Tapered unsymmetrical cantilever beam*

The tapered beam problem setting is illustrated in figure 6.27, showing the tangential load distribution acting over the right face and giving the original coarse mesh definition. This problem has been resolved with a uniform refinement procedure, as well as an adaptive refinement procedure, to make a close comparison with the results obtained by the reference work. A yielding stress value of $\sigma_y = \sqrt{3}$ and b=1 (off-plane thickness) have been used.

As in most of the previous cases, an exact solution for this problem is not available, so dependence on the coincidence between the present results and the results obtained by Ciria and Peraire will be emphasised to assess the performance of the present solution.

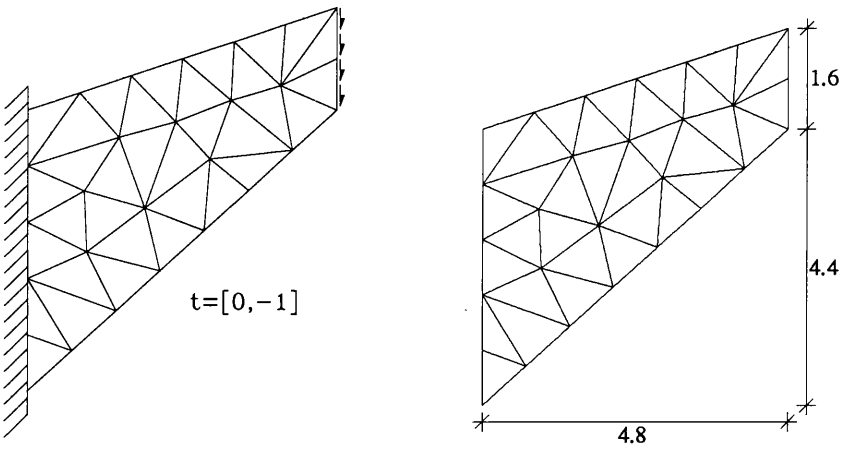

Figure 6.27 Problem setting for the tapered cantilever beam

6.3.1a) *Uniform refinement*

In figure 6.28 the velocity field of a coarse mesh solution step is presented, corresponding to the mode of failure of the body. Note that the actual velocity values are not relevant. Only the velocity field configuration is important to determine the *failure mechanism* resulting from the application of a given load configuration.

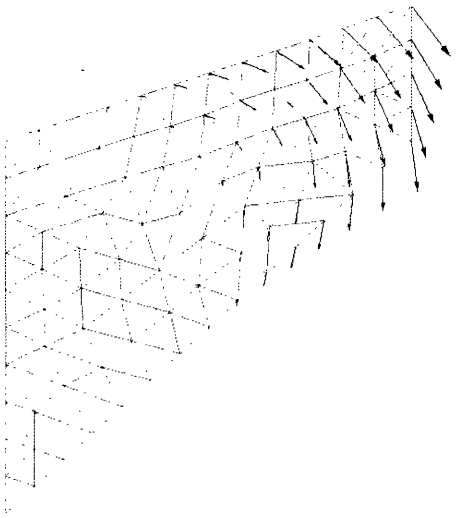

Figure 6.28 Velocity field for a coarse uniform mesh solution (step 1)

A series of three uniform refinement steps are shown in figure 6.29, depicting the deformed mesh over a phantom undeformed mesh.

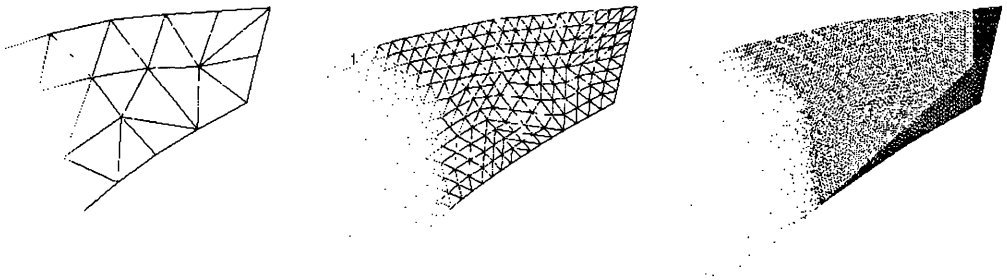

Original mesh Inermediate mesh Final mesh

Figure 6.29 Deformed over original mesh for three uniform refinement steps

Figure 6.30 presents the distribution of *Von Misses stresses* and the *equivalent strain rate* over the domain.

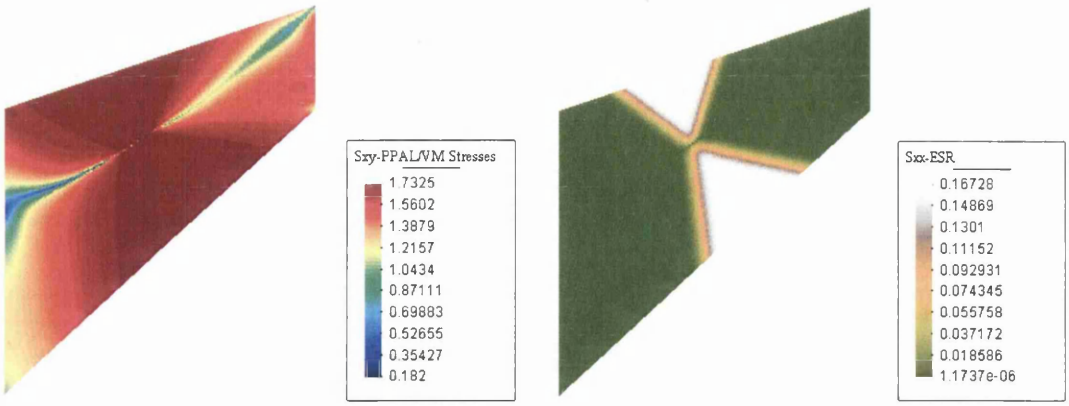

Figure 6.30 Von Mises stress ($\sigma_y = \sqrt{3}$) and equivalent strain rate distributions for the tapered beam

The stress distribution shows a broad plastic region in dark red indicating an area of significant plastic dissipation. A high straining zone in bright colours (white to green) is observed over the equivalent strain rate distribution. Elements in this area actually contribute heavily to the plastic dissipation. The dark green areas lead to a virtually zero contribution to the plastic work rate regardless of the local stress distribution. These represent regions of rigid-body motion.

The bound progression graph for the uniform refinement sequence is presented in figure 6.31. A very small discrepancy in the upper bound values (of 0.061%) between the reference and present solutions is observed, justifying the omission of the reference upper bound progression in figure 6.31 (see comments below).

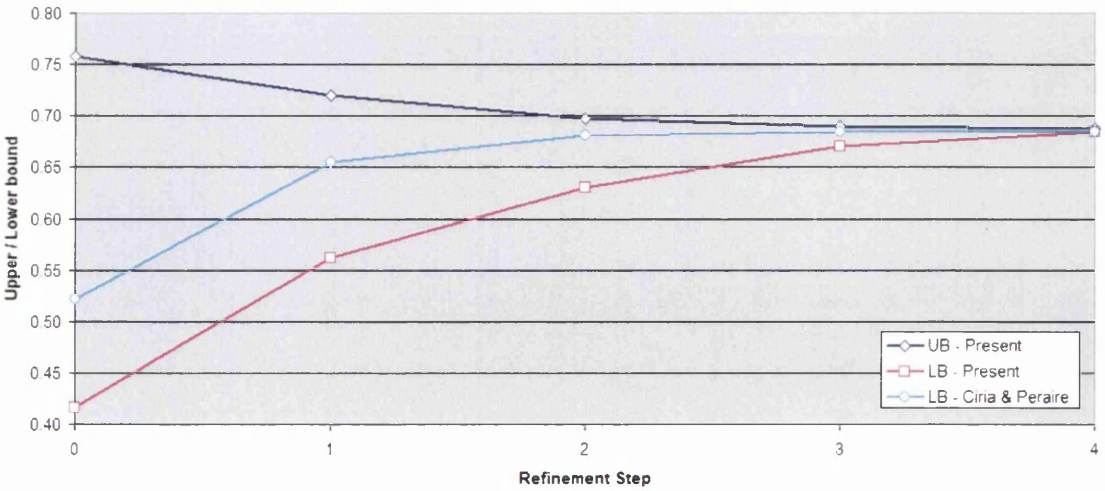

Figure 6.31 Bound progression for the tapered cantilever beam – *uniform refinement*

The numerical results for this uniform refinement sequence are presented in tables 6.12a) and 6.12b); these show the results for this test case as obtained by Ciria and Perarire [5] and through the present work, respectively. Both tables are given in standard format.

Tappered Cantilever Beam / Uniform refinement / Ciria & Peraire						
Step i	Number of Elements	Upper Bound γ_H	Lower Bound $\hat{\gamma}_h$	Predictor p_i	Bound Gap g_i	Deviation δ_i (%)
0	34	0.75759	0.52186	0.63973	0.23573	18.4243
1	136	0.71936	0.65432	0.68684	0.06504	4.7347
2	544	0.69704	0.68079	0.68892	0.01625	1.1794
3	2176	0.68983	0.68349	0.68666	0.00634	0.4617
4	8704	0.68662	0.6844	0.68551	0.00222	0.1619

Table 6.12a. Reference bound progression table for cantilever beam – *uniform refinement*

Tappered Cantilever Beam / Uniform refinement / Present						
Step i	Number of Elements	Upper Bound γ_H	Lower Bound $\hat{\gamma}_h$	Predictor p_i	Bound Gap g_i	Deviation δ_i (%)
0	34	0.75805	0.41621	0.58713	0.34185	29.1117
1	136	0.71973	0.56188	0.64080	0.15784	12.3160
2	544	0.69708	0.63007	0.66357	0.06702	5.0496
3	2176	0.68992	0.66938	0.67965	0.02054	1.5112
4	8704	0.68675	0.68351	0.68513	0.00324	0.2368

Table 6.12b. Present bound progression table for cantilever beam – *uniform refinement*

An important observation to make in these tables is the closeness in the *upper bound* computation by both of the solution procedures. As indicated, the deviation between the upper bound values has a maximum of 0.061%, so that it is acceptable to omit one of the two upper bound progressions in the graph, as can be observed in figure 6.31. In this and the following sequences, only the upper bound progression obtained by the present solution has been plotted.

In the graphical results shown in figure 6.31, a noticeable difference between both *lower bound* approaches is observed. Recall that the present solution uses a set of recovered stress definitions that actually have their origin in a discontinuous velocity field. No recovering method is known to capture the precise stress distribution that produces similar results as those obtained by a strict static analysis, that is, one that is based on stresses rather than on velocities as the solution variables. However, a good convergence behaviour is observed for the sequence resulting from the present

solution. This convergence property leads to an enclosing interval at the end of the sequence, which coincides with that generated by the strict lower bound procedure.

Figure 6.32 shows a convergence plot comparing the results for the reference and the present solution. This graph is based on the total bound gap.

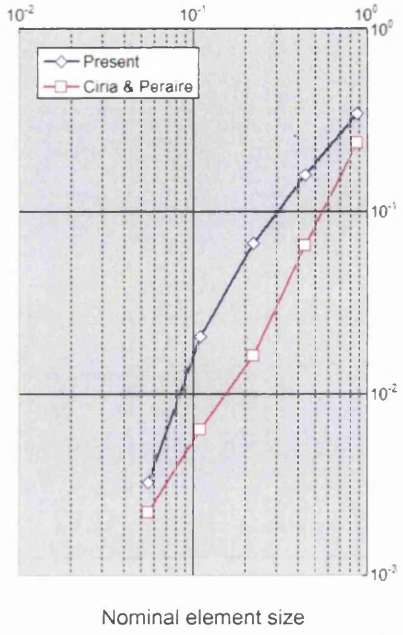

Figure 6.32 Convergence graph: *Nominal element size versus gap,* for the reference and the present solutions.

This plot has to be read from right to left, that is, the rightmost points corresponding to *step 0* and progressing through to the leftmost points to *step 4*, for the present sequence. With this in mind, for the reference results, we find a convergence order around $\mathcal{O}(h^2)$ between *step 0* and *step 2*, changing to around $\mathcal{O}(h^{1.5})$ for the rest of the sequence. Meanwhile, for the present solution we observe a convergence starting just above $\mathcal{O}(h)$ for the first segment (between *step 0* and *step* 1) and varying towards a final rate near $\mathcal{O}(h^3)$.

6.3.1b) *Adaptive refinement*

A sequence of results similar to those of the uniform refinement scheme is now presented for the problem in figure 6.27, but under an *adaptive refinement* procedure.

A value of $\kappa = 0.005$ has been used in the refinement criteria. The sequence of refined meshes is given in figures 6.33a, 6.33b and 6.33c.

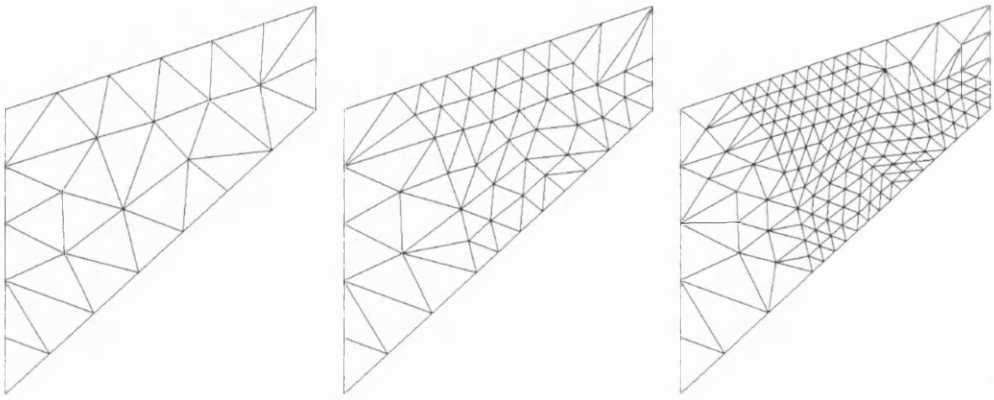

Step 0 Step 1 Step 2

Figure 6.33a. A sequence of refined meshes for the tapered cantilever beam

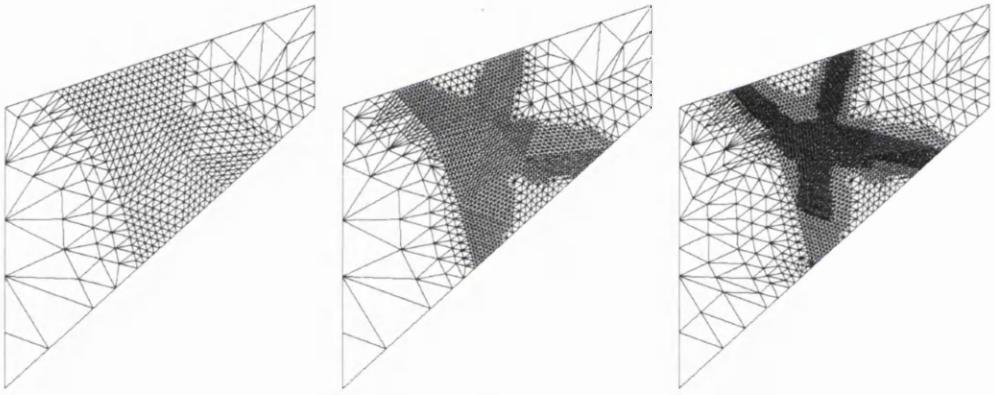

Step 3 Step 4 Step 5

Figure 6.33b. A sequence of refined meshes for the tapered cantilever beam (continued)

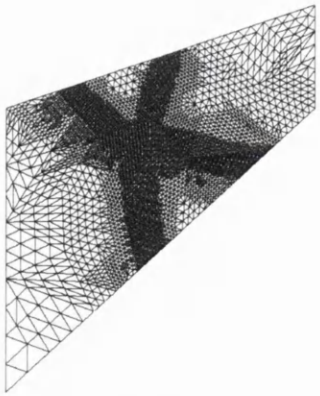

Final

Figure 6.33c. The final refined mesh for the tapered cantilever beam (continued)

These meshes relate to the comparative bound progression shown in figure 6.34.

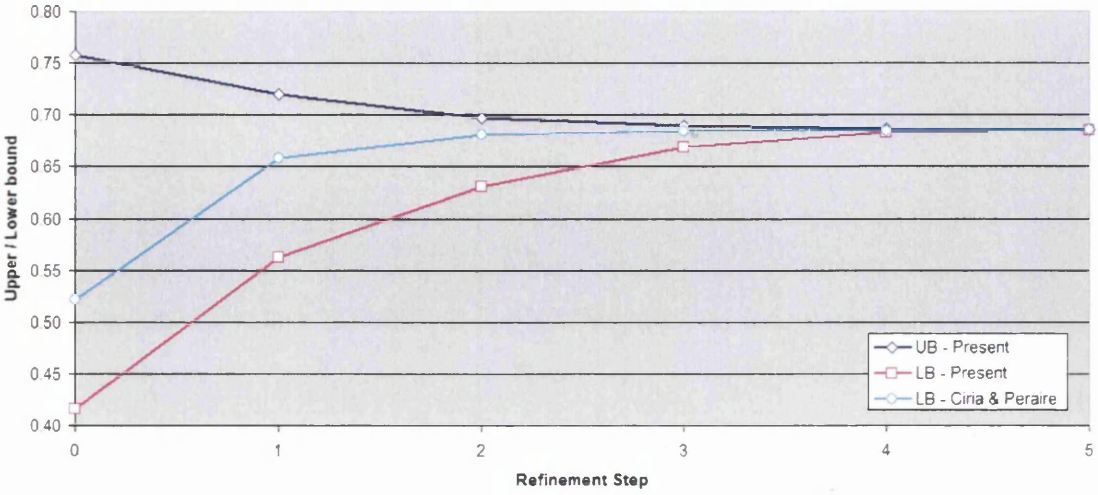

Figure 6.34 Bound progression for the tapered cantilever beam – *adaptive refinement*

Similar comments can be made over the results of this adaptive scheme to those made for the uniform procedure, but in addition a clear difference on the number of elements produced by both solutions can be observed (see tables 6.13a. and 6.13b.).

Tappered Cantilever Beam / Adaptive refinement / Ciria & Peraire						
Step i	Number of Elements	Upper Bound γ_H	Lower Bound $\hat{\gamma}_h$	Predictor p_i	Bound Gap g_i	Deviation δ_i (%)
0	34	0.75759	0.52186	0.63973	0.23573	18.4243
1	90	0.71951	0.65782	0.68867	0.06169	4.4790
2	300	0.69704	0.68079	0.68892	0.01625	1.1794
3	882	0.68989	0.68349	0.68669	0.00640	0.4660
4	2450	0.68667	0.68440	0.68554	0.00227	0.1656
5	5506	0.68549	0.68459	0.68504	0.00090	0.0657

Table 6.13a. Reference bound progression table for cantilever beam – *adaptive refinement*

Tappered Cantilever Beam / Adaptive refinement / Present						
Step i	Number of Elements	Upper Bound γ_H	Lower Bound $\hat{\gamma}_h$	Predictor p_i	Bound Gap g_i	Deviation δ_i (%)
0	34	0.75805	0.41621	0.58713	0.34185	29.1117
1	90	0.71982	0.56304	0.64143	0.15679	12.2216
2	301	0.69698	0.63043	0.66371	0.06655	5.0132
3	960	0.68981	0.66921	0.67951	0.02061	1.5162
4	2987	0.68663	0.68326	0.68495	0.00337	0.2457
5	7180	0.68543	0.68536	0.68539	0.00007	0.0052

Table 6.13b. Present bound progression table for cantilever beam – *adaptive refinement*

The difference in number of elements obtained with both formulations is clearly due to the difference in the distribution of the local contributions to the total bound gap. A more precise local contribution is attributed to the strict lower bound solution by Ciria and Peraire. Apart from the higher number of elements produced in the present solution, a very close behaviour between the two approaches can be observed.

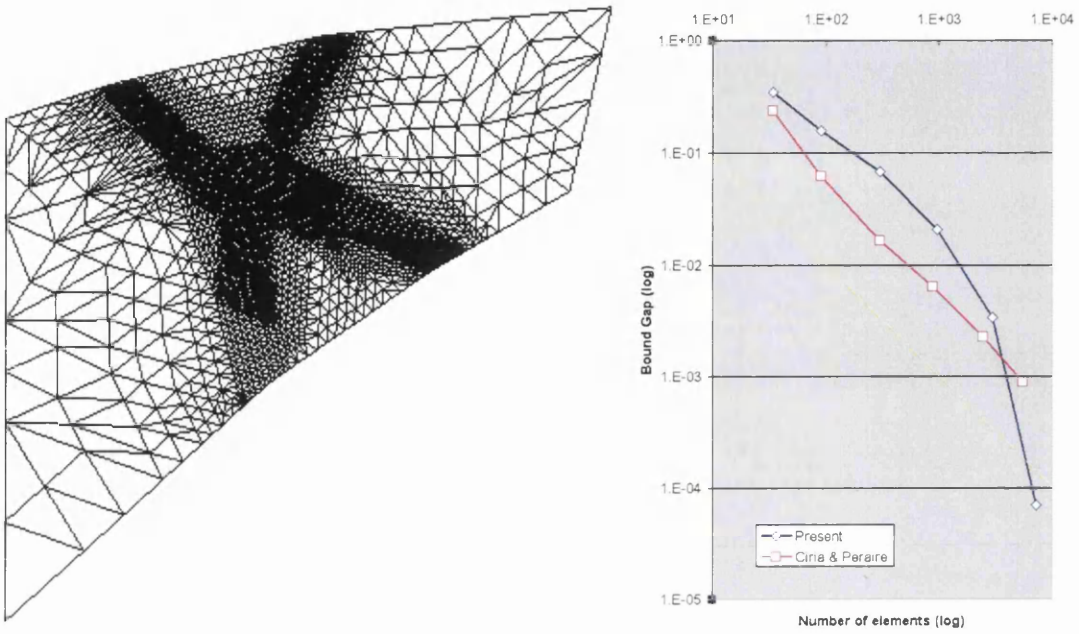

Deformed mesh at step 5 Convergence curve

Figure 6.35 Refined mesh at step 5 and convergence plot for the reference and present solutions.

The final deformed refined mesh is depicted in figure 6.35 along with the convergence plot for this adaptive process; a close plot to that of figure 6.32 is observed, except for the additional fifth step taken in this last sequence. Recall that the convergence plots are based on the total bound gap. Overall the same order of convergence as those of the uniform refinement scheme can be drawn out of these results. In both schemes the proposed solution method seems to converge at a higher rate near the exact solution.

Finally, a short sequence of deformed and refined meshes is presented in figure 6.36 for this adaptive scheme, again showing the reference non-deformed mesh. Note that the process ends with a finer mesh generated along the neighbourhood of the lines of high strain rate gradient, as observed in figure 6.30 over the strain rate distribution. These lines draw zones where slip-lines occur.

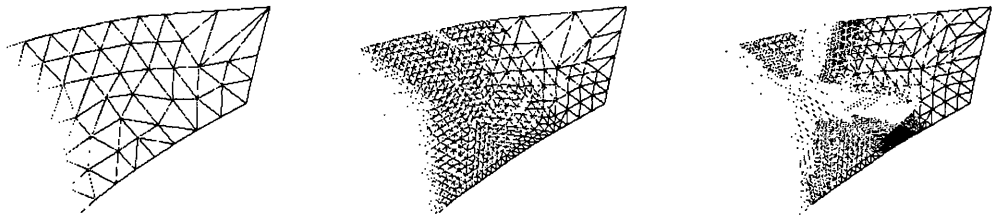

At step 1 Intermediate mesh Final mesh

Figure 6.36 Deformed over original mesh for three adaptive refinement steps

6.3.2 *Square slotted block*

The second test case to be compared with the results obtained by Ciria and Peraire [5] corresponds to the problem described in figure 6.37.

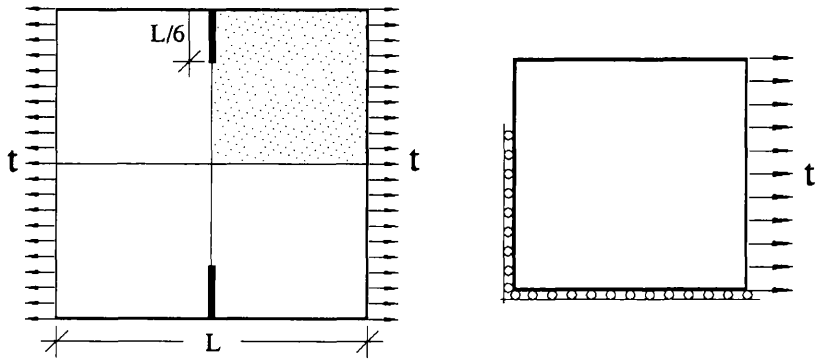

i) *ii)*

Figure 6.37 The square slotted block problem setting

A unit stress is applied as load, a yielding stress value of $\sigma_y = \sqrt{3}$ and a value of L=2 and b=1 (off-plane thickness) have been used. A refinement criteria as that of section 6.3.1 is used for this problem. Similarly, the results of the present procedure will be assessed by comparison to the results obtained by Ciria and Peraire [5].

6.3.2a) *Uniform refinement*

The velocity field produced from the kinematic solution is presented in figure 6.38, again for a conveniently coarse mesh.

Observe a noticeable rigid-body motion of the upper triangular half, and a velocity pattern along a 45° line, originating near the slot base.

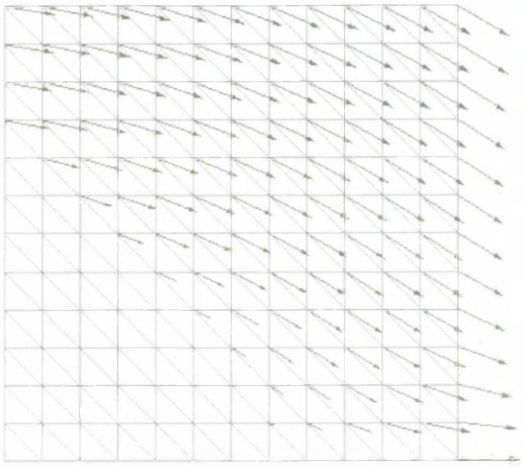

Figure 6.38 Velocity field for a coarse uniform mesh solution (at step 2)

A short series of mesh refinement steps are presented in figure 6.39.

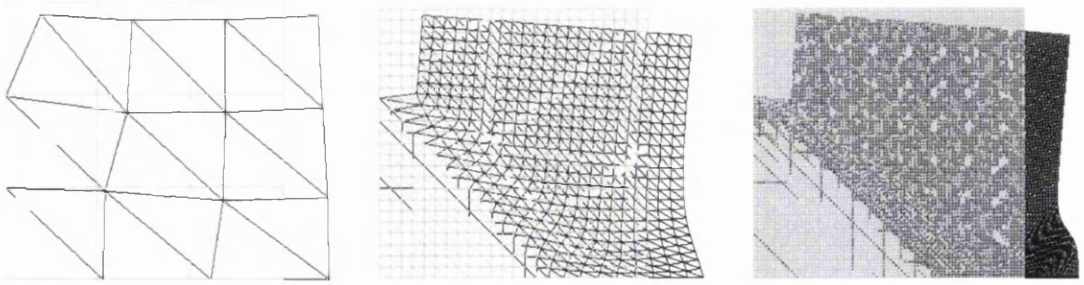

Original mesh Intermediate mesh Final mesh

Figure 6.39 Deformed over original mesh for three uniform refinement steps

Description of the *Von Mises stress* and *equivalent strain rate* distribution over the volume are depicted in figure 6.40.

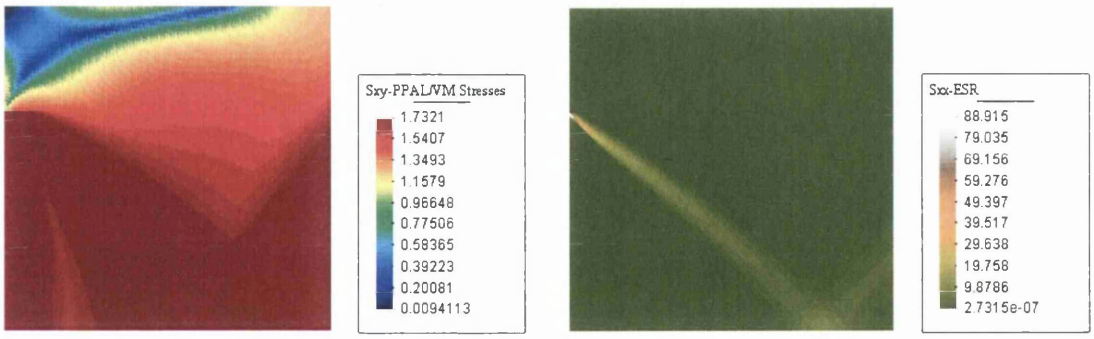

Figure 6.40 Von Mises stress ($\sigma_y = \sqrt{3}$) and equivalent strain rate distributions for the slotted block

Notice the *v-shape* pattern drawn by the distribution of the *equivalent strain rate* in a near 45° angle. The centre line along these fringes marks the most probable location for the occurrence of slip-lines. Also note again, that the area of significant strain rate is completely enclosed by the plastic zones in dark red working at the limiting stress level in the stress distribution graph; rigid-body motion areas are shown in dark green over the equivalent strain rate graph.

The bound progression for the uniform refinement sequence is presented in figure 6.41, where again only the upper bound sequence for the present solution procedure is plotted, as the maximum deviation between the reference and the present values is 0.002% (see tables 6.14a. and 6.14b., and related comments).

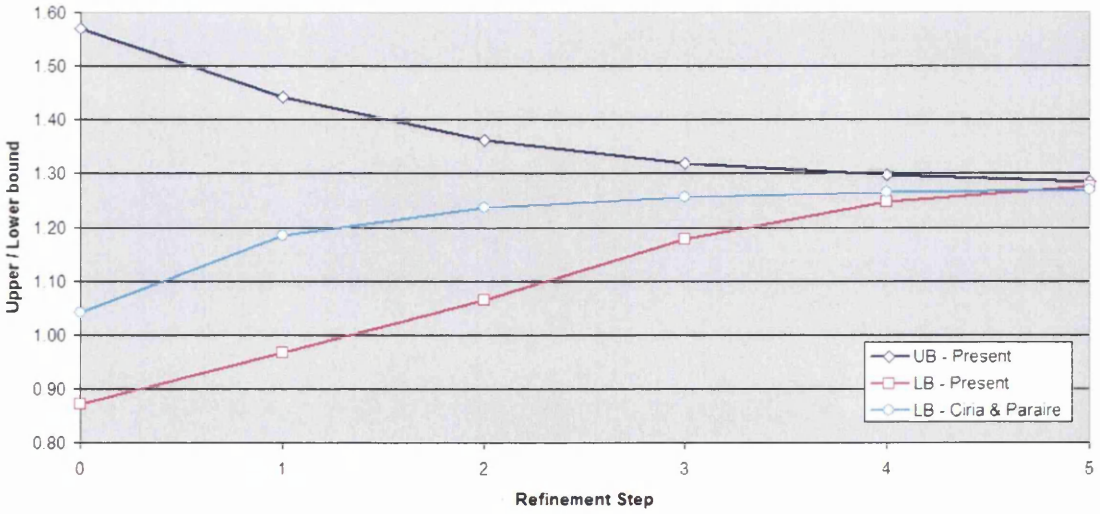

Figure 6.41 Bound progression for the slotted block – *uniform refinement*

Tables 6.14a and 6.14b list the reference and present values plotted in figure 6.41 for the bounds sequence.

Slotted Square Block / Uniform refinement / Ciria & Peraire						
Step i	Number of Elements	Upper Bound γ_H	Lower Bound $\hat{\gamma}_h$	Predictor p_i	Bound Gap g_i	Deviation δ_i (%)
0	18	1.56900	1.04140	1.30520	0.52760	20.2115
1	72	1.44080	1.18300	1.31190	0.25780	9.8254
2	288	1.36190	1.23520	1.29855	0.12670	4.8785
3	1152	1.31830	1.25530	1.28680	0.06300	2.4479
4	4608	1.29600	1.26390	1.27995	0.03210	1.2540
5	18432	1.28440	1.26790	1.27615	0.01650	0.6465

Table 6.14a. Reference bound progression table for the slotted block – *uniform refinement*

Slotted Square Block / Uniform refinement / Present						
Step i	Number of Elements	Upper Bound γ_H	Lower Bound $\hat{\gamma}_h$	Predictor p_i	Bound Gap g_i	Deviation δ_i (%)
0	18	1.56903	0.87065	1.21984	0.69839	28.6262
1	72	1.44078	0.96655	1.20367	0.47423	19.6995
2	288	1.36187	1.06523	1.21355	0.29664	12.2221
3	1152	1.31832	1.17749	1.24790	0.14082	5.6424
4	4608	1.29600	1.24621	1.27110	0.04979	1.9587
5	18432	1.28442	1.27463	1.27953	0.00979	0.3824

Table 6.14b. Present bound progression table for the slotted block – *uniform refinement*

Note the good value-by-value agreement of the results for the upper bound values in both approaches, roughly ten times better than for the tapered cantilever beam.

Figure 6.42 depicts the convergence rate coming out of both these sequences. Note the almost perfect linear $\mathcal{O}(h)$ convergence rate for the reference gap values. For the present solution an average computation suggests a convergence rate of $\mathcal{O}(h^{1.25})$. An approximate quadratic convergence $\mathcal{O}(h^2)$ is observed for the last two observations.

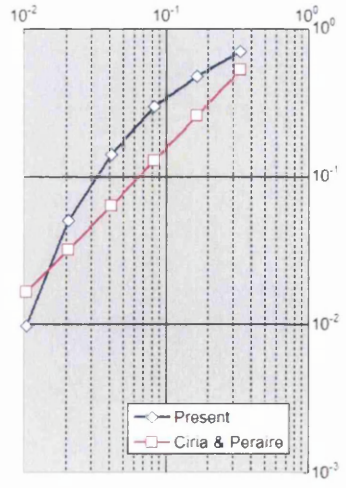

Figure 6.42 Convergence graph: *Nominal element size versus gap,*
for the reference and the present solutions.

6.3.2b) *Adaptive refinement*

As well as for the tapered cantilever beam, the adaptive approach is compared next to the results obtained by Ciria and Peraire [5]. Figure 6.43a to 6.43d give the sequence of adaptively refined meshes for the slotted block problem.

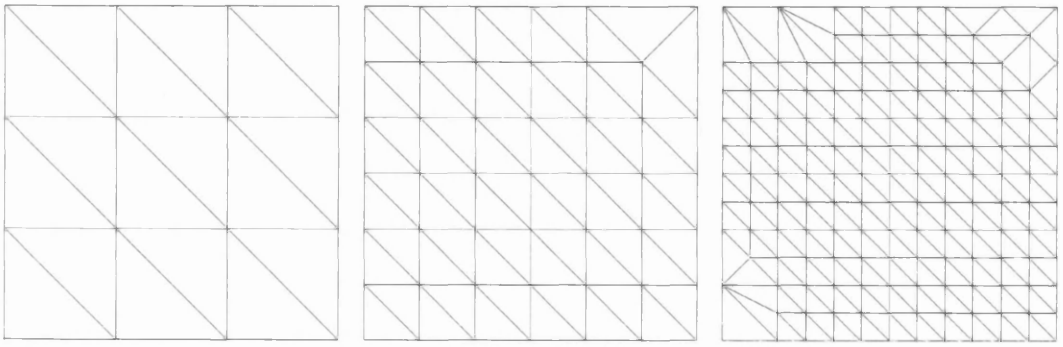

Step 0 Step 1 Step 2

Figure 6.43a. A sequence of refined meshes for the slotted block

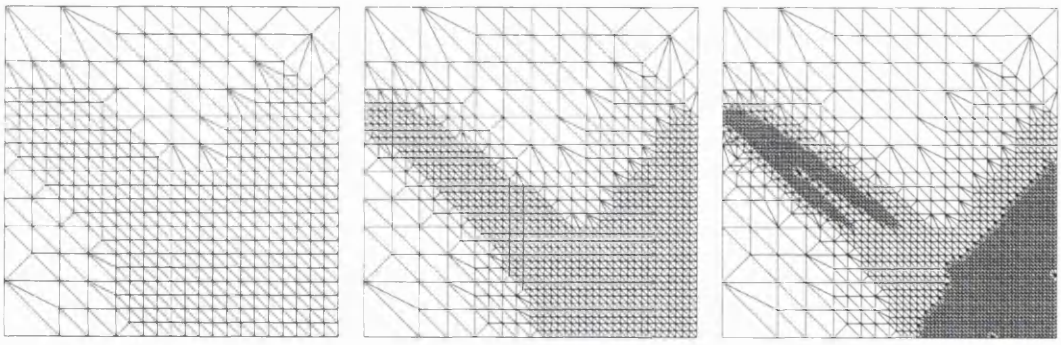

Step 3 Step 4 Step 5

Figure 6.43b. A sequence of refined meshes for the slotted block (continued)

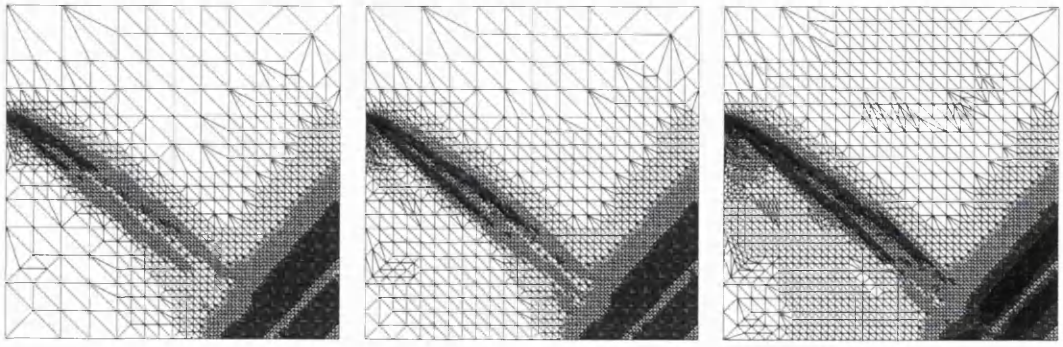

Step 6 Step 7 Step 8

Figure 6.43c. A sequence of refined meshes for the slotted block (continued)

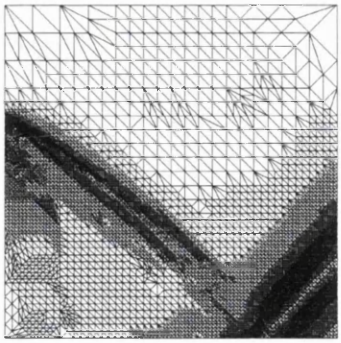

Final

Figure 6.43d. The final refined mesh for the slotted block (continued)

The bound sequence is drawn in figure 6.44, under the same well-known considerations. Although this time a deviation of 0.515% is observed between the upper bound reference values and the ones obtained through the present solution procedure. This difference suggests that the disparity observed in the total bound gap for both approaches, when it comes to a large sequence, causes a noticeable difference in the number of elements produced by the refinement process, leading to differences in the upper bound value. Recall that a higher number of elements over the domain implies a broader area of fine element size, consequently producing a lower upper bound value.

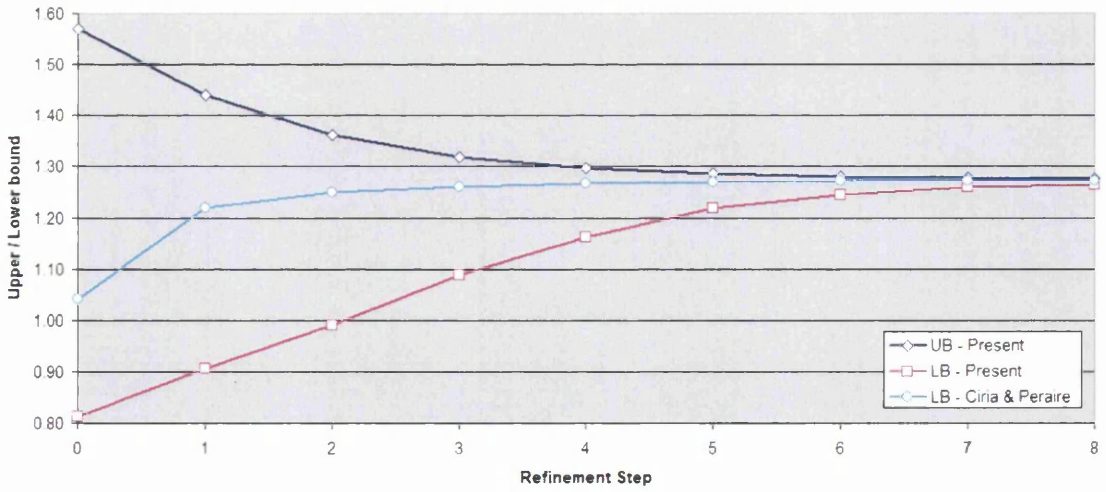

Figure 6.44 Bound progression for the slotted block – *adaptive refinement*

The numerical bound values are listed in table 6.15a and 6.15b in the customary fashion. Note a high increase in the number of elements from step 3 for the present solution proposal with respect to the reference solution.

Slotted Square Block / Adaptive refinement / Ciria & Peraire						
Step i	Number of Elements	Upper Bound γ_H	Lower Bound $\hat{\gamma}_h$	Predictor p_i	Bound Gap g_i	Deviation δ_i (%)
0	18	1.56900	1.04140	1.30520	0.52760	20.2115
1	70	1.44020	1.21810	1.32915	0.22210	8.3550
2	254	1.36150	1.24960	1.30555	0.11190	4.2856
3	483	1.32020	1.25930	1.28975	0.06090	2.3609
4	714	1.30280	1.26630	1.28455	0.03650	1.4207
5	1082	1.29070	1.26900	1.27985	0.02170	0.8478
6	1550	1.28550	1.27030	1.27790	0.01520	0.5947
7	2538	1.28080	1.27100	1.27590	0.00980	0.3840
8	3564	1.27850	1.27140	1.27495	0.00710	0.2784

Table 6.15a. Reference bound progression table for the slotted block – *adaptive refinement*

Slotted Square Block / Adaptive refinement / Present						
Step i	Number of Elements	Upper Bound γ_H	Lower Bound $\hat{\gamma}_h$	Predictor p_i	Bound Gap g_i	Deviation δ_i (%)
0	18	1.56903	0.81260	1.19082	0.75643	31.7611
1	70	1.44022	0.90633	1.17327	0.53388	22.7519
2	264	1.36150	0.98981	1.17565	0.37169	15.8077
3	746	1.31830	1.08924	1.20377	0.22906	9.5143
4	1971	1.29608	1.16272	1.22940	0.13336	5.4240
5	4449	1.28461	1.21872	1.25166	0.06590	2.6324
6	9159	1.27918	1.24549	1.26233	0.03370	1.3347
7	10921	1.27698	1.25883	1.26791	0.01815	0.7156
8	21371	1.27425	1.26447	1.26936	0.00979	0.3856

Table 6.15b. Present bound progression table for the slotted block – *adaptive refinement*

A similar gap convergence plot can be drawn out of these results as shown in figure 6.45, along with the final refined deformed mesh.

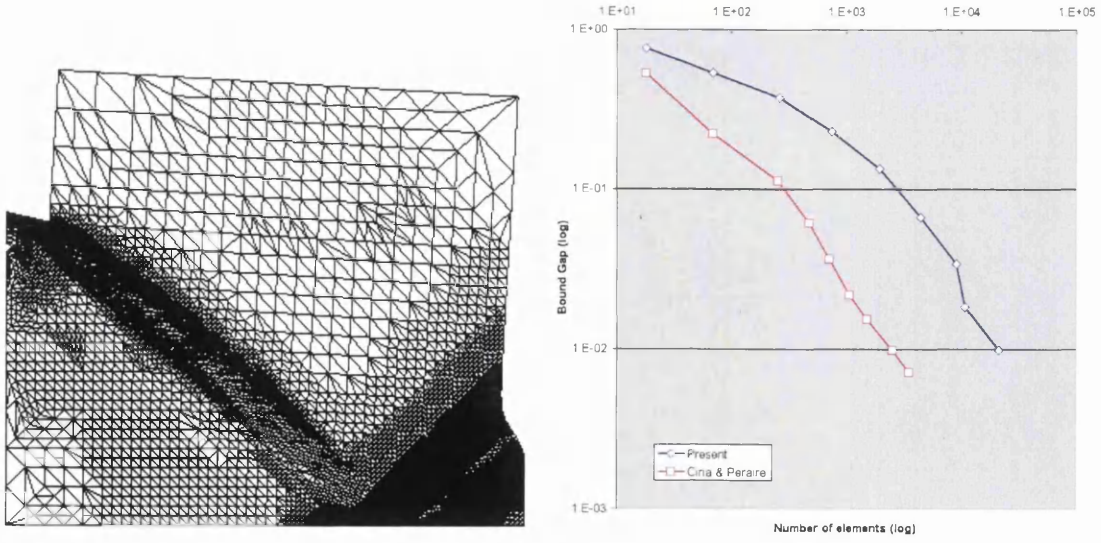

Deformed final mesh

Convergence curve

Figure 6.45 Final refined mesh and convergence plot for the reference and present solutions.

Note however that in this case the reference gap values produce a varying convergence slope leading to an averaging order of $\mathcal{O}\left(h^{0.77}\right)$. It is interesting to note that based on an average slope, the order of the present solution gap convergence is also $\mathcal{O}\left(h^{0.77}\right)$.

Finally, a short sequence of adaptively refined deformed meshes for the slotted block is presented in figure 6.46.

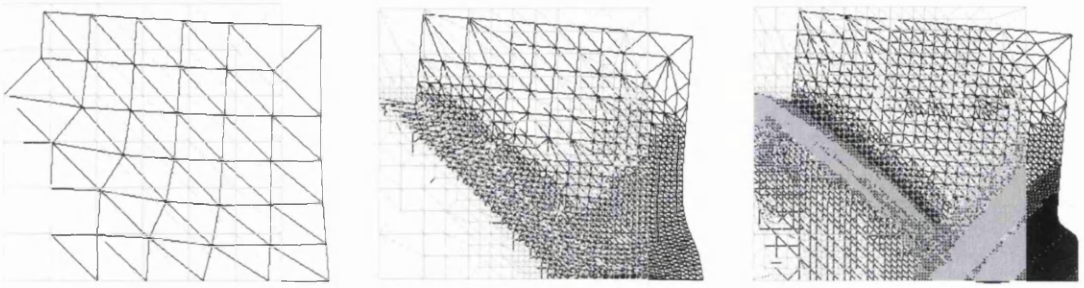

At step 1 Intermediate mesh Final mesh

Figure 6.46 Deformed over original mesh for three adaptive refinement steps

6.4 Comparison between the proposed *minimizer* and *integral* solutions

In the preceding sections 6.1 and 6.2, all the test cases have been analysed using the solution proposal arising from this research work, namely the *integral approach*, which accounts for local contributions to the total plastic dissipation in the evaluation of the *lower bound*. As a reminder of equation (4.29), the lower bound based on this concept is given by

$$\hat{\gamma}_h = \sum_e \hat{\Pi}_t^e \left(\boldsymbol{v}_H^e\right) \Pi_p^e \left(\hat{\boldsymbol{v}}_h^e\right)$$

But as described in chapters 4 and 5, there is yet another definition proposed originally to compute the lower bound to the collapse multiplier, and is based on the *minimizer* given by

$$\hat{\gamma}_h = \min_{e=1..m_h} \hat{\gamma}_h^e \equiv \hat{\gamma}_h^E$$

as written in equation (4.19). Refer to section 4.2.3 for details on this solution procedure.

We are here concerned with the bound progression graph resulting from the application of both methods to illustrate the poor performance of the minimizer solution. For that purpose we will refer to one of the problems presented in section 6.2 to contrast graphically both lower bound procedures.

In figure 6.47 a bound progression graph is given for the *upper bound*, the *integral approach* to the *lower bound*, and finally the *minimizer approach* to the *lower bound.* This sequence corresponds to the *tapered cantilever beam* in section 6.3.1 for the uniform refinement process.

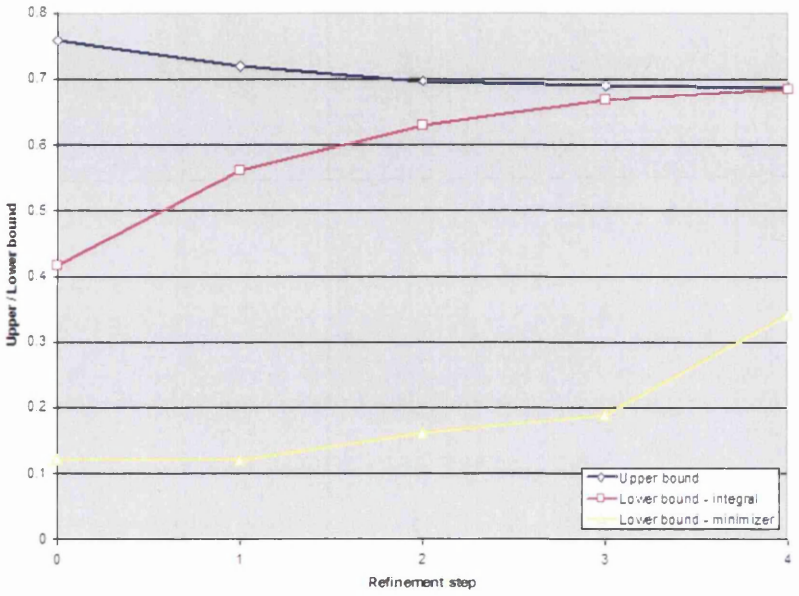

Figure 6.47 Comparative bound progression for the minimizer and integral approach to the lower bound

The *average and maximum residual force indicators* r_{ave} and $r_{\max}$ as described in appendix B, can be used to monitor the lack of equilibrium of an element when average stress distributions are applied over its edges. In chart *i*) of figure 6.48 a logarithmic plot of the progression of both indicators is given.

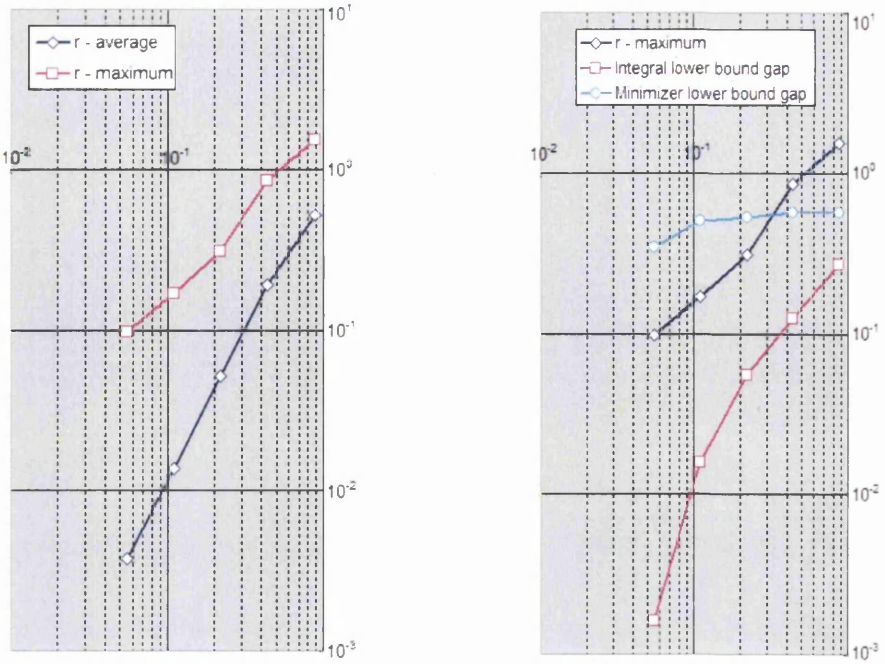

i) *ii)*

Figure 6.48 Logarithmic plot for: *i)* h versus r_{ave} and $r_{\max}$; *ii)* h versus $r_{\max}$, integral lower bound gap and minimizer lower bound gap.

From plot *i)* in figure 6.48 a clear quadratic convergence can be observed for the average residual force indicator, but a linear one is observed for the maximum residual force indicator. On the other hand, we are interested in assessing the effect of the linear convergence in $r_{\max}$ due to the nature of the minimizer proposal, which intuitively seeks for the most demanded local volume, that is the one subject to a high level of stress (on the limit) and strain. One possible form of evaluating this condition is to search for the highest level of discontinuity in stress along the element edges. This is attempted using the $r_{\max}$ indicator.

In plot *ii)* of figure 6.48 a comparison showing again the linear nature of the $r_{\max}$ convergence contrasted with the convergence of both, the lower bound *gap* obtained from the integral and the minimizer solutions. These gaps are computed as the difference between the predictor collapse multiplier for the finest mesh and the corresponding lower bound value. We can clearly observe the quadratic convergence of the integral solution against a poor convergence rate of the minimizer solution. No direct relation can be established between the $r_{\max}$ behaviour and the low numbers for

the lower bounds curve observed because many factors contribute to the results, and the effect of the rate of stress discontinuity reflected in r_{max} provides only limited explanation as to the observed results.

6.5 Beam and frame applications

In this section a series of typical 2-dimensional problems for beams and frames is presented in a simple, graphical format, to provide a sense of practicality of the present solution package for the *limit analysis in plane stress* of basic engineering problems. Comparison against some theoretical estimation of the collapse multiplier is given, when available. Some problems are provided with an *equilibrium check* to assess the level of accuracy of the solution obtained.

Typical problem and solution parameters are: a) off-plane thickness of $b=1$ and height of $H=1$; b) yield stress of $\sigma_y=\sqrt{3}$; c) solution precision of 1×10^{-5}; d) *Equivalent Strain Rate offset* of $\dot{\bar{\varepsilon}}_{offset}=1\times10^{-5}$; e) refinement parameter of $\kappa=0.005$; f) prismatic structural members; g) loads and lengths given in consistent units: $\mathbf{t}=1$ in units of *force/length* and P=1 in units of *force*; L given in units of *length.*

6.5.1 Fixed-ends beam

Figure 6.49 describes the characteristics of the solution for a typical fixed-ends beam.

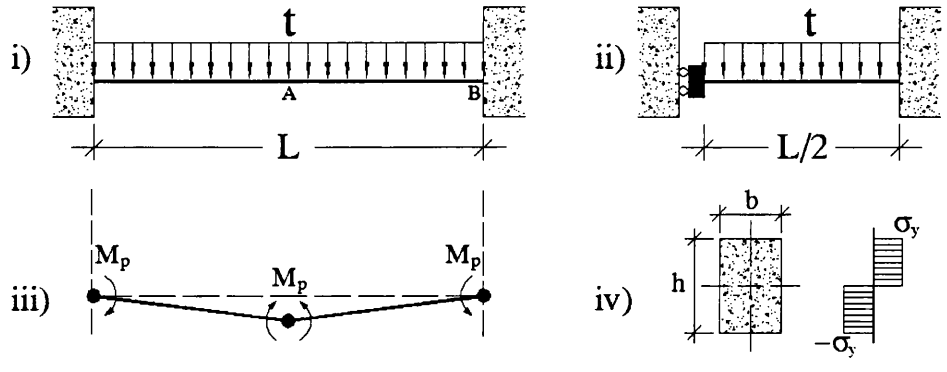

Figure 6.49 Fixed-ends beam problem setting

In this set of figures, 6.49i) gives a general description of the problem, while figure 6.49ii) depicts the actual problem setting solved due to the uniaxial symmetry. Figure 6.49iii) shows the well-known collapse mechanism for this case. Finally, in figure 6.49iv) a typical cross-section is drawn along with a yield stress distribution corresponding to a *pure plastic bending* condition, which provides a direct value for the limiting plastic moment M_p, clearly given by

$$M_p = \frac{\sigma_y b h^2}{4}$$

The results out of the present solution package for this problem are given in figure 6.50. This plot shows a comparison between the theoretical ultimate load computed from pure bending

$$t_u = \frac{16 M_p}{L^2}$$

and the bound progression obtained from the present finite element solution. It also presents a reference to a value computed from an *equilibrium check* which is a procedure that has been used to validate the collapse multiplier values obtained in some of the cases by checking equilibrium conditions on the collapsing structural member, as discussed next.

An equilibrium check can be carried out to assess the simulation results obtained. This is based on the approximate computation of the cross-sectional moment coming from the axial stress distribution of the finite element solution and applied over a specific section of the member. This computation entails the use of a structured mesh in which a given numbering order is in place. As a result a complementary algorithm is used to compute sectional moments out of stress distributions over a series of cross-sections along the collapsing structural member. The results of this procedure provide a *moment distribution graph* as shown in figure 6.52, below.

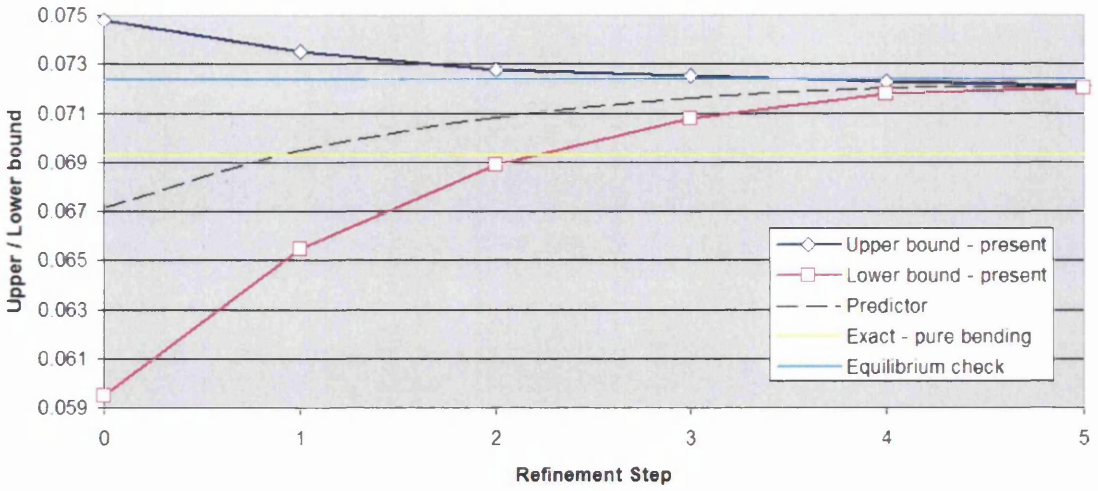

Figure 6.50 Bound progression for the fixed-ends beam

Table 6.16 lists the values corresponding to figure 6.50.

Fixed-ends beam					
Step	Upper Bound	Lower Bound	Predictor	Theoretical	Equilibrium
0	0.07480	0.05948	0.06714		
1	0.07352	0.06546	0.06949		
2	0.07276	0.06889	0.07083		
3	0.07251	0.07078	0.07164		
4	0.07225	0.07179	0.07202		
5	0.07210	0.07202	0.07206	0.06928	0.07235

Table 6.16 Bound progression list for the fixed-ends beam

The velocity field is used to describe the collapse mechanism shown in the deformation figure 6.51.

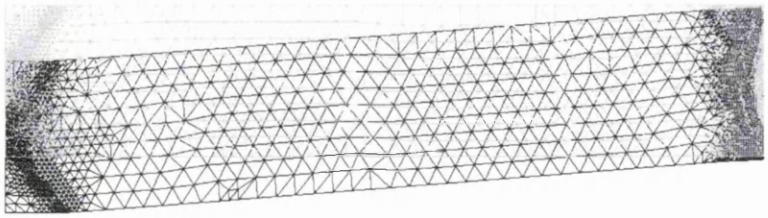

Figure 6.51 Collapse mechanism for the fixed-ends beam

Refer to the moment distribution graph for this problem, in figure 6.52. This curve gives the moments from the central section A in figure 6.49 to the extreme right section B.

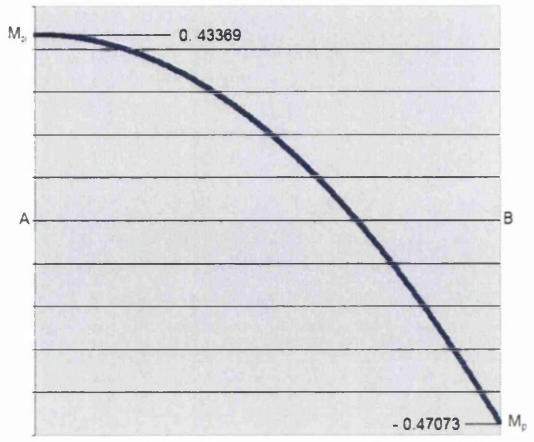

Figure 6.52 Moment distribution for the model in figure 6.54ii)

Ideally, the maximum positive and negative moments are equal due to the redistribution of moments after the formation of the first hinge on the right support. Due to various finite element modelling factors the numbers are different, but still we are most interested in the difference between these two extreme moments $M_p^+ = 0.43369$ and $M_p^- = 0.47073$ rather than on their individual values. Using simple equilibrium conditions, we can write the well-known relation

$$M_p^+ - M_p^- = \frac{t_u^{eq} L^2}{8}$$

where t_u^{eq} is the ultimate load distribution to be evaluated by equilibrium check, and $L = 10$ for this case. As a result we get $t_u^{eq} = 0.07235$ as indicated in table 6.16. A deviation of 0.40578% is obtained with this last check, as opposed to the deviation of the theoretical value: 4.0127%. The most direct explanation to the difference between theoretical multipliers and the ones obtained with the finite element simulation is given by the *pure plastic bending* assumption of the theoretical analysis, that is, these do not account for the effect of the axial and shear internal forces, whereas a finite element simulation inherently considers these effects.

6.5.2 Unsymmetrical two span beam

Figure 6.53 describes the problem setting for an *unsymmetrical two span beam* with different section members. Note that a section height of $h = \sqrt{3/2}$ is considered for segment B-C, and $h = 1$ for the segment A-B.

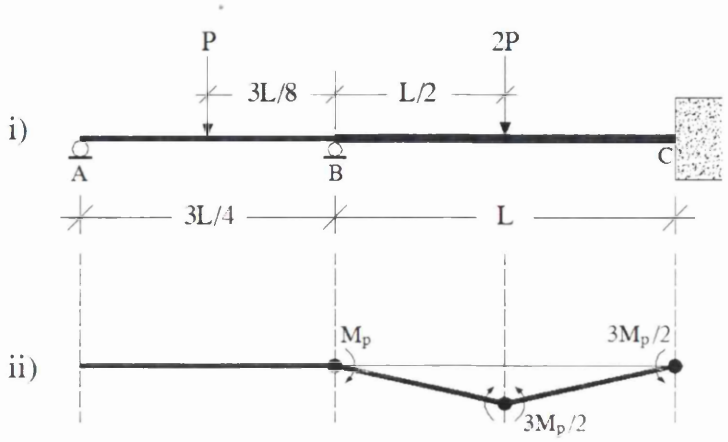

Figure 6.53 Unsymmetrical two span beam problem setting

For this case $L = 10$ units, and the segment A-B of the beam has a plastic moment capacity M_p while the segment B-C has a $1.5M_p$ plastic moment. The results obtained by the finite element simulation are depicted in figure 6.54.

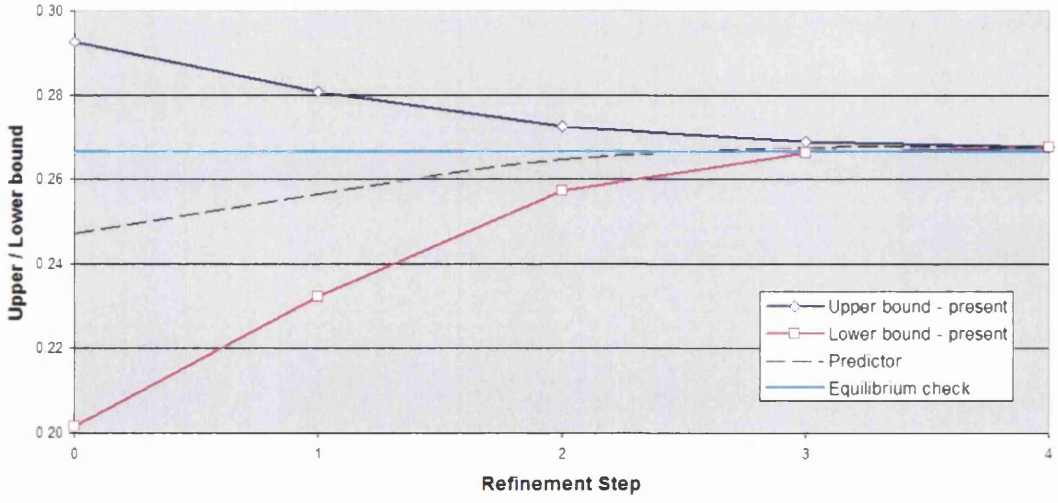

Figure 6.54 Bound progression for the continuous beam

No theoretical solution has been computed for this case, so we recur again to the equilibrium check procedure for comparison. Listing of the bounds sequence is given in table 6.17, with the equilibrium checking value computed below.

Unsymmetrical two span beam				
Step	Upper Bound	Lower Bound	Predictor	Equilibrium
0	0.29253	0.20155	0.24704	
1	0.28054	0.23217	0.25636	
2	0.27251	0.25711	0.26481	
3	0.26889	0.26618	0.26753	
4	0.26765	0.26765	0.26765	0.26639

Table 6.17 Bounds listing for the two span beam

In figure 6.55 the collapse mechanism is drawn for this two-span beam case. Note the concentration of fine elements in the plastic regions produced by the adaptive procedure, as in figure 6.51 for the fixed-ends beam.

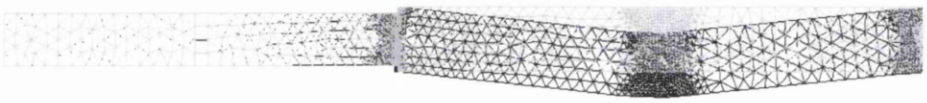

Figure 6.55 Collapse mechanism for the two span beam

The equilibrium check can be carried out by considering the *moment distribution* in figure 6.56. Only the B-C segment is graphed in accordance with the failing mechanism. Note again the slight difference between the moment value over the face at the centre of the span and at the extreme right face. Let us denote the three moment readings as $M_B^- = -0.48575$, $M^+ = 0.72348$ and $M_C^- = -0.7312$. The relation of plastic moments capacities can be checked as

$$\frac{M^+ - M_C^-}{2M_B^-} = 1.49735 \simeq 1.5$$

which meets the expectations for the moment distribution.

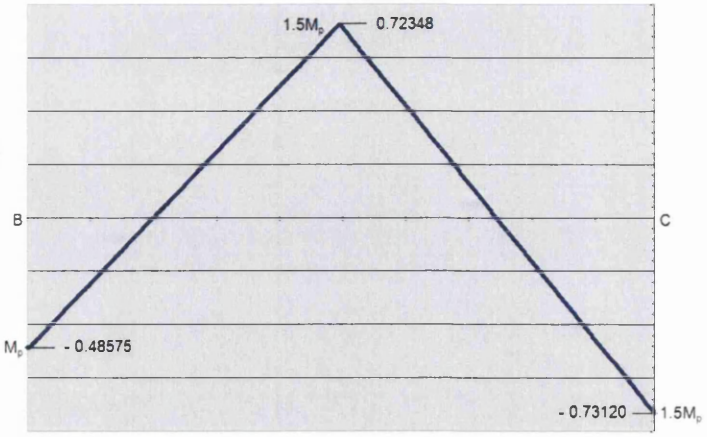

Figure 6.56 Moment distribution for the segment B-C of the two span beam

Finally, the value of P_u^{eq} reported in the *equilibrium* column in table 6.17 is computed from relation

$$M^{+} - \frac{M_B^{-} + M_C^{-}}{2} = \frac{2P_u^{eq}L}{4}$$

This yields a discrepancy of 0.4707% with respect to the reported fine mesh predictor.

6.5.3. Reticular frame with distributed load

A two storey frame taken from Chakrabarty [6] is next analysed as depicted in figure 6.57i) and subject to gravitational and wind load distribution.

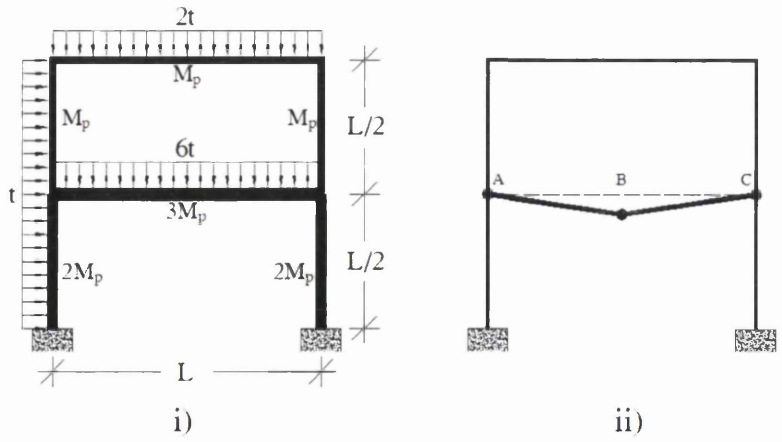

Figure 6.57 Problem setting for reticular frame W

The collapse mechanism of the failing member is drawn in figure 6.57ii). Note that the members possess different plastic moment capacity (see figure 6.57i)).

The bounds progress is shown in figure 6.58, in which a comparison with the theoretical solution and the equilibrium check is presented.

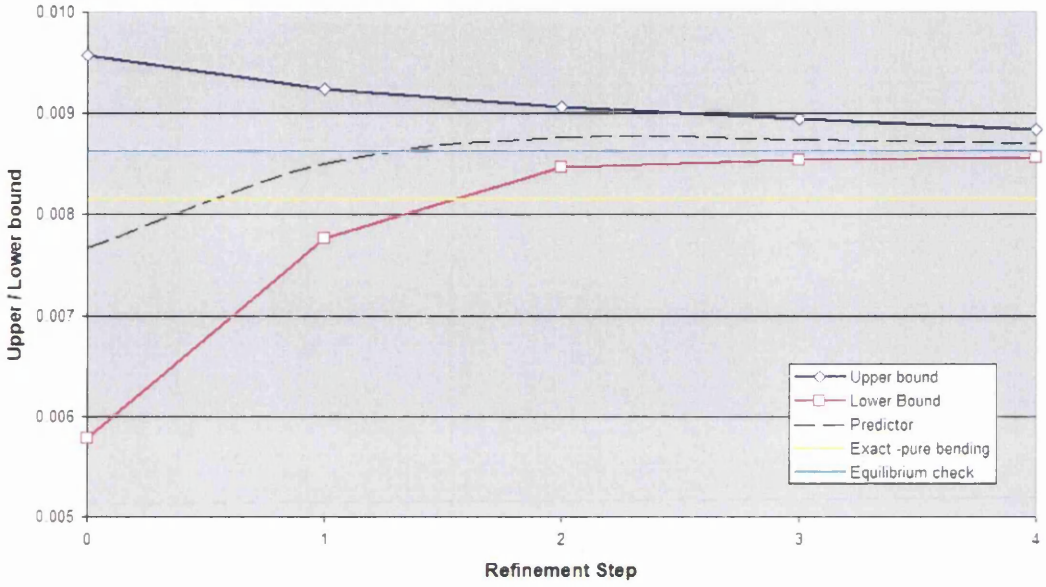

Figure 6.58 Bound progression for the reticular frame W

The bound listing is presented in table 6.18, along with the aforementioned comparison values.

Reticular frame W					
Step	Upper bound	Lower bound	Predictor	Theoretical	Equilibrium
0	9.5757E-03	5.7803E-03	7.6780E-03		
1	9.2403E-03	7.7656E-03	8.5030E-03		
2	9.0676E-03	8.4702E-03	8.7689E-03		
3	8.9406E-03	8.5390E-03	8.7398E-03		
4	8.8334E-03	8.5678E-03	8.7006E-03	8.1508E-03	8.6260E-03

Table 6.18 Bounds listing for the reticular frame W

The collapse mechanism obtained from the finite element simulation is depicted in figure 6.59.

Figure 6.59 Collapse mechanism for the reticular frame W

Observe in figure 6.59 that the L-shaped mechanism formed by the right part of the upper girder and the right upper column does not imply a collapsing condition by its own, and that the rigid-body motion of the C-shaped frame on the upper left of the mechanism suggests that the L-shaped mechanism can not occur independently.

The equilibrium check in this case uses the moment distribution in figure 6.60.

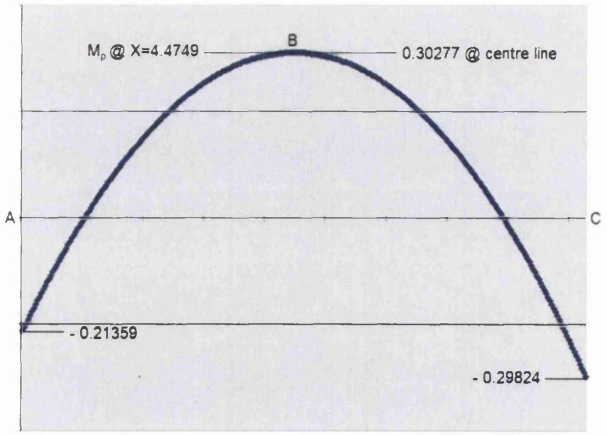

Figure 6.60 Moment distribution for the reticular frame W

If we denote the accurate moments as $M_A^- = -0.2135954$, $M_B^+ = 0.3027734$ and $M_C^- = -0.2982442$, the expression to compute t_u^{eq} is given by

$$M_B^+ - \tfrac{1}{2}\left(M_A^- + M_C^-\right) = \tfrac{6}{8} t_u^{eq} L^2$$

with $L = 9.292893$ due to the off-sided position of the sections at A and C necessary to define a structured mesh, note that the change in section forces this shifting of sections A and C.

This equilibrium check gives a deviation of 0.8574% with respect to the finite element simulation result, in contrast with a deviation of 6.3191% computed from the pure bending theoretical value.

6.5.4 L-shaped frame

In figure 6.61*i*) the problem details of an L-shaped frame taken from Jirásek and Bazant [7] are given, as well as the collapse mechanism in figure 6.61*ii*) resolved from pure plastic bending conditions.

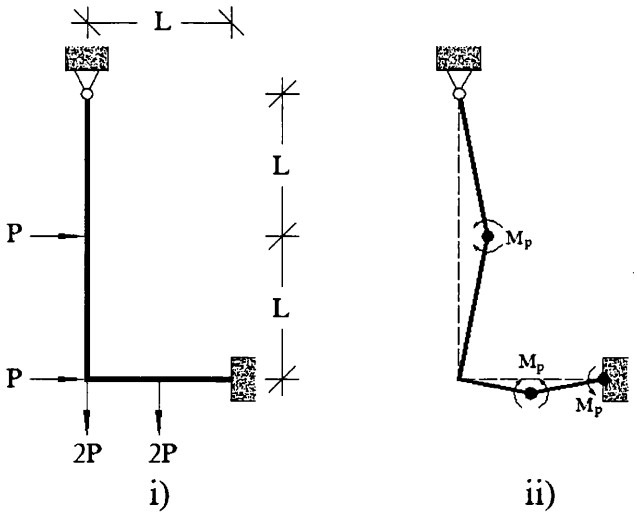

Figure 6.61 Problem setting and collapse mechanism for the L-shaped frame

The bounds sequence is presented in figure 6.62 with a comparison of the pure bending solution obtained form the reference authors.

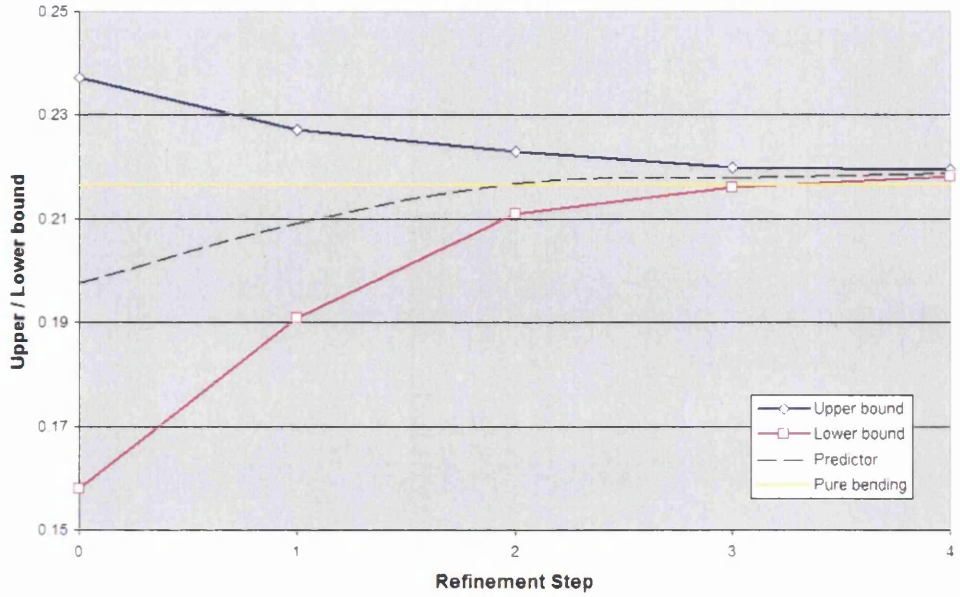

Figure 6.62 Bound progress for the L-shaped frame

As customary, the list of bound values is given in table 6.19 along with the comparison value.

L-shaped frame				
Step	Upper bound	Lower bound	Predictor	Theoretical
0	0.23726	0.15789	0.19757	
1	0.22718	0.19098	0.20908	
2	0.22301	0.21092	0.21697	
3	0.21974	0.21600	0.21787	
4	0.21937	0.21821	0.21879	0.21651

Table 6.19 List of bounds for the L-shaped frame

A discrepancy of 1.0530% is observed for the fine mesh predictor with respect to the theoretical value. The collapse mechanism using the refined deformed mesh is given in figure 6.63. Note the hinge formation according to the theoretical hinge locations.

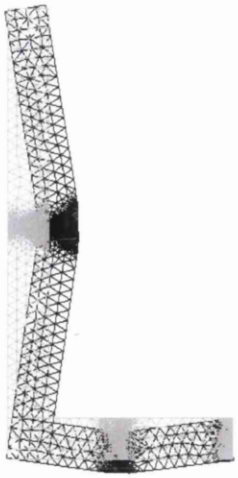

Figure 6.63 Collapse mechanism for the L-shaped frame

Jirásek and Bazant [7] arrive at a theoretical expression under pure bending conditions given by $P_u = 2.5M_p / L$ which leads to the number in table 6.19. The reference authors also solve the problem using *linear programming* taking axial forces into account and arrive at the expression $P_u = 2.303M_p / L$, which would produce a deviation of 9.6972%, a result that shifts away from our findings. Greater insight over their solution is needed here, but it escapes the intention of this presentation. However, observing details of the stress distribution we can conclude on the level of effect of the axial force at least qualitatively. In figure 6.64 the distribution of stress σ_x and σ_y is given for the L-shaped frame.

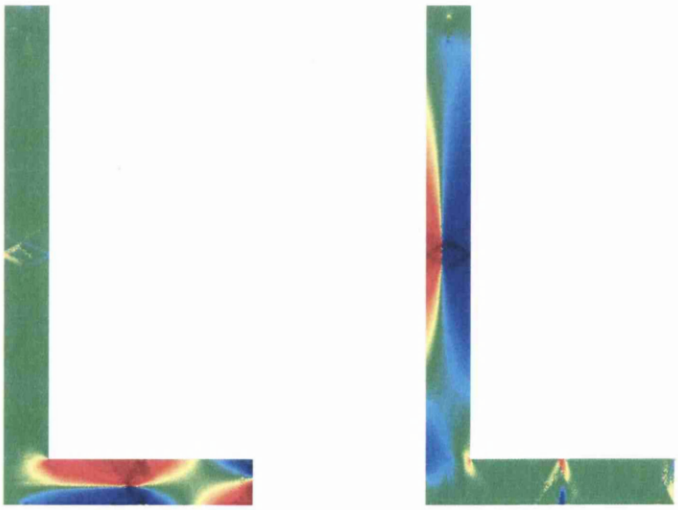

i) *ii)*

Figure 6.64 Stress distribution for the L-shaped frame: a) σ_x; b) σ_y.

In this figure, compression is given in *red* while tension in *blue.* An off-centre shifting of the neutral axis occurs at each hinge location, shifting downwards (additional compression) in the centre hinge of the horizontal member, which indicates significant compression axial force in place. Similarly, for the hinge at the right of the horizontal girder, the axis shifts upwards, signalling again the occurrence of the compressive force. Finally the centre hinge in the vertical column, showing a neutral axis shifting (additional tension) left indicates the action of a tension axial load. The axial load effect is clear, however the collapsing mode is still controlled by flexure.

6.5.5 Gabled frame

The problem description of a *gabled frame* subject to concentrated loads is shown in figure 6.65i), together with the collapse mechanism in figure 6.65ii). A single section shape is used for all members.

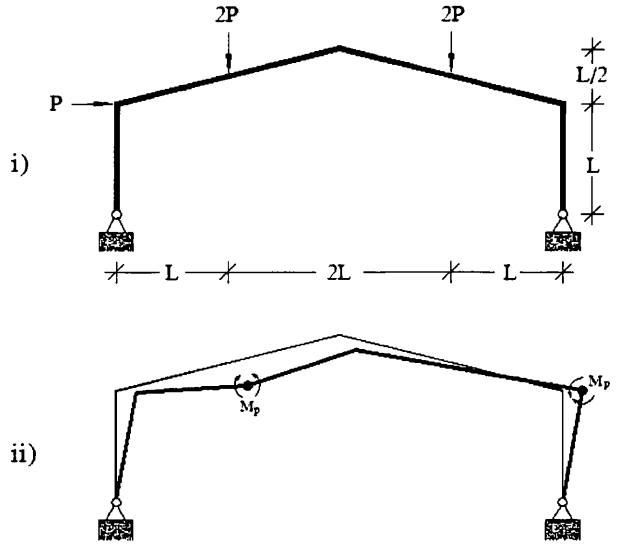

Figure 6.65 Problem setting for the gabled frame

The bounds sequence obtained for the present solution is presented in figure 6.66 along with the theoretical value of $P_u = 9M_p/11L$, taken from Beedle [8].

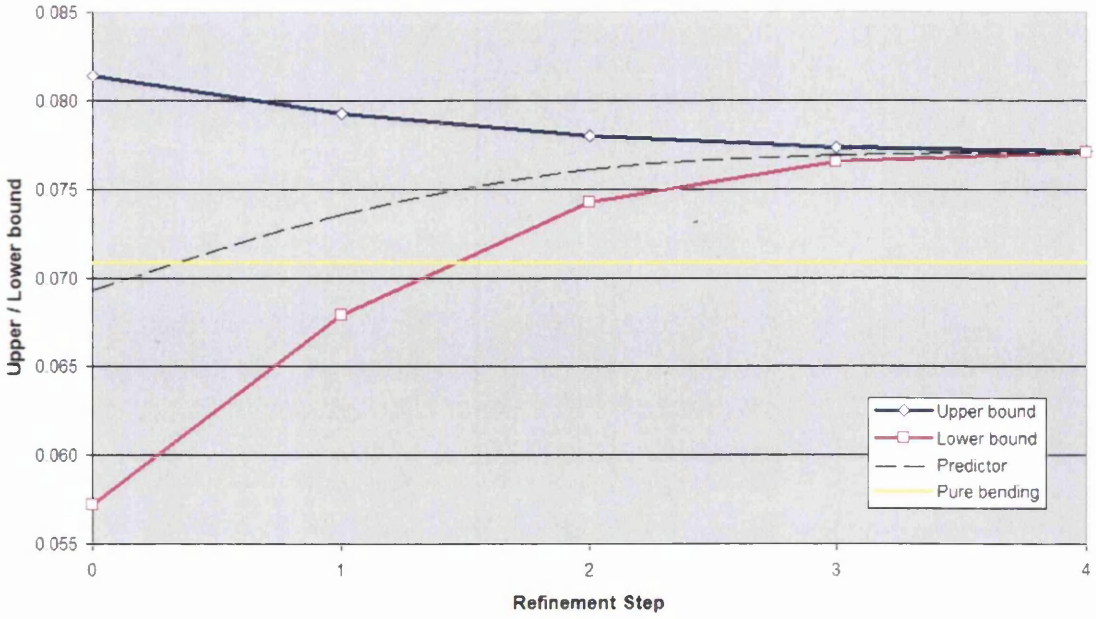

Figure 6.66 Bound progress for the gabled frame

Table 6.20 shows the corresponding bound values. A discrepancy of 8.7496% is observed for the simulated results with respect to the theoretical value.

Gabled frame				
Step	Upper bound	Lower bound	Predictor	Theoretical
0	0.08136	0.05720	0.06928	
1	0.07925	0.06788	0.07357	
2	0.07799	0.07424	0.07611	
3	0.07733	0.07651	0.07692	
4	0.07709	0.07702	0.07706	0.07086

Table 6.20 Bound values for the gabled frame

Figure 6.67 depicts the collapse mechanism obtained from the present finite element simulation.

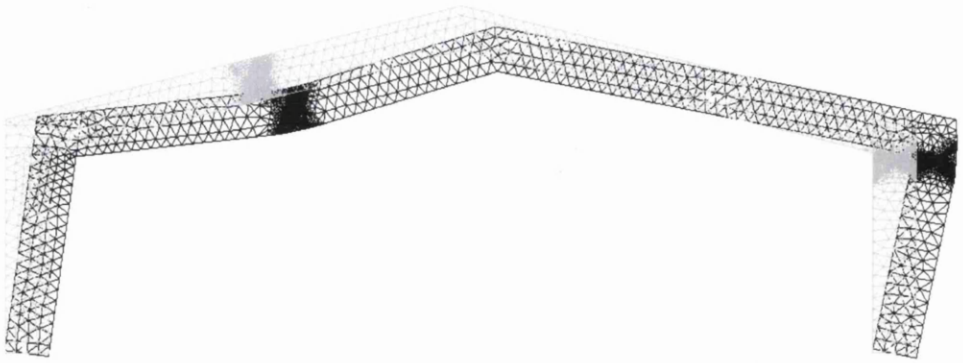

Figure 6.67 Collapse mechanism for the gabled frame

6.5.6 Reticular frame with concentrated loads

The two-storey frame taken from Jirásek and Bazant [7] and sketched in figure 6.68 is next analysed. Again, the problem description and the collapse mechanism found by the referred authors are given in figure 6.68i) and 6.68ii), respectively.

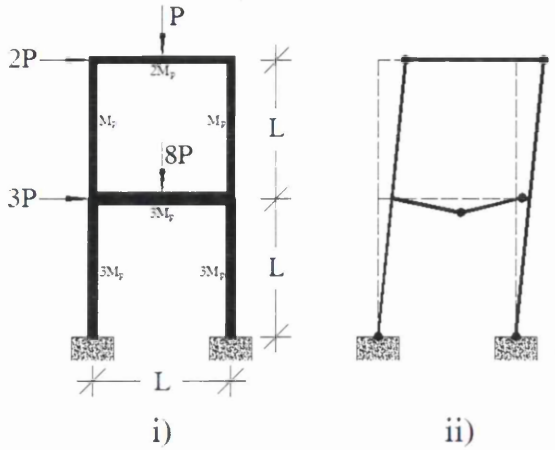

Figure 6.68 Problem setting for the frame P

The bounds sequence graph is presented in figure 6.69 along with the theoretical reference value line. The simulation bounds listing for this problem is written in table 6.21. A kinematical solution found by Jirásek and Bazant leads to expression $P_u = 5M_p / 11L$, showing a simulation discrepancy of 9.248%

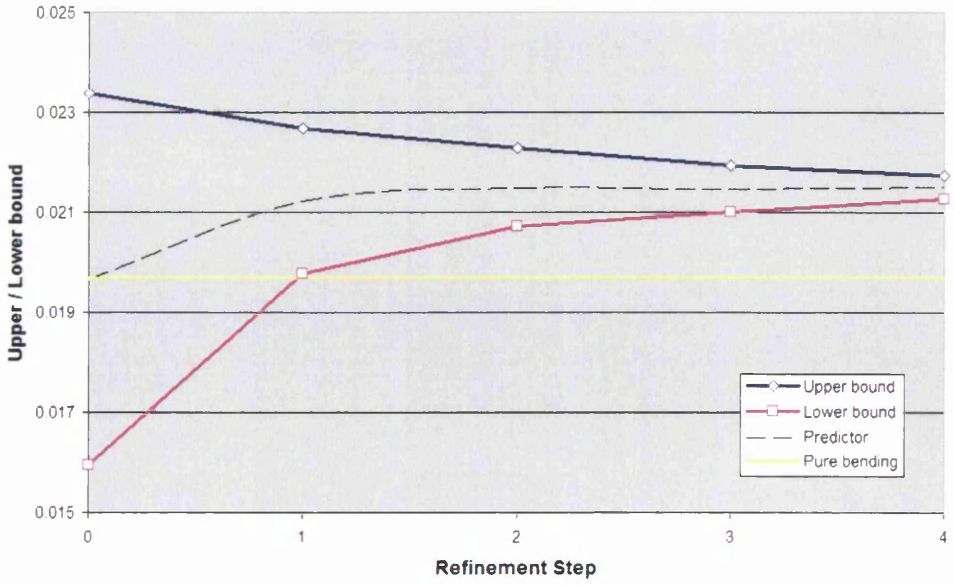

Figure 6.69 Bound progression for frame P

Reticular frame P				
Step	Upper bound	Lower bound	Predictor	Theoretical
0	0.02336	0.01594	0.01965	
1	0.02267	0.01977	0.02122	
2	0.02228	0.02071	0.02149	
3	0.02193	0.02100	0.02147	
4	0.02174	0.02127	0.02150	0.01968

Table 6.21 Bounds listing for frame P

The failure mode produced from the finite element solution is given in figure 6.70, note the resemblance with the mechanism found by the referred authors using a kinematical solution.

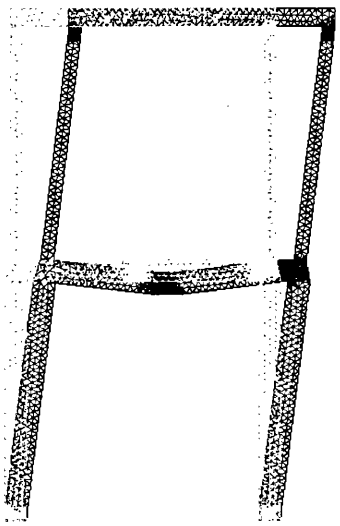

Figure 6.70 Collapse mechanism for frame P

6.6 References

1. Gaydon F.A., McCrum A.W. *A theoretical investigation of the yield point loading of a square plate with a central circular hole.* Journal of Mechanics and Physics of Solids, Vol. 2, 1954, pp. 156-169.
2. Gaydon F.A. *On the yield-point loading of a square plate with concentric circular hole.* Journal of Mechanics and Physics of Solids, Vol. 2, 1954, pp. 170-176.
3. Borges L.A., Zouain N., Huespe A.E., *A nonlinear optimisation procedure for limit analysis.* European Journal of Mechanics and Solids, Vol. 15, No. 3, 1996, pp. 487-512.
4. Casciano R., Cascini L., *A mixed formulation and mixed finite elements for limit analysis.* International Journal for numerical Methods in Engineering, Vol.18, 1982, pp. 211-243.

5. Ciria H., Peraire J. *Computation of upper and lower bounds in limit analysis using second-order cone programming and mesh adaptivity*. MSc Thesis, Massachusetts Institute of Technology, 2004.
6. Chakrabarty J., *Theory of plasticity*. McGraw-Hill, 1987.
7. Jirazek M., Bazant Z. *Inelastic analysis of structures*. John Wiley & Sons, Ltd., Chichester, 2001.
8. Beedle L.S., *Plastic design of steel frames*. John Wiley and Sons, Inc., 1958.

Chapter 7

Conclusions

7.1 Overview

A new approach to the *limit analysis* problem has been developed in the course of the present research work. The investigation aims to present the computational mechanics community, especially with emphasis in engineering applications, with a new procedure to help assess the collapse load multiplier for a given problem setting in *plane stress*. With the intention of providing a cost-effective solution, the present proposal represents the first step in the application of this new procedure for the analysis of *plane problems*.

The conventional *finite element* discretization procedure is used to construct a *kinematic* solution to the limit analysis problem, that is, to find an *upper bound* to the collapse load multiplier. A *plastic potential* derived from the principle of *maximum plastic dissipation* is employed for this purpose. The construction of a basic finite element discretisation space with the use of constant strain 3-noded triangular elements is employed to assess the applicability and further potential of the method. The use of linear elements is preferred in conjunction with an *h*-adaptive scheme based on element subdivision, as a means to enhance the accuracy in the evaluation of the limit load. The minimization problem implied by the *upper bound theorem* of limit analysis is resolved through the definition of a Lagrangian functional, by which a minimum can be attained. The discrete form of the finite element optimisation problem leads to a nonlinear problem resolved by the Newton-Raphson method. An

iterative form of the minimization problem is then produced, which reflects the characteristics of a conventional non-linear finite element problem.

The solution of the kinematic problem yields a velocity field, as is usual in this approach, and a set of point-wise stress and strain-rate tensor definitions, in the conventional sense.

With the kinematic solution at hand, a *static* solution is sought. However, in contrast with the elastic problem, the lack of complementary energy (or plastic potential) implied by the stress-strain curve for a rigid-plastic material makes it impossible to define a *force*-method (static approach) as opposed to the *displacement*-method (kinematic approach). Under these circumstances, instead of considering the application of a costly optimisation procedure based on static conditions under a finite element discretization, a more practical, less resource demanding solution is proposed.

The static approach, that is, a *lower bound* evaluation of the collapse load multiplier, should: a) comply with equilibrium conditions, that is, internally and externally (at the boundary); and b) meet conditions of *plastic admissibility* over the stress field. Under this conditions a new proposal to the lower bound evaluation is assessed, based on the kinematic solution of the local problems, i.e. on elemental volumes, after a flux equilibration procedure allows us to determine stress distributions along the inter-element edges. These distributions meet local equilibrium, and continuity conditions across the inter-element edges. An aggregate solution, referred to as *the integrated approach* in the present work, produces a lower bound to the collapse load multiplier. This bound is computed by summing all the elemental contributions to the static limit capacity. This approach rests on the attainment of a proper kinematic solution, as the flux equilibration procedure is carried out from the data sets produced by the upper bound finite element procedure.

To enhance the accuracy of the solution within the practical limits, an adaptive refinement scheme has been developed, in order to provide an enclosing interval defined by the bound values, that is, the upper and lower bounds, which reduces as the refinement steps progress up to the definition of an interval close enough to predict a

collapse load multiplier. An *adaptive indicator* has been defined to control the adaptive refinement process. This is computed as the local contributions to the *total bound gap*. The option of a uniform refinement sequence is also provided, leading to the same bound progression sequence but implying an increased amount of storage and processing time due to a greater number of unknowns in the solution.

The theoretical aspects of this proposal and the details of their implementation into a computational tool are described in the previous chapters. In the present chapter, a series of conclusive statements are made to assess the validity and scope of the present approach, based on the main theoretical characteristics of the procedures, and on the analysis of the results in chapter 6. Steps forward within the context of the present proposal are also given below.

7.2 Contributions

Within the present research framework, a series of elements pertaining to this solution proposal represent specific contributions to the current state of developments on limit state analysis, as discussed in the introductory chapter 1. An account of these characteristic elements of the proposed solution is given in the following paragraphs.

Upper bound implementation

A strict kinematic finite element limit analysis solution, i.e. leading to an upper bound to the true collapse load multiplier has been attained. The velocity (displacement) based finite element solution approach has been brought forward previously through the work of Ponter and Carter [1], and of Ponter, Fuschi and Engelhardt [2]. However, an optimisation procedure based on the Newton-Raphson, that is a *tangent* method, has been used in the present work, rather than a *secant* method, as used by Ponter *et al.* In the present solution, a regularizing parameter and a degree-of-freedom reduction procedure in the tangent matrix have been used to be able to compute the upper bound value through the Newton-Raphson method. Note that various approaches use the finite element discretization basis, but the solution methods can be notably different. For instance, the case of a bounds approach which exploits duality, as presented by Christiansen [3] and recently by Ciria and Peraire [4]; or the mixed

finite element solutions presented by Casciaro and Cascini [5], or the mixed formulation solved by optimality conditions presented by Borges, Zouain and Huespe [6]. Another good example is the recent work of Lyamin and Sloan [7,8]. All of these authors use an optimisation approach requiring the use of resource demanding procedures to solve both the kinematic and static limit analysis problem. Refer to chapter 3 and chapter 5 for a detailed description of the present upper bound implementation.

Lower bound formulation

A new lower bound formulation has been proposed and tested in the course of the present research work. A solution to the limit analysis static problem is attained through a procedure that accounts for every local contribution to the static plastic capacity of the body, in an integrated approach. A local contribution is determined from the solution of a local problem. Only kinematic solutions are required, either for the global, coupled kinematic solution, or for the local problems. This fact makes the proposed solution independent of a stress-based finite element analysis. To the best of our knowledge, this approach has not been undertaken previously. We refer the reader to the details of this new proposal and implementation in chapter 3, chapter 4 and chapter 5.

Bound gap and Adaptivity

With the aim of providing an efficient solution, the original goals set at the beginning of the present research work included the implementation of an adaptive refinement scheme for the limit analysis problem. This implies the definition of an adaptivity control parameter, in order for the adaptive procedure to distribute the parameter evenly across the body volume. Typically an error bound is used; however in the present approach the fact that the difference between the kinematic load multiplier, i.e. the upper bound, and the static load multiplier, i.e. the lower bound, provides a measure of closeness to the true collapse multiplier, understood as an enclosing interval, confining the true value. This interval reduces progressively as the number of elements in the mesh increases, that is, through a uniform or adaptive mesh refinement, thus setting a measure of the *error* incurred in finding the true collapse

load multiplier at each refinement step. As the enclosing interval is computed from the bound values, it has been termed *bound gap*. A local bound gap can be determined from the difference in contributions to both the upper and lower bounds at the element level. This *elemental gap* is used as the adaptivity control parameter in the proposed adaptive refinement procedure. Refer to chapter 3, chapter 4 and chapter 5 for details on the formulation and implementation of the adaptive scheme.

A good performance of the present solution has been observed when compared against reference results, especially with the results obtained by Borges, Zouain and Huespe [6] and more recently by Ciria and Peraire [4]. In addition, an adaptive refinement strategy applied also by Ciria and Peraire, permits us perform a thorough comparison of the adaptive scheme as developed in the present solution package, with a very good outcome.

7.3 Future work

At present, the variety of approaches taken to solve the limit analysis problem is vast. The solution procedures developed in the course of this research work represent a first approach to this new lower bound formulation for plane modelling, specifically for plane-stresss problems. In view of the present achievements, many possibilities arise for the extension of the present state of the investigations to broader modelling conditions, criteria and applications. A series of opportunity areas for extension of the present work can be envisaged within the following set of applications:

1. *Plane strain modelling conditions.* This is a natural step forward given the present analysis conditions. A new plastic potential definition will be needed and a way of coping with the incompressibility condition.
2. *Three-dimensional limit analysis.* An extension of the present solution procedures can be developed to produce an analysis package for standard materials. An extended version of the flux equilibration procedure will be required.
3. *Alternative yield criteria.* Consideration of other yield criteria as that of the Mohr –Coulomb criterion for porous materials constitutes an ample area of application.

4. *Structural elements, including plates and shells.* A complete reformulation is implied by this approach, using the basic concepts and procedures included in the present solution.
5. *Shakedown analysis.* Extension to cyclic loading-unloading conditions, instead of constant load *static collapse*, implies an extended, more complex analysis due to consideration of elastic-plastic conditions. The present approach can provide some of the elements required by such an analysis, but extensive reformulation is probably required.

7.4 References

1. Ponter A.R.S., Carter K.F., *Limit state solutions, based upon linear elastic solutions with a spatially varying elastic modulus*, Comput. Methods Appl. Mech. Engrg. Vol. 140 (1997) 237-258.
2. Ponter A.R.S., Fuschi P., Engelhardt M., *Limit analysis for a general class of yield conditions*, Eur. J. Mech. A/Solids, Vol. 19 (2000) 401-421.
3. Christiansen, E. *Computation of limit loads*. International Journal for Numerical Methods in Engineering. Vol. 17 (1981) 1547-1570.
4. Ciria H., Peraire J., *Computation of upper and lower bounds in limit analysis using second-order cone programming and mesh adaptivity*. MSc Thesis, Massachusetts Institute of Technology, 2004.
5. Casciaro R., Cascini L., *A mixed formulation and mixed finite elements for limit analysis*. International Journal for Numerical Methods in Engineering, Vol. 18 (1982) 211-243.
6. Borges L.A., Zouain N., Huespe A.E. *A nonlinear optimization procedure for limit analysis*. European Journal of Mechanics, A/Solids, Vol. 15, No. 3 (1996) 487-512.
7. Lyamin A.V., Sloan S.W., *Upper bound limit analysis using linear finite elements and nonlinear programming*. Research Report 199.01.2001, Dept. of Civil, Surveying and Environmental Engineering, The University of Newcastle, Australia, 2001.
8. Lyamin A.V., Sloan S.W., *Lower bound limit analysis using non-linear programming*. International Journal for Numerical Methods in Engineering, Vol. 55 (2002) 573-611.

Appendix A

Dual finite element discretization

In his work, Christiansen [1] used a family of discretizations of the mixed form in (2.63) to solve the continuous duality problem in expressions (2.58) to (2.63). The approximation is made by a Finite Element approach, in which the volume V is divided into elements and corresponding finite element function spaces are considered, namely X_h for $\boldsymbol{\sigma}$ and Y_h for $\dot{\boldsymbol{u}}$, where h is a discretization parameter conventionally indicating the linear size of the elements. Under these conditions the problem can be solved as a discrete mathematical programming formulation, so that a number of optimisation techniques can be used, and collapse stress and velocity fields can be approximated simultaneously. For triangular elements a linear finite element function for $\dot{\boldsymbol{u}}_h$ is used, letting the discrete velocities to be continuous, and to have bounded first order derivatives. When computing the internal work rate from expression (2.55), $\boldsymbol{\sigma}_h$ need not be continuous, and hence X_h may be defined by constant element functions, and since the collapse fields may have discontinuities, the functions need not be smoother than necessary, thus for triangular elements constant-linear function spaces can be used for the pair $(\boldsymbol{\sigma}_h, \dot{\boldsymbol{u}}_h)$. Under these conditions an easier discretization is used with $\dot{\boldsymbol{u}}_h$ continuous, as follows. Let

$$B_h \subseteq B \cap X_h \tag{A.1}$$

and

$$C_h = \left\{ \dot{\boldsymbol{u}}_h \in Y_h \mid F\left(\dot{\boldsymbol{u}}_h\right) = 1 \right\} \tag{A.2}$$

So that the discrete problem becomes

$$\gamma_h^c = \max_{\boldsymbol{\sigma}_h \in B_h} \min_{\dot{\boldsymbol{u}}_h \in C_h} a(\boldsymbol{\sigma}_h, \dot{\boldsymbol{u}}_h) = \min_{\dot{\boldsymbol{u}}_h \in C_h} \max_{\boldsymbol{\sigma}_h \in B_h} a(\boldsymbol{\sigma}_h, \dot{\boldsymbol{u}}_h) \tag{A.3}$$

The following bases for the finite dimensional spaces X_h and Y_h are defined

$$\boldsymbol{\sigma}_h = \sum_{j=1}^{M} x_j \varphi_j \ , \ \dot{\boldsymbol{u}}_h = \sum_{i=1}^{N} y_i \psi_i \tag{A.4}$$

where M is 3 times the number of nodes for $\boldsymbol{\sigma}_h$ in bi-dimensional models, while N is 2 times the number of nodes for $\dot{\boldsymbol{u}}_h$, with

$$F(\dot{\boldsymbol{u}}_h) = \sum_{i=1}^{N} y_i F(\psi_i) = \sum_{i=1}^{N} y_i F_i = \langle \mathbf{F}_h, \mathbf{y} \rangle_N \tag{A.5}$$

where $\mathbf{F}_h$ is the vector $\left(F(\psi_i)\right)_{i=1}^{N}$, and $\langle \cdot, \cdot \rangle_N$ is the inner product in $\mathbb{R}^N$. Also we have

$$a(\boldsymbol{\sigma}_h, \dot{\boldsymbol{u}}_h) = \sum_{j=1}^{M} \sum_{i=1}^{N} x_j y_i \ a(\varphi_j, \psi_i) = \sum_j \sum_i x_j y_i \ a_{ij} \tag{A.6}$$

$$a(\boldsymbol{\sigma}_h, \dot{\boldsymbol{u}}_h) = \langle \mathbf{A}\mathbf{x}, \mathbf{y} \rangle_N = \langle \mathbf{x}, \mathbf{A}^T \mathbf{y} \rangle_M \tag{A.7}$$

where $\mathbf{A}$ is the $N \times M$ matrix with

$$a_{ij} = a(\varphi_i, \psi_i) \tag{A.8}$$

and with $\mathbf{A}^T$ being the transposed matrix.

Thus, the discrete problem can be rewritten as

$$\gamma_h^c = \max_{\mathbf{x} \in B_h} \min_{\mathbf{y} \in C_h} \langle \mathbf{A}\mathbf{x}, \mathbf{y} \rangle = \min_{\mathbf{y} \in C_h} \max_{\mathbf{x} \in B_h} \langle \mathbf{x}, \mathbf{A}^T \mathbf{y} \rangle \tag{A.9}$$

$$\gamma_h^c = \max_{\substack{\mathbf{x}\in B_h \\ \mathbf{Ax}=\gamma\mathbf{F}_h}} \gamma = \min_{\mathbf{y}\in C_h} D_h(\mathbf{y}) \tag{A.10}$$

where

$$D_h(\mathbf{y}) = \max_{\mathbf{x}\in B_h} \langle \mathbf{x}, \mathbf{A}^T\mathbf{y} \rangle \tag{A.11}$$

The set B_h should be convex and closed, and either bounded or the sum of a bounded set. It is worth noting that problems modeled in plane stress imply a bounded set, while plane strain and three-dimensional models have unbounded sets.

Definition A.1

The discretization in expressions (A.3) to (A.10) is called *purely static* if on X_h the discrete equilibrium equation implies the continuous equilibrium equation, both on weak form. This is equivalent to the following implication for any $\boldsymbol{\sigma}_h \in X_h$

$$a(\boldsymbol{\sigma}_h, \dot{\boldsymbol{u}}_h) = F(\dot{\boldsymbol{u}}_h) \ \forall \dot{\boldsymbol{u}}_h \in Y_h \ \Rightarrow \ a(\boldsymbol{\sigma}_h, \dot{\boldsymbol{u}}) = F(\dot{\boldsymbol{u}}) \ \forall \dot{\boldsymbol{u}} \in Y \tag{A.12}$$

Since $B_h \subseteq B$, it follows from the maximization in (A.10) that a purely static method approximates γ^c from below and then is a lower bound method. It suffices that the static problem in (2.59) be satisfied for the discrete collapse stress field $\boldsymbol{\sigma}_h^c$.

Definition A.2

The discretization in expressions (A.3) to (A.10) is called *purely kinematic* if on Y_h the discrete energy dissipation rate in (A.11) is exact, or equivalently

$$\max_{\boldsymbol{\sigma}_h\in B_h} a(\boldsymbol{\sigma}_h, \dot{\boldsymbol{u}}_h) = \max_{\boldsymbol{\sigma}\in B} a(\boldsymbol{\sigma}, \dot{\boldsymbol{u}}_h) \ \ \forall \dot{\boldsymbol{u}}_h \in Y_h \tag{A.13}$$

From the minimization in expression (A.10) it follows that a purely kinematic method is an upper bound method, and that $\gamma_h^c \geq \gamma^c$ if only (A.13) holds for $\dot{\boldsymbol{u}}_h^c$.

Christiansen further describes a dependency of the discretization, either static or kinematic, on the choice of external forces and elements, which is established on the following theorems.

Theorem A.1

Assume that in the discrete duality the following implication holds for any $\boldsymbol{\sigma}_h \in X_h$:

$$a(\boldsymbol{\sigma}_h, \dot{\boldsymbol{u}}_h) = 0 \quad \forall \dot{\boldsymbol{u}}_h \in Y_h \;\Rightarrow\; div\, \boldsymbol{\sigma}_h = 0 \text{ in } V \text{ and } \boldsymbol{\sigma}_h \mathbf{n} = 0 \text{ on } S_t \qquad \text{(A.14)}$$

Let the external forces be of the form

$$\mathbf{f} = -div\, \boldsymbol{\tau} \text{ in } V \text{ and } \mathbf{g} = \boldsymbol{\tau}\mathbf{n} \text{ on } S_t \qquad \text{(A.15)}$$

for some discrete stress tensor $\boldsymbol{\tau} \in X_h$. Then the method is purely static and we have

$$\gamma_h^c \leq \gamma^c \qquad \text{(A.16)}$$

This theorem expresses the fact that a stress field-velocity field combination exists that produces a zero dissipation rate, and with the work rate produced by the external forces being positive, the static discretization must approach the collapse multiplier from bellow.

From these statements, it can be shown that condition (A.14) holds with piecewise linear elements for $\dot{\boldsymbol{u}}_h$ and piecewise constant elements for $\boldsymbol{\sigma}_h$. Condition (A.15) is satisfied if the external forces are piecewise constant.

Theorem A.2

Assume that the material is homogeneous. Choose piecewise linear elements for $\dot{\boldsymbol{u}}_h$ and piecewise constant elements for $\boldsymbol{\sigma}_h$ such that $B_h = B \cap X_h$. Then the method is

purely kinematic with

$$\gamma_h^c \geq \gamma^c \tag{A.17}$$

We can see that for $\dot{\boldsymbol{u}}_h \in Y_h$ we have

$$D(\dot{\boldsymbol{u}}_h) = \sup_{\boldsymbol{\sigma} \in B} \int_V \sigma_{ij} \frac{\partial \dot{u}_{hj}}{\partial x_i} \, dV \tag{A.18}$$

So that, since $\partial \dot{u}_{hj} / \partial x_i$ is constant on each element, σ_{ij} in the above optimisation is piecewise constant with the optimal value in B. Hence the supremum is obtained for $\boldsymbol{\sigma} \in B \cap X_h = B_h$, which implies $D(\dot{\boldsymbol{u}}_h) \leq D_h(\dot{\boldsymbol{u}}_h)$. These conditions permit the kinematic solution to closely approximate or actually equal the true collapse multiplier.

If a sequence of the discrete solutions $(\boldsymbol{\sigma}_h^c, \dot{\boldsymbol{u}}_h^c)$ converges, then the limit is a solution to the continuous problem. From the discussion above, it is strongly recommended to use piecewise linear elements for $\dot{\boldsymbol{u}}_h$ combined with constant elements for $\boldsymbol{\sigma}_h$. In some cases depending on the external load (piecewise constant), the exact limit multiplier $\gamma_h^c = \gamma^c$ can be obtained.

References

1. Christiansen, E. *Computation of limit loads*. International Journal for Numerical Methods in Engineering. Vol. 17, 1981, p.1547-1570.

Appendix B

Residual Force indicator

Let us consider a body in plane stress, which is subject to proper boundary conditions, load and support as shown on the figure B.1. Let us further identify an internal portion of the body defined by area $\bar{A}$ as depicted in the figure.

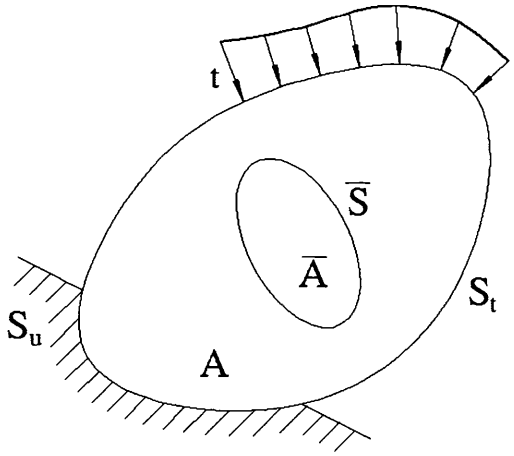

Figure B.1 Body in plane stress with an isolating portion $\bar{A}$

If the body conforms to equilibrium conditions, neglecting body forces, we have:

$$\begin{aligned} -div\ \boldsymbol{\sigma} &= 0 \quad \text{in } \bar{A} \\ \boldsymbol{\sigma}\mathbf{n} &= \mathbf{t} \quad \text{on } S_t \end{aligned} \tag{B.1}$$

If we isolate the portion of the body, as shown in figure B.2, to retain equilibrium the body piece would have to be acted upon by an equilibrating stress distribution along the surface $\bar{S}$, of equal magnitude and opposite direction to the action the portion

itself exerts over the rest of the body along $\bar{S}$. Let us denote this internal *equilibrating* distribution as $\mathbf{t}_{int}(s)$, so that equilibrium conditions can be verified by stating

$$\oint_{\bar{S}} \mathbf{t}_{int}(s)\,ds = 0 \tag{B.2}$$

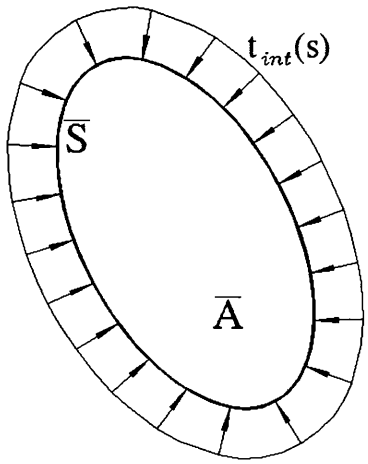

Figure B.2 Isolated portion of the original body

Now let there be an external distribution $\mathbf{t}_{int}(s)$, coming from the adjacent portion of the body. If we consider a discretized solution space, then distribution $\mathbf{t}_{int}(s)$ does not necessarily comply with equilibrium conditions, which we will call a *disequilibrated* stress distribution. This kind of distribution would not meet equilibrium conditions, but would produce what we call a *residual force* vector $\mathbf{R}_F$, so that

$$\oint_{\bar{S}} \mathbf{t}_{int}(s)\,ds = \mathbf{R}_F \tag{B.3}$$

From all the possible distributions of this kind, we are interested in the special case of a distribution resulting from an approximate finite element solution.

Given the conditions of our analysis, i.e. plane stress with triangular linear elements, we specialize our discussion by considering the portion of a body described above as a triangular linear element, shown in figure B.3. Note that $\bar{S}^e = \bar{S}_1^e \cup \bar{S}_2^e \cup \bar{S}_3^e$ as implied in figure B.3. Thus, let us define the *element stress distribution* on each of these surfaces by

$$\mathbf{t}_i^e = \boldsymbol{\sigma}_{a_i} \mathbf{n}_i^e \quad \text{with surface index } i = 1,2,3 \tag{B.4}$$

with $\boldsymbol{\sigma}_{a_i}$ being the stress tensor of an adjacent element at its Gauss point, and $\mathbf{n}_i^e$ the unit vector normal to the surface i. Note that the notation $\mathbf{t}_i^e$ indicates a traction coming from the stress in element a_i adjacent to element e. For the present finite element discretization, this gives a constant stress distribution along the surface. Clearly, the adjacent elements would contribute a disequilibrated distribution along surface $\overline{S}^e$.

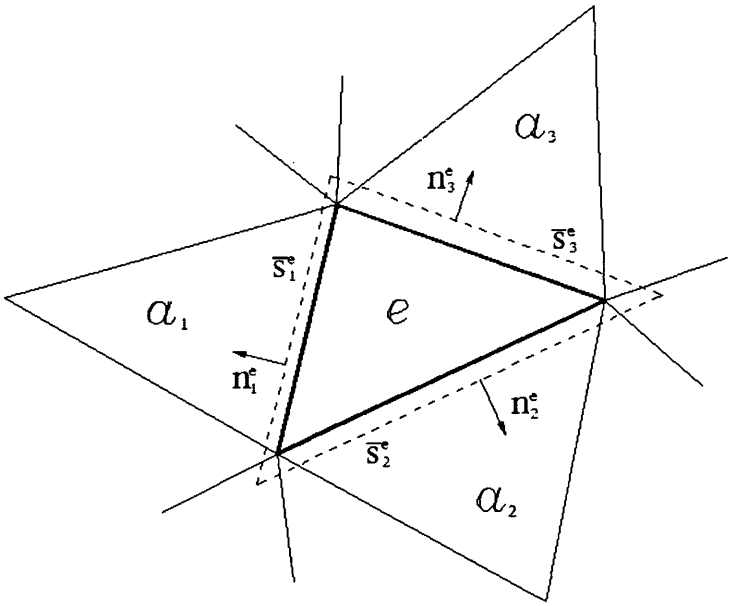

Figure B.3 Finite element as the local volume and its adjacent elements

Under this conditions and using the notation just described, the value of $\mathbf{R}_F$ can be computed as

$$\mathbf{R}_F = \sum_{i=1,2,3} \mathbf{t}_i^e \overline{S}_i^e = \sum_{i=1,2,3} \sigma_{a_i} \mathbf{n}_i^e \overline{S}_i^e \tag{B.5}$$

in which i is a surface index.

All the definitions discussed above are defined over a single element, but for these concepts to be useful we need to apply them over the whole domain, that is

considering all the elements in the finite element mesh. In fact, we are interested in two special values resulting from these formulas, that is, the *average residual force indicator* r_F^{ave}, and *maximum residual force indicator* $r_F^{\max}$, defined as follows

$$r_F^{ave} = \sqrt{\frac{\sum_e \left\| \mathbf{R}_F^e \right\|^2}{m}} \tag{B.6}$$

and

$$r_F^{\max} = \max_e \left(\left\| \mathbf{R}_F^e \right\| \right) \tag{B.7}$$

where $e = 1,...,m$ is an element index and m is the total number of elements in the mesh. Clearly, $\left\| \mathbf{R}_F^e \right\|$ represents the magnitude of the residual force vector for element e, considering only in-plane components.